STRESS CORROSION CRACK INITIATION OF ALLOY 600 AND ALLOY 690 IN HYDROGENATED SUPERCRITICAL WATER

by

Tyler Elliot Moss

A dissertation submitted in partial fulfillment
of the requirements for the degree of
Doctor of Philosophy
(Materials Science and Engineering)
in The University of Michigan
2015

Doctoral Committee:

Professor Gary S. Was, Chair
Professor J. Wayne Jones
Associate Research Scientist John F. Mansfield
Professor Phillip Savage

ACKNOWLEDGMENTS

I would first like to thank my advisor and committee chair, Dr. Gary Was, for his continued support and guidance in completing this work. I would also like to offer my thanks to the members of my dissertation committee, Dr. Wayne Jones, Dr. John Mansfield, and Dr. Phillip Savage for their time and insight.

I thank my colleagues Dr. Elaine West, Dr. Pantip Ampornrat, Dr. Janelle Wharry, Dr. Anne Campbell, Dr. Cheng Xu, Dr. Mike McMurtrey, Dr. Gokce Gulsoy, Kale Stephenson, Stephen Raiman, Shyam Dwaraknath, Elizabeth Getto for their support and encouragement.
I would like to give special thanks to Dr. Zhijie Jiao, Stephen Raiman, and Dr. Kai Sun for their valuable assistance and mastery of operating the transmission electron microscope, Dr. Guoping Cao for conducting exposures of corrosion coupons at the University of Wisconsin, and Alexander Flick for his guidance in the high temperature corrosion laboratory.

Finally, I would like to thank my family: my parents, Cheryl and Eric, and my siblings, Colby and Brandon, and my future in-laws, Mary and Rich, for their continued support. Most of all I need to thank my fiancé, Alan Teets, for his love and support when I needed it most.

This work was supported by the Electric Power Research Institute under contract EP-P35621 and by Pacific Northwest National Laboratory under contract 102038.

TABLE OF CONTENTS

LIST OF TABLES

LIST OF FIGURES

LIST OF APPENDICES

ABSTRACT

STRESS CORROSION CRACK INITIATION OF ALLOY 600 AND ALLOY 690 IN HYDROGENATED SUPERCRITICAL WATER

by

Tyler Elliot Moss

Chair: Gary S. Was

Stress corrosion crack (SCC) initiation of highly resistant materials can be studied by conducting accelerated testing as long as there is no change in the cracking mechanism. The objective of this dissertation is to determine if accelerated SCC initiation testing of Alloy 600 and Alloy 690 can be conducted without changing the mechanism of crack initiation between subcritical and supercritical water. Unfortunately, the mechanism of crack initiation of these alloys is not known. This makes demonstrating whether there is a change in the SCC mechanism dependent on determining if there is a change in the oxidation, stress corrosion crack initiation morphology, and the temperature dependence of crack initiation between subcritical and supercritical water.

The corrosion environment was maintained at a fixed electrochemical potential above the Ni/NiO phase transition in the NiO stable regime by controlling the dissolved hydrogen concentration, with the location of the boundary determined by exposures of pure nickel. Exposures of unstressed corrosion coupons of Alloy 600 and 690 were conducted in

hydrogenated subcritical and supercritical water for characterization of the oxide morphology, structure, and composition. Tensile bars of Alloy 600 and Alloy 690 were strained in constant extension rate tensile experiments in both environments to characterize the crack initiation morphology and to determine the temperature dependence of crack initiation.

The oxidation for both alloys was consistent between subcritical and supercritical water, composed of a multi-layer oxide structure composed of particles of NiO and $NiFe_2O_4$ formed by precipitation on the outer surface and a chromium rich inner oxide layer formed by diffusion of oxygen to the metal-oxide interface. The crack initiation morphology of Alloy 690 was consistent between subcritical and supercritical water, and a mechanism of crack initiation was developed. The SCC initiation temperature dependence of both alloys shows no discontinuity or change in slope in the activation energy at the critical point. All available evidence supports a consistent mechanism of stress corrosion crack initiation in both hydrogenated subcritical and supercritical water for Alloy 600 and Alloy 690.

CHAPTER 1 - INTRODUCTION

Stress corrosion cracking of nickel alloys used in steam generators of pressurized water reactors (PWRs) has been a focus of intense investigation since the mid 1970's when the community realized the high degree of susceptibility of these alloys. A steam generator's purpose is to transfer the heat from water in the core (primary water) to a secondary water loop which then flashes to steam to turn turbines. Each steam generator contains thousands of tubes under high pressure made of Alloy 600 (Ni-16Cr-9Fe), which was found to be susceptible to stress corrosion cracking (SCC) after an incubation period of many years. A new alloy was developed with higher chromium content, Alloy 690 (Ni-30Cr-9Fe), and has proven to be resistant to cracking. There has been no evidence of primary water stress corrosion cracking (PWSCC) of Alloy 690 tubes in steam generators since they were first installed in 1989. This alloy has an excellent track record of no cracking observations in thousands of tubes and in cold worked tube plugs. Primary water reactors were initially licensed by the US Nuclear Regulatory Committee to operate for 40 years. Current regulations allow for life extensions of up to an additional 20 years. With the prospect of reactors operating even longer, up to 80 years, the need to understand degradation modes of materials used in steam generators has become more pressing even for materials that show excellent resistance to date. Given the past experience with long incubation times to crack initiation in Alloy 600, there is concern that SCC could eventually occur in the replacement material Alloy 690.

One of the major hurdles in studying SCC of Alloy 690 is its resistance to crack initiation. Accelerated testing can be used to study the cracking behavior and susceptibility of resistant materials as long as the acceleration method doesn't change the mechanism. Accelerated cracking tests are typically conducted by increasing the test temperature. To date, experiments have been conducted up to 360°C since further increases of the temperature would mean entering the supercritical water phase. If cracking continues to accelerate with temperature, testing in the supercritical regime could provide a very rapid test technique. However, it is unclear if the mechanism for cracking in supercritical water is the same as in subcritical water.

This thesis seeks to determine whether there is a change in the mechanism of crack initiation between subcritical and supercritical water in Alloy 690 and also in Alloy 600. Chapter 2 of describes relevant background information on SCC and oxidation of nickel alloys. Chapter 3 provides the experimental procedure and techniques used to generate the results presented in chapter 4. Chapter 5 discusses the results, focused on characterization of cracking in Alloy 690 and determining whether there is a change in the crack initiation mechanism between subcritical and supercritical water conditions. Chapter 6 lists the conclusions of this thesis.

CHAPTER 2 - BACKGROUND

In this chapter, a review of the published literature provides the background relevant to understanding the objectives, goals, and outcomes of this thesis. Section 2.1 describes the properties of materials used in this dissertation, nickel base Alloys 600 and 690. Section 2.2 reviews the properties of water used in pressurized water reactors and supercritical water, the accelerated testing environment. Section 2.3 provides an overview of the corrosion behavior of Alloys 600 and 690 in subcritical and supercritical water. Section 2.4 reviews the current state of knowledge of stress corrosion crack initiation of Alloy 600 and Alloy 690. The final section states the objective of this dissertation and outlines the experimental approach.

2.1 Metallurgy and mechanical behavior of nickel alloys

2.1.1 Microstructure

In service environments, the corrosion and embrittlement of nickel alloys has been found to be ultimately linked to the metallurgical structure. Intergranular corrosion, stress corrosion cracking, and corrosion fatigue have been associated with grain boundary microstructure and microchemistry and a host of other physical metallurgy attributes. Alloy 600, a nickel based alloy with 16% chromium has been widely used in pressurized water reactors (PWRs) and is largely representative of the characteristics of nickel alloys. Alloy 690 has the same iron content as Alloy 600 but with 30% chromium.

During aging, Inconel 600 undergoes a number of processes between the temperatures of 500 and 800°C. Chromium carbides precipitate at grain boundaries in the form of $M_{23}C_6$ or M_7C_3. This is accompanied by chromium depletion in the surrounding matrix. Trace elements such as P, S, Ti may also migrate to grain boundaries[1].

2.1.2 Plastic deformation of nickel alloys

Deformation of nickel alloys is initially characterized by an elastic response, where the material returns to its original shape after unloading and the strain is proportional to the load. At high enough stress (the yield stress), plastic flow occurs by movement of dislocations along their preferred slip plain. Additional dislocations are generated as yielding progresses and they begin to interact, increasing the flow stress required to move dislocations (work hardening). At the temperatures of interest, between 320°C and 450°C, and at slow tensile strain rates the deformation of austenitic alloys is characterized by dynamic strain aging (DSA). Dynamic strain aging is the mechanism of deformation that induces the Portevin-Le Chatelier effect, characterized by bursts of dislocation movement resulting in strain. At certain strain rates and temperatures the diffusion rates of solutes and velocity of dislocations are such that solutes can act to strengthen pinning of dislocations when they are temporarily arrested. Eventually the stress will be high enough to overcome the pinning, causing a burst of strain and a drop in the load on the sample, this process then repeats.[2] Many engineering alloys used in the nuclear power industry experience dynamic strain aging. This effect has been extensively studied in 316 stainless steel, but there have been only a few DSA studies published on Alloys 600 and 690. Mulford and Kocks[3] calculated an activation enthalpy of 0.92 eV for Alloy 600. Hänninen[4]

found that the enthalpy for Alloy 690 is about 1.65 eV. Samuel et al. and Almeida et al.[5,6] calculated the same enthalpy for Alloys 316 and 304 of 1.38 eV. Hale et al.[7] used several methods to calculate the enthalpy for Alloy 718 and found it lay between 1.0 and 1.4 eV. The above authors used their calculated enthalpy to link the interstitial atoms, either carbon or nitrogen, as the source of pinning sites. Moss and Was[8] studied dynamic strain aging of the same heat of Alloy 690 used in this work and 800H and observed type B serrations for the temperatures and strain rates used in this study as shown in Figure 2.1.

2.2 Water chemistry

2.2.1 Pressurized water reactor primary water

The primary loop PWRs is termed primary water, and consists of water with dissolved hydrogen to ~30cc/kg and additions of 2ppm lithium in the form of LiOH and 1200 ppm boron in the form of H_3BO_3. The addition of hydrogen reduces the free oxygen in the water and helps mitigate stress corrosion cracking by lowering the corrosion potential. While the overall cracking propensity is lower with hydrogen additions, there is a local maximum of cracking susceptibility of nickel alloys at dissolved hydrogen concentrations corresponding to the Ni/NiO boundary. Attanasio et al.[9] plotted the stress corrosion crack growth rate as a function of hydrogen level for Alloy 600 shown in Figure 2.2. The author observed an increase in crack growth rate by a factor of 3-4 when hydrogen was added in the amount of 13.8 cc/kg at 338°C. This concentration coincides with the Ni/NiO phase transition as measured by Attanasio et al.[10] using the contact electrical resistance method as shown in Figure 2.3. Morton et al.[11] concluded that the stability of NiO, not the dissolved hydrogen concentration, was the fundamental parameter influencing the susceptibility of nickel alloys to SCC.

The idea that the thermodynamic stability of nickel oxide imposed by the corrosion potential is key to SCC has been supported by Scott and Combrade's review[12] of the work of Economy et al.[13]. Economy[13] conducted RUB experiments at 400°C using a combination of steam and hydrogen partial pressures and did not observe a strong trend based on hydrogen partial pressure. However, when Scott re-plotted Economy's data based on the ratio between hydrogen and steam partial pressure he noted that the fastest time to failure occurred in experiments where the environment was close to the Ni/NiO transition line. A possible complication was found by Attanasio. During the contact electrode resistance measurements the author observed a difference between the theoretical and measured Ni/NiO boundary as shown in Figure 2.3. Attanasio's measurements of the phase boundary were verified using corrosion coupons.

Extensive experiments on the stability of nickel in water as a function of dissolved hydrogen concentration have been conducted by Attansio et al. [9,14] by contact electrode resistance measurements of oxide films up to 360°C. Further work was conducted to determine the thermodynamics of nickel oxidation by measuring the fugacity of hydrogen using a palladium-silver thimble and estimations of the Henry's law constant from unpublished data of Moshier and Witt [15]. However, Attanasio and Morton[10] found that the measured standard state entropy and enthalpy disagree slightly with data from thermodynamic tables. Kishima and Sakai [16] determined Henry's law constants for hydrogen in water in subcritical and supercritical water, but did not conduct experiments close to the critical point. Kishima also observed that the Henry's law constant varies with overall system pressure, such that higher pressures give higher values of Henry's constant.

2.2.2 Supercritical water

The water chemistry of high temperature water cooled reactors has a large effect on corrosion of structural materials. The standard water chemistry for PWR primary water is composed of water with a pH around 7.2, H_2 fugacity of 3 parts per million, and of a temperature ranging from 290 to 340°C. Of these factors, the fugacity and temperature are the most important when considering the Ni/NiO phase boundary. At these temperatures the physical properties of water are fairly consistent with many other water cooling systems. However, when the pressure is increased at sufficient temperature, the water undergoes a phase transition to supercritical water. In supercritical water properties relevant to corrosion such as density, pH, and the dielectric constant all begin to behave like a dense gas.

The supercritical water occurs above the critical point of water, 22.1 MPa and 37.4°C (Figure 2.4). Supercritical water (SCW) exhibits properties that are very different from the surrounding vapor and condensed phases. In the supercritical phase, hydrogen bonding is much weaker than in the liquid phase giving it properties similar to a dense gas[17]. Because of this, the density can vary greatly with small changes in temperature and pressure with the most significant changes in density occurring close to the critical point.

The density variations in SCW can be traced back to the effect of hydrogen bonding. At low density, water molecules can be present in the form of monomers or dimers[18]. At high density more complex forms may be present. The density of SCW has been found to be a function of pressure and temperature, as shown in Figure 2.5. At low pressures the density can be as low as

0.1 g/cc, and at high pressures it can be as high as 0.6 g/cc. For example, the low pressure region of SCW has a density comparable to that of argon at 10MPa. As the temperature is increased through the critical point, the density falls with the greatest change at low pressures. The density continues to change at low pressures until around 500°C where it levels off.

Variations in the dielectric constant, which is a measure of the extent to which ions are stabilized has been widely studied. Similar to the density trend, the dielectric constant drops rapidly beyond the critical point as shown in Figure 2.6. Because of this drop, SCW is able to dissolve organic substances that cannot be normally dissolved in regular water. This drop results in the poor ionization of electrolytes such as acids and salts in SCW, which is similar to the behavior of a gas.

The pH as a function of the ionic product (K_w) also changes drastically beyond the critical point. Below the critical point, the ionic product increases with temperature until it reaches a maximum around 300°C then drops rapidly in the supercritical regime as shown in Figure 2.7. Similar to the trends of density and dielectric constant, the ionic product decreases with increasing temperature but increases with increasing pressure. This trend indicates that most small organics and gases will be fully miscible in SCW. The ionic product has the following relation to pH:

$$\mathrm{pH} = -\frac{1}{2}\log \mathrm{K_w} \qquad (2.1)$$

This trend indicates that if neutral water is fed into a supercritical water system, the pH of the water will change as shown in Figure 2.8. For example, at STP neutral water has a pH of 7 where the same water will have a pH of close to 8.3 at 400°C and 25MPa.

2.3 Oxidation of Alloy 600 and Alloy 690

2.3.1 Supercritical water oxidation thermodynamics

Work by MacDonald et al.[19] and Cook et al.[20–22] has extended Pourbaix diagrams of nickel, iron, and chromium into the supercritical water regime. MacDonald et al. found that while the potential of the Ni/NiO boundary does change as a function of temperature, the phases present remain the same as shown in Figure 2.9 for pure water at 50 MPa. The slope of the pH dependent lines change with temperature due to the relationship of the corrosion potential (E) on the free energy of the reaction defined by the Nernst equation:

$$E = E^o - \frac{RT}{nF} \ln \frac{(\mathrm{B})^b (\mathrm{H_2O})^d}{(\mathrm{A})^a (\mathrm{H^+})^m} \qquad (2.1)$$

Where E^o is the standard state corrosion potential, R is the gas constant, T is Temperature, and F is Faraday's constant. The terms in the natural logarithm are the activities of the reaction: $a\mathrm{A} + m\mathrm{H^+} + n\mathrm{e^-} = b\mathrm{B} + d\mathrm{H_2O}$. Similar behavior was observed by Cook et al.[20–22] for nickel, iron, and chromium at 25 MPa and an ion concentration of 10^{-8} mol/kg between 350°C and 400°C as shown in Figure 2.10 to Figure 2.12. Dashed vertical lines indicate the pH of neutral water at each condition. The effect of pressure on the stability of oxides is shown in Figure 2.13 for the supercritical water conditions[19]. From the diagram it is clear that the water equilibrium lines do not change but there is a shift in the Fe lines. As the pressure is reduced to 30 MPa, the diagram shifts down along the same slope as the water lines with no apparent change to the equilibrium points above a pH of 6.

2.3.2 Alloy 600 oxidation

Oxide films on nickel base alloys in PWR conditions consist of a duplex oxide structure with an iron-rich spinel outer oxide and a chromium-rich inner oxide as shown in Figure 2.14[23–31] . The composition and thickness of the oxide layers are highly dependent upon exposure conditions[24,28,32,33]. By varying the hydrogen concentration around the Ni/NiO transition in experiments on Alloy 600, Peng et al.[28] were able to create a thick inner oxide layer deficient in Cr at low hydrogen concentrations, and a thin chromium rich oxide layer at high hydrogen concentrations as shown in Figure 2.15. The surface condition of exposed coupons can affect the oxide formed, and Carrette[33] observed an increase in the thickness of the oxide layer, and a Cr depleted surface layer in the alloy with higher cold work. No Cr depleted layer was observed on electropolished samples and the oxide layer was discontinuous, highlighting the importance of short-circuit diffusion in low temperature exposures. It is also observed that surface cold work increases the cation release kinetics[33,34]. The metal ion concentration of the test solution has also been observed to affect the size, density, and occurrence of crystallite oxidation on the surface. Crystallite size and density decreased[33] when corrosion tests were carried out in continuously cleaned and purified solutions. Experiments conducted in titanium autoclaves have shown an absence of surface oxide particles usually observed on coupons exposed in stainless steel autoclaves, demonstrating the effect of metal ion contribution from the vessel material[24].

In experiments conducted in PWR primary water in stainless steel autoclaves, surface films observed on Alloy 600 have exhibited variations in the microstructure. However, intergranular oxidation has been consistently observed in laboratory tests with varying levels of porosity in the attacked boundary and shows the presence of Cr_2O_3 in the grain boundary oxide[35,36].

Combrade et al.[30] observed a multi-layer oxide structure with iron-rich spinel particles on the surface and a dual layer inner oxide composed of chromium-rich spinel and Cr_2O_3 as seen in planar view in Figure 2.16. Very similar oxidation behavior was observed in studies focusing on the effect of hydrogen at levels close to primary water conditions[28,29]. The main discrepancy between studies is the presence of Cr_2O_3 at the metal-oxide interface. Figure 2.18 shows a TEM micrograph of an electropolished coupon of Alloy 600 with a continuous chromium rich spinel layer and no formation of Cr_2O_3[27,31]. The electropolished condition agrees well with investigations performed on steam generator tubes removed from U.S. and French PWRs, where the inner layer consisted of chromium-rich spinel[37,38].

2.3.3 Alloy 690 oxidation

Surface films observed on Alloy 690 exposed to PWR primary water conditions have also shown some variation, but generally have a structure similar to that on Alloy 600. Micrographs of Alloy 600 and Alloy 690 are shown from the same exposure in Figure 2.16 and Figure 2.17, demonstrating the similarity in the oxide layers formed. Sennour and et al.[23] and Combrade et al.[30] found a multi-layer structure with an outer layer of iron-rich spinel particles and a continuous inner layer of chromium-rich spinel with Cr_2O_3 present at the metal-oxide interface with no preferential grain boundary oxidation shown in TEM micrographs in Figure 2.19 and schematically in Figure 2.20. However, investigations conducted by Olszta et al. [25,26] revealed internal oxidation in the matrix below the continuous chromium rich oxide layer consisting of Cr_2O_3 platelets surrounded by chromium rich MO (Fm-3m space group) phase oxide penetrations. Figure 2.21 shows SEM backscatter electron micrographs of surface cross sections of Alloy 690 corrosion coupons exposed to 360°C PWR primary water for 1000h. Higher magnification images of the highlighted regions show a thin oxide layer above oxide

filaments as small as ~5nm[26]. The continuous oxide layer was found via TEM to have a MO structure (Fm-3m space group), but APT analysis has shown that the composition is closer to a M_3O_4 spinel. The internal oxidation zone was observed to thin at chromium depleted grain boundaries, attributed to fast diffusion of chromium along the boundary to form a protective layer of Cr_2O_3 at the surface above the grain boundary shown in the cross section SEM micrograph in Figure 2.22 and the schematic in Figure 2.23. The internal oxidation morphology bears a striking similarity to that observed by Wood et al.[39] during high temperature gas exposures of binary nickel-chromium alloys shown in Figure 2.24.

2.4 Crack initiation of Alloy 600 and Alloy 690

2.4.1 Characteristics of Alloy 600 crack initiation

Alloy 600 has been shown to initiate and grow cracks in service conditions as well as in the laboratory setting since the 1960's. Since then, a greater understanding has developed regarding the factors affecting cracking, but the mechanism is still uncertain. Environmental effects such as the amount of dissolved hydrogen have been demonstrated to affect the crack growth and initiation behavior[11,40,41]. Morton et al.[11] observed up to 3 times higher crack growth rates at dissolved hydrogen concentrations close to the Ni/NiO phase boundary shown. The peak in the crack growth could potentially be an issue for laboratory testing because the amount of dissolved hydrogen required to remain a fixed electrochemical potential from the Ni/NiO boundary changes as a function of temperature[14]. Morton et al.[42] demonstrated that errors could be introduced in measurements of the activation energy of crack growth by testing at a fixed hydrogen concentration and at a constant electrochemical potential from the Ni/NiO boundary as shown in Figure 2.25. The effect of hydrogen was also seen in crack initiation

experiments performed by Etien et al.[41], where Alloy 600 tensile bars held at constant load in hydrogenated water on the Ni stable side of the phase boundary were more susceptible to crack initiation. The activation energy for crack initiation of mill annealed Alloy 600 was measured by Richey et al.[43] to be 140±25 kJ/mol by electric potential drop in situ monitored smooth constant load samples. Richey et al.[43] also observed that the crack initiation susceptibility of Alloy 600 increased at the Ni/NiO boundary, roughly following the trend observed in crack growth experiments as shown in Figure 2.26.

The morphology of cracking and grain boundary degradation in Alloy 600 have been studied in detail by several researchers[35,36,44]. Fournier et al.[44] conducted exposures of unstressed tensile bars in 325°C PWR primary water and found that cracking occurred during post exposure room temperature straining due to preferential oxidation of grain boundaries. The depth of grain boundary oxidation was observed to have a maximum at hydrogen concentrations corresponding to the Ni/NiO boundary. The oxidation consisted of a chromium rich spinel structure with chromium depletion in the grain boundary ahead of the oxidation front, suggesting that accelerated mass transport may play an important role in the oxidation process shown in Figure 2.27. Sennour et al.[35] investigated crack tips from U-bend samples of Alloy 600 exposed to 330°C PWR primary water. Cr_2O_3 was observed at crack tips with chromium depletion in the grain boundary ahead of the cracks and porous NiO structured oxide filling the crack shown in Figure 2.28. Similar observations were made by Thomas et al.[36] where Cr_2O_3 was observed at crack tips and the crack was filled with porous NiO structured oxide. Thomas also observed oxidized regions ahead of crack tips, but was not able to identify its structure due to the high plastic strains.

2.4.2 Characteristics of Alloy 690 crack initiation

Stress corrosion cracking of Alloy 690 has only been recently studied and is largely limited to accelerated testing, either by cold working or testing at elevated temperatures[45–49]. Crack growth is generally fairly slow (10^{-8} to 10^{-9} mm/s), but has consistently been observed in cold worked compact tension specimens. However, crack initiation has been very sparsely studied as the material has proven to be largely resistant[50,51]. No instances of crack initiation have been observed in reactor service since Alloy 690 parts were first installed in 1989; including thousands of tubes as well as high stress and cold worked tube plugs. Laboratory tests to study crack initiation have shown that the material is resistant to cracking in constantly loaded samples. Mitsubishi Heavy Industries has conducted tests of various mockup components subjected to uniaxial static tensile load up to 95,000 hours and observed no rupture shown in Figure 2.29[50]. Knolls Atomic Power Laboratory tested 24 ring loaded pre-cracked compact tension specimens from a variety of heats, form factors, and orientations loaded to 36 MPa $m^{1/2}$ at 338°C. After 5.8 years of exposure, 2 specimens showed minor pockets of SCC corresponding to crack growth of approximately 20μm[51]. Pacific Northwest National Lab conducted constant load experiments on tensile bars machined from a cold worked heat of Alloy 690 known to have a high crack growth rate[52]. Transgranular and intergranular cracking was observed to initiate from TiN particles and was attributed to mechanical failure and not SCC shown in Figure 2.30. Crack initiation has been observed on smooth surfaces of Alloy 690 tensile bars from experiments using dynamic strain. Teysseyre et al.[53] conducted constant extension rate tensile (CERT) experiments on elecropolished tensile bars of Alloy 690 in deaerated supercritical water and observed initiation of intergranular SCC with crack depths up to 96 μm at 500°C. The

deepest cracks were observed from cracks that had transgranular initiation then transitioned to intergranular growth as shown in Figure 2.31.

Crack growth rate studies on compact tension specimens of Alloy 690 have revealed some similar cracking trends to those observed in Alloy 600[46–48,54]. Like alloy 600, hydrogen has been shown to have an effect on the crack growth rate of Alloy 690. Peng et al.[48] observed a 2.5 times increase in the crack growth rate in proximity of the Ni/NiO boundary. Medway also observed the effect of hydrogen on crack growth rate of four heats of Alloy 690, with an increase of 2.5 to 3 times that at the Ni/NiO boundary for crack growth rate experiments conducted at 350°C in PWR primary water conditions. Cold work has also been shown to increase the crack growth rate of Alloy 690[46,49,54], similar to observations on Alloy 600[55].

Detailed investigations of the morphology of crack tips in Alloy 690 has been performed by Bruemmer et al.[46] Cracks in compact tension samples of cold rolled Alloy 690 were characterized by a combination of scanning electron microscopy and transmission electron microscopy. Cracks were observed to prefer a path along grain boundaries even when voids or cracked carbides were present as shown in Figure 2.32. Carbides were also found at many of the crack tips which appeared blunted, suggesting that they carbides arrested the cracks shown in Figure 2.33. No evidence of intergranular oxidation was found from primary cracks even though grain boundaries ahead of cracks were depleted in chromium, unlike observations of cracking in Alloy 600. Internal oxidation was observed on the crack walls in the form of filaments of MO structured oxide decorated by discrete Cr_2O_3 platelets.

2.4.3 Accelerated SCC testing

Accelerated testing of stress corrosion crack initiation and growth of Alloy 600 and Alloy 690 in pressurized water reactor (PWR) is routinely conducted to reduce the time of the experiment on materials that are relatively resistant to SCC[36,56–59]. Cracking is often accelerated by increasing the temperature to 360°C, a limit imposed by the phase change to supercritical water at 374°C. Increasing the temperature further is appealing for highly resistant alloys such as Alloy 690, but only if the mechanism of stress corrosion crack initiation in supercritical water is the same as that in subcritical water. SCC of Alloy 600 was shown to be a temperature activated process by Bandy and Van Rooyen[60], who demonstrated that it followed an Arrhenius relationship between 290°C and 365°C. Similarly, Economy et al.[13] increased the temperature further into the high density steam phase between 332°C and 400°C and also observed an Arrhenius relationship for crack initiation of Alloy 600. In both cases a single activation energy was fit the data over the entire temperature range, which was interpreted to mean that there was no change in the cracking mechanism. Furthermore, Economy observed that the cracking susceptibility for Alloy 600 exposed to 368°C 19.3 MPa steam was nearly the same as experiments conducted in 368°C 20.5 MPa water.

Cracking susceptibility can also be changed by varying the applied load or pre-strain in stress corrosion crack initiation tests. Etien et al.[41] summarized testing of six different heats of Alloy 600 and found that the crack initiation time of constantly loaded tensile bars decreased from ~2000 hrs at a load of 310 MPa to ~250 hrs at 655 MPa. The crack initiation time also decreased for samples with higher plastic strains. The crack growth rate of Alloy 690 has been shown to depend on the amount of cold work and also the way in which cold work was applied. Andresen

et al.[45] reviewed the current understanding of crack growth in Alloy 690 and highlighted that the orientation of the CT sample in the rolled plate (S-L vs. S-T) could cause an order of magnitude change in the crack growth rate. Heats of Alloy 690 that have higher concentrations of chromium or niobium can develop compositional banding, which has been shown to be associated with high crack growth rates[45].

The application of accelerated testing has varied and different modes of acceleration are appropriate depending on the objective of the experiment. If the objective is to evaluate different welding procedures or to locate areas of a fabricated that may be susceptible to cracking due to elevated stress, a severe test using chemical additions such as doped steam or immersion testing may be appropriate. Kroenke et al.[61] conducted accelerated hydrogenated steam experiments doped with 100 ppm chloride, fluoride, and sulfate as sodium salts and nitrate salt to measure the threshold stress needed to initiate cracks in Alloy 600. Scott[62] supported the use of doped steam testing for Alloy 600 to simulate potential steam pockets in reactor conditions. However, doped steam may not be useful if the goal of the experiment was to compare two alloys. For example if the objective is to measure a factor of improvement of Alloy 600 over Alloy 690, it is not clear if the addition of dopants would affect one alloy more than the other. Some common methods of performing accelerated testing on stainless steels don't appear to be appropriate for nickel alloys, such as the Huey test (ASTM A 262 Practice C). Sedricks et al.[63] found that Alloy 690 could not be sensitized by the Huey test, immersion in boiling nitric acid, if the carbon content is kept below 0.02%. Sarver et al.[64] compared the effect of sensitization due to the Huey test between Alloy 690 an Alloy 600 with varying carbon content. The researchers found that the highest degree of sensitization according to the Huey test was also the most resistant to

cracking for both alloys. If the objective of the test is to measure activation energies for cracking and make comparisons between alloys, a simple test environment without the complications of chemical additions may be most appropriate.

2.5 Objective and Approach

Laboratory testing of cracking resistant materials can aid in understanding the mechanisms of cracking, help develop ways to mitigate cracking, and aid in lifetime predictions of materials in service. Accelerated testing is commonly used to simulate reactor conditions without changing the mechanism of crack initiation in susceptible materials such as Alloy 600. However more cracking resistant materials have proven to be resistant to SCC initiation in conventional accelerated testing. The testing environment can be made more aggressive by increasing the experiment temperature further, into the supercritical water regime. However, it is not presently clear if the mechanisms of corrosion and stress corrosion crack initiation are the same in supercritical water as in subcritical water. ***The objective of this dissertation is to determine if the mechanism of stress corrosion crack initiation of Alloy 600 and Alloy 690 is the same in both subcritical and supercritical water.*** This will be accomplished by three phases of experimentation. First, the environment in which the stress corrosion cracking experiment is conducted must be specified. It was decided to conduct experiments at a fixed increment of electrochemical potential from the Ni/NiO boundary by control of the dissolved hydrogen concentration. Second, exposures of unstressed coupons will be conducted to determine if the oxidation behavior of the alloy in supercritical water is fundamentally different from that in subcritical water. Third, the crack initiation morphology and susceptibility to crack initiation will be characterized. If the behavior of the oxidation, SCC initiation morphology, and susceptibility

to cracking vary smoothly across the subcritical/supercritical transition, then it is implied that the mechanism doesn't change.

To measure accurate activation energies for crack initiation, the environment needs to be controlled such that the electrochemical potential is a fixed increment from the Ni/NiO boundary. However, the location in terms of dissolved hydrogen content of the Ni/NiO boundary is not known in supercritical water. Direct exposures of nickel to hydrogenated subcritical and supercritical water were used to determine the stability of nickel oxide as a function of dissolved hydrogen concentration. The fugacity at the Ni/NiO boundary was determined by first measuring the Henry's law constant in subcritical and supercritical water by use of a palladium-silver tube. The Henry's law constant was used to calculate the fugacity of hydrogen at the Ni/NiO boundary and develop a thermodynamic model for the oxidation of nickel in supercritical water.

Stress corrosion cracking, as the name implies, relies on a combination of stress and corrosion and if either of these have a change in mechanism in supercritical water the SCC mechanism could change. Coupons with an electropolished surface finish were exposed in hydrogenated water, a fixed electrochemical potential (ECP) increment above the Ni/NiO boundary between 360°C and 400°C. Because oxides on both alloys change with exposure time, detailed examinations focused on time-temperature equivalent samples chosen by calculating the time needed to form an oxide of specific thickness at each temperature from the activation energy for oxidation. The morphology, structure, and composition of oxides were measured and used to show that a consistent oxidation mechanism is operating in subcritical and supercritical water.

The character of stress corrosion cracking is the final piece of evidence needed to show whether the same mechanism for SCC initiation is consistent between subcritical and supercritical water. Samples of Alloy 600 and tensile pre-strained Alloy 690 were strained in CERT experiments in subcritical and supercritical water to determine the temperature relationship for crack initiation and the morphology of cracking. The environment for all experiments was controlled by additions of dissolved hydrogen to be in the NiO stable regime a fixed electrochemical potential increment above the Ni/NiO boundary. The cracking susceptibility was measured by determining the average crack length, crack density, crack length per unit area, and crack depth. The morphology of cracks was determined by scanning electron microscopy and transmission electron microscopy on either side of the critical point and a mechanism for crack initiation of Alloy 690 was developed.

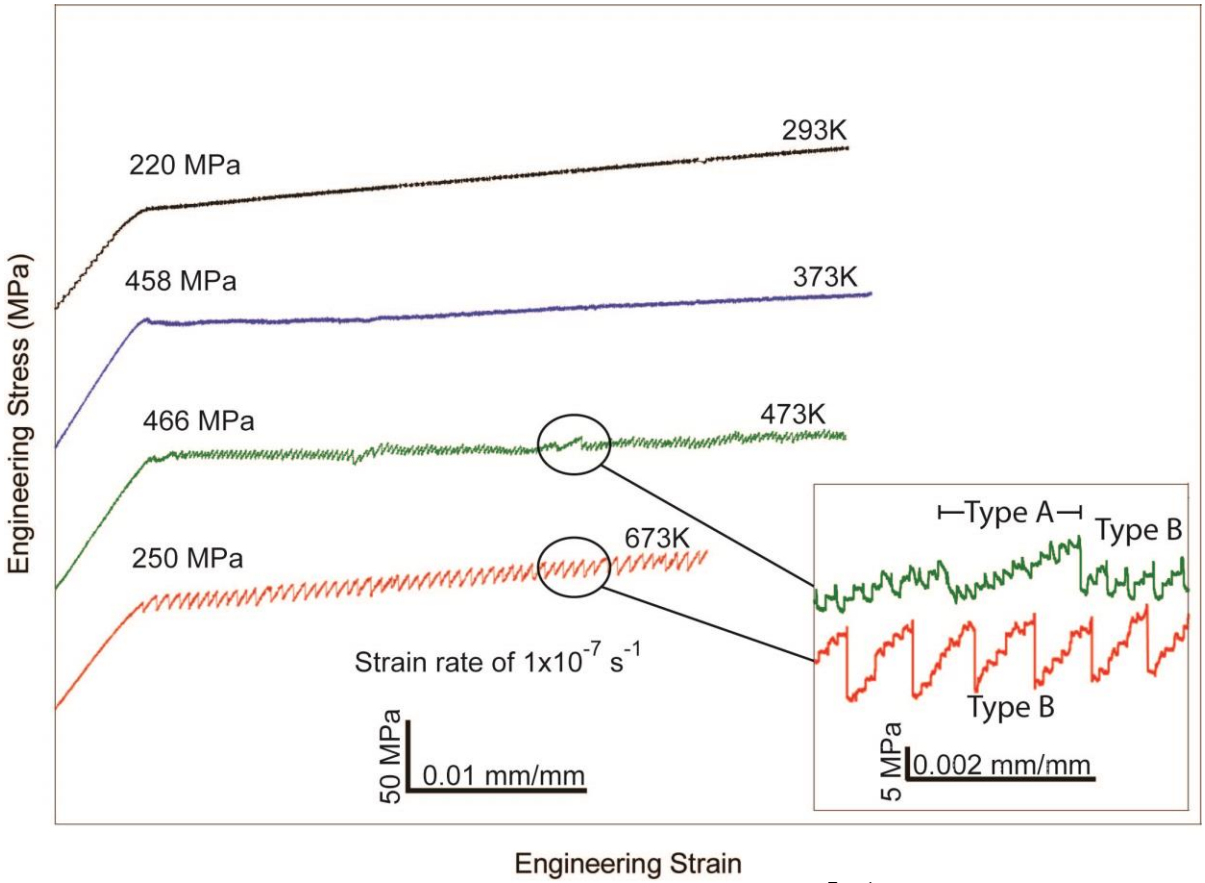

Figure 2.1. Engineering stress-strain curves at a strain rate of 10^{-7} s^{-1} for sample 800H-2. The inset is a magnification of the 673K and 473K stress-strain curves showing the type of serrations. The 673K curve shows only type B serrations. The 473K curve shows a type A serration in the middle and type B on either side.[8]

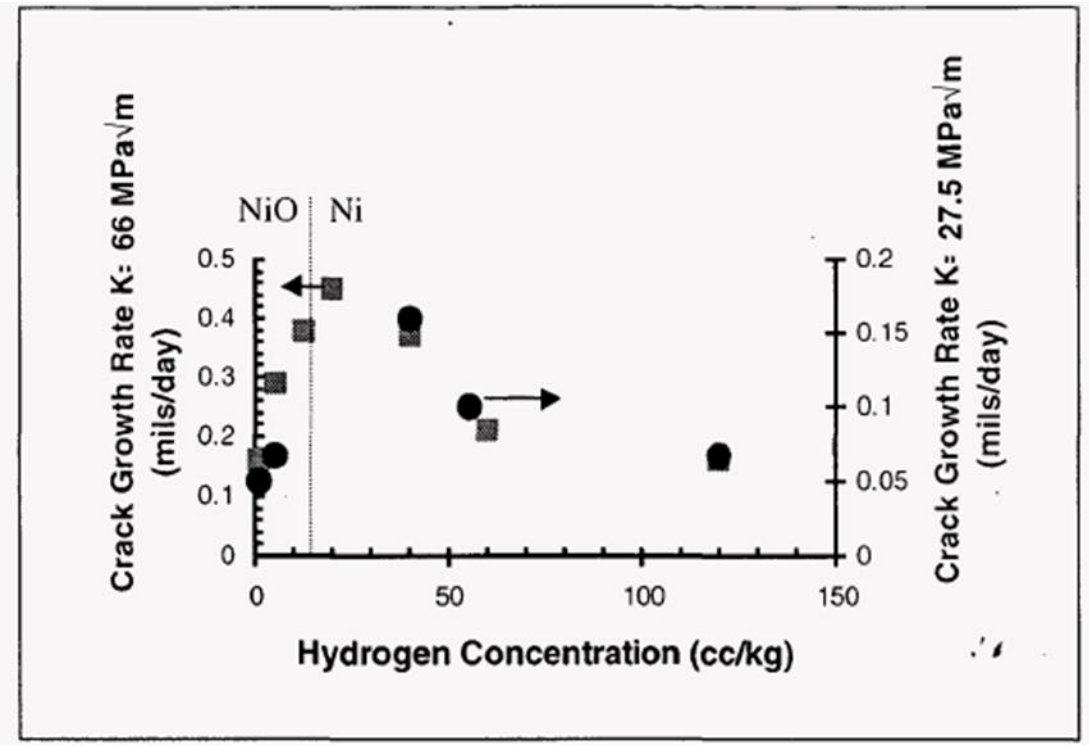

(a)

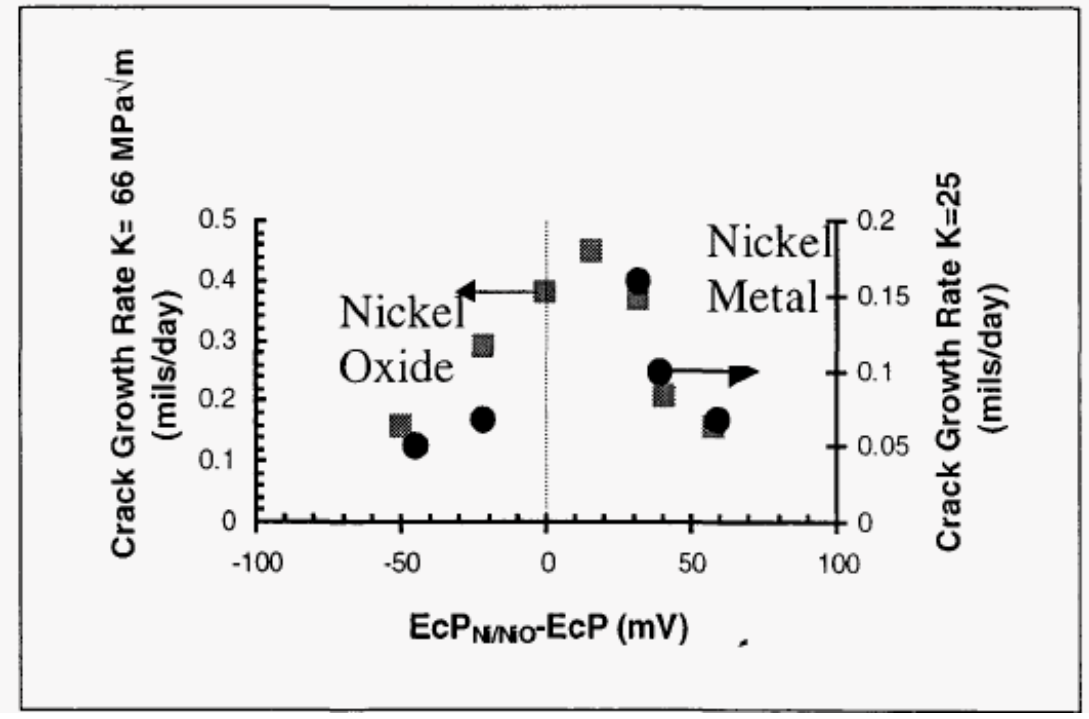

(b)

Figure 2.2. Alloy 600 crack growth rate at 338°C (a) plotted versus the aqueous hydrogen concentration and (b) the electrochemical potential difference versus the measured Ni/NiO transition.[9]

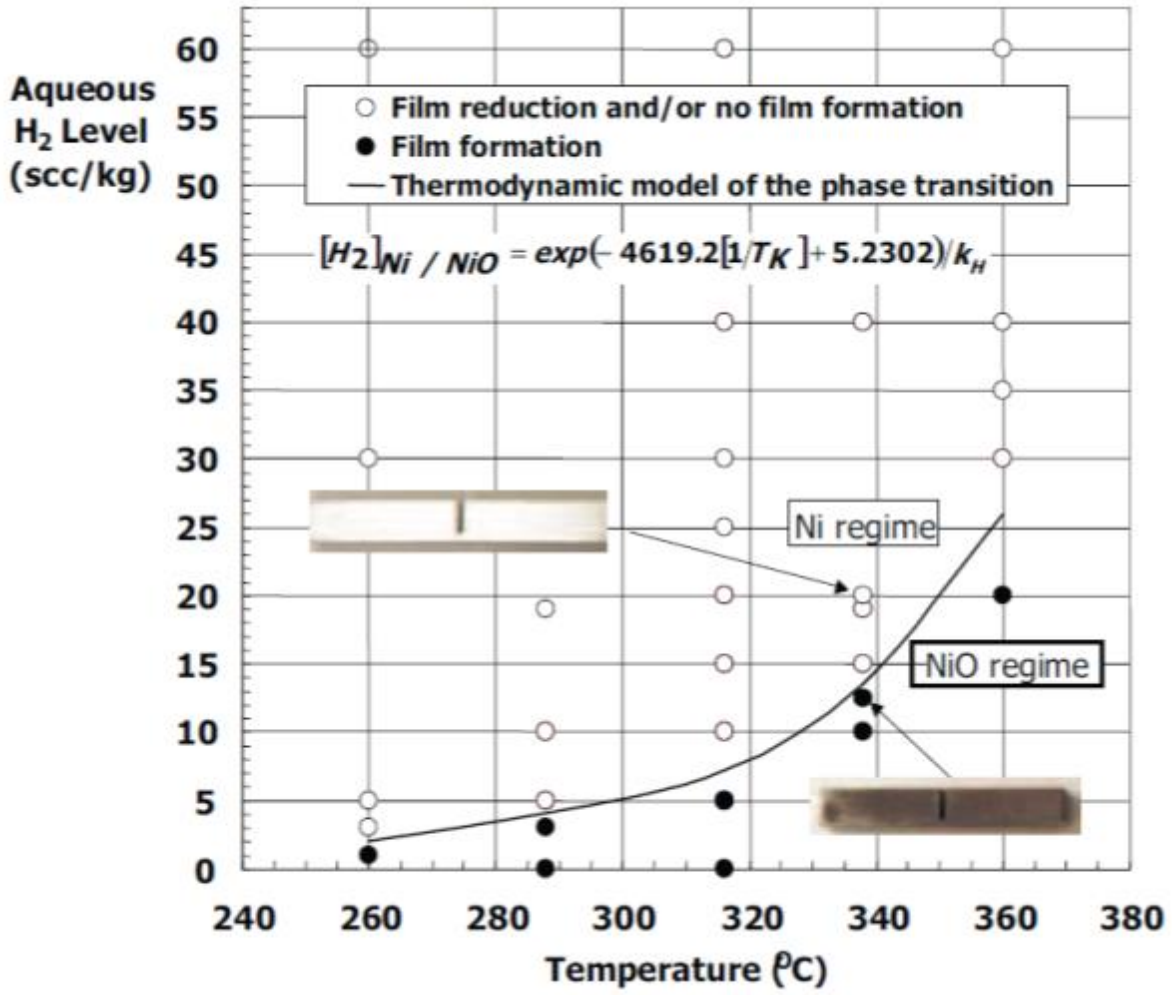

Figure 2.3. Summary of CER and corrosion coupon data. $[H_2]_{Ni/NiO}$ is the phase transition in cc/kg. T_K is the temperature in Kelvin and k_H is the Henry's law coefficient in atm/(cc/kg).[10]

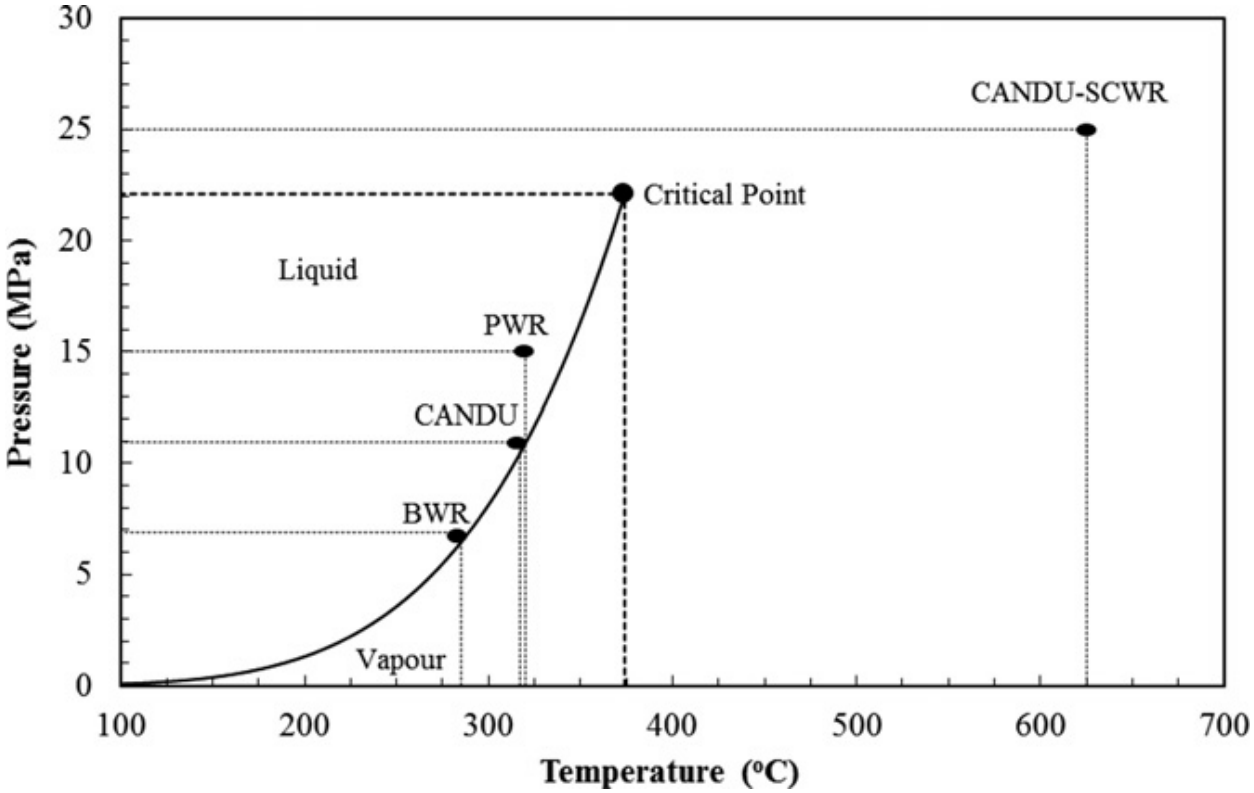

Figure 2.4. Phase diagram for water indicating the operating conditions for current nuclear reactors relative to those proposed for the CANDU ®-SCWR.[22]

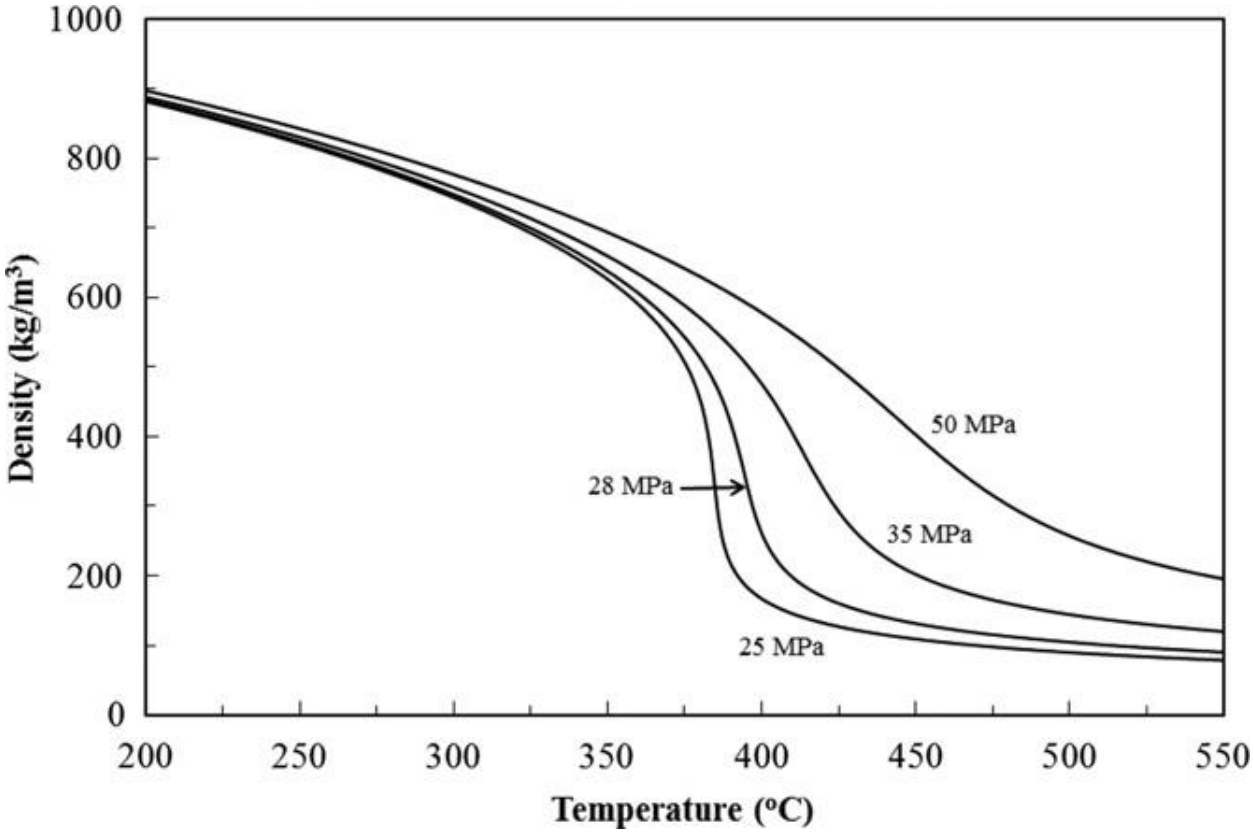

Figure 2.5. Density of water as a function of temperature.[22]

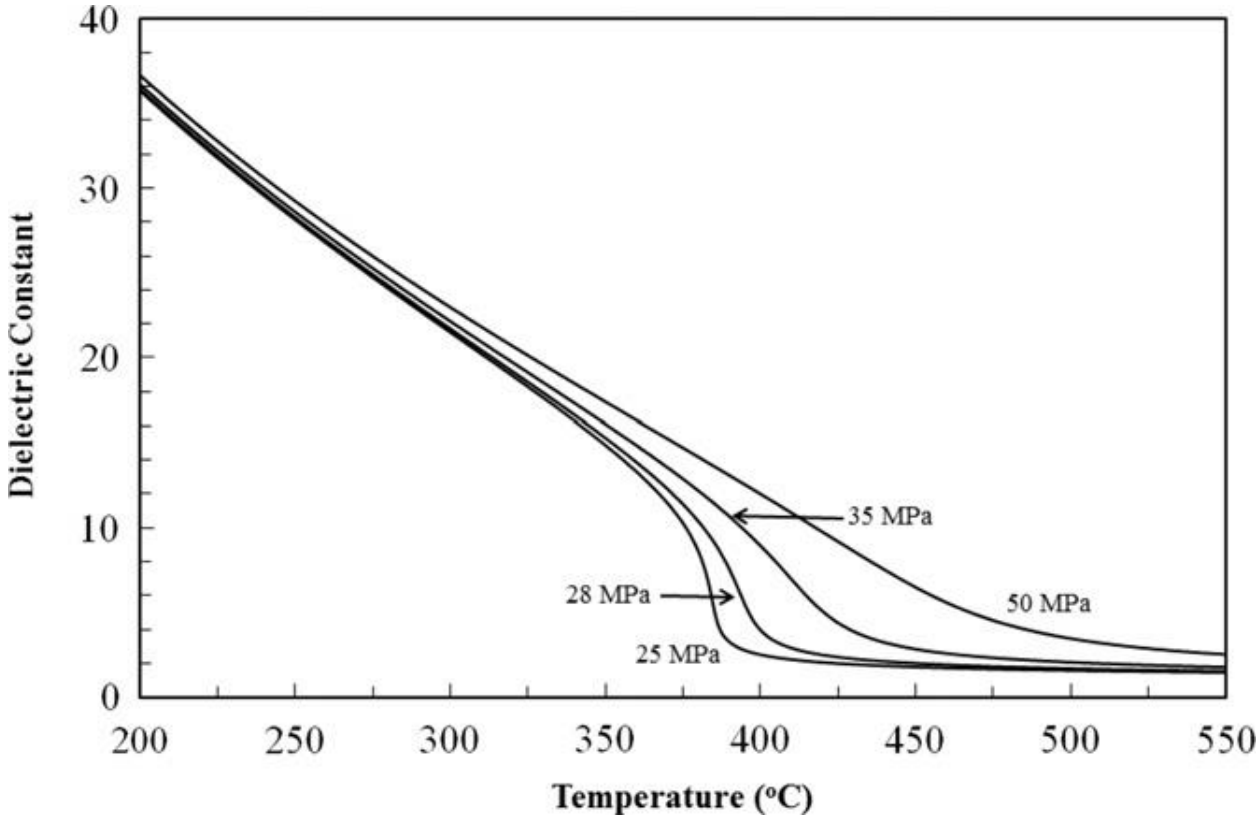

Figure 2.6. Dielectric constant of water as a function of temperature.[22]

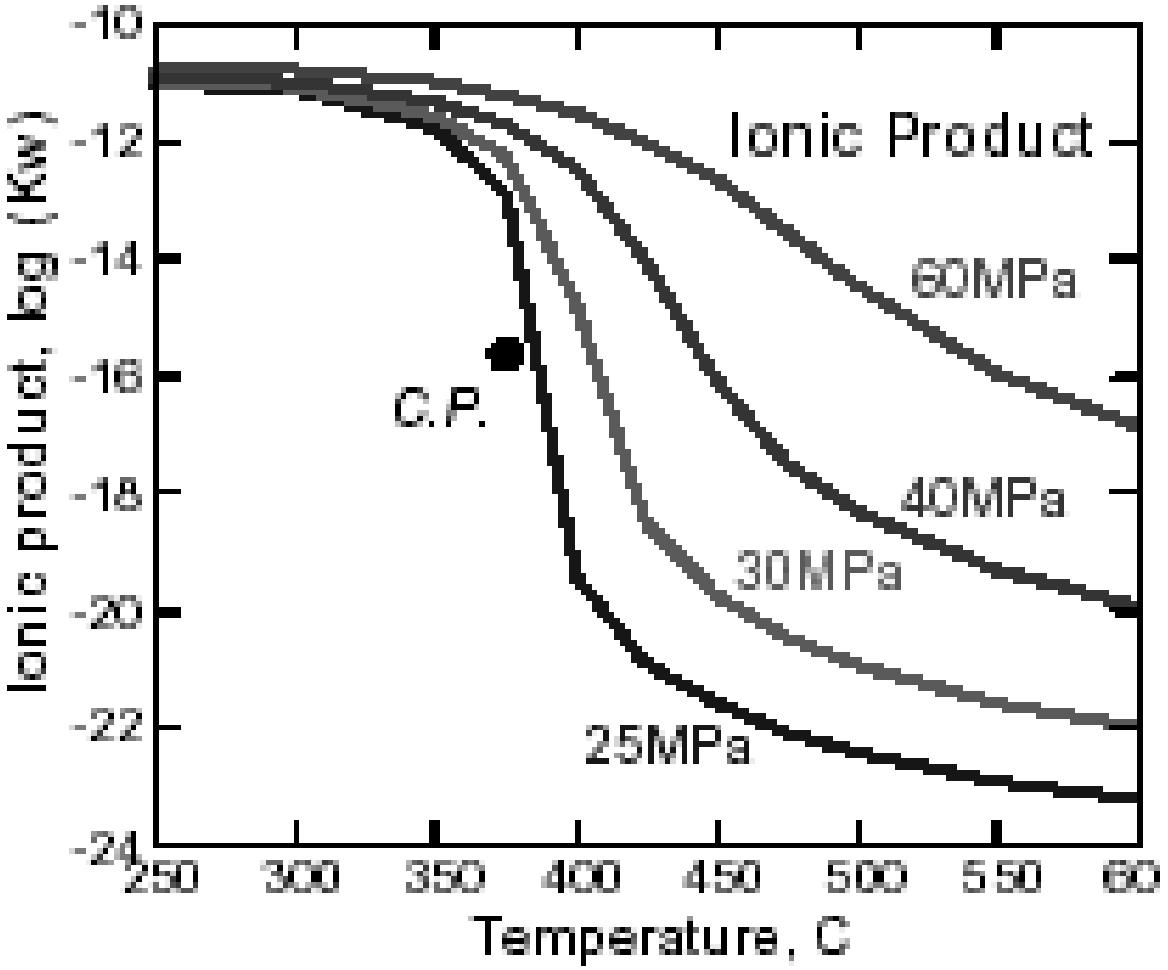

Figure 2.7. Variation in the ionic product of water with temperature. [65]

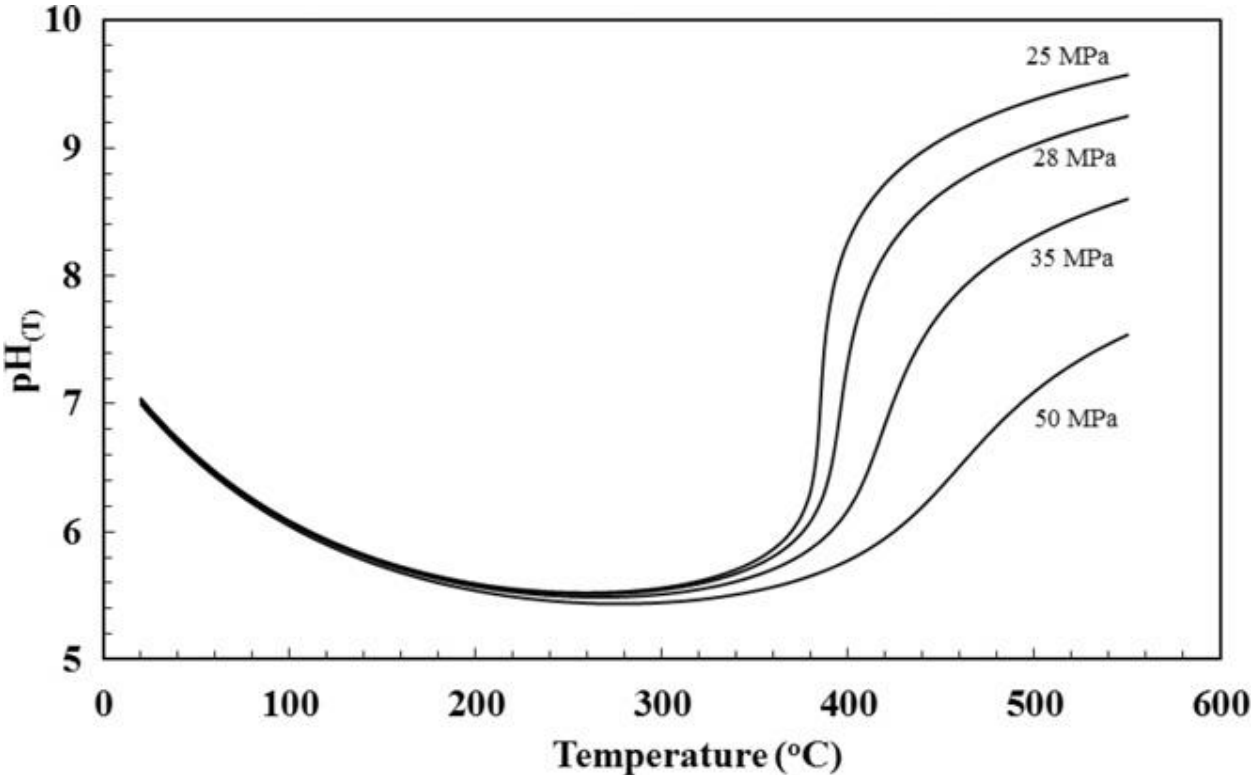

Figure 2.8. pH of neutral water as a function of temperature.[22]

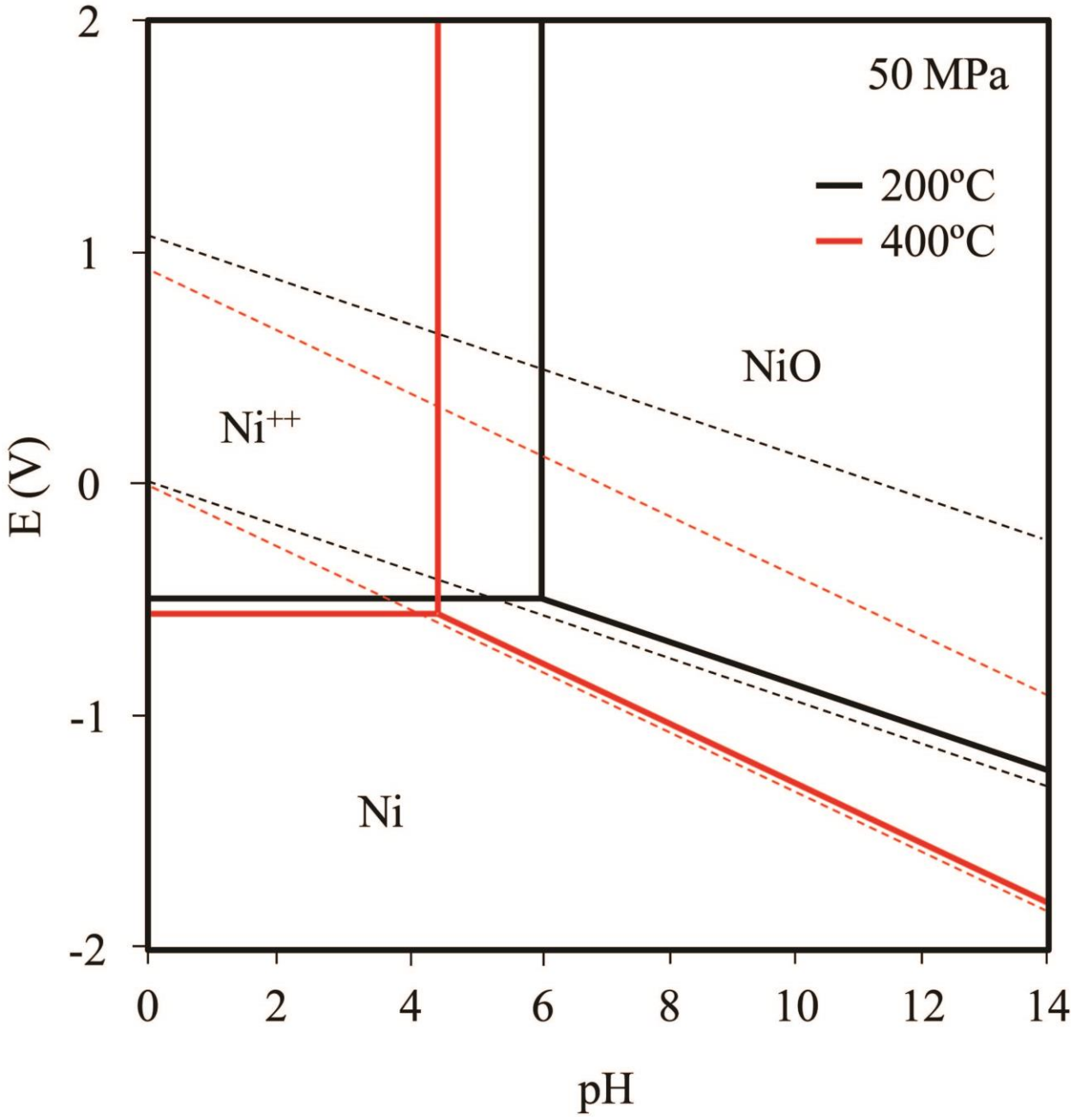

Figure 2.9. Pourbaix diagram of nickel in pure water in subcritical and supercritical water at 50 MPa.[19]

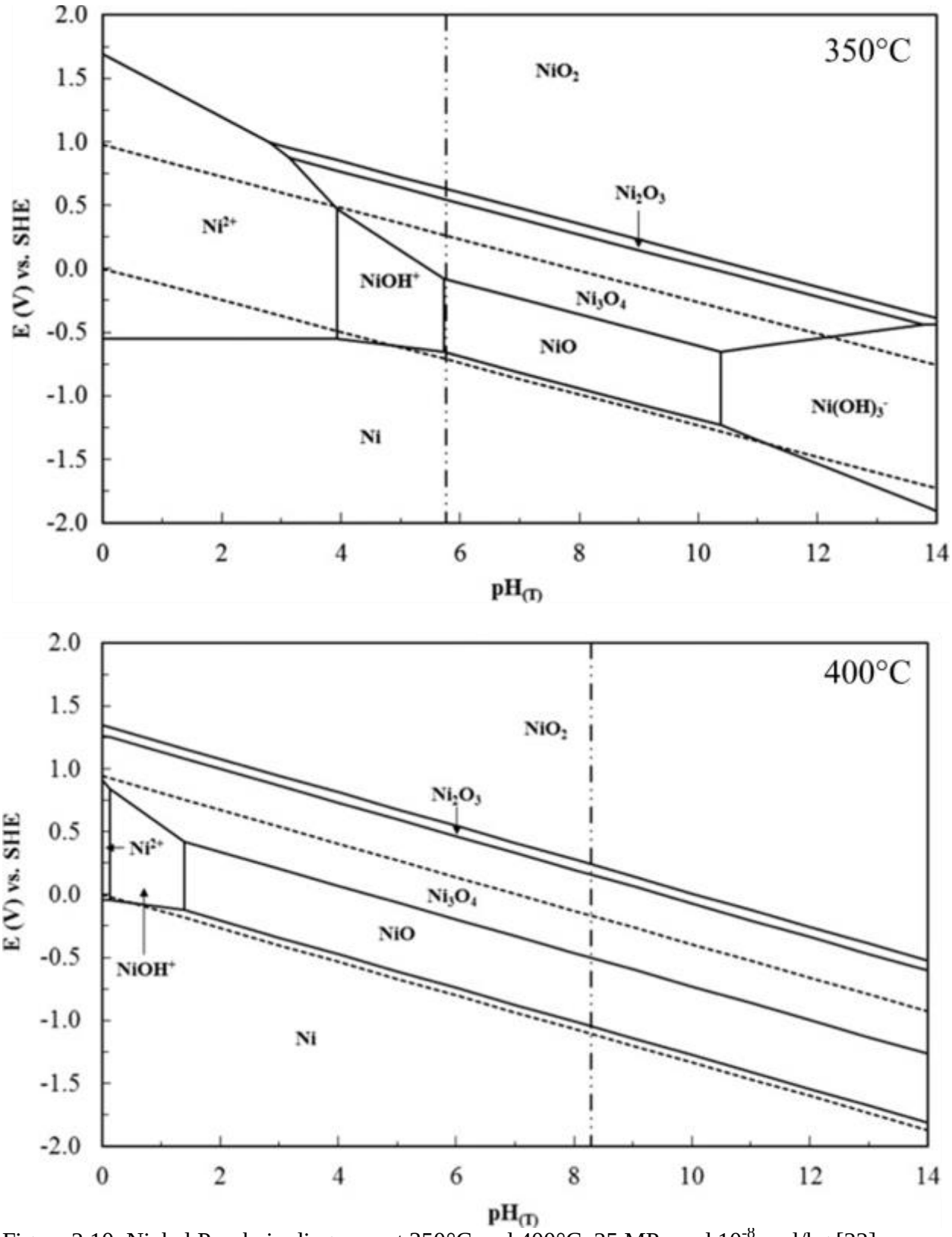

Figure 2.10. Nickel Pourbaix diagrams at 350°C and 400°C, 25 MPa and 10^{-8} mol/kg.[22]

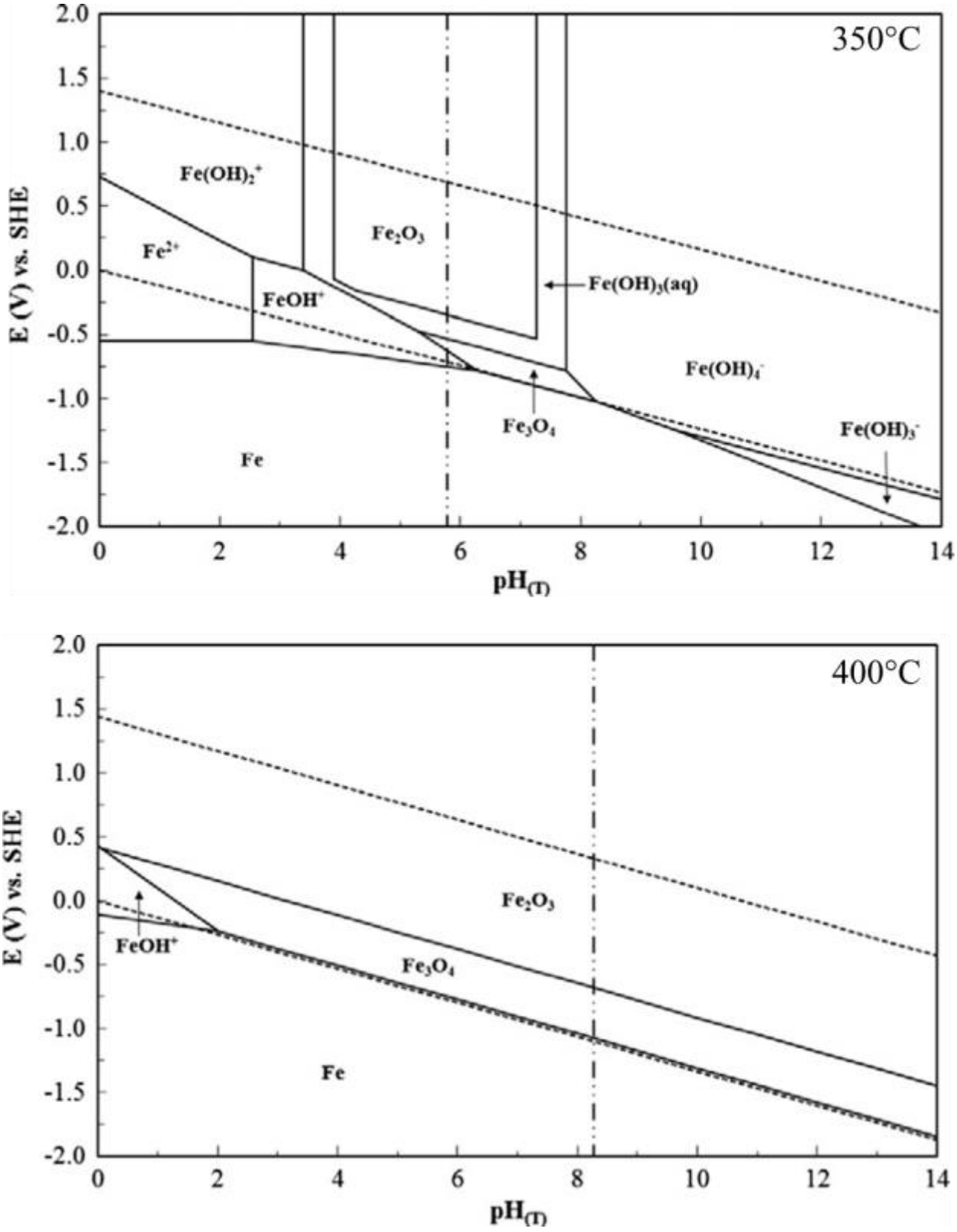

Figure 2.11. Iron Pourbaix diagrams at 350°C and 400°C, 25 MPa and 10^{-8} mol/kg.[21]

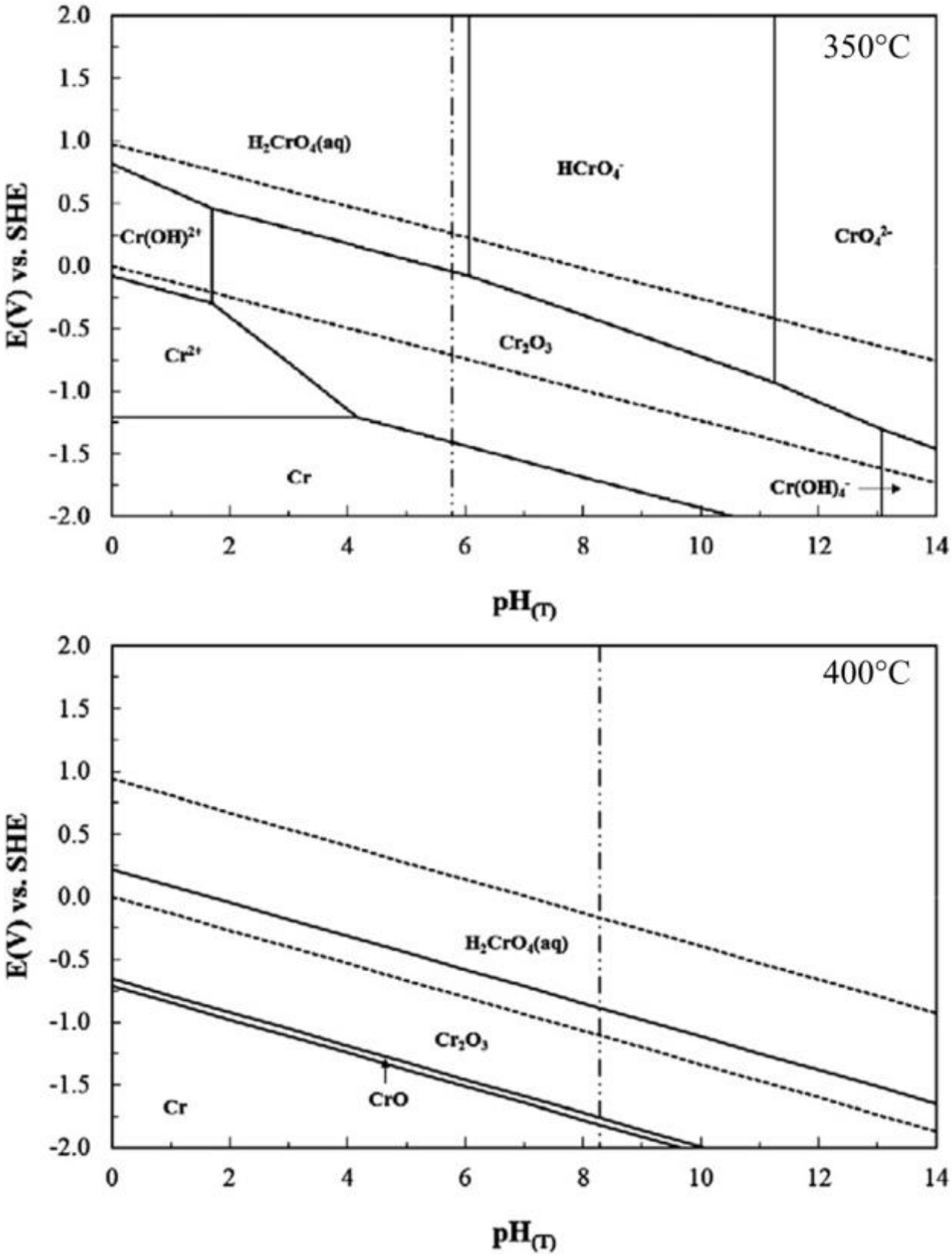

Figure 2.12. Chromium Pourbaix diagrams at 350°C and 400°C, 25 MPa and 10-8 mol/kg.[20]

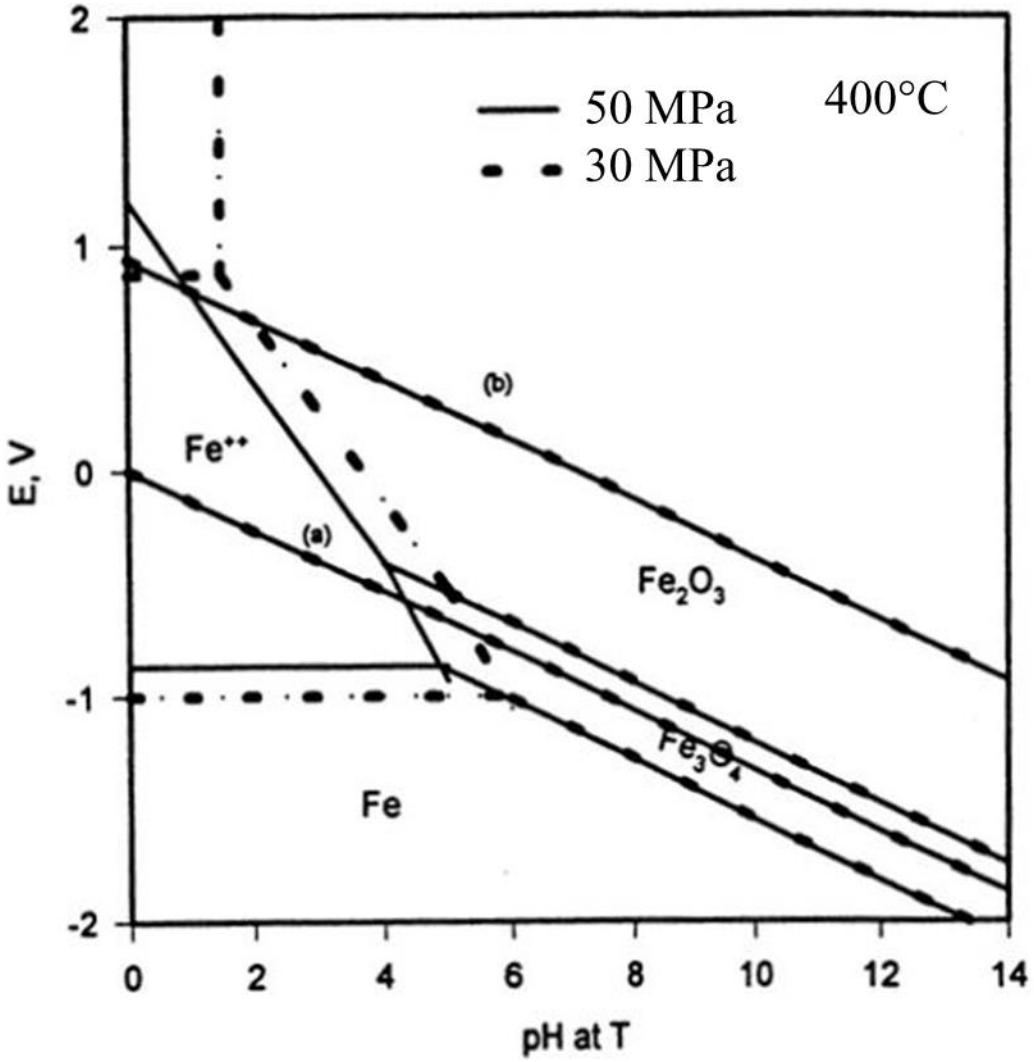

Figure 2.13. Pourbaix diagram for iron in 400°C water at 50 MPa and 30 MPa.[19]

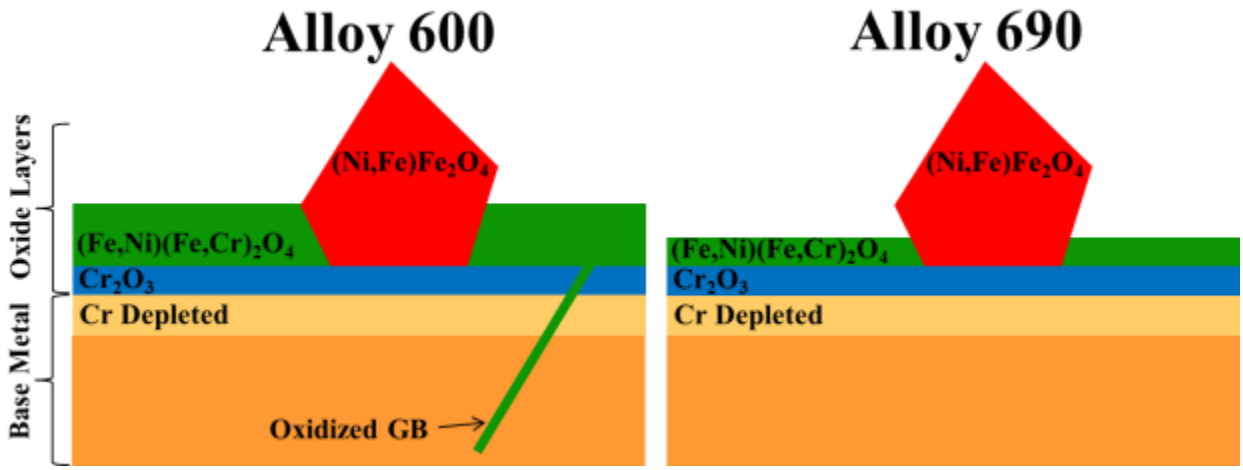

Figure 2.14. Dual layer oxide structure on nickel alloys in PWR primary water.[30]

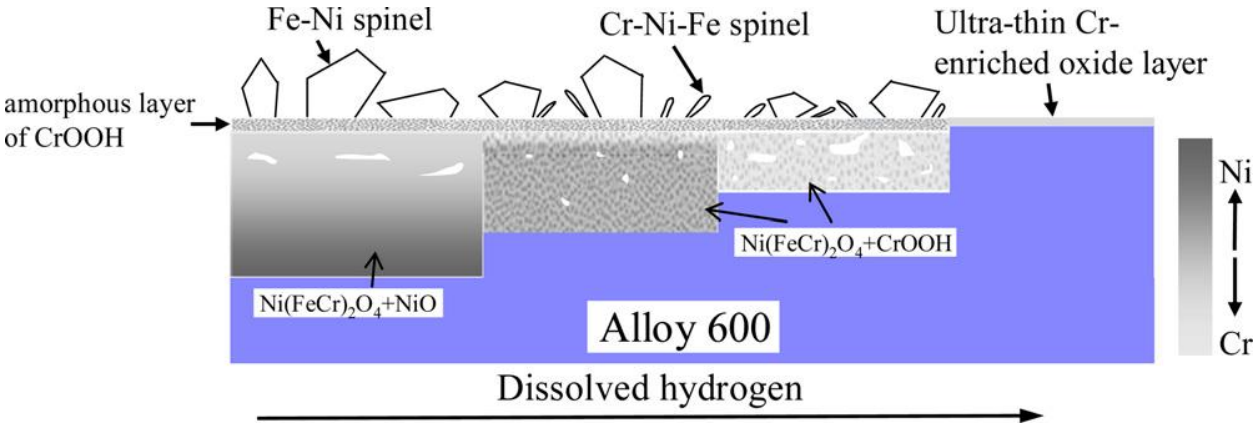

Figure 2.15. Schematic drawing showing the dissolved hydrogen dependence of the structure, thickness, and composition of the oxide formed on Alloy 600 at 288°C.[28]

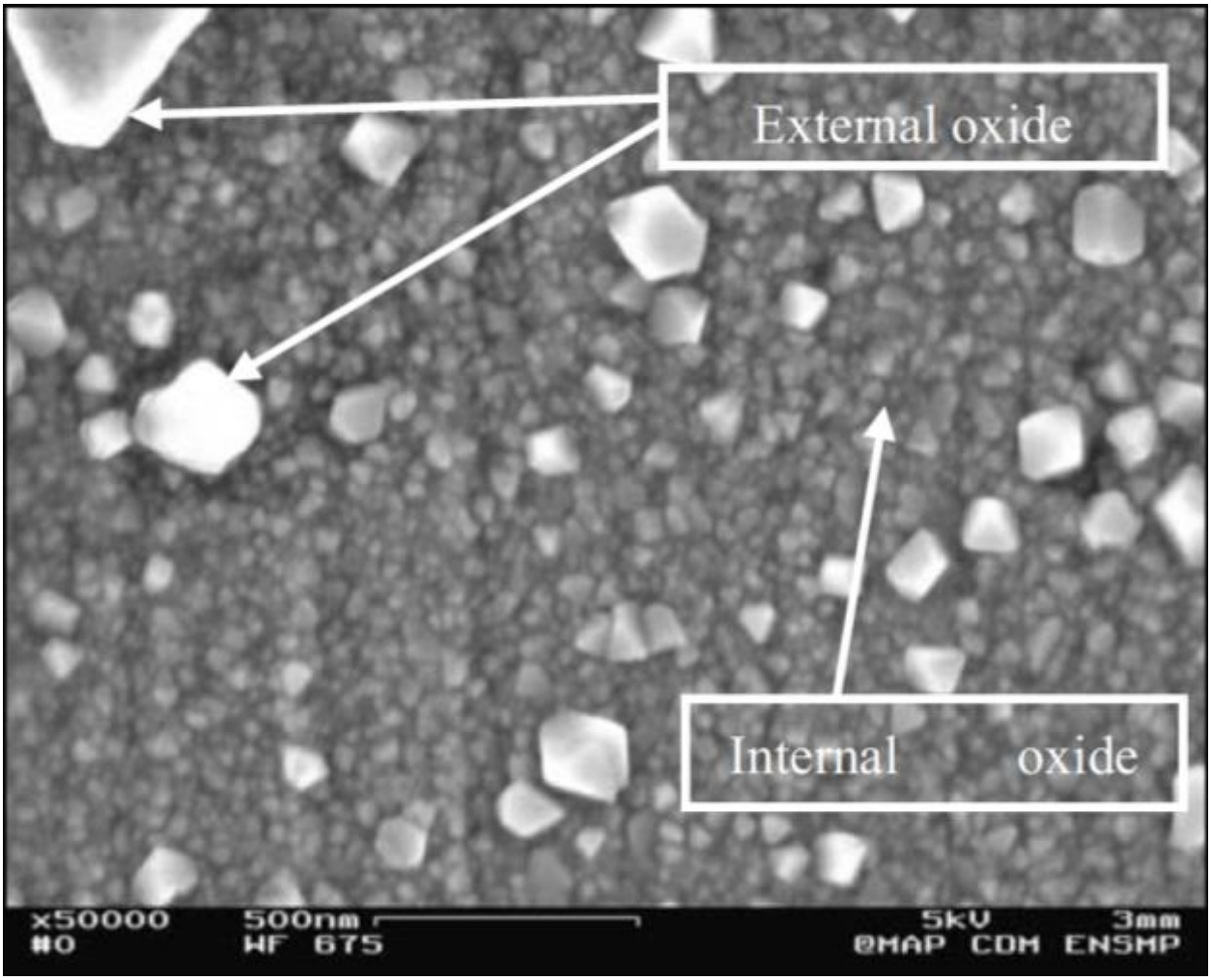

Figure 2.16. FEG-SEM view of the surface of Alloy 600 oxidized 300h at 360°C in simulated PWR primary water.[30]

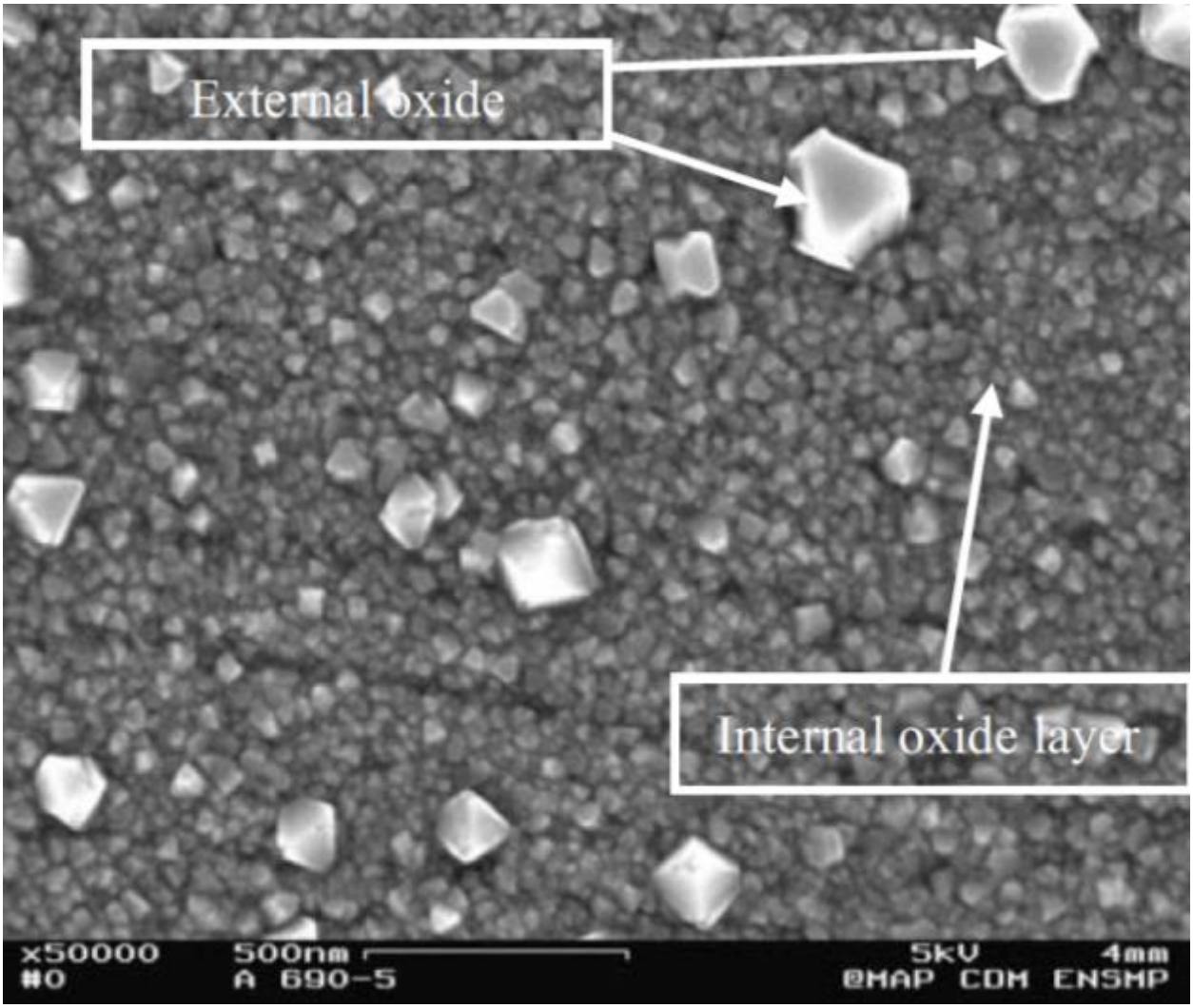

Figure 2.17. FEG-SEM view of the surface of Alloy 690 oxidized 300h at 360°C in simulated PWR primary water.[30]

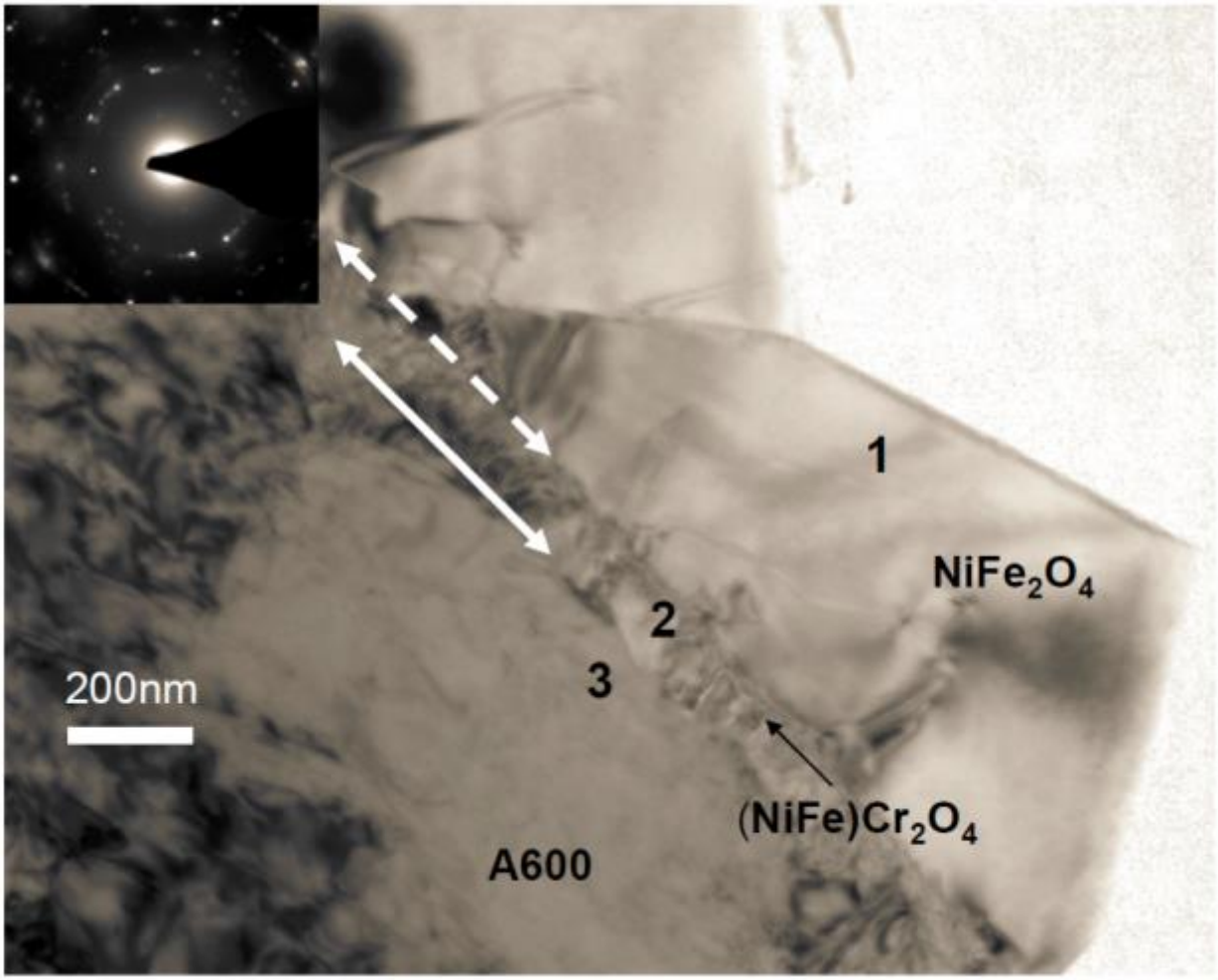

Figure 2.18. Low magnification analytical electron microscope image of an electrochemically polished specimen of Alloy 600 exposed to 338°C hydrogenated water.[31]

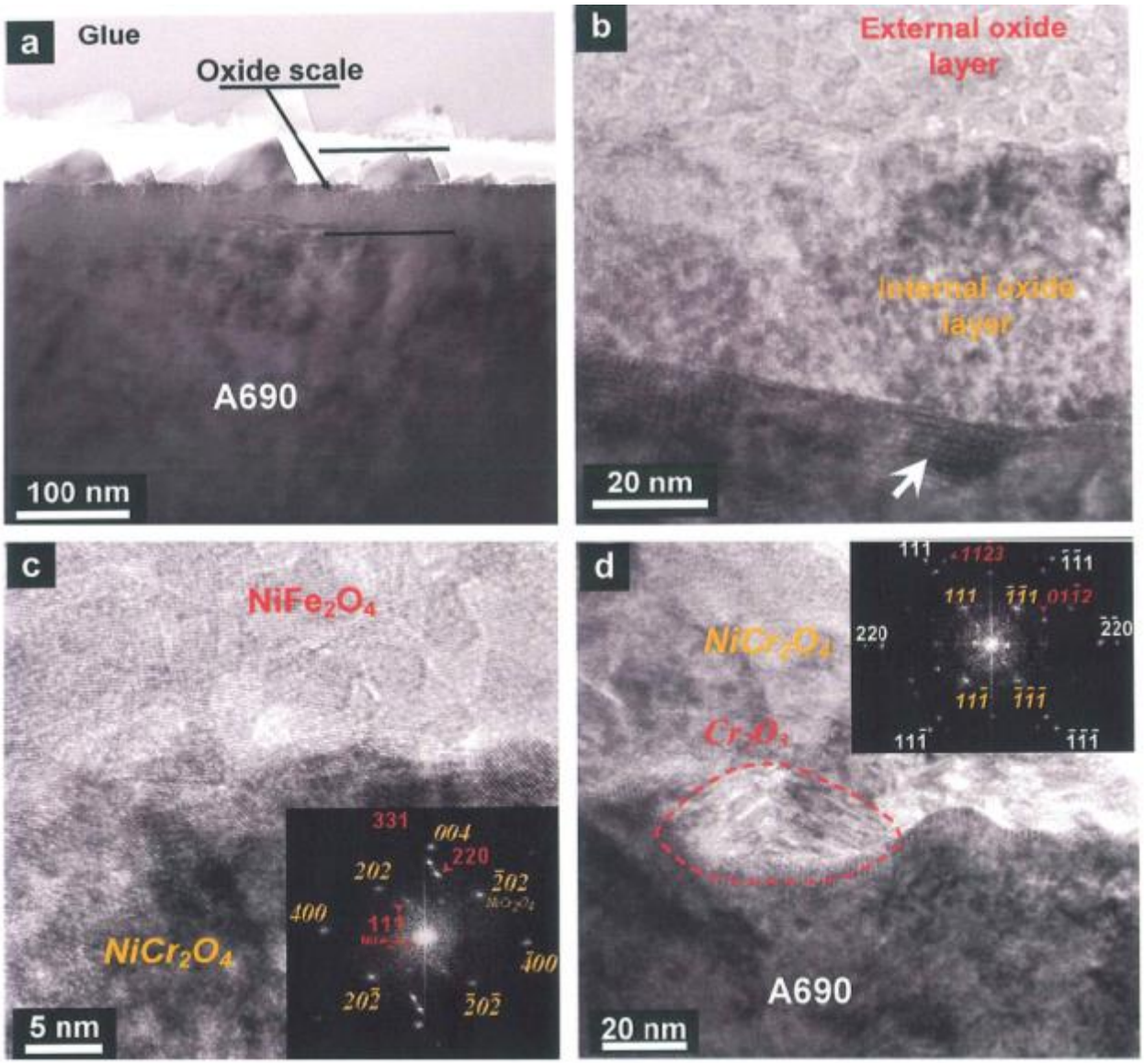

Figure 2.19. TEM (a) and HRTEM (b and c) images of the oxide layer developed on Alloy 690 exposed 858 h showing the large crystallites forming the external oxide layer and the continuous and compact internal layer. Analysis of image FFT diffractograms (inset in 6c) established the $NiCr_2O_4$-structure of the internal layer and the $NiFe_2O_4$ - structure of the large crystallites with orientation relationships between both layers; (d) HRTEM image and corresponding FFT diffractogram showing epitaxy between Cr_2O_3-structure nodules (dashed-line delimited zone) and spinal $NiCr_2O_4$-structure internal layer at the oxide/alloy interface. [23]

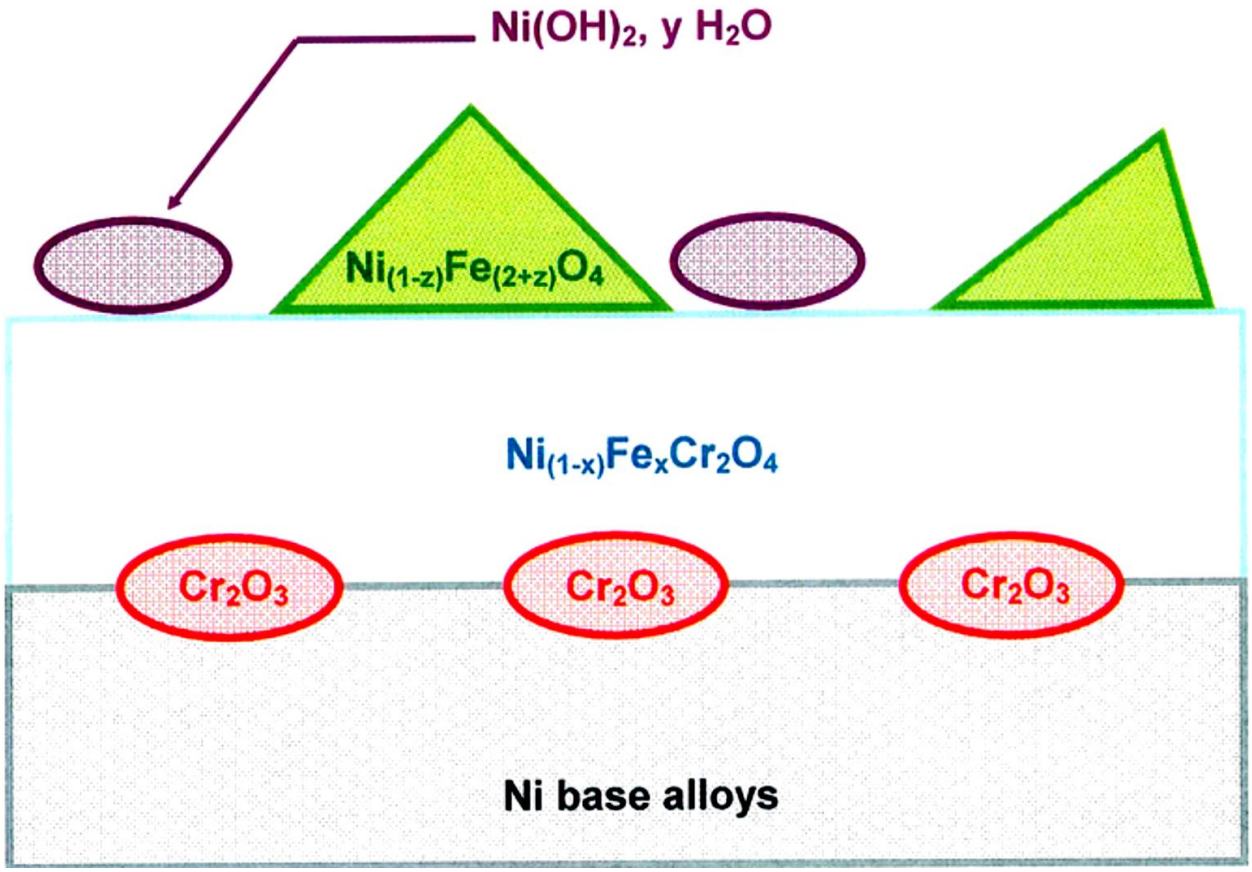

Figure 2.20. Schematic view of the oxide scale that forms during the exposure of Alloy 600 in PWR primary water. [23]

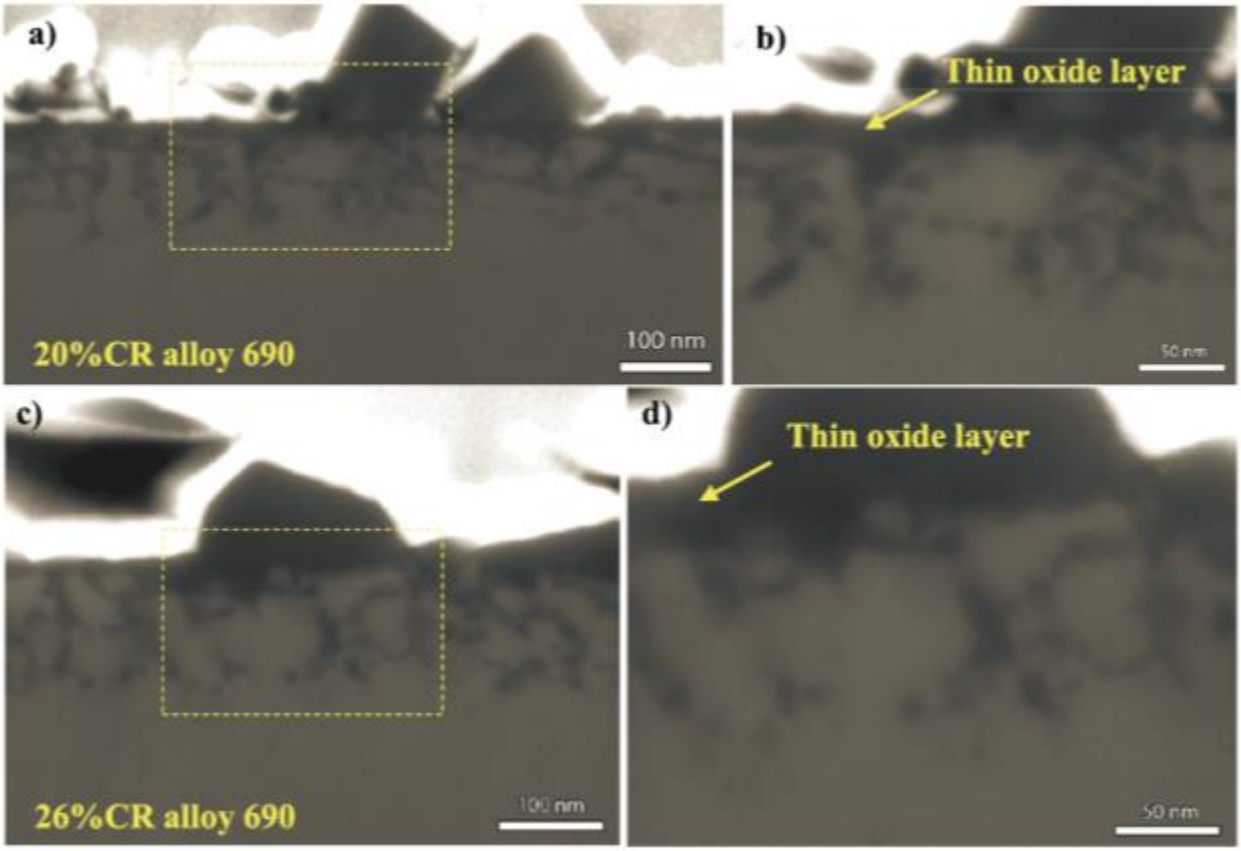

Figure 2.21. SEM backscatter electron micrographs of surface cross sections of Alloy 690 corrosion coupons exposed to 360°C PWR primary water for 1000h. Higher magnification images of the highlighted regions show a thin oxide layer above oxide filaments as small as ~5nm. [26]

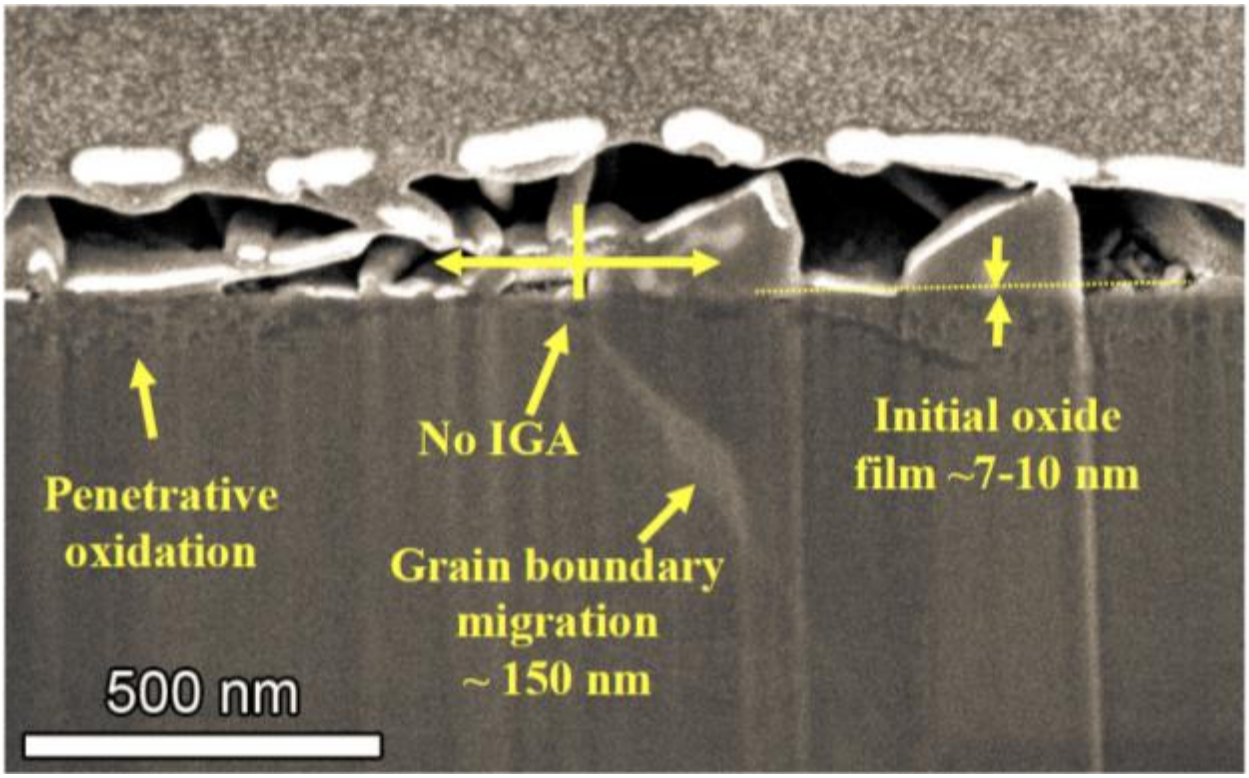

Figure 2.22. SEM micrograph illustrating the cross-section and near-surface grain boundary oxidation of 20% cold rolled material exposed to 360°C simulated PWR primary water for 1000 hr. No intergranular attack (IGA) was observed for Alloy 690. [25]

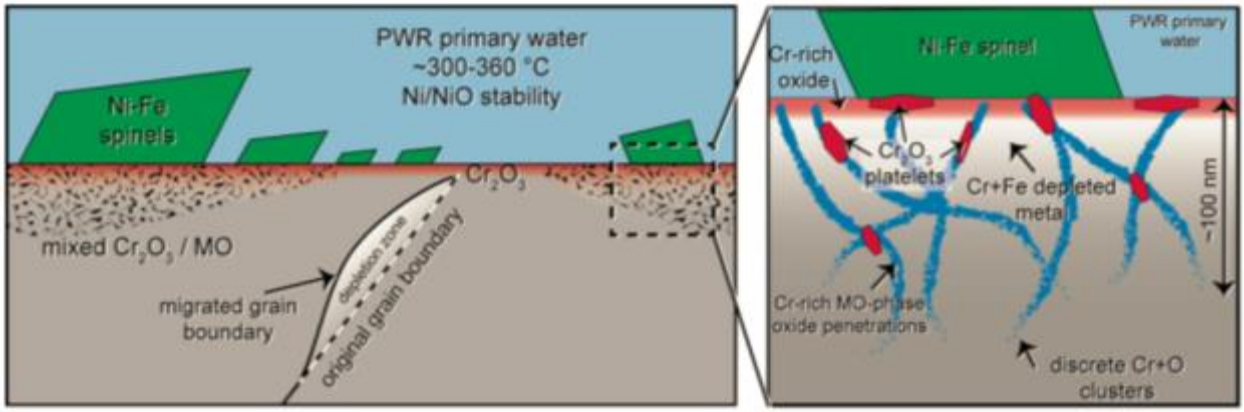

Figure 2.23. Schematic of Alloy 690 oxidation in PWR primary water. [25]

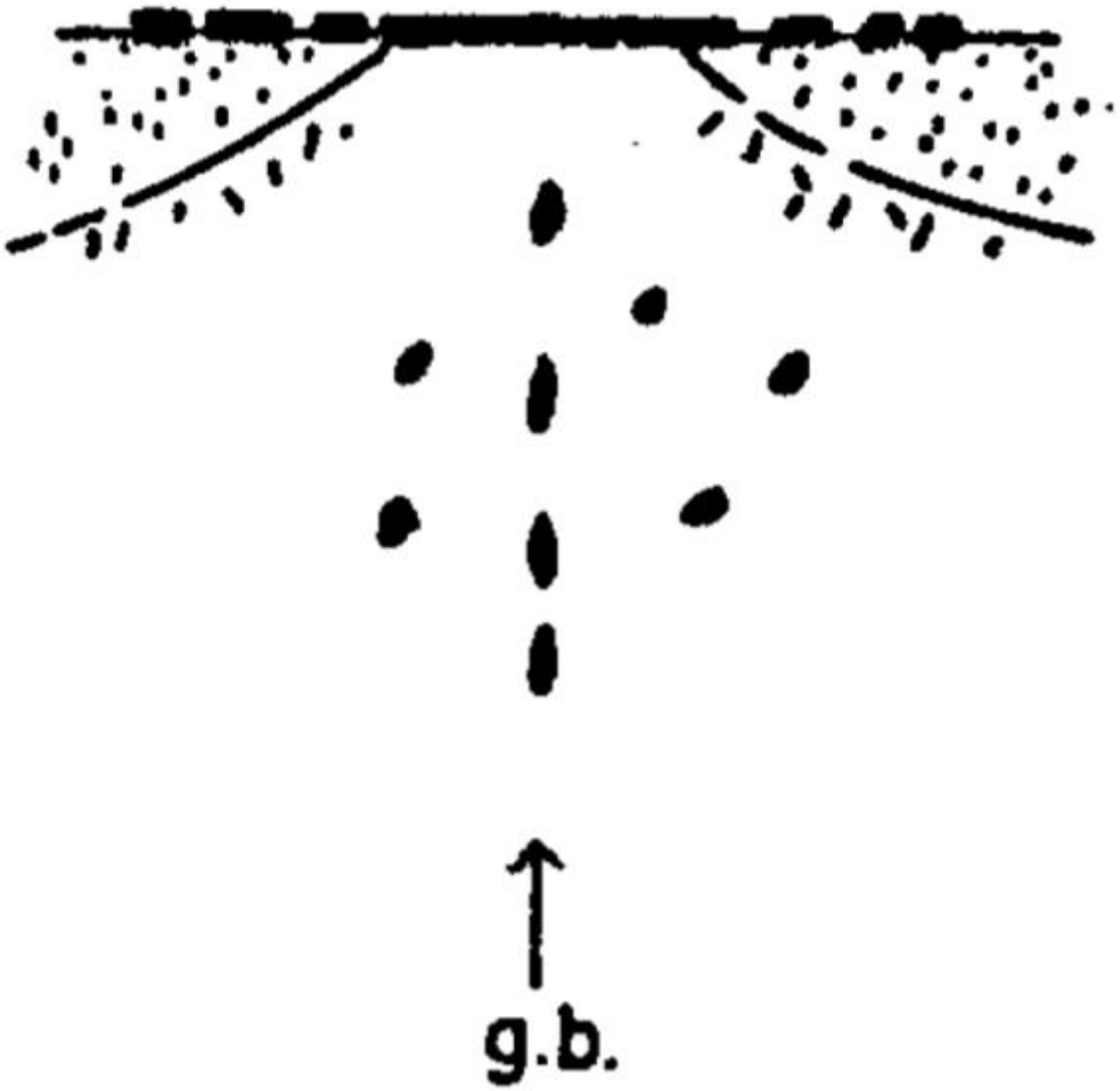

Figure 2.24. High temperature gas corrosion of Ni-Cr binary alloy in a Ni-NiO Rhines pack. [39]

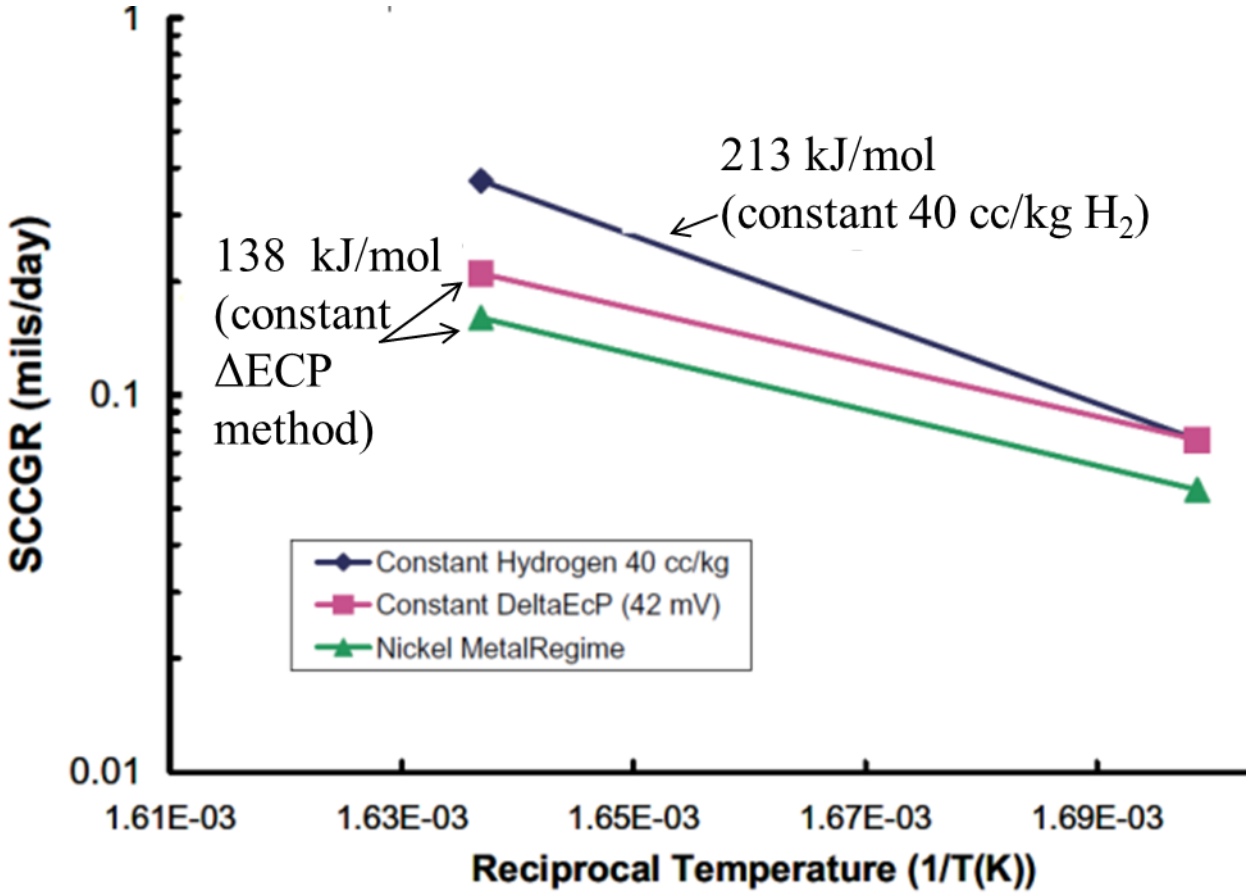

Figure 2.25. Alloy 600 thermal activation energies (kJ/mol) determined using a constant hydrogen content of 40 cc/kg shown in blue triangles and a fixed electrochemical potential from the Ni/NiO boundary in green triangles and purple squares. [42]

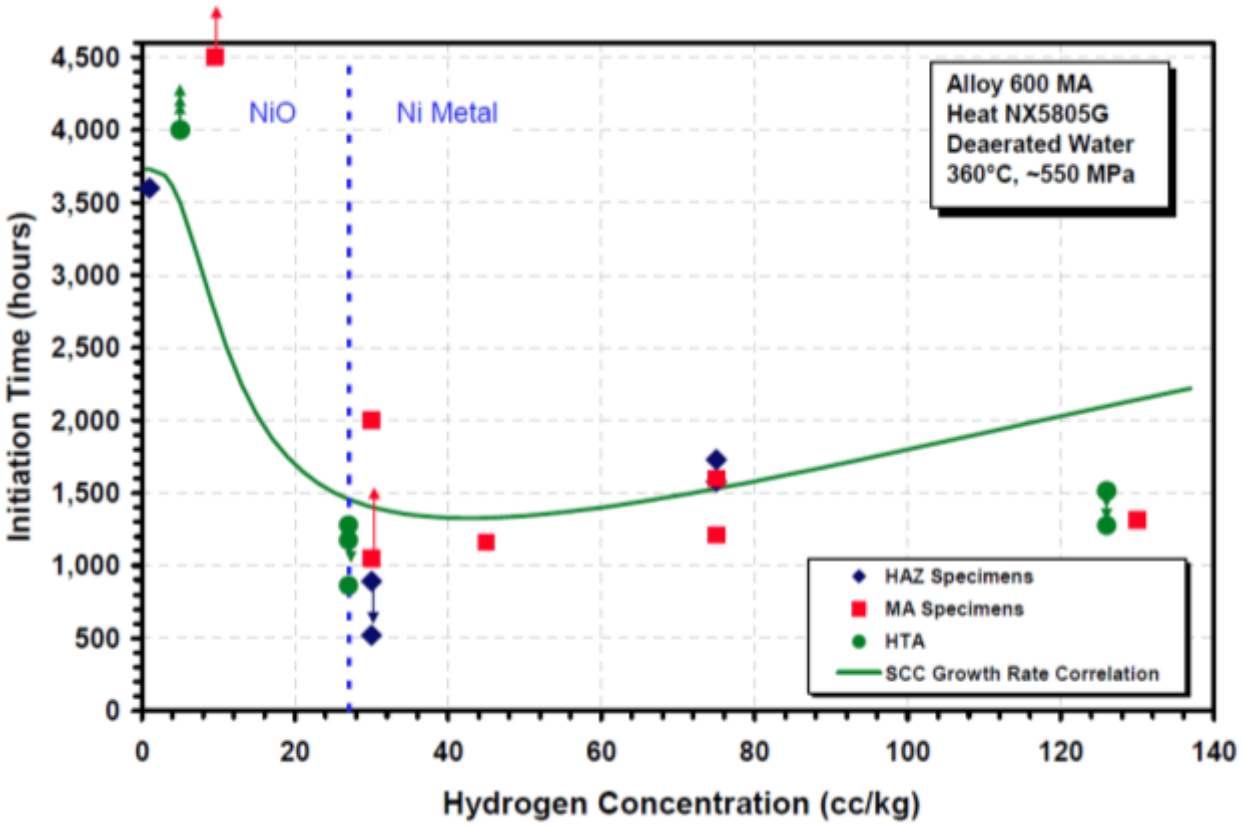

Figure 2.26. Effect of dissolved hydrogen on crack initiation in constant load of Alloy 600 in heat affected zone (HAZ), mill annealed (MA), and high temperature annealed (HTA) specimens.[43]

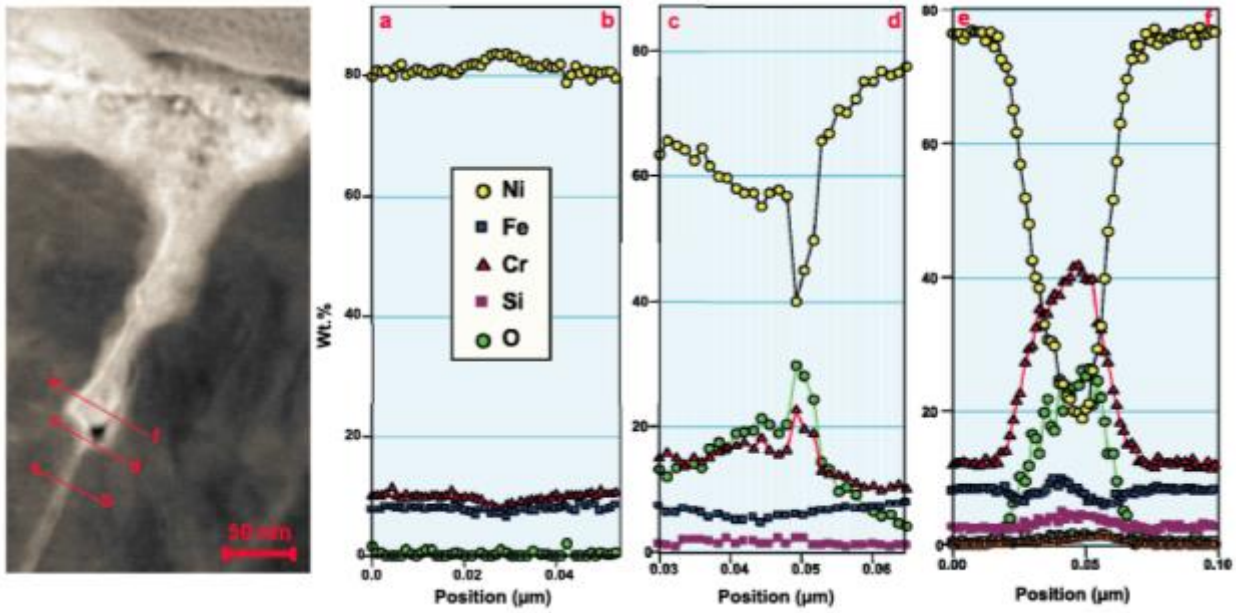

Figure 2.27. STEM high angular bright field micrograph and EDS composition profiles of an intergranular oxide penetration in Alloy 600 exposed to 325°C hydrogenated water. [44]

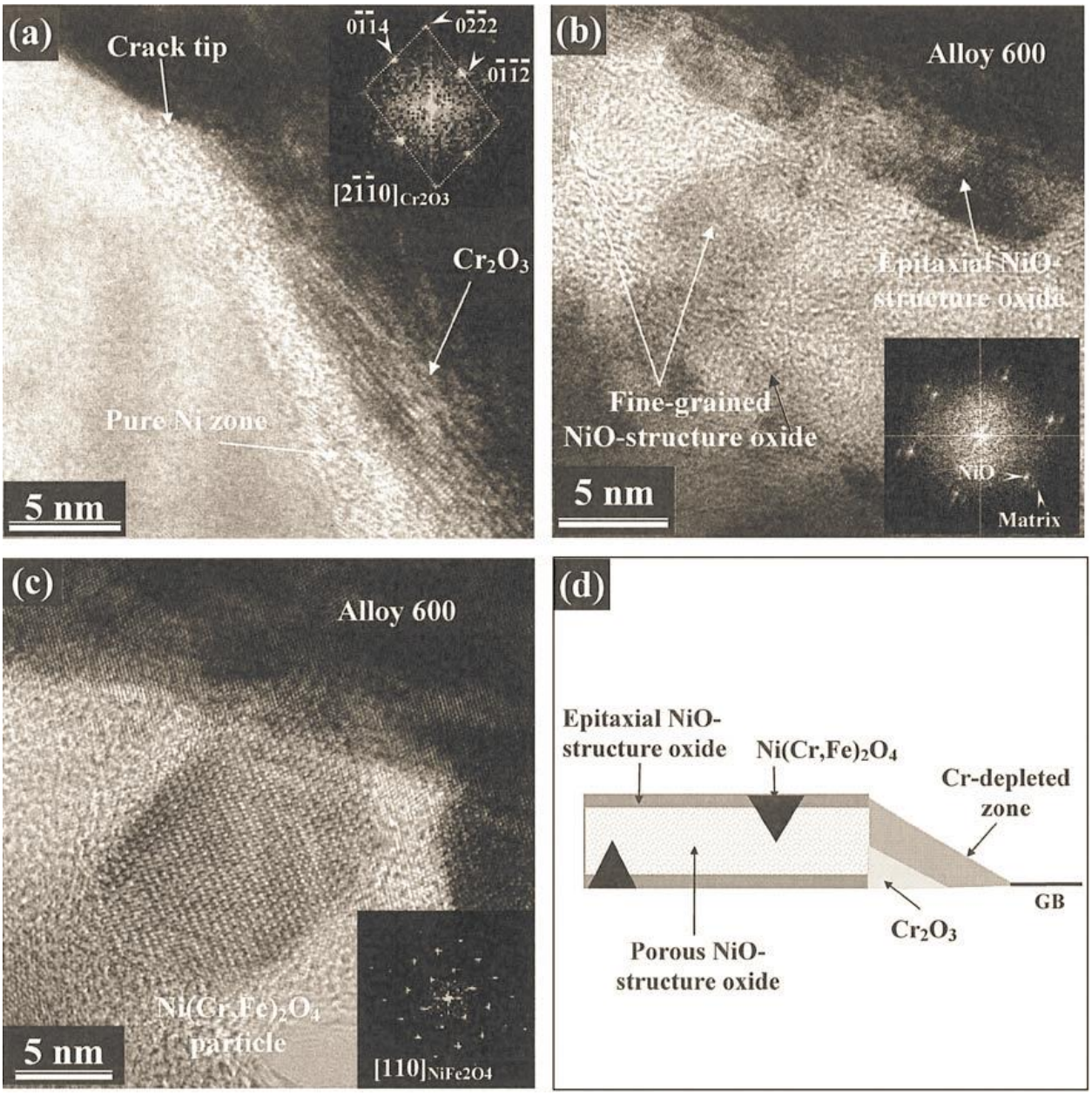

Figure 2.28. Lattice images obtained along (110) zone axis from an Alloy 600 U-bend exposed to 330°C PWR primary water. The crack tip is characterized by a region of Cr_2O_3 and chromium depleted metal. NiO grows epitaxial from crack flanks and porous NiO fills the crack. [35]

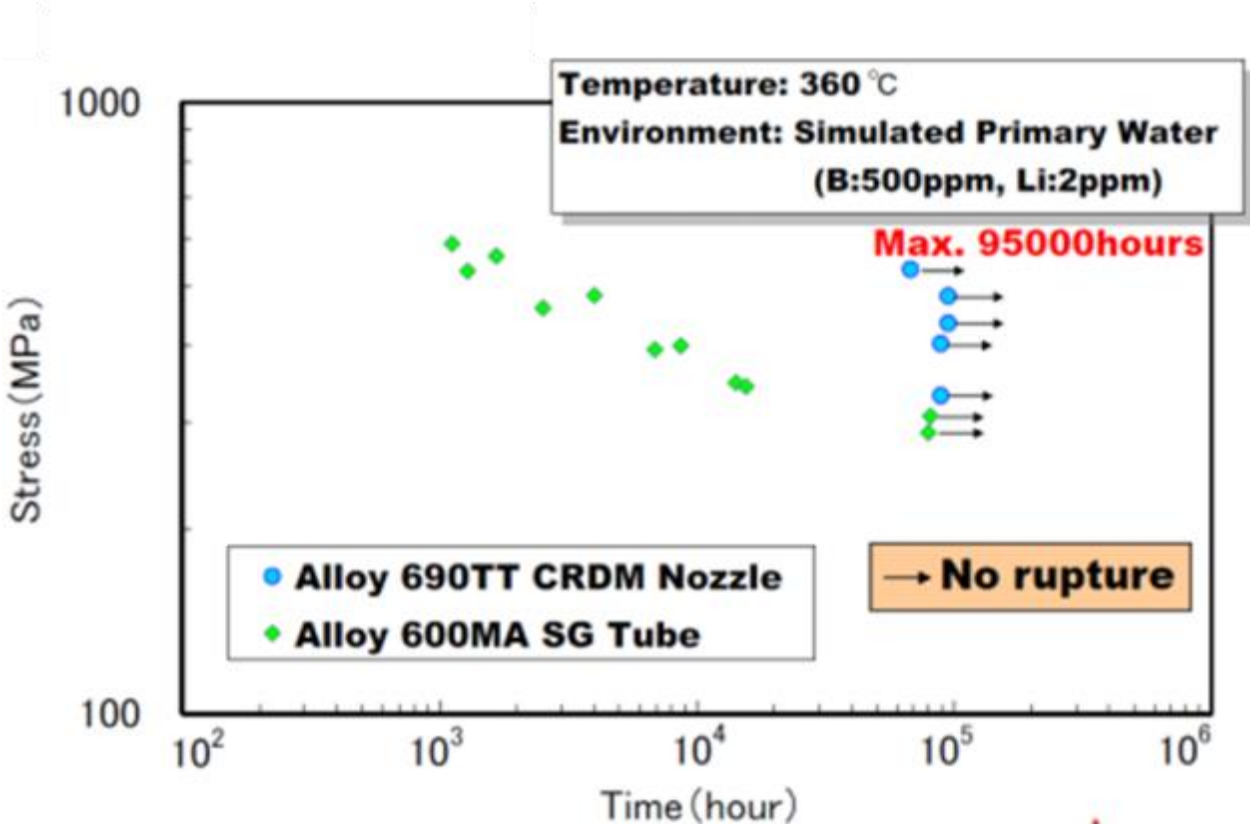

Figure 2.29. Crack initiation testing of Alloy 600 and Alloy 690 under active load tension in simulated PWR primary water. No rupture is observed for Alloy 690 after 95,000 hr (10.8 years). [50]

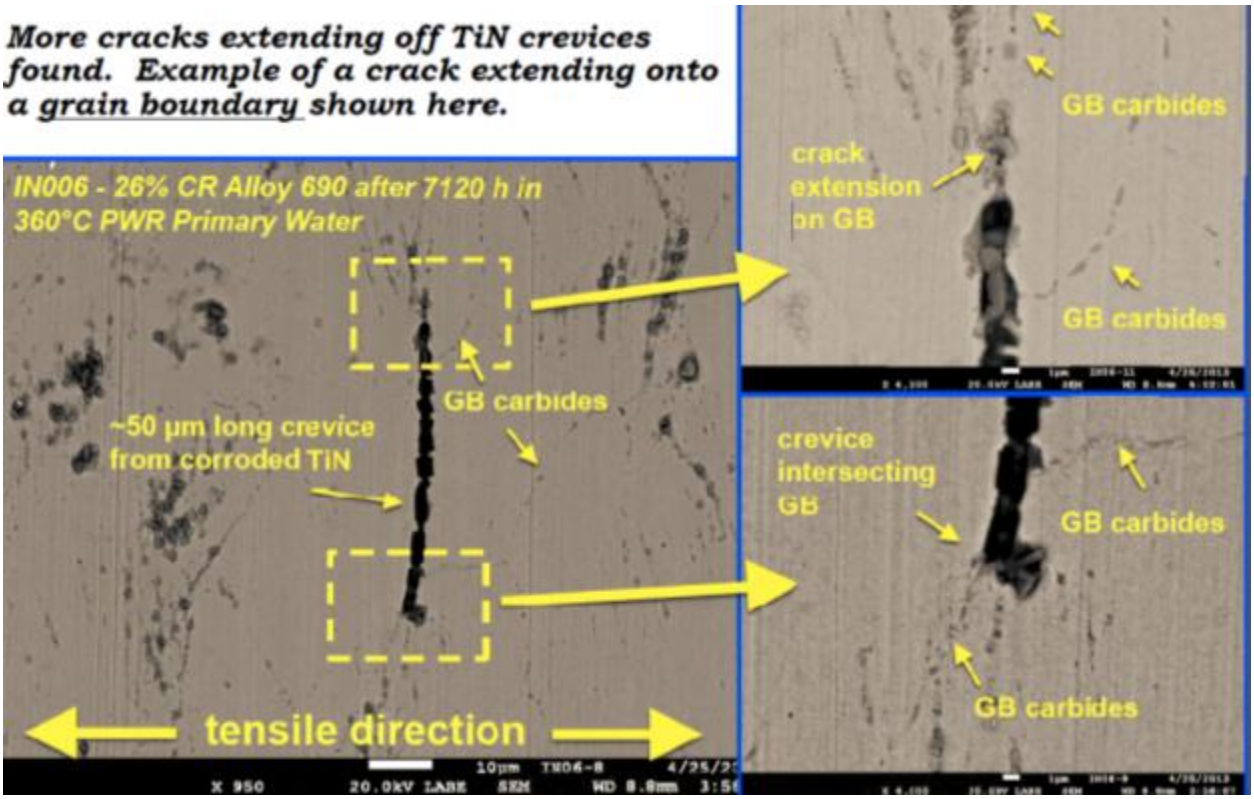

Figure 2.30. Cracking observed off TiN particles in 26% cold rolled Alloy 690 exposed to 360°C PWR primary water in constant load, not considered to be SCC. [52]

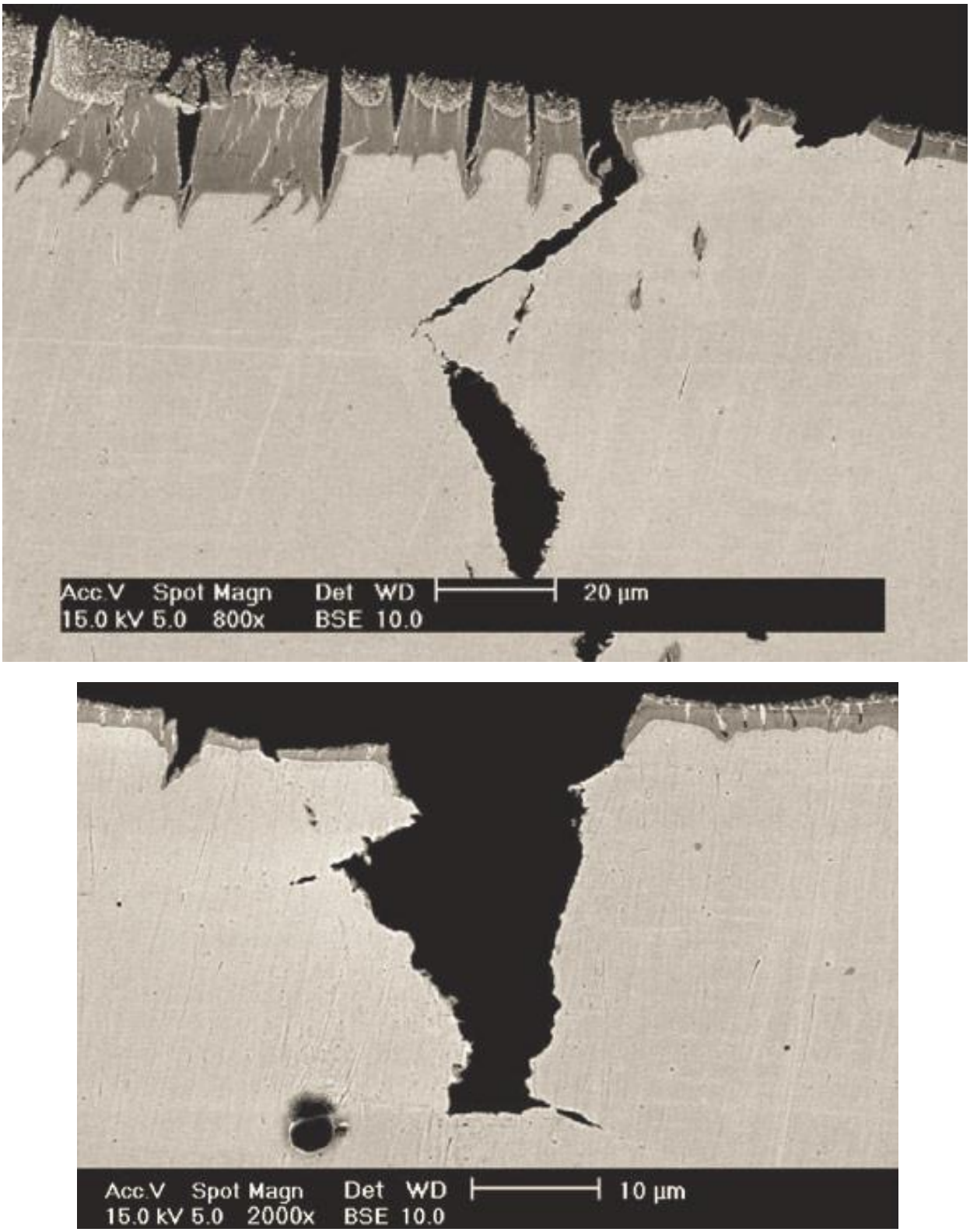

Figure 2.31. Cross section of an electropolished Alloy 690 SCC sample tested in deaerated supercritical water at 500°C strained to failure at $3x10^{-7}$ s^{-1}. [53]

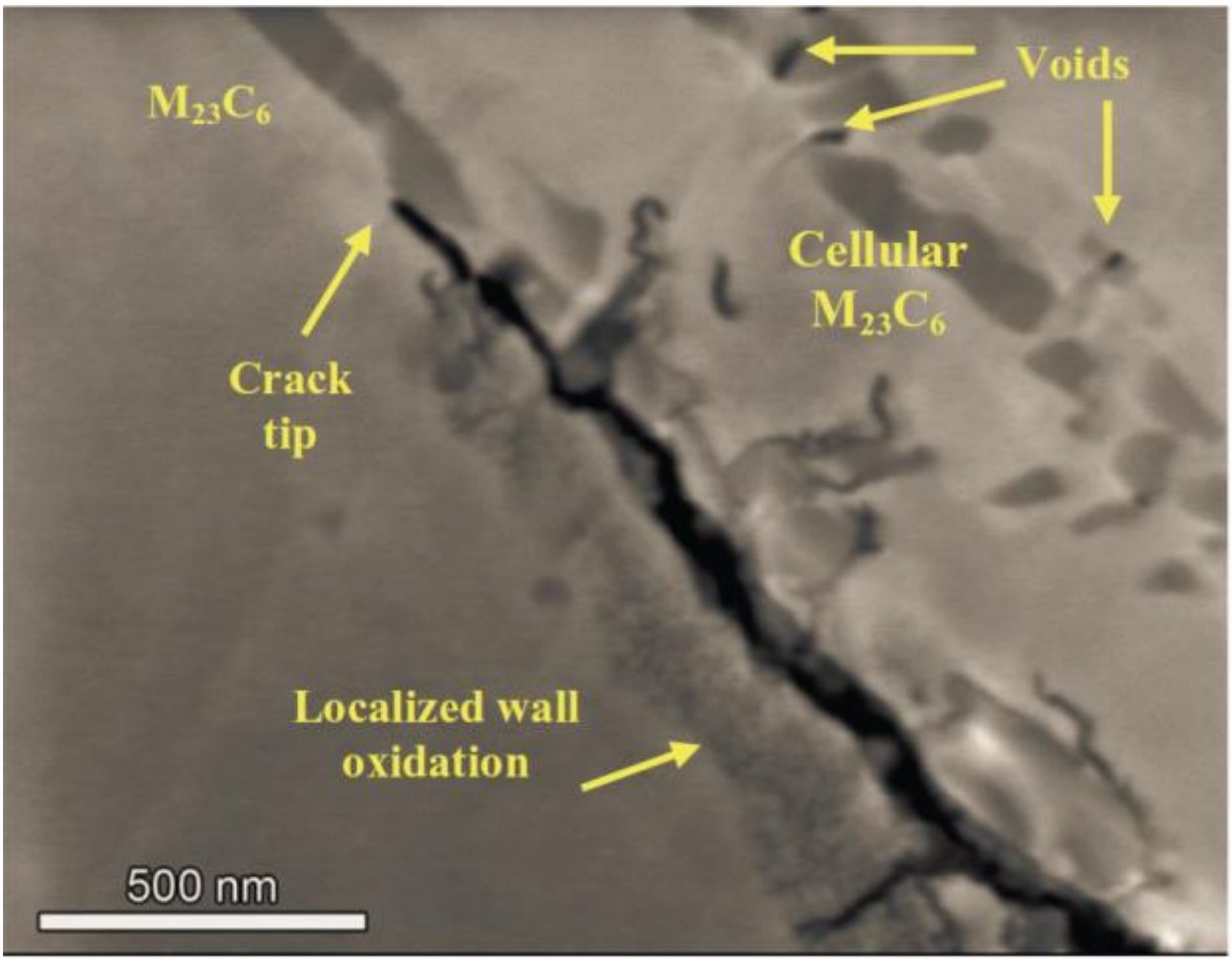

Figure 2.32. SEM-BSE micrograph of SCC in 30% cold rolled Alloy 690 from crack growth rate testing at 360°C in PWR primary water. The crack appears to follow the grain boundary instead of growing along open voids and cavities formed during the cold work. [46]

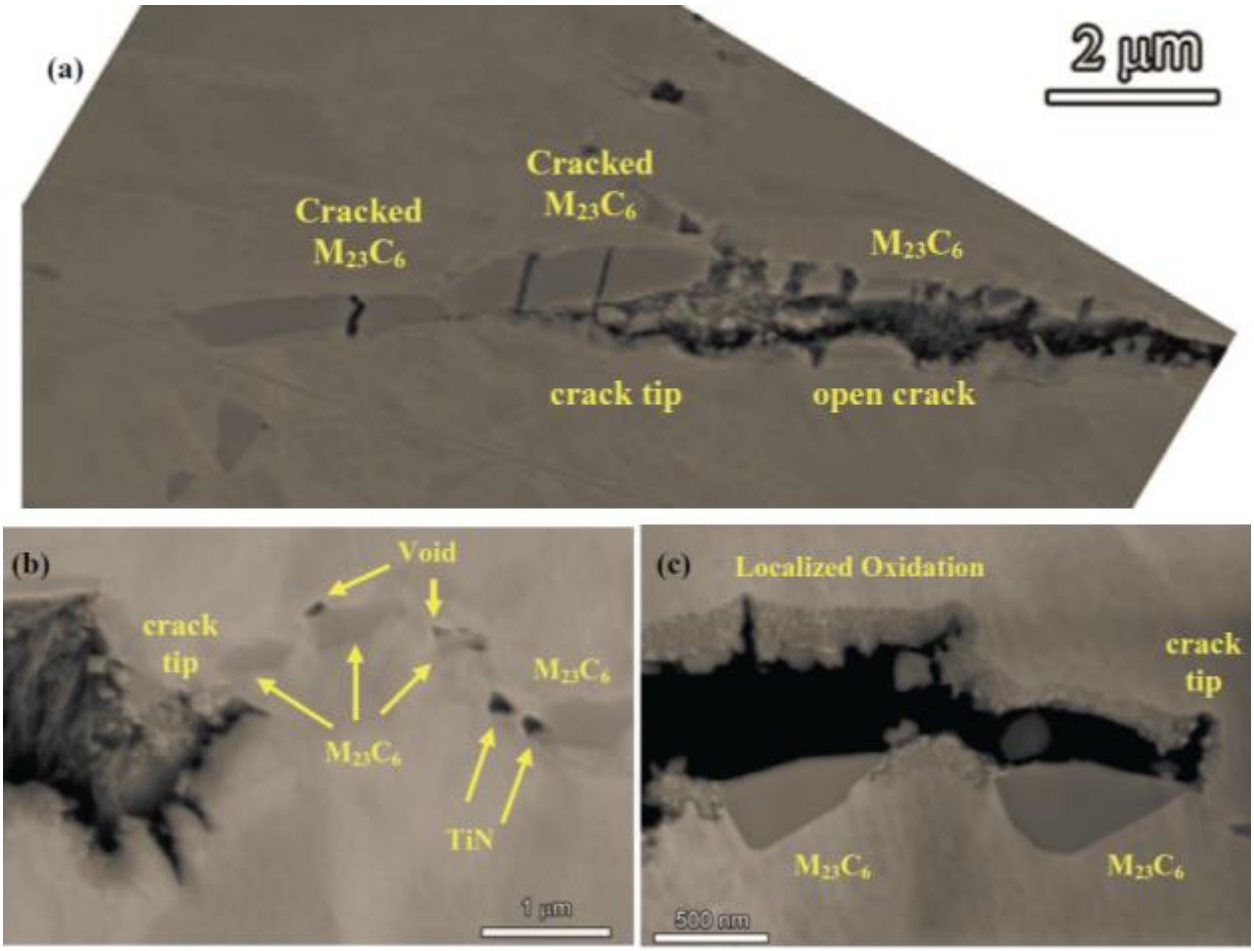

Figure 2.33. High magnification SEM-BSE micrographs of SCC tip regions in 26% cold rolled Alloy 690: (a) IG tip ending at cracked carbide, (b) blunt IG tip with shallow TG cracks and (c) open blunt IG tip adjacent to carbide.[46]

CHAPTER 3 - EXPERIMENTAL PROCEDURE

Determination of whether the mechanism of SCC initiation is consistent between subcritical water and supercritical water will be accomplished by three sets of experiments; first to define the environment, then to determine the oxidation behavior, and finally to determine the cracking behavior. Exposure of nickel coupons was used to determine the location of the Ni/NiO boundary in supercritical water and the hydrogen at the boundary was then used for the subsequent oxidation and SCC testing. Exposures of Alloys 600 and 690 were conducted at the University of Wisconsin and the corrosion behavior is analyzed by electron microscopy and X-ray diffraction. The stress corrosion cracking susceptibility of Alloy 600 and 690 was determined by constant extension rate testing in subcritical and supercritical water and characterized by electron microscopy to determine if there is a change in the activation energy or the morphology of cracking.

3.1 Alloy description

Two nickel-based alloys, 690 and 600 in the mill annealed condition, were used for this study. The Alloy 690 heat had an average grain size of 40 μm with discontinuous $M_{23}C_6$ carbides precipitated along the grain boundaries as shown in Figure 3.1. The composition of grain boundaries exhibited chromium depletion to 25 atomic% from the base metal composition of 29.5 at% to 25 at% by scanning Auger microscopy. The Alloy 600 heat had an average grain size of 60 μm with no carbides along the grain boundaries as shown in Figure 3.2. Both alloys

contained titanium nitride particles ranging from 5-10 μm in diameter uniformly dispersed in the matrix. The chemical compositions of both alloys are presented in Table 3.1. Alloy 600 was provided by GE Global Research Center from a control rod drive mechanism (CRDM) supplied by AREVA which has been shown to be susceptible to stress corrosion cracking[56,66]. It was annealed at 918°C for 20 minutes followed by water quench. Alloy 690 was supplied by Special Metals in plate form and was also shown to be susceptible to SCC initiation in supercritical water during CERT testing[53].

3.2 Sample design and preparation

Corrosion coupons of dimension 1.3 cm x 1.6 cm x 0.1 cm were prepared by electric discharge machining. Tensile bars were machined with the tensile axis oriented in the rolling direction. The tensile bars were 38.6 mm in length, had a gage section with a diameter of 2 mm and a length of 20.5 mm and threaded ends as shown in Figure 3.3. Samples were mechanically polished with silicon carbide abrasive paper from 400 to 1200 grit then electropolished in perchloric acid (10% $HClO_4$) and methanol (CH_3OH) solution maintained at -40°C, applying 30 V for 30 s to obtain a mirror finish. Uniform mechanical polishing of round gauge tensile bars was accomplished by inserting the sample into a Dremel® tool and applying wetted abrasive paper attached to a block. This method minimized variation in the gage diameter to less than 10 μm, Some of the Alloy 690 tensile bars were pre-strained at room temperature at a strain rate of $1x10^{-5}$ s^{-1} to 20% strain after mechanical polishing, but before electropolishing.

3.3 Supercritical water systems

Two autoclave systems were used in the University of Michigan High Temperature Corrosion Laboratory to conduct exposures of pure nickel coupons and to strain tensile bars, the multi-specimen supercritical water (MSCW) and single-specimen supercritical water (SSCW). The MSCW has a 4 L water capacity and can strain up to four CERT specimens, while the SSCW has a 1 L capacity and can strain one sample at a time. The systems have flowing water loops with external water columns that can accept gas additions. The loops consist of the vessel which is made of Inconel 625, two high-pressure liquid chromatography pumps, pre-heaters, and a back pressure regulator. The water is pressurized by the pumps and heated to supercritical temperatures before entering the vessel. From the vessel the water flows through a tube in tube heat exchanger and is chilled before reaching the BPR. The water then flows through several sensors that measure its conductivity and dissolved oxygen content. Finally it is fed through an ion exchanger before entering the main column again. Below 172 kPa (25 psi), the amount of dissolved hydrogen is controlled by using an overpressure of hydrogen in the glass water column as shown in Figure 3.4. To achieve pressures above 172 kPa (25 psi), a portable stainless steel tank replaces the glass water columns for both systems as shown in Figure 3.5 and Figure 3.6. Tensile samples were strained using a stepping motor in the constant displacement rate condition. The crosshead displacement was measured using a linear variable differential transformer (LVDT) with a displacement resolution of 0.5 μm.

3.4 Corrosion coupon exposures

3.4.1 Exposures of Alloy 600 and Alloy 690 at the University of Wisconsin

Coupons were exposed to subcritical and supercritical water conditions at the University of Wisconsin. All the samples were mounted on an Inconel 625 sample holder and placed in high temperature/high pressure autoclave with the surface of the coupons parallel to the water flow direction. A schematic of the autoclave system for corrosion experiments is shown in Figure 3.7. Corrosion coupon exposures at the University of Wisconsin were conducted at: 360°C 20.8 MPa 18cc/kg H_2, 390°C 25 MPa 70 cc/kg H_2, and 400°C 25 MPa 107cc/kg H_2. The dissolved hydrogen concentration was maintained at a fixed ECP above the Ni/NiO phase transition in the NiO stable regime. The dissolved hydrogen was controlled by the overpressure of the hydrogen above the water reservoir as calculated from Henry's law at room temperature. Before the corrosion experiments were begun, the system was flushed with high purity argon to achieve less than 10 ppb dissolved oxygen. Hydrogen was then introduced using a fixed overpressure for a period of two days before heating the system. The water conductivity was less than 0.2 μS/cm. Samples of the two alloys were exposed at 360°C and 400°C for 250, 500, 1000 and 2000 hr. Exposures at 390°C were conducted for 100, 400, and 700 hr. After each exposure period, two coupons of each alloy were removed for weight change measurements and surface characterization. The majority of the oxide analysis focuses on exposures conducted at 360°C 2000h, 390°C 400h, and 400°C 250h. These exposure times were chosen by assuming an activation energy for oxidation of 180 kJ/mol for both alloys[31,67] with the expectation of observing a similar extent of oxidation at the different temperatures.

3.4.2 Pure nickel exposures

To determine whether nickel or nickel oxide was stable, exposures of pure nickel coupons were performed in hydrogenated subcritical and supercritical water. Nickel coupons were prepared from 99.99% pure nickel foil with an elecropolished surface finish. Exposures of nickel coupons were conducted for 72 hours in the MSCW and SSCW at a variety of dissolved hydrogen concentrations and temperatures as shown in Table 3.2. The amount of dissolved hydrogen was controlled by fixing the overpressure of hydrogen in the room temperature feed water and was calculated via Henry's law using a Henry's law coefficient of 1282.05 L atm/mol. Pre-purified hydrogen and mixtures of hydrogen with argon were used to achieve the desired hydrogen concentrations. The error in the dissolved hydrogen was estimated by taking the average of the concentration difference due to the weight of the water from the top to the bottom of the water column and adding that to the variation caused by a 1 psi fluctuation over the course of the experiment.

3.5 Hydrogen fugacity and Henry's law constant measurement

The Henry's law constant was determined by measuring the fugacity of hydrogen at several hydrogen concentrations at various temperatures in subcritical and supercritical water. The fugacity was measured using a palladium-silver alloy (80/20 wt%) tube with a length of 1", outer diameter of 1/8" and inner diameter of 1/16". The tube was sealed at one end with Swagelok fittings and installed in the vessel at the same position at which exposures were conducted and next to the thermocouple. The tube was connected through the vessel to a vacuum pump with 316 stainless steel tubing. Measurements were taken by pulling a vacuum on the inside of the tube, sealing the vacuum, and then measuring the pressure rise due to the diffusion of hydrogen through the tube wall with a transducer. A measurement was considered to be at equilibrium

when the pressure increase was less than 0.0013 atm/hour. The measured pressure was taken as the fugacity of hydrogen in the vessel at the measured water pressure, temperature, and dissolved hydrogen concentration. Henry's constant at each temperature and pressure was determined by averaging the ratio of the measured fugacities to the dissolved hydrogen concentrations.

Typical measurement procedure for the hydrogen fugacity is shown in Figure 3.8 at 320°C at a vessel pressure of 25MPa. The calculated Henry's law constant is plotted in red on the right axis and the measured hydrogen fugacity inside the Pd/Ag tube is plotted in black on the left axis. With 48 cc/kg H_2 added to the autoclave, the measurement was taken by pulling a vacuum at t=0 h with the rough pump and closing off the valves to measure the diffusion and equilibrium pressure of hydrogen into the tube. At t=46 h the overpressure of hydrogen in the feed water tank is lowered to fix the concentration at 28 cc/kg. Correspondingly the fugacity of hydrogen drops and the Henry's law constant temporarily increases until the concentration of hydrogen dissolved in the water reaches equilibrium. The system is pumped to vacuum again at t = 70 h for the measurement at 28 cc/kg. The Henry's law constant agrees very well between the two measurements. Figure 3.9 demonstrates the linearity of the fugacity with dissolved hydrogen concentration at 400°C, which experimentally validates the use of Henry's law for these measurements. The linear fit to the data has an R^2 of 0.999 and an offset of 0.0006 atm.

3.6 Constant extension rate tensile (CERT) testing

All water CERT experiments were conducted in the NiO stable regime, a fixed electrochemical potential (ECP) above the Ni/NiO boundary from 320°C and 450°C in pure hydrogenated water at the conditions listed in Table 3.3. The required dissolved hydrogen concentration for each

temperature was determined by the results of the pure nickel exposures in this work. The flow rate was set at 40 mL/min and the conductivity was maintained to be under 0.1 μS/cm on the inlet and outlet by resin ion exchange filters.

In order to measure an accurate temperature dependence of crack initiation over the entire proposed temperature range (320-450°C), a set of probing experiments was conducted. The upper bound of validity is dictated by the saturation of crack nucleation, the case where most or all grain boundaries have cracked. The lower bound of validity is dictated by the statistics of the measurement, for example only observing ten cracks in the entire sample is not useful data. To measure the temperature dependence of crack initiation for Alloy 600, samples were strained in the MSCW at a strain rate of $3x10^{-7}$ s^{-1}. It was found that at temperatures above 425°C all grain boundaries normal to the tensile axis had cracked (Figure 3.10), causing saturation. An additional set of CERT tests were conducted on Alloy 600 in the SSCW at a strain rate of $3x10^{-7}$ s^{-1} to 2% strain to avoid saturation of the crack density in supercritical water. Samples of Alloy 690 strained to 7% at $5x10^{-8}$ s^{-1} did not have enough crack initiation in subcritical water to provide meaningful statistics. To measure the temperature dependence of crack initiation for Alloy 690, samples were made more susceptible by applying a pre-strain at room temperature to 20% then further strained in the MSCW at a strain rate of $5x10^{-8}$ s^{-1} to 7% strain in the water environments. To determine the effect of pre-strain, Alloy 690 was strained without pre-strain in supercritical water with a strain rate of $5x10^{-8}$ s^{-1} to 7%. To determine the contribution of creep on crack initiation, samples of Alloy 690 with and without pre-strain, and Alloy 600 without pre-strain were strained in high purity argon at 450°C at a strain rate of $5x10^{-8}$ s^{-1} to 7% and 8%, respectively. The argon, initially 99.999% purity, was purified further to 99.99999% purity to

remove any trace water and oxygen that could cause oxidation, using a 27601-U Supelco purifier. An overpressure of 20 kPa (3 psi) of argon was maintained with a flow rate of approximately $9x10^{-6}$ m^3/s.

Experiments were conducted by first preparing the vessel gasket and cleaning the interior of the vessel with acetone, methanol, and ethanol. Samples were then loaded into electrically isolated clevises attached to the pull-rods. Any corrosion coupons were then hung from posts by nickel wire surrounded by zirconia sleeves. The autoclave was then sealed, filled with water, checked for leaks, and pressurized to 25 MPa. The vessel was heated when the water conductivity dropped below 0.1 μS/cm and straining was begun when at the conductivity once again dropped below 0.1 μS/cm at the desire d temperature. Tensile samples were first loaded by hand to balance the load on the crosshead. Samples with prior cold work were pre-loaded to 100 MPa below their yield stress at a strain rate of $5x10^{-5}$ s^{-1}. Once the desired total strain was reached, samples were unloaded and the vessel was cooled over a period of 6-8 hours.

3.7 Post exposure and CERT straining sample characterization

3.7.1 Fractography

After removal from the autoclave, samples were examined by scanning electron microscopy (SEM) to characterize the cracking on the gauge section. Crack density, crack length, and crack length per unit area were measured from images taken at a fixed magnification spaced evenly over the sample. Only intergranular cracks were considered for the measurement, excluding cracks along TiN particles. For branched cracks, the longest possible crack was measured and branches were considered to be separate cracks. The length of cracks was measured by tracing

cracks in Adobe Photoshop® with a 1 pixel wide pen and measuring the area of traced cracks in ImageJ®. An example of a gauge section of Alloy 600 with cracks and the traced cracks is shown in Figure 3.11. Crack depth was measured by cross sectioning and mechanically polishing the tensile bars.

Confidence intervals for measures of cracking in CERT testing were determined by calculating the error of the measurement and then propagating that error to the fit of the temperature dependence by simulation. The error of the crack length per unit area measurement was found using the method developed by Alexandreanu and Was[68]. The cracking was modeled as a binomial distribution where the standard deviation of the density is defined as,

$$\sigma_\rho = p\left(\frac{1}{N}\frac{1-p}{p}\right)^{\frac{1}{2}} \tag{3.1}$$

where σ_ρ is the standard deviation of the crack density, N is the number of measured grain boundaries, and p is the fraction of cracked boundaries. The standard deviation of the average length measurement is defined as,

$$\sigma_l = \frac{\sqrt{\sigma_m{}^2\, M}}{M} \tag{3.2}$$

where σ_l is the standard deviation of the average crack length, σ_m is the error in the length measurement of a single crack, and M is the number of cracks. The error in the length measurement of a single crack was found to be 0.2 μm. Because the length per unit area is equal to the product of the density and the average length, the uncertainty from the length and density measurements was propagated to the length per unit area measurement as follows:

$$\frac{\sigma_{L_A}}{L_A} = \sqrt{\frac{{\sigma_p}^2}{\rho} + \frac{{\sigma_l}^2}{l}} \tag{3.3}$$

where σ_{L_A} is the standard deviation of the crack length per area, L_A is the value of the crack length per area, ρ is the value of the crack density, l is the value of the average crack length. The 95% confidence intervals for the activation energy were simulated by assuming that the uncertainty of the crack length per unit area followed a normal distribution for each data point. For each temperature the value was randomly generated following the normal distribution and a fit was calculated from the generated data as shown in Figure 3.12 for 4 different trials. This process was repeated 100 times and the standard deviation of the fits was calculated as shown in Figure 3.13. After 30 iterations the standard deviation did not vary by more than 1 kJ/mol. All 95% confidence intervals were calculated by taking the P = 0.05 quantile of the standard deviations by multiplying the standard deviations by 1.96. Fits for the activation energy were performed by a nonlinear robust regression following the Arrhenius relationship in GraphPad Prism©. The metric used to determine the activation energy for crack initiation is the crack length per unit area, which is a combination of crack density and average crack length. The crack density is the number of cracks in a given area and can be thought of as a measure of the crack nucleation. The average crack length is more a measure of the crack growth rate on the surface.

Samples were prepared for detailed examination of crack morphology, chemistry, and structure by focused ion beam scanning electron microscopy (FIB-SEM) at the University of Michigan Electron Microbeam Analysis Laboratory. FIB lift-outs of cracks were performed by following the sample preparation method developed by Lozano-Perez[69]. High resolution SEM examination and FIB serial sectioning was performed on a Helio Nanolab 650. Transmission

electron microscopy (TEM) was performed on a 200 keV JEOL 2010F Analytical Electron Microscope. Scanning Auger Microscopy (SAM) was performed on a Physical Electronics Auger Nanoprobe 680. Surface cleaning was performed by sputtering the sample surface with 2 keV argon at a current of 1 μA. Elemental analysis was calibrated by collecting spectra from oxide standards of Cr_2O_3 and Fe_2O_3 without sputtering the surface. Spectra were collected using a 10 keV 10nA electron beam which yielded a spot size of around 50 nm.

3.7.2 Corrosion product analysis

The structure of surface oxides was measured using X-ray diffraction performed on select coupons to determine the structure of the oxides formed during exposures. Scans of Alloy 600 and Alloy 690 coupons were conducted with an incident angle of 20° and a scan rate of 0.025°/min on a Rigaku rotating anode X-ray diffractometer using copper radiation (1.5406 Å). Scans of pure nickel were conducted with an incident angle of 1.5° and a scan rate of 0.3°/min. The patterns were analyzed by fitting the peaks to likely structures in JADE ® using diffraction data from the Joint Committee on Powder Diffraction Standards (JCPDS). The following JCPDS cards were used for analysis of X-ray diffraction and electron diffraction: Ni (4-0850), $Ni(OH)_2$ (1-080-2855), NiO (47-1049), Cr_2O_3 (6-0504), $NiCr_2O_4$ (54-0961), and $NiFe_2O_4$ (54-0964). The space group and lattice parameters used for phase identification is listed in Table 3.4. Also listed is the phase MO with the same space group as NiO, but with a non-standard lattice parameter. In this case, M corresponds with metal content and O corresponds with oxygen in a 50/50 atomic% mixture. The metal content can consist of varying concentrations of Ni, Fe, Cr. Because the metal composition is variable, the lattice parameter would also change accordingly. When

indexing diffraction patterns, the MO phase was assumed to have the same lattice parameter as NiO.

Analysis of the oxide morphology was conducted by surface examination and examination in cross section. Surface examinations were focused primarily on using secondary electrons to image fine details of the surface, however limited examination was conducted with backscattered electrons to interrogate deeper into the samples. Secondary electrons were collected using the through lens detector with the beam was set to an accelerating voltage of 5 keV to optimize the resolution. Imaging in backscatter mode was used at higher voltages between 15-30 keV, which was able to highlight sub-surface features. FIB cross sections were made by the standard method of laying a platinum cap and trenching the material at high current, with low current to clean the surface for imaging. The depth of internal oxidation was measured at 360°C at 250, 500, 1000, and 2000 hr by cross section FIB-SEM. For each condition, approximately 25 μm of material was examined and over 400 measurements were taken for each case. Images were taken without correcting for specimen tilt, however the tilt was taken into account during the quantitative analysis of oxide depth by dividing the measured depth by sin(52°).

Lift-out samples were prepared for detailed examination of oxide morphology, chemistry, and structure by focused ion beam scanning electron microscopy. For TEM sample preparation, platinum coating was deposited to protect the oxide surface before cutting. TEM lamellae were created by coarse FIB trenching of samples with dimension 20 μm × 3 μm × 4 μm. The samples were then welded to a copper TEM grid thinned by FIB at 30 kV to a final thickness of roughly 100 nm. Transmission electron microscopy (TEM) was performed on a JEOL 2010F Analytical

Electron Microscope. Examination of the surface and cross section oxide morphology were performed using high resolution SEM on a Helios Nanolab 650 at the University of Michigan Electron Microbeam Analysis Laboratory. High resolution images of lift-outs and cross sections were taken using mode 2 with the through lens detector in secondary electron mode. The concentric backscatter detector was used to collect backscattered electron information, which emanated from deeper in the lift-outs. Images of cross sections were taken at 5 keV with a current of 100-400 pA. Phase identification using electron diffraction patterns was conducted by comparing lattice plane spacing of Cr_2O_3, $NiFe_2O_4$ (same as $NiCr_2O_4$), NiO, and 690 metal to the observed diffraction spots. In most cases selected area diffraction was performed on nanocrystaline oxides which yielded multiple spots for each lattice plane, necessitating use of ring patterns to index patterns. During each TEM session, a diffraction pattern of the base metal was taken to calibrate the camera length used in oxide diffraction. The lattice parameter of Alloy 690 was measured by X-ray diffraction (Figure 0.1) and the lattice parameter was measured at 3.5773Å.

Scanning Auger Electron Microscopy (SAM) of the surfaces and cross sections were performed on a Physical Electronics Auger Nanoprobe 680 to determine the composition of oxides. Depth profiling and surface cleaning were performed by sputtering the sample surface with 2 keV argon at a current of 1 μA. Elemental analysis was calibrated by collecting spectra from oxide standards of Cr_2O_3 and Fe_2O_3 without sputtering the surface. Spectra were collected using a 10 keV 10nA electron beam which yielded a spot size of around 50 nm. Depth profiling was conducted by first sputtering with argon for 0.5 or 1 minute followed by a 10 second hold before

collecting spectra from points selected on the surfaces. Image registration was performed between each sputtering step to ensure that the same location was analyzed. Correlating the observed oxide thickness with the oxygen concentration suggested a sputter rate of approximately 1 nm/minute. Argon sputtering was also used to highlight the location of the grain boundary after migration had occurred, due to the differences in sputtering rates based on grain orientation. The sputtering was performed in the scanning Auger microscope on a liftout of Alloy 690 exposed at 400°C for 250 hours using the same parameters that were used to clean the surface (2 keV, 1μA) for 5 minutes.

Determining the error in the measured Auger data is slightly complicated by the fact that multiple phases are being measured on a surface that is not perfectly flat. The measured composition of element *i* is calculated as follows:

$$C_i = F_{Matrix} * F_{Calibration} * \frac{N_i}{N_{Standard}} \qquad (3.4)$$

where C_i is the composition of element *i*, F_{matrix} is the effect of the matrix, and $F_{calibration}$ is the scaling factor determined from the calibration. The scaling factor due to the matrix is slightly complex and a function of the backscattering efficiency, mean free path, and density. The scaling factor for the calibration was determined first by measuring the bulk Alloy 690 to determine the scaling factor between the metallic elements. To determine the scaling factor to oxygen, two elemental standards of Cr_2O_3 and Fe_2O_3 were used. Once the calibration was set, several checks were conducted to determine if the calibration was correct. The calibration was set first using patterns from the Cr_2O_3, which was then confirmed to read the correct composition from the Fe_2O_3 sample. The calibration was conducted at the same conditions that the measurement was taken, 10 keV at a stage tilt of 30°. However, the calibration performed was not able to account

for the matrix correction factor. Assuming a matrix correction factor of 1, the error of the measurement can be calculated by standard error propagation techniques:

$$\frac{\sigma_{C_i}}{C_i} = \sqrt{\left(\frac{\sigma_{N_i}}{N_i}\right)^2 + \left(\frac{\sigma_{N_{standard}}}{N_{standard}}\right)^2}. \quad (3.5)$$

By substituting equation 3.4 into 3.5, the error in the concentration based on the counting statistics is as follows:

$$\sigma_{C_i} = C_i \sqrt{\left(\frac{1}{N_{standard}}\right)\left(\frac{F_{Calibration}}{C_i} + 1\right)}. \quad (3.5)$$

The number of counts in the standard patterns for all peaks is approximately 10^6, which yields errors in the concentration up to 0.1 atomic%. While this error is small, the factors that influence the matrix correction factor are not insignificant. However, the technique did not allow for measurement of those factors. This makes it difficult to speculate on the error bars needed on the Auger composition data. The statistics suggest very little error, however it is unknown what effect the surface topology has for each data point. It is worth noting that repeated measurements of the same feature on different sections of the sample yielded deviations less than 3 atomic% in most cases, shown in Table 4.3.

To determine if the stable form of nickel was metal or oxide from the exposures of pure nickel, the coupons were examined optically and the amount of oxygen was determined by nuclear reaction analysis using the reaction $^{16}O_{(d,p1)}{}^{17}O$. The analysis was conducted at the Michigan Ion Beam Laboratory using an 850 keV deuterium beam with the detector at an angle of 150° from the incident beam. The amount of oxygen in the surface was determined by integrating the $^{16}O_{(d,p1)}{}^{17}O$ peak and taking a ratio to the integrated charge. Samples were determined to be NiO

stable if the counts/charge (#/μC) in the $^{16}O_{(d,p1)}{}^{17}O$ peak was above 10 counts/μC. A freshly polished sample of nickel was used to determine the thickness of the air formed film.

Table 3.1. Alloy Composition (Weight Percent)

Alloy/Heat	C	Mn	Fe	S	Si	Cu	Ni	Cr	Co	P	Nb	Ti
Alloy 600 / 93510	0.047	0.23	8.94	0.002	0.3	0.01	Bal	15.42	0.057	0.005	NM	NM
Alloy 690 / NX3151HK	0.03	0.18	10	0.001	0.03	0.01	Bal	29.4	NM	NM	NM	0.34

NM = Not Measured

Table 3.2. Summary of nickel exposures.

Temperature (°C)	Dissolved Hydrogen (cc/kg)
320	6 ± 0.76
	8.5 ± 0.76
330	8 ± 0.76
350	13 ± 1.5
360	10 ± 0.76
	13 ± 1.5
	18 ± 1.5
	26 ± 2.2
	47 ± 3.8
385	35 ± 3.8
	50 ± 3.8
	70 ± 3.8
390	70 ± 3.8
400	47 ± 3.8
	75 ± 3.8
	107 ± 3.8
	137 ± 3.8
	200 ± 3.8
425	150 ± 3.8
	200 ± 3.8
	250 ± 3.8
450	200 ± 3.8
	290 ± 3.8
	380 ± 3.8

Table 3.3. CERT experiment conditions

	Dissolved Hydrogen		Alloy 600 $3x10^{-7}$ s^{-1}		Alloy 690 $5x10^{-8}$ s^{-1} 7%	
Temperature (ºC)	cc/kg	ppm	2%	8%	20% Pre-Strain	No Pre-Strain
320	6	0.5	x	x	x	
330	8	0.7		x		
350	13	1.2		x	x	
360	18	1.6	x	x	x	
390	70	6.3	x		x	x
400	107	9.6	x	x	x	
425	200	18	x	x	x	x
450	290	26.1		x	x	x

Table 3.4 Crystallography and lattice parameters used for phase identification.

Phase	Crystal System	Space Group	Lattice Constants (Å)		
			a	b	c
Ni	Cubic	Fm-3m	3.5238	3.5238	3.5238
Alloy 690	Cubic	Fm-3m	3.577279	3.577279	3.577279
NiO	Cubic	Fm-3m	4.1771	4.1771	4.1771
MO	Cubic	Fm-3m	Not Standard	Not Standard	Not Standard
$Ni(OH)_2$	Hexagonal	P-3m1	3.1268	3.1268	4.606
Cr_2O_3	Hexagonal	R-3c	4.958	4.958	13.593
$NiCr_2O_4$	Diamond Cubic	Fd-3m	8.322	8.322	8.322
$NiFe_2O_4$	Diamond Cubic	Fd-3m	8.33567	8.33567	8.33567

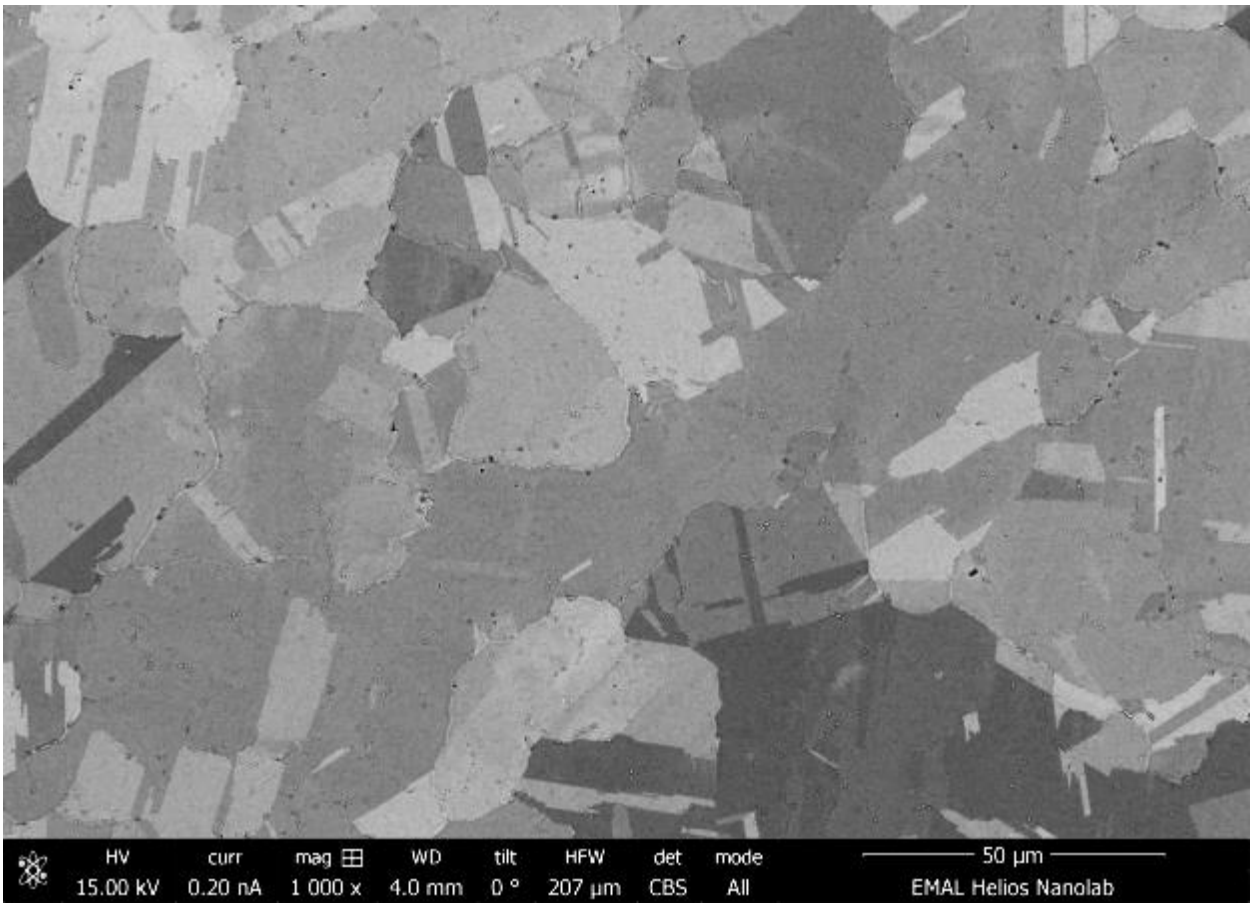

Figure 3.1. SEM backscatter image of electropolished Alloy 690

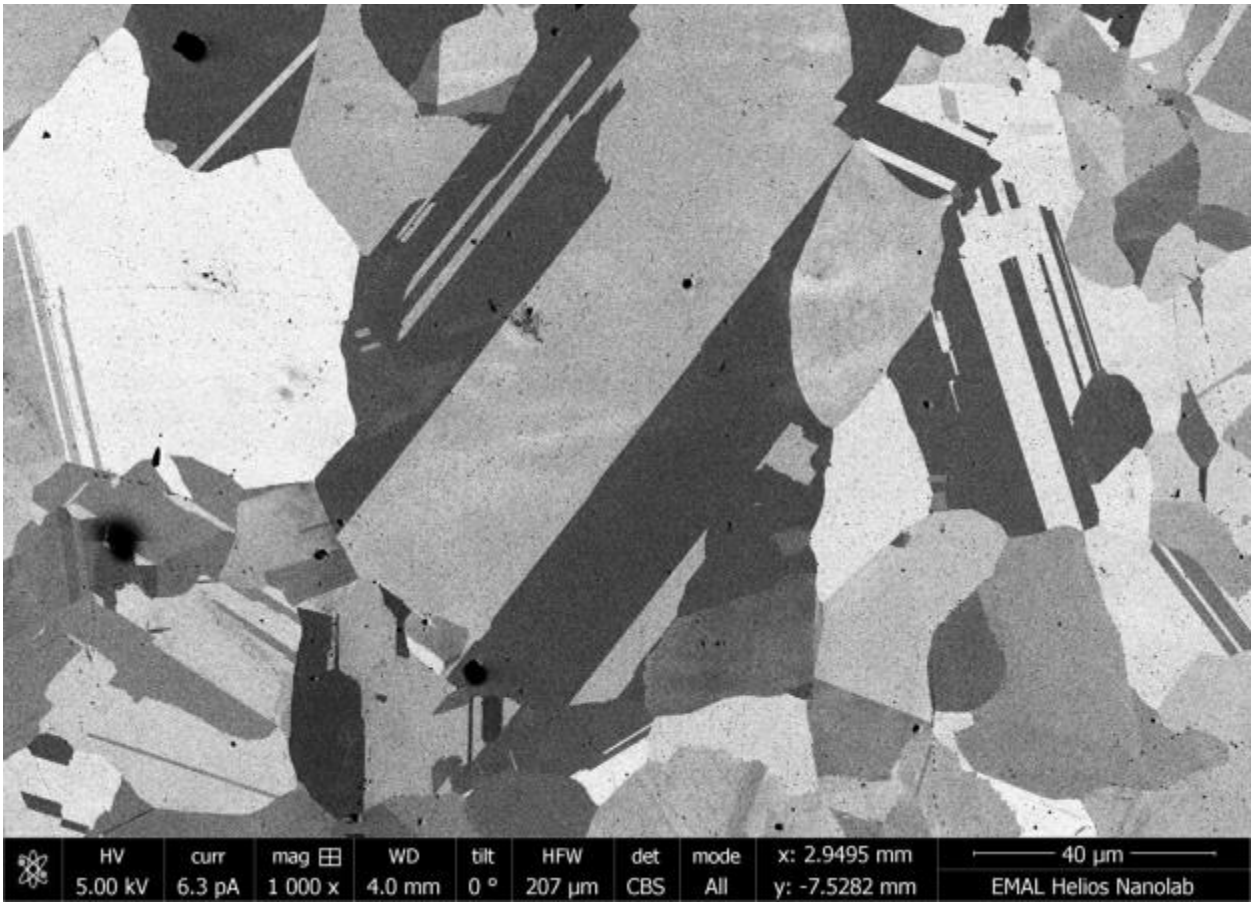

Figure 3.2. SEM backscatter image of electropolished Alloy 600.

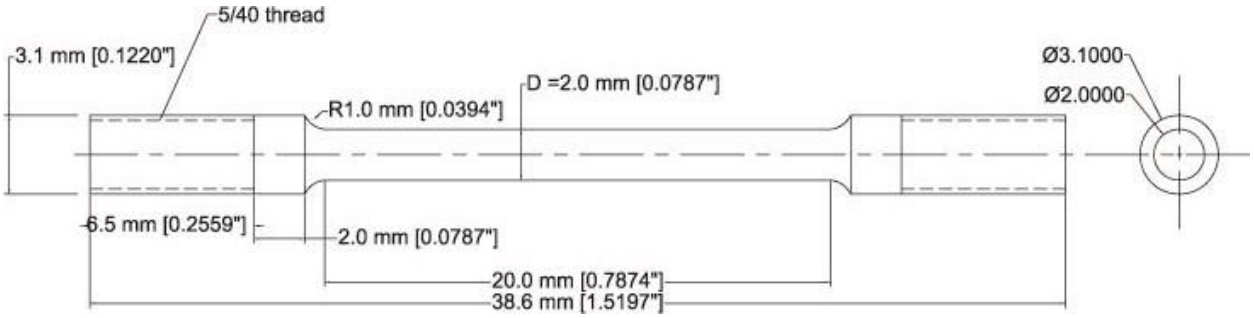

Figure 3.3. Schematic of tensile specimen

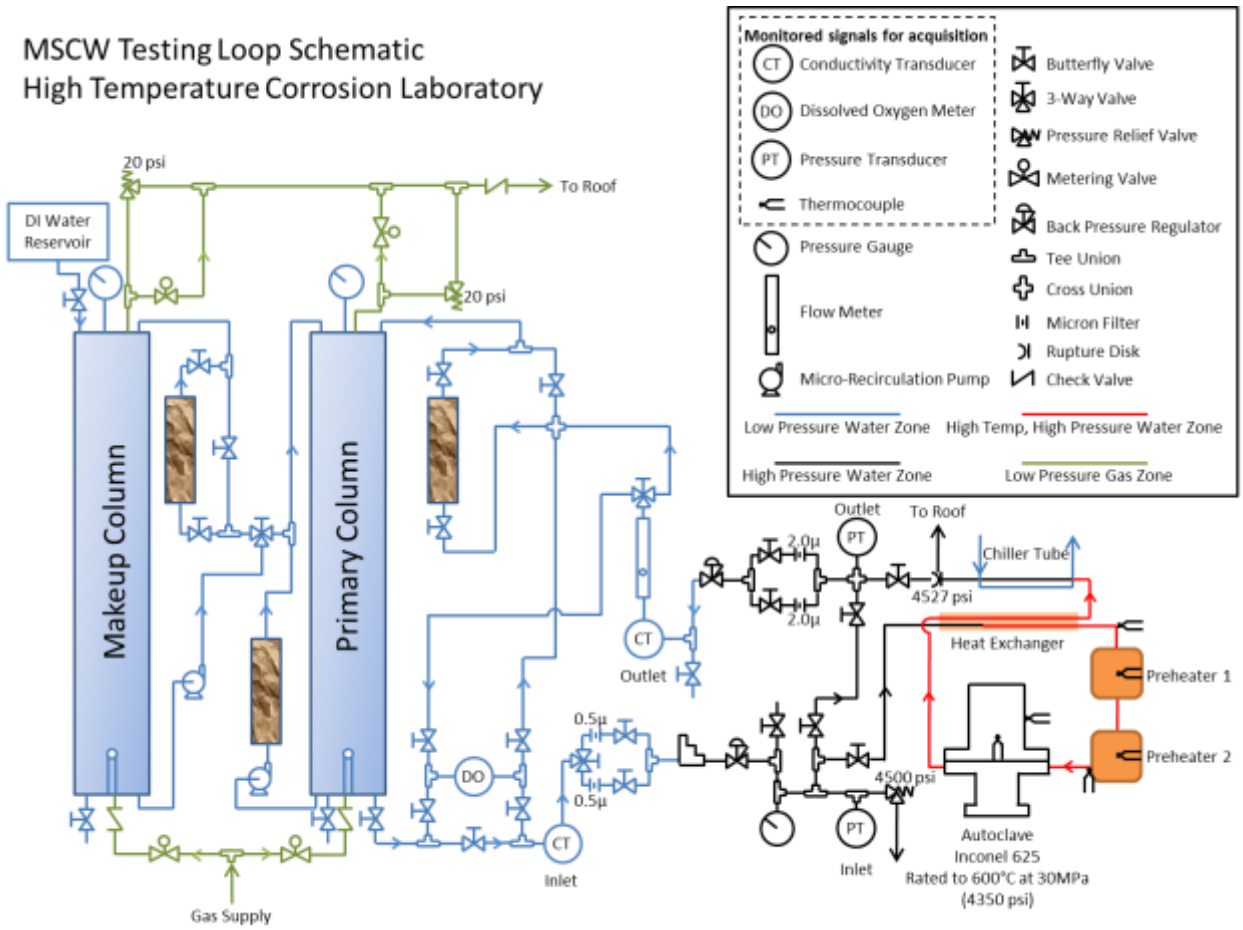

Figure 3.4. Schematic of the MSCW.

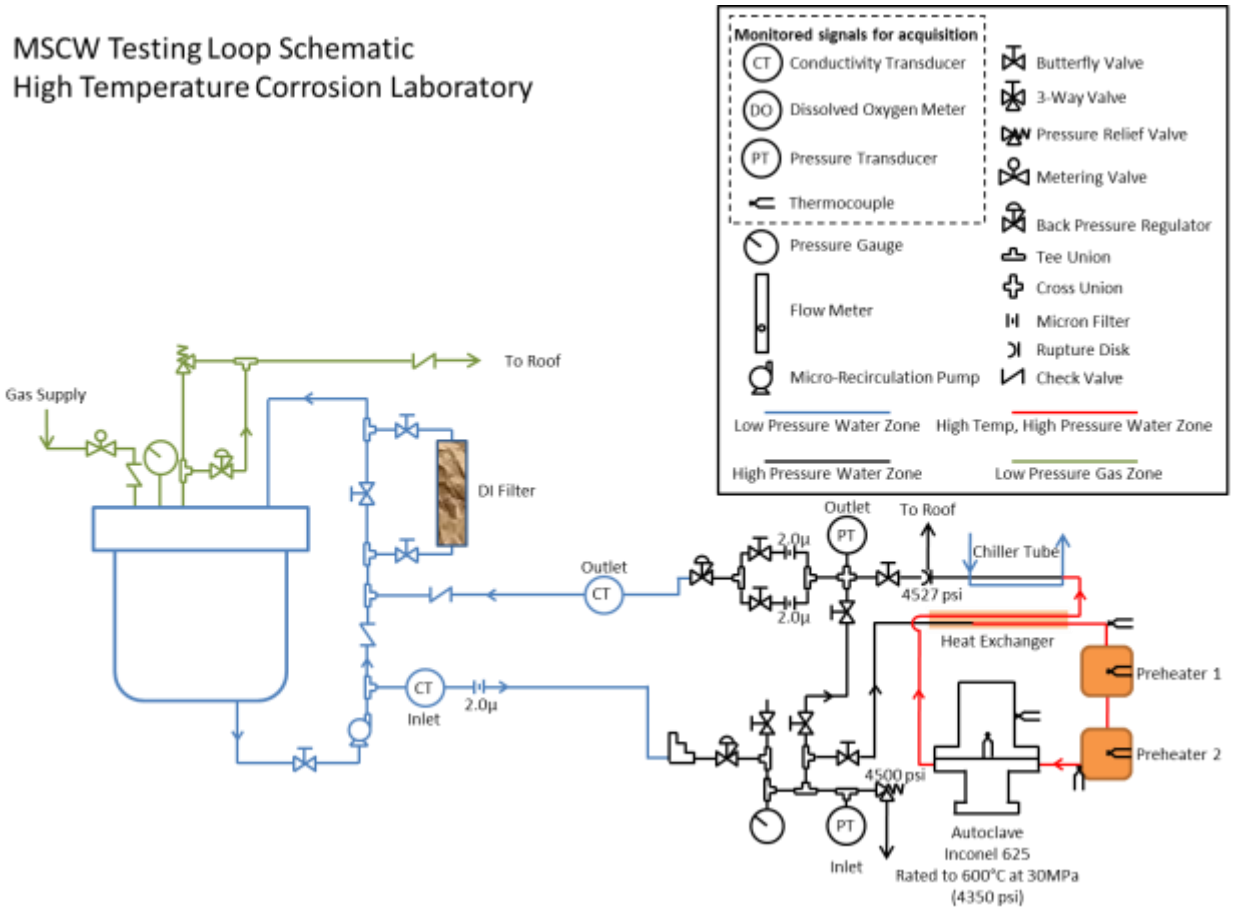

Figure 3.5. Schematic of the MSCW with the high pressure water reservoir attached.

Figure 3.6. Feed water (Frank da) tank.

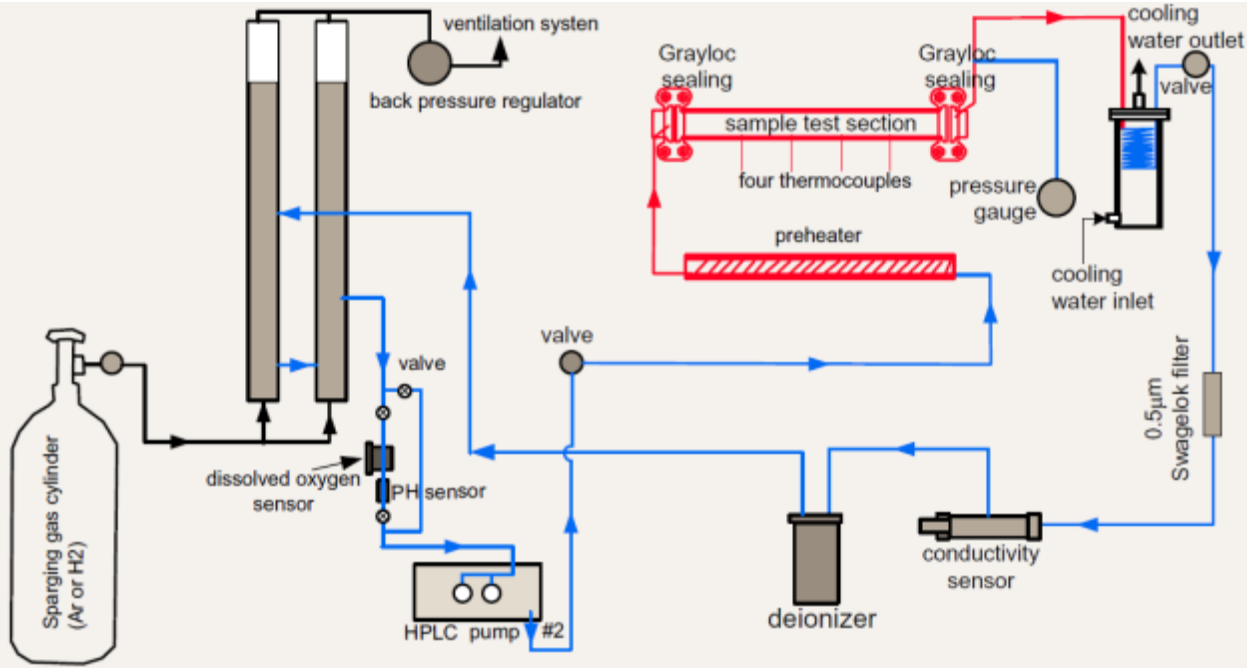

Figure 3.7. Schematic of high temperature, high pressure water loop used for exposure of corrosion coupons at the University of Wisconsin.

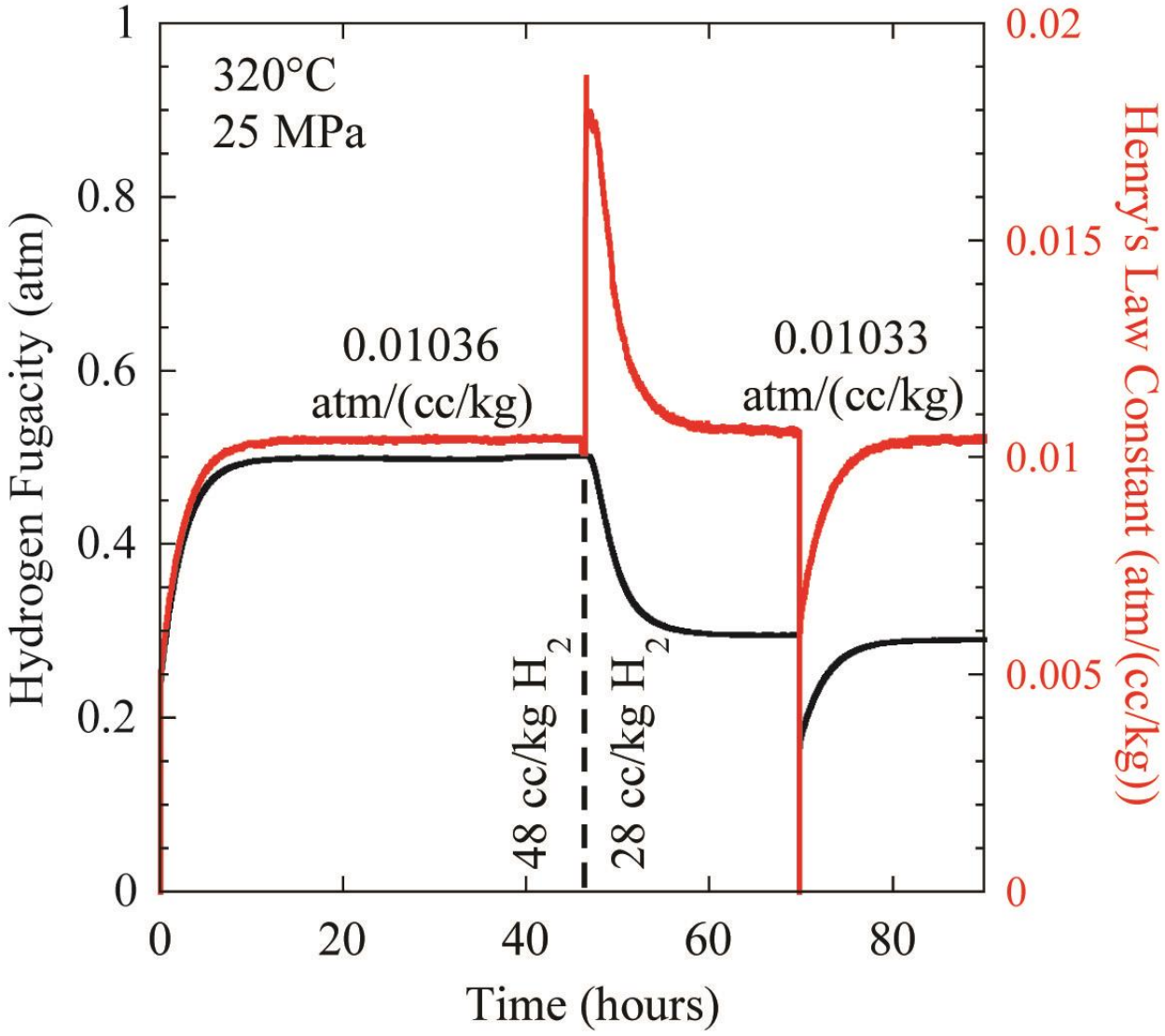

Figure 3.8. Example of hydrogen fugacity and Henry's law constant measurement procedure for dissolved hydrogen concentrations of 48 and 28 cc/kg.

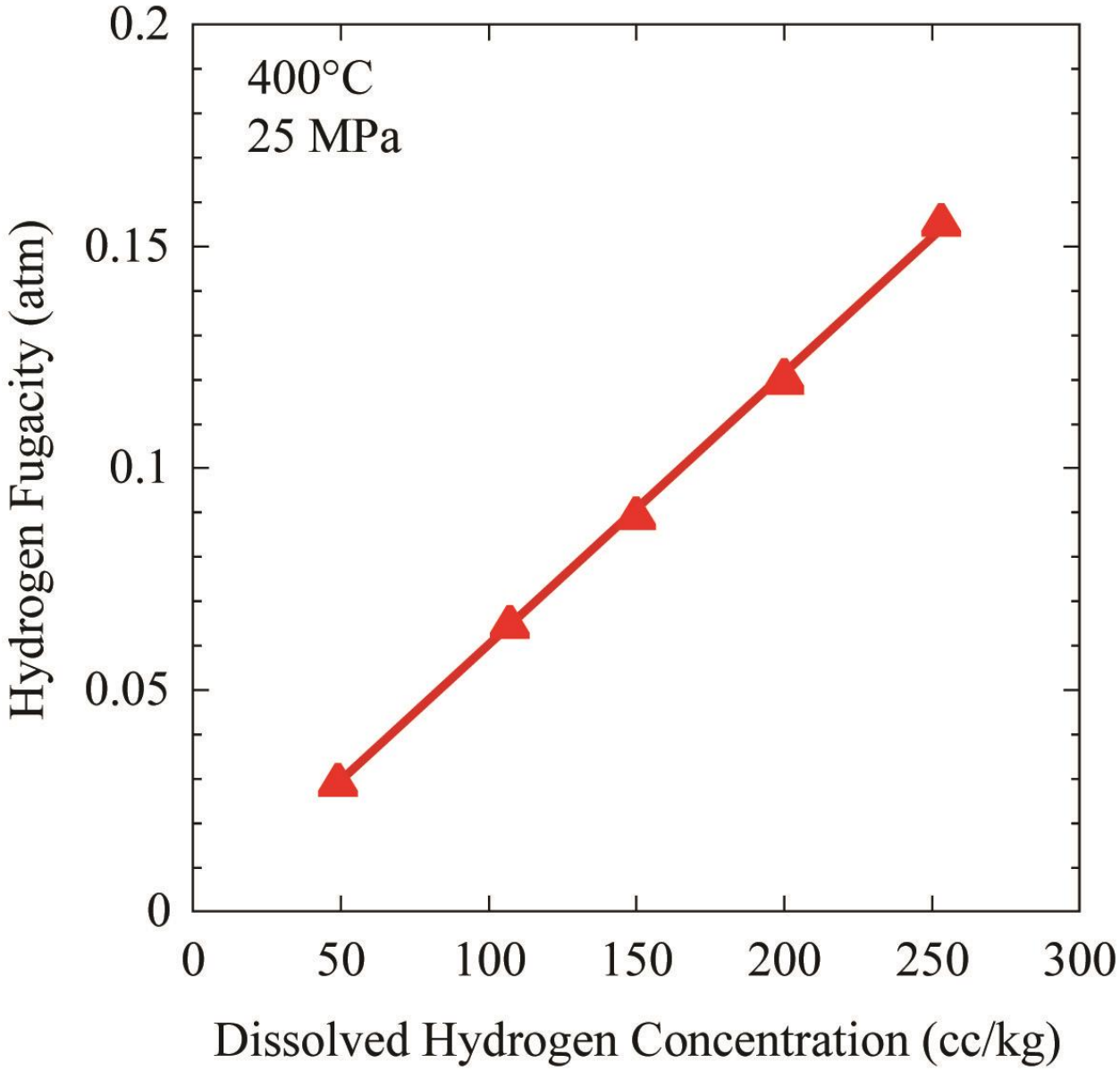

Figure 3.9. Demonstration of linearity of hydrogen fugacity vs dissolved hydrogen concentration at 400°C and 25MPa, validating use of Henry's law.

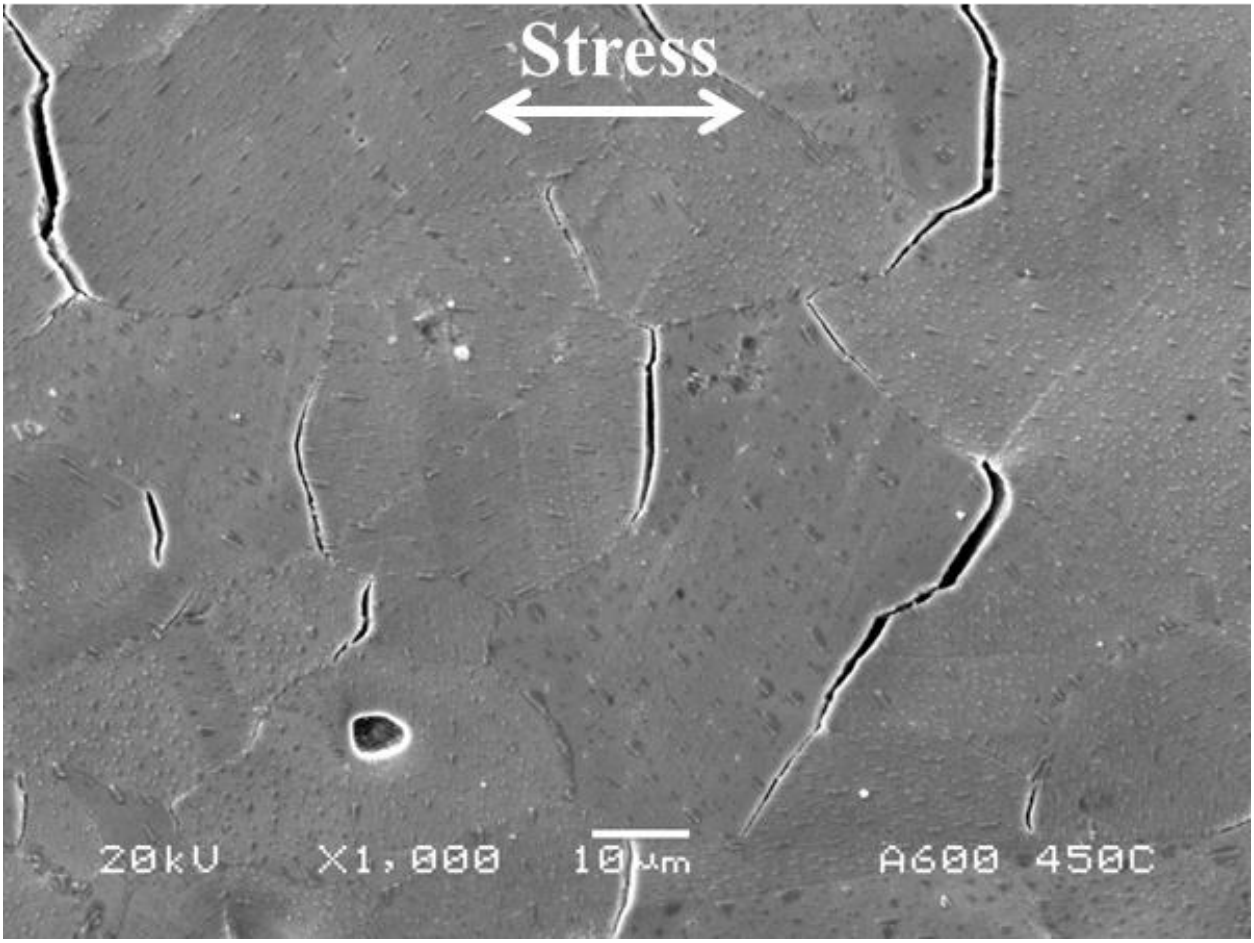

Figure 3.10. Gauge surface of Alloy 600 strained at 450°C in CERT to 8% at $3x10^{-7}$ s^{-1} showing cracking saturation.

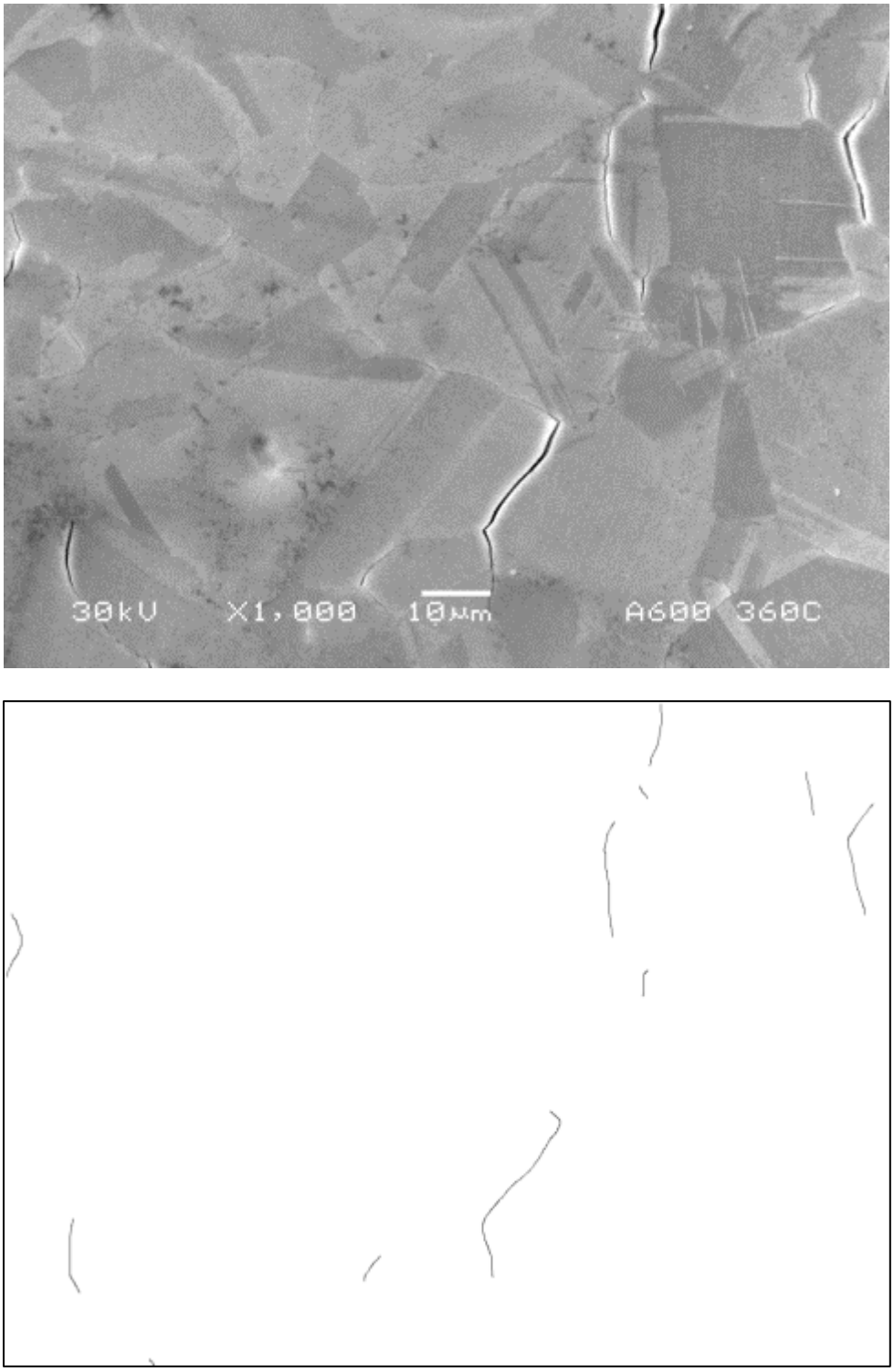

Figure 3.11. Example of crack counting on Alloy 600 strained at 360°C $3x10^{-7}$ s^{-1} with 18 cc/kg dissolved hydrogen

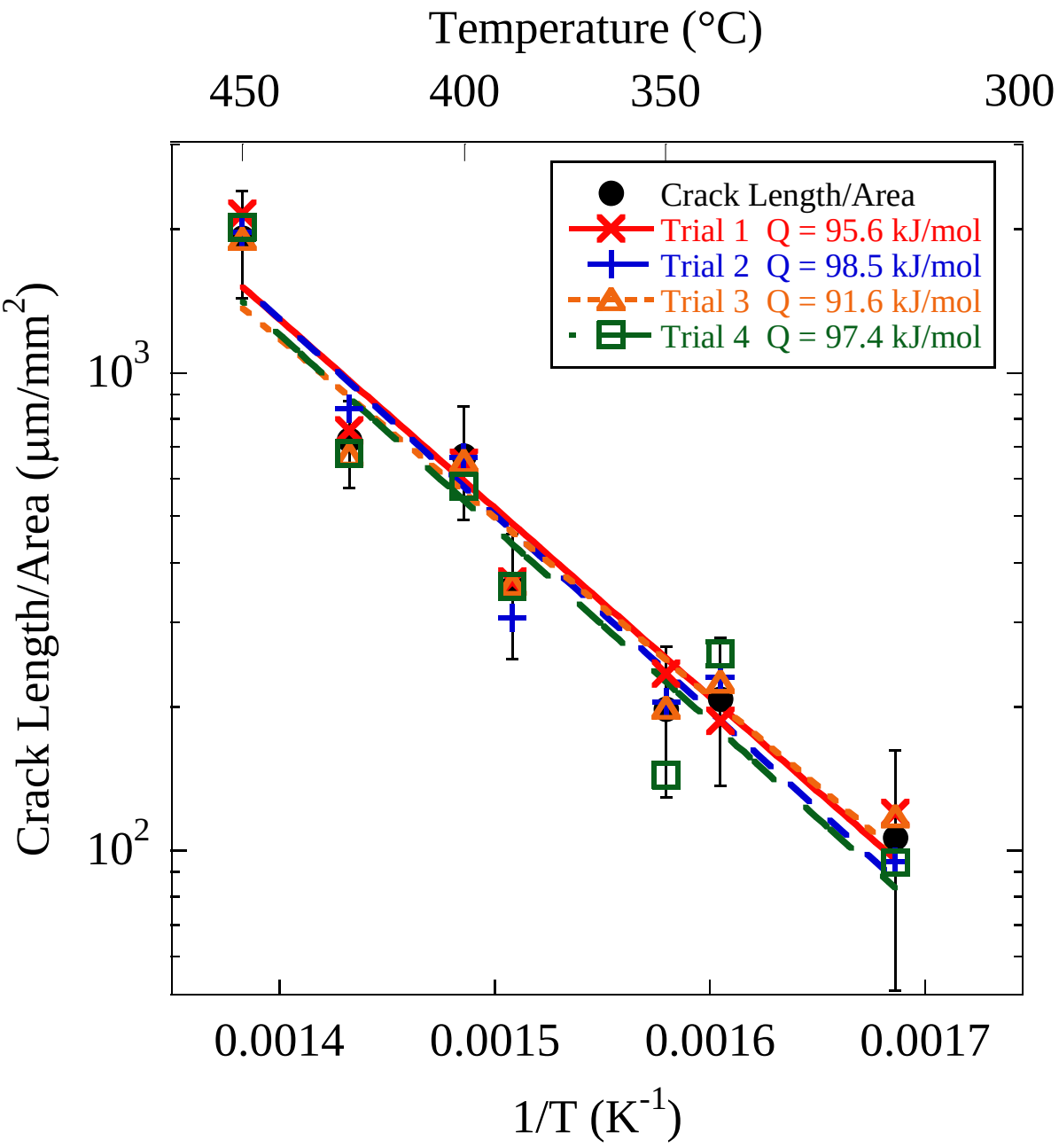

Figure 3.12. Example of trial fits to simulate the error of the activation energy for crack initiation of Alloy 690.

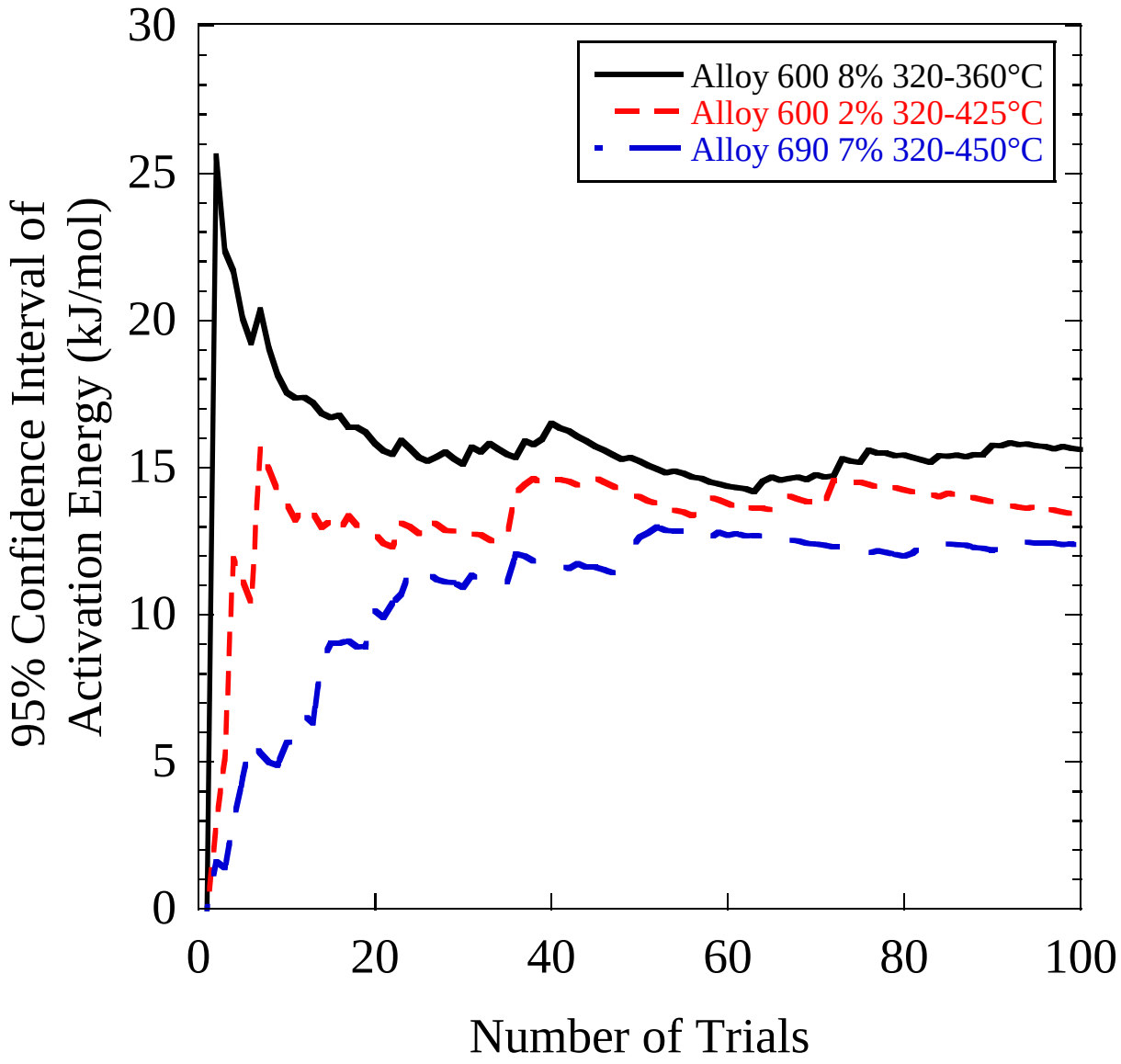

Figure 3.13. 95% confidence interval as a function of number of trial fits to the crack length per unit area temperature dependence.

CHAPTER 4 - RESULTS

In this chapter, results from the experiments described in Chapter 3 will be presented. The significant results include the determination of the stability of nickel in high temperature water, characterization of the oxidation on Alloys 600 and 690, characterization of crack initiation on Alloy 690, and measurements of the crack initiation susceptibility of Alloy 600 and Alloy 690.

4.1 Fugacity measurement and pure Ni exposures

Figure 4.1 and Table 4.1 show the coupon exposures conducted in subcritical and supercritical water to determine the oxide stability of nickel with varying dissolved hydrogen levels. Filled black squares correspond with conditions where NiO was stable and open black squares are where Ni was stable. The data from subcritical water fits very well to exposure data from Attanasio and Morton shown by the solid red curve [70].

Before exposure, coupons had a reflective, film free surface finish. After exposure in conditions where NiO was stable, the coupons appeared visibly tarnished. In conditions where Ni was stable there was no observed surface film and coupons were still reflective. Optical observations of the oxide stability were confirmed with nuclear reaction analysis (NRA) as shown in Figure 4.2 and Figure 4.3. An example of the NRA spectra is shown in Figure 4.2 for samples exposed at 360°C with 18 and 26 cc/kg dissolved hydrogen. Figure 4.3 shows the ratio of counts from the

$^{16}O(d,p_1)^{17}O$ peak to the integrated charge collected on each sample as a function of the dissolved hydrogen concentration and exposure temperature. Exposure conditions below 10 counts/μC were considered to be Ni stable and above that were NiO stable.

To confirm that there was not a change in the oxide structure, grazing incidence X-ray diffraction was performed on flags exposed at 360°C with 18 cc/kg H_2 for 150h and 400°C with 107 cc/kg H_2 for 120h as shown in Figure 4.4. The peaks in both samples correspond with NiO and Ni, no other phases were observed. The intensity of oxide peaks are larger for the supercritical water condition and the metal peak is smaller, indicating a thicker oxide layer.

Measurements of the fugacity of hydrogen are shown in Table 4.2. The interpretation of these results is discussed in Section 5.1. In general, the measurements of the fugacity of hydrogen were very repeatable, as demonstrated in Section 3.5. One parameter that did vary with temperature was the time required for the fugacity to reach equilibrium by diffusion through the palladium-silver. The time to equilibrate decreased as temperature increased and appeared to follow an Arrhenius relationship with an activation energy of approximately 80 kJ/mol as shown in Figure 4.5.

4.2 Oxidation of Alloy 600 and Alloy 690

4.2.1 Oxide Morphology

Analysis of the surfaces of exposure coupons for both alloys shows an uneven surface oxide dependent on grain orientation. SEM images of Alloy 600 show two different oxide particle

morphologies and sizes, Figure 4.6a-f. A high density of bright oxide particles, with sizes around 100nm, cover the surface and the density appears to be highly grain orientation dependent. Large dark contrast faceted oxide particles are also observed at a lower density, labeled as spinels in Figure 4.6e. Surface Cr carbides are surrounded by a lower density of large particles and are coated in an oxide with needle-like morphology, shown in Figure 4.6c-d. The surface oxide morphology does not change appreciably with temperature as all of the same phases are observed but at lower densities at lower temperatures. Across the entire temperature range the grain boundary region exhibits a higher density of particles.

The surface of Alloy 690 has very similar oxide morphology to that of alloy 600, but with a lower density of oxide particles and a different morphology of oxides decorating grain boundaries as shown in Figure 4.6g-l. Light contrast oxide particles with a size around 100nm are observed with the particle number density dependent upon the metal grain orientation. Large dark contrast faceted particles are also observed, which are oriented per grain, labeled as spinels in Figure 4.6i. Grain boundaries are decorated with darker contrast blocky particles with sizes ranging from 10-50 nm. Needle-like oxides are also observed above grain boundaries, with a similar morphology and contrast to those found on surface Cr carbides. The number density of particles decreases with temperature, but all of the same particles are observed in the same morphologies across the entire temperature range. A grain boundary in a sample of Alloy 690 exposed to 360°C water for 2000h was imaged in SEM at 15 keV using secondary electrons and backscattered electrons shown in Figure 4.7. Backscatter imaging revealed subsurface features not observed in the secondary electron image. The backscatter electron micrograph in Figure

4.7b reveals that along the grain boundary the contrast is lighter, and needle-like dark contrast sub-surface oxides are observed in the matrix.

The morphology of oxides along grain boundaries was observed in cross section by FIB-SEM of Alloys 600 and 690 as shown in Figure 4.8. The surfaces were coated first with a layer of platinum deposited by the electron beam, which has dark contrast, then a layer deposited with the ion beam which has light contrast. The oxide surface is typically delineated by the presence of oxide particles with a dark layer of platinum above. Cross sections of Alloy 600 reveal a dark contrast continuous oxide layer under the oxide particles with a grain orientation-dependent thickness as shown in Figure 4.8c. Grain boundaries show preferential oxidation with darker contrast observed at the oxide termination. The depth of oxidation is greater at lower temperatures, which is opposite the trend observed for surface particle density. Cross sections of Alloy 690 reveal a sub-surface layer of internal oxidation with a mixture of needle-like and particulate morphology, depending on grain orientation. Near the surface, grain boundaries appear to be tortuous and have lighter contrast suggesting grain boundary migration. The grain boundary migration as well as the width of the thinned internal oxide layer above grain boundaries increases at higher temperatures. Grain boundary migration was also more prominent at the surface, and was not observed in unexposed coupons. Figure 4.9 shows micrographs of Alloy 690 taken prior to exposure. Figure 4.9a is taken of the surface with backscattered electrons, highlighting grains by different channeling contrast. The grain boundaries along twins appear very sharp, with no change in contrast near the grain boundary. The high angle grain boundaries follow carbides and show slightly lighter contrast, corresponding to the observed chromium depletion prior to exposure. However, there is no oscillation or bowing of the grain

boundaries observed. The same is true when the grain is observed in cross section, as shown in Figure 4.9b. None of the five grain boundaries observed on the unexposed coupon showed evidence of migration, whereas every grain boundary that intersected the surface in the samples exposed to the water environment did undergo grain boundary migration.

An example of the grain boundary migration in Alloy 690 exposed at 400°C for 250 hours is shown in Figure 4.10. The cross section shows the typical thinning of the internal oxide at the grain boundary intersection with the surface. The grain boundary appears very jagged, or tortuous in appearance up to the depth at which it intersects a Cr carbide. The grain boundary appears to oscillate from left to right with lighter contrast between the migrated boundary and a straight line indicating the original position of the grain boundary. The sample was sputtered with argon to reveal the grain boundary, which indeed oscillates between the carbide and surface. The change in contrast observed in SEM suggests either a chemical or microstructural change during the migration. A lighter contrast would suggest a chemical change, enrichment of nickel or depletion of chromium or iron. A lighter contrast could also indicate a change in the crystal orientation or defect density. The argon sputtering result observed in Figure 4.10 suggests that there is not a change in orientation between the adjacent grain and the migrated region. Strain contrast was not observed in the rest of the sample and the even contrast in the migrated region suggests that the change in contrast is not due to a change in the defect density. The composition of the grain boundary was measured at 200 nm below the surface with scanning Auger microscopy shown in Figure 4.11 with the lighter contrast area found to be depleted in chromium to 20 atomic% while nickel enriched to 70 atomic% with no change in the iron content.

Examples of typical surface and internal oxide morphology observed on Alloy 690 are shown in Figure 4.12. There is a thin (~10nm) layer on the surface which appears to be a continuous oxide layer. Deeper into the sample the oxidation morphology consists of filaments of width <5nm. The orientation of filaments varies by grain, suggesting that they may lie along slip planes. Below the filaments, individual oxide particles appear to be unconnected to the surface.

4.2.2 Oxide Structure

A bulk measurement of the oxide structure was collected by X-rayX-ray diffraction (XRD). Figure 4.13 shows the 2-theta plots for Alloy 600 and Alloy 690 exposed at 360°C for 2000 hours, 390°C for 400 hours, and 400°C for 250 hours. Results are plotted for Alloy 600 in Figure 4.13a and show that the dominant phase is NiO with no peaks observed corresponding to Cr_2O_3 or $NiFe_2O_4$. An unidentified peak at 39.1° is observed at all three temperatures, which may correspond with a spinel structure. Figure 4.13b plots the results for Alloy 690 showing several oxide phases including NiO, Cr_2O_3, $NiFe_2O_4$, and a peak corresponding to $M_{23}C_6$ carbides. Peaks for oxide phases other than NiO are weak and fairly broad, suggesting low abundance and small grain size. The intensity of the spinel peak increases at higher temperatures, which corresponds with the abundance of the dark contrast faceted particles observed on the surface in Figure 4.6g-l. The XRD analysis provides a good measure of the dominant phases present. However, due to the low brightness of the X-ray source, the signal is weak for oxides with low volume fraction. To better correlate the observed microstructure with crystal structure of oxides, electron diffraction in TEM was used.

TEM analysis focused on samples of Alloy 690 exposed at 360°C for 2000h and 400°C for 250 hours. The structure of the 100nm bright contrast oxides was confirmed as NiO from selected area diffraction from the surface of Alloy 690 exposed at 400°C as shown in Figure 4.14. The diffraction pattern was taken from a [011] zone axis on the oxide particle and rings from the platinum deposition were observed. The structure of the internal oxide was also investigated on the sample exposed to 400°C supercritical water by selected area diffraction as shown in Figure 4.15. A dark field STEM micrograph is shown in Figure 4.15a with dashed circles indicating the location of selected area diffraction. The fine dashed circle includes the metal and encompasses the edge of the internal oxide with the diffraction shown in Figure 4.15b. The Alloy 690 metal pattern had a [011] zone axis and spots corresponding to Cr_2O_3 were observed. The coarse dashed circle encompasses both the continuous oxide and the internal oxide with the diffraction pattern shown in Figure 4.15c. When comparing the two patterns, additional Cr_2O_3 spots corresponding to the {104} family of planes are observed but the major difference is the strong spots corresponding to NiO structured oxide but does not have a NiO composition, because of this it is referred to as MO. The MO diffraction spots shown in green partially overlap with those of the metal matrix, shown in red.

Selected area diffraction and nano-diffraction were performed on a lift-out from a grain boundary of Alloy 690 exposed to 360°C water for 2000h. Figure 4.17 shows a STEM dark field image with a selected area diffraction pattern taken from the region denoted by the circle in Figure 4.16a, which encompasses the internal oxide and the surface oxide. The pattern shows spots corresponding with Cr_2O_3, the metal matrix from the {110} family of planes, and MO structured oxide oriented to the metal matrix observed again from double spots overlapping with

the metal matrix. Nano-diffraction was taken of oxide formed at the surface above the grain boundary shown in Figure 4.17. The only clear pattern found is shown in the inset of Figure 4.17 and is indexed as Cr_2O_3. To image Cr_2O_3 in the internal oxide, the sample was tilted away from the zone axis and a spot from chromia corresponding to the {110} family of planes was selected to image in weak beam condition in the diffraction pattern taken from the surface shown in Figure 4.18. The dark field image in Figure 4.18b shows illuminated platelets of Cr_2O_3 in the internal oxide.

4.2.3 Oxide Composition

The composition of surface oxides measured by scanning Auger microscopy is listed in Table 4.3. All compositions were taken after 2 min of sputtering with 2 keV argon at a current of 1 μA. The compositions of three oxide structures were characterized; NiO, surface oxide, and spinel. Examples of spectra taken from each feature are shown in Figure 4.19. NiO compositions were taken from light contrast, 100nm surface particles that were found, from TEM results, to correspond to a MO structured oxide. The composition matches with NiO, but is slightly oxygen deficient. Surface oxide measurements were taken from the flat surface oxide layer where no oxide particles were observed, which would correspond with the continuous oxide layer found on the surface when observing in cross section. The composition of surface oxide observed on alloy 600 is almost that of NiO, but with Cr and Fe occupying 1/3 of the metal content. Spectra from the large, dark contrast spinel particles showed no presence of chromium but were also slightly nickel-rich to match the composition of $NiFe_2O_4$. For both alloys across all temperatures, the oxide particles on the surface show good agreement in composition. The surface oxide for Alloy

600 has lower chromium content than that measured for Alloy 690, but the oxides show consistent composition across the subcritical-supercritical water transition for each alloy.

Depth profiling in SAM was performed on Alloy 690 to determine the composition of oxides found over grain boundaries and the composition of the internal oxide layer. Figure 4.20 shows the composition as a function of sputter time for grain boundary oxides on Alloy 690 exposed in subcritical and supercritical water. The depth profiles show no significant difference in composition between the oxides observed in subcritical and supercritical water. For both profiles the surface composition of the oxide is nickel rich (Ni-Cr-Fe MO zone) and transitions to chromium rich (Cr_2O_3 zone) just 2 minutes of sputtering. The chromium content peaks at the oxide/metal interface with concentration greater than the base metal and corresponding well to the composition Cr_2O_3. The concentration of oxygen at the metal/oxide interface decreases gradually over 4-18nm, suggesting either dissolved oxygen in the matrix or oxide particles that are finer than the SAM can resolve. Figure 4.21 shows the concentration as a function of sputter time taken from the middle of a grain in an area free of surface oxide particles on Alloy 690. The concentration profiles are similar to those observed on oxides above grain boundaries. The major difference between the two is the required sputter time to reach the base metal after the surface oxide is removed, where the measurements away from the grain boundary took about two times as long to reach the metal composition. This agrees well with the observation of thinning of the internal oxide layer above grain boundaries.

4.2.4 Oxidation Rate

Measurements of the average weight gain for all exposed coupons as a function of time are plotted in Figure 4.22. Alloy 600 shows parabolic oxide growth with the weight gain increasing at higher temperatures. Alloy 690 shows non parabolic oxide growth with an initially higher weight gain that appears to level out after 500 hr of exposure. The depth of internal oxidation was measured at 360°C at 250, 500, 1000, and 2000 hr by cross section FIB-SEM as plotted in Figure 4.23. After 500 hr of exposure the internal oxide depth appears to cease growing into the material, however some coarsening of the oxide is observed. Representative SEM micrographs of the internal oxide morphology are shown in Figure 4.24. At 250 hours the oxide appears to be entirely composed of fine and uniform oxide platelets or spheres with little interconnectivity. At 500 hr the oxide has a finger-like morphology and is oriented, possibly following slip planes in the grain. After 1000 hr a continuous surface oxide is observed, which coarsens at 2000 hr.

4.3 Stress corrosion crack initiation morphology of Alloy 690

Engineering stress-strain curves for pre-strained Alloy 690 strained to 7% at $5x10^{-8}$ s^{-1} are shown in Figure 4.25 for CERT tests conducted at 320°C, 360°C, and 400°C. The average yield strength for 20% pre-strained Alloy 690 was 710 MPa. Samples strained over the entire temperature range exhibited dynamic strain aging with type B character. The magnitude of serrations averaged 23 MPa and did not measurably change with strain. The yield stress and work hardening rate did not noticeably vary as a function of temperature over the range tested. Intergranular SCC initiation was observed on samples of Alloy 690 strained in CERT over the entire temperature range. SEM micrographs of select cracks on the gage surface of Alloy 690 from samples strained at 320°C and 400°C are shown in Figure 4.26. Surface oxidation increased

with temperature and faceted oxide particles were observed more often as the temperature increased.

Focused ion beam milling in conjunction with high resolution SEM allowed examination of intact and cracked grain boundaries. Cross sections of un-cracked grain boundaries showing grain boundary oxidation from samples strained at 360°C and 400°C are shown in Figure 4.27. Internal oxidation to a depth of ~100 nm were observed in the matrix, which thinned where the grain boundary meets the surface. Small protrusions of dark contrast oxide were observed along the grain boundary at the surface. The morphology of cracking in cross section on Alloy 690 in subcritical and supercritical water is shown in Figure 4.28 and Figure 4.29, respectively. Oxidation on the crack walls were similar to that on the surface with NiO particles filling the crack, and chromium rich, internal oxidation extending into the crack walls as shown in Figure 4.28 for a sample strained in 360°C hydrogenated water. The internal oxidation from the surface appeared to be thinner at the crack mouth than in the matrix, similar to that on the intact grain boundaries (Figure 4.27). Dark contrast oxide was observed along a migrated portion of the grain boundary above the crack tip. Similar crack morphology was observed in supercritical water as shown in the crack in Figure 4.29 for a crack in a sample strained in 400°C water. Light contrast NiO particles were observed on the crack walls with chromium rich internal oxidation extending into the metal. Like the subcritical water case, the crack mouth also had thinner internal oxidation than away from the crack. This crack appeared to have arrested at a string of chromium carbides. Scanning Auger maps in Figure 4.29b,c confirmed the composition of oxides and revealed oxygen present beyond the crack tip along carbides.

4.3.1 Morphology of cracks in 360°C, subcritical water

Detailed analysis of cracks in Alloy 690 was conducted using high resolution SEM and STEM on FIB lift-outs prepared from samples strained in 360°C subcritical water. Before thinning to electron transparency, a crack in the 360°C sample was imaged with the through-lens detector in SEM as shown in Figure 4.30a. After thinning to electron transparency the crack was observed in TEM and STEM to determine the crystal structure and chemistry of oxides as shown in Figure 4.30b. The two images in Figure 4.30 are at the same scale with the difference in the surface level due to the thinning in FIB. The features between the two are fairly similar, but the STEM was more sensitive to lighter elements. The SEM image exhibits a greater sensitivity to metallic constituents with nickel having the lightest contrast and chromium and iron having darker contrast. The combination of STEM and SEM allows for a more complete understanding of the crack structure. For example, above the crack tip in STEM there is a 20-30nm dark contrast region indicating an oxide. In SEM, half of that oxide has dark contrast and the other half has light contrast, suggesting the left wall of the crack is chromium rich and the right wall is nickel rich. This observation is confirmed by STEM-EDS (Figure 4.31) performed in the same region as that of the crack in Figure 4.30. One line scan was conducted above the crack tip, Figure 4.31b, and one across the grain boundary beyond the crack, Figure 4.31c. The scan above the crack tip supports the observations in SEM of a chromium rich oxide on the left wall and a nickel rich oxide on the right wall. In the grain boundary below the crack, chromium depletion was observed but there was no indication of oxygen.

To determine the structure of oxides in the crack from the 360°C sample, selected area electron diffraction and dark field imaging were performed. Figure 4.32a shows the crack from Figure

4.30 imaged in STEM dark field mode alongside a dark field TEM image in Figure 4.32b taken by selecting a diffraction spot corresponding with Cr_2O_3. The diffraction pattern was taken from a region just above the tip of the crack and has spots corresponding to Cr_2O_3 and NiO. Light contrast Cr_2O_3 particles were observed throughout the crack in Figure 4.32b, corresponding to the darker contrast oxides in the STEM image. One of the key features was the observation of a Cr_2O_3 particle beyond the crack tip. Cr_2O_3 was also observed in the internal oxidation zone adjacent to the crack walls of the crack in Figure 4.30, as shown in Figure 4.33. Figure 4.33a was taken in conventional TEM bright field mode with the crack walls indicated by dashed lines and the internal oxide shown by darker contrast off the crack walls. The dark field image in Figure 4.33b was taken by selecting a Cr_2O_3 spot and shows discrete platelets of Cr_2O_3 in the internal oxide.

4.3.2 Morphology of cracks in 400°C SCW

After thinning to electron transparency, a crack in the 400°C sample was imaged with the backscatter detector in SEM and in STEM dark field mode as shown in Figure 4.34. Both imaging methods show similar features to other cracks imaged in cross section: thinner internal oxidation at the crack mouth, NiO on the crack walls, chromium-rich internal oxide adjacent to the crack walls, and oxidation beyond the crack tip. The presence of NiO on the crack walls in Figure 4.34 is confirmed by selected area diffraction of the oxide filling the crack as shown in Figure 4.35. The diffraction pattern is taken from the area indicated in the dark field image and shows spots consistent with NiO. High resolution micrographs of the crack tip region from Figure 4.34 are shown in Figure 4.36 imaged in SEM with the through-lens detector for secondary electrons, the concentric backscatter detector for backscattered electrons, and in

STEM dark field. All three images are of the same location of the crack in Figure 4.34 and at the same magnification. The crack tip is discerned in the STEM and backscattered electron images by the termination of dark contrast, but at same location in the secondary electron image is where NiO ends with dark contrast oxide beneath. Beyond the crack tip, a particle is observed with the same contrast as the dark oxide which appears to be connected to the crack tip in the secondary electron image, but isolated in the backscatter and STEM images.

4.3.3 Crack arrest by chromium carbides

The effect of grain boundary chromium carbides in Alloy 690 on surface crack length and crack depth was investigated by SEM of the gage surface and by serial sectioning in FIB-SEM. Carbides formed a thick oxide faster than the metal surface, allowing for easy identification, particularly at low temperatures. Cracks were observed to arrest at surface carbides as shown in Figure 4.37 for Alloy 690 strained in 320°C water. The majority of cracks were observed on sections of grain boundaries free of carbides. Figure 4.37b shows an example of a crack that appeared to have propagated on either side of a carbide, but was arrested in the middle. Grain boundaries oriented parallel to the tensile direction showed voids between carbides that initiate short transgranular cracks as shown in Figure 4.37c. Serial sectioning was performed on a crack in Alloy 690 strained in 360°C water and is shown in Figure 4.38. The top micrograph shows the gage surface with yellow dashed lines to indicate the locations of sections spaced 200nm apart. Figure 4.38a-c show the crack with an average depth of 0.97 μm, including the oxidation beyond the crack tip. In Figure 4.38c the crack was bisected by a chromium carbide that appeared to have suffered no damage itself, but the crack likely propagated around the carbide out of plane

and still had the full depth. Figure 4.38d shows the crack arrested at a depth of just 0.15 μm with the grain boundary decorated by carbides.

4.4 Crack initiation susceptibility of Alloy 600 and Alloy 690

Representative engineering stress-strain curves for Alloy 600 strained to 8% at $3x10^{-7}$ s^{-1} and $5x10^{-8}$ s^{-1} and Alloy 690 strained to 7% at $5x10^{-8}$ s^{-1} with and without pre-strain are shown in Figure 4.39. Samples strained over the entire temperature range and for both strain rates exhibited dynamic strain aging with type B character. The magnitude of serrations observed for Alloy 600 averaged 113 MPa and increased with strain. That for Alloy 690 averaged 23 MPa and did not change with strain. The yield stress and work hardening rate did not noticeably vary as a function of temperature over the range tested. The average yield strength for Alloy 600 was 210 MPa. Alloy 690 without pre-strain had an average yield strength of 250 MPa, whereas the average for 20% pre-strained Alloy 690 was 710 MPa.

Results of cracking analysis from CERT tests for both alloys are presented in Table 4.4. Alloy 600 tested in all conditions exhibited significant amounts of intergranular crack initiation with no evidence of transgranular cracking. Micrographs of the gauge surfaces of Alloy 600 strained to 2% at 320°C and 425°C are shown in Figure 4.40 with the tensile axis oriented left to right. For all samples, the majority of cracking was observed on grain boundaries perpendicular to the tensile axis. The cracking severity was highly temperature dependent and increased with temperature. The amount of surface oxidation also increased with temperature as evidenced by the coarsening of the surface oxide particles. The cracking severity as a function of inverse

temperature of Alloy 600 is plotted for samples strained to 2% in Figure 4.41. The cracking follows an Arrhenius relationship for sample strained to 2% over the entire temperature range.

Intergranular SCC initiation was observed on samples of Alloy 690 strained in CERT over the entire temperature range. Micrographs of the gauge surfaces Alloy 690 at 320°C and 450°C strained 7% after a 20% pre-strain are shown in Figure 4.42. The images are shown at the same magnification as the micrographs for Alloy 600 in Figure 4.40, but far less cracking is visible. Similar to Alloy 600, the surface oxidation increases with temperature and faceted oxide particles delineating grain orientation were observed at higher temperatures. The crack initiation susceptibility of Alloy 690 in terms of crack length per unit area, crack density, and crack length is plotted in Figure 4.43 for 20% pre-strained samples.

Samples of Alloy 600, Alloy 690, and pre-strained Alloy 690 were strained in 450°C argon to determine whether creep was a major contributor for the cracking observed at higher temperatures. All samples were strained at an initial strain rate of $5x10^{-8}$ s^{-1} with Alloy 600 strained to 8% and Alloy 690 strained to 7%. No cracking was observed on any of the samples. The experiment was concluded after 696 hours and even though pre-purified argon was used, light oxidation was observed. Oxidized regions showed evidence of metal nodules on the surface decorating grain boundaries and slip lines as the light contrast particles shown in Figure 4.44a. Grain boundary migration was also observed in backscatter imaging by an increase in the tortuosity of grain boundaries as shown in Figure 4.44b.

Table 4.1. Summary of nickel exposures with hydrogen fugacity calculated from Henry's law.

Temperature (°C)	Dissolved Hydrogen (cc/kg)	Hydrogen Fugacity (atm)	Stable Phase
320	6 ± 0.76	0.063	NiO
	8.5 ± 0.76	0.090	Ni
330	8 ± 0.76	0.075	NiO
350	13 ± 1.5	0.090	NiO
360	10 ± 0.76	0.057	NiO
	13 ± 1.5	0.074	NiO
	18 ± 1.5	0.103	NiO
	26 ± 2.2	0.149	Ni
	47 ± 3.8	0.269	Ni
385	35 ± 3.8	0.087	NiO
	50 ± 3.8	0.124	Ni
	70 ± 3.8	0.173	Ni
390	70 ± 3.8	0.086	NiO
400	47 ± 3.8	0.029	NiO
	75 ± 3.8	0.045	NiO
	107 ± 3.8	0.065	NiO
	137 ± 3.8	0.083	Ni
	200 ± 3.8	0.121	Ni
425	150 ± 3.8	0.063	NiO
	200 ± 3.8	0.085	NiO
	250 ± 3.8	0.106	Ni
450	200 ± 3.8	0.072	NiO
	290 ± 3.8	0.105	NiO
	380 ± 3.8	0.138	Ni

Table 4.2. Summary of hydrogen fugacity and Henry's law constant measurements.

Vessel Temperature (°C)	Vessel Pressure (MPa)	Dissolved Hydrogen Concentration (cc/kg)	Hydrogen Fugacity (atm)	Henry's Law Constant (atm/(cc/kg))	Time to Equilibrate (hours)
320.1	24.83	28	0.289	0.01033	10.3
320.1	25.01	48	0.498	0.01036	12.5
319.9	24.63	66	0.713	0.01083	11.0
320.0	24.51	92	0.984	0.01066	10.0
360.0	24.81	49	0.276	0.00563	5.6
360.0	24.84	49	0.276	0.00563	5.8
360.0	24.65	69	0.403	0.00582	5.6
360.1	24.65	100	0.576	0.00578	5.8
385.1	25.21	47	0.119	0.00256	2.5
385.0	24.79	49	0.116	0.00237	2.1
385.0	24.85	49	0.117	0.00239	2.6
385.1	24.06	68	0.122	0.00179	1.7
385.2	24.12	68	0.127	0.00186	1.6
384.9	25.23	68	0.182	0.00266	2.2
384.9	25.16	68	0.181	0.00264	2.3
385.0	25.12	69	0.183	0.00267	1.5
385.1	25.11	88	0.228	0.00258	1.7
385.1	25.06	116	0.296	0.00256	1.7
390.0	25.00	47	0.059	0.00125	1.4
390.0	25.01	48	0.061	0.00126	1.0
390.0	24.77	49	0.051	0.00105	1.2
390.0	24.17	69	0.057	0.00083	1.8
389.9	24.17	69	0.056	0.00081	2.1
390.1	25.02	133	0.166	0.00125	0.8
390.0	25.00	133	0.167	0.00126	1.3
390.1	25.00	165	0.209	0.00126	2.1
390.1	25.00	193	0.239	0.00124	1.4
399.9	24.80	49	0.030	0.00061	1.4
400.0	24.87	107	0.065	0.00061	1.3
400.0	24.87	150	0.090	0.00060	0.8
400.0	24.89	200	0.121	0.00060	1.0

400.0	24.88	200	0.120	0.00060	1.0
400.0	24.92	253	0.156	0.00062	1.9
424.9	24.95	97	0.041	0.00043	1.0
425.0	24.96	200	0.085	0.00043	1.1
424.9	24.90	250	0.105	0.00042	1.0
425.0	24.91	310	0.129	0.00042	1.0
450.0	24.97	193	0.072	0.00037	0.9
450.0	24.96	256	0.092	0.00036	0.8
450.0	24.92	256	0.092	0.00036	0.7
450.1	24.95	310	0.111	0.00036	0.9
450.0	24.93	311	0.113	0.00036	0.9

Table 4.3. Composition of surface oxides measured by scanning Auger microscopy.

Alloy/Condition	Feature Composition (at%)											
	NiO				Surface Oxide				Spinel			
	O	Cr	Fe	Ni	O	Cr	Fe	Ni	O	Cr	Fe	Ni
Alloy 600 360C 18cc/kg H_2 2000h	39.1	0.0	3.2	57.7	41.4	13.3	6.4	38.9	29.1	0.0	37.0	34.0
Alloy 600 390C 70 cc/kg H_2 400h	41.8	0.0	2.4	55.8	41.4	8.7	8.5	41.4	NM			
Alloy 600 400C 107 cc/kg H_2 250h	41.1	0.0	3.0	55.9	37.1	15.5	4.1	43.4	40.4	0.0	21.6	37.8
Alloy 690 360C 18 cc/kg H_2 2000h	36.3	0.0	4.4	59.3	48.7	29.4	5.6	16.2	NM			
Alloy 690 400C 107 cc/kg H_2 250h	41.3	0.0	4.5	54.2	48.0	32.2	6.4	13.4	30.1	0.0	36.2	33.7

NM = Not Measured

Table 4.4. Results for crack initiation in CERT tests of Alloy 690 and Alloy 600.

Alloy	Temperature (°C)	Dissolved Hydrogen Concentration (cc/kg)	Strain (%)	Strain Rate (1/s)	Total Test Time (Hours)	Crack Length (μm)	Crack Density (#/mm^2)	Crack Length/ Unit Area (μm/mm^2)	Average Crack Depth (μm)	Maximum Crack Depth (μm)	# of Cracks Measured for Depth
690	320	6	20 Air + 7	$5x10^{-8}$	565	3.5	30.8	106.3	NM	NM	NM
	350	13			572	2.6	78.9	207.5	NM	NM	NM
	360	18			474	2.9	67.8	197.7	NM	NM	NM
	390	70			514	3.4	102.9	354.8	2.0	4.4	7
	400	107			651	6.5	103.2	668.5	2.0	6.0	19
	425	200			595	3.3	222.4	722.8	1.8	4.2	16
	450	290			630	7.0	273.0	1912.0	5.1	10.3	9
	390	70	7		514	3.7	33.0	122.2	NM	NM	NM
	425	200			595	3.7	93.9	350.9	NM	NM	NM
	450	290	8		630	6.5	75.1	487.7	NM	NM	NM
	450	290	16		1260	9.6	203.5	1994.8	NM	NM	NM
600	320	6	8	$5x10^{-8}$	565	7.9	1311.3	10413.3	NM	NM	NM
	320	6		$3x10^{-7}$	93	7.4	211.6	1573.9	1.4	3.7	28
	330	8			104	6.7	339.1	2271.3	4.2	16.5	44
	350	13			100	9.5	445.0	4195.1	4.1	14.9	32
	360	18			112	10.2	735.1	7463.4	5.8	19.0	34
	400	107			99	11.7	1290.5	15134.2	7.5	27.7	58
	425	200			113	13.8	1470.5	20341.1	8.6	25.4	119
	450	290			97	13.2	1597.8	21154	10.7	50.8	96
	320	6	2		46	3.8	188.0	722.0	NM	NM	NM
	360	18			46	5.0	431.9	2140.1	NM	NM	NM
	390	70			47	7.1	613.1	4418.4	NM	NM	NM
	400	107			38	8.4	968.4	8116.3	NM	NM	NM
	425	200			49	10.9	1774.1	19294.8	NM	NM	NM

NM = Not Measured

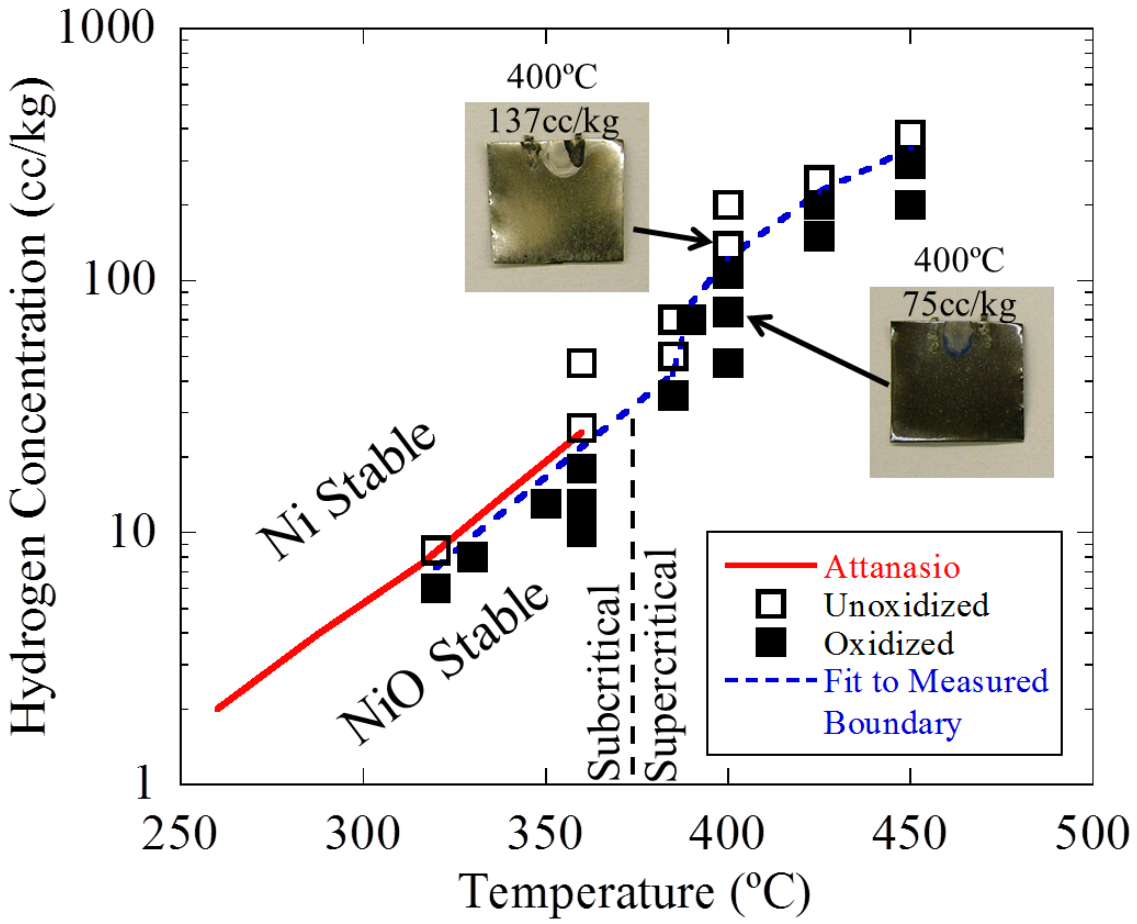

Figure 4.1. Summary of Ni coupon exposures to determine the location of the Ni/NiO boundary in supercritical water as a function of temperature and dissolved hydrogen concentration. Open squares indicate no oxide formation and filled squares indicate conditions where oxide was found. A Fit to the measured boundary was taken as the midpoint between Ni stable and NiO stable conditions. Subcritical data in red was obtained from Attanasio and Morton [70].

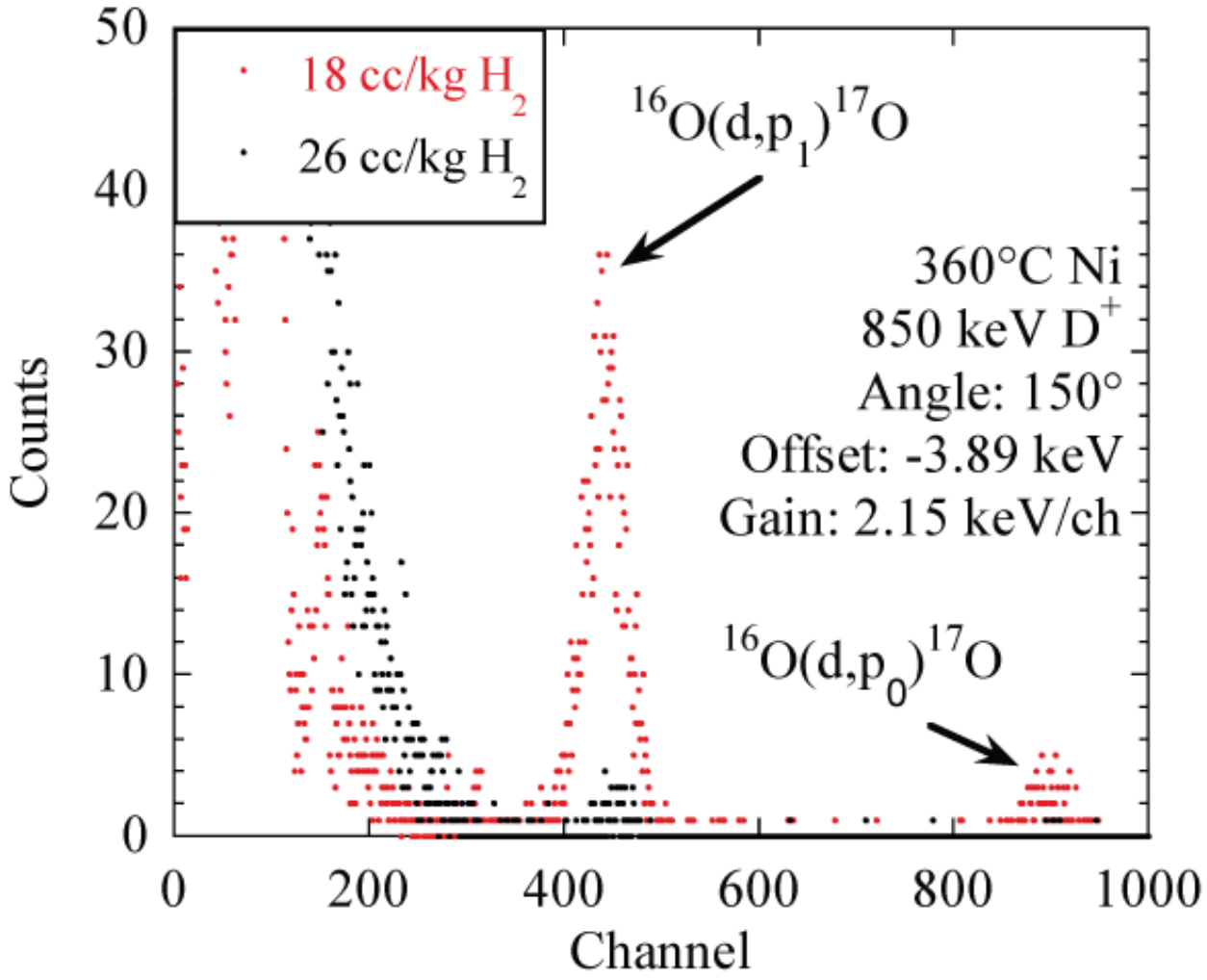

Figure 4.2. Example of nuclear reaction analysis data taken from two samples tested at 360°C with 18 and 26 cc/kg dissolved hydrogen.

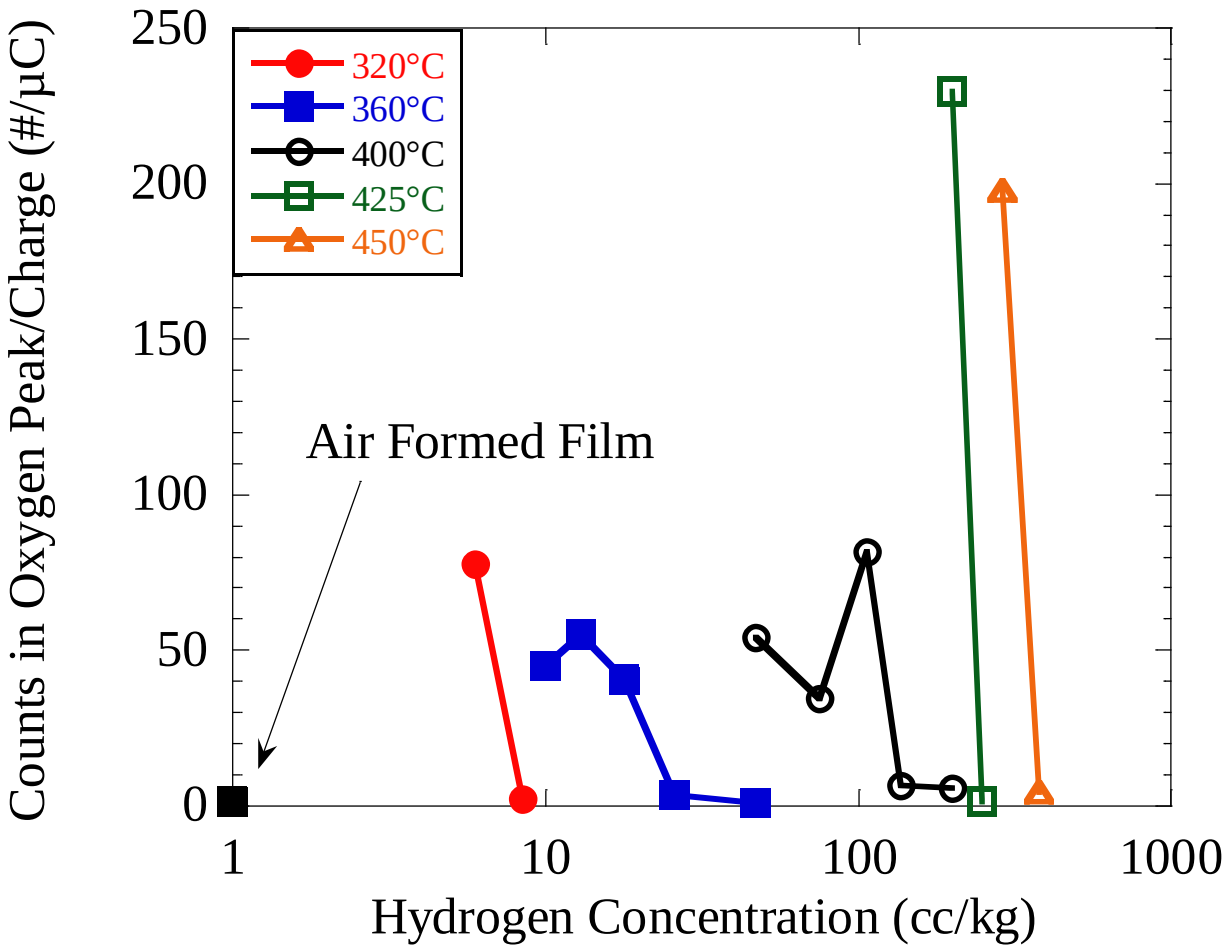

Figure 4.3. Oxygen content on the surface of Ni coupons as a function of temperature and dissolved hydrogen concentration.

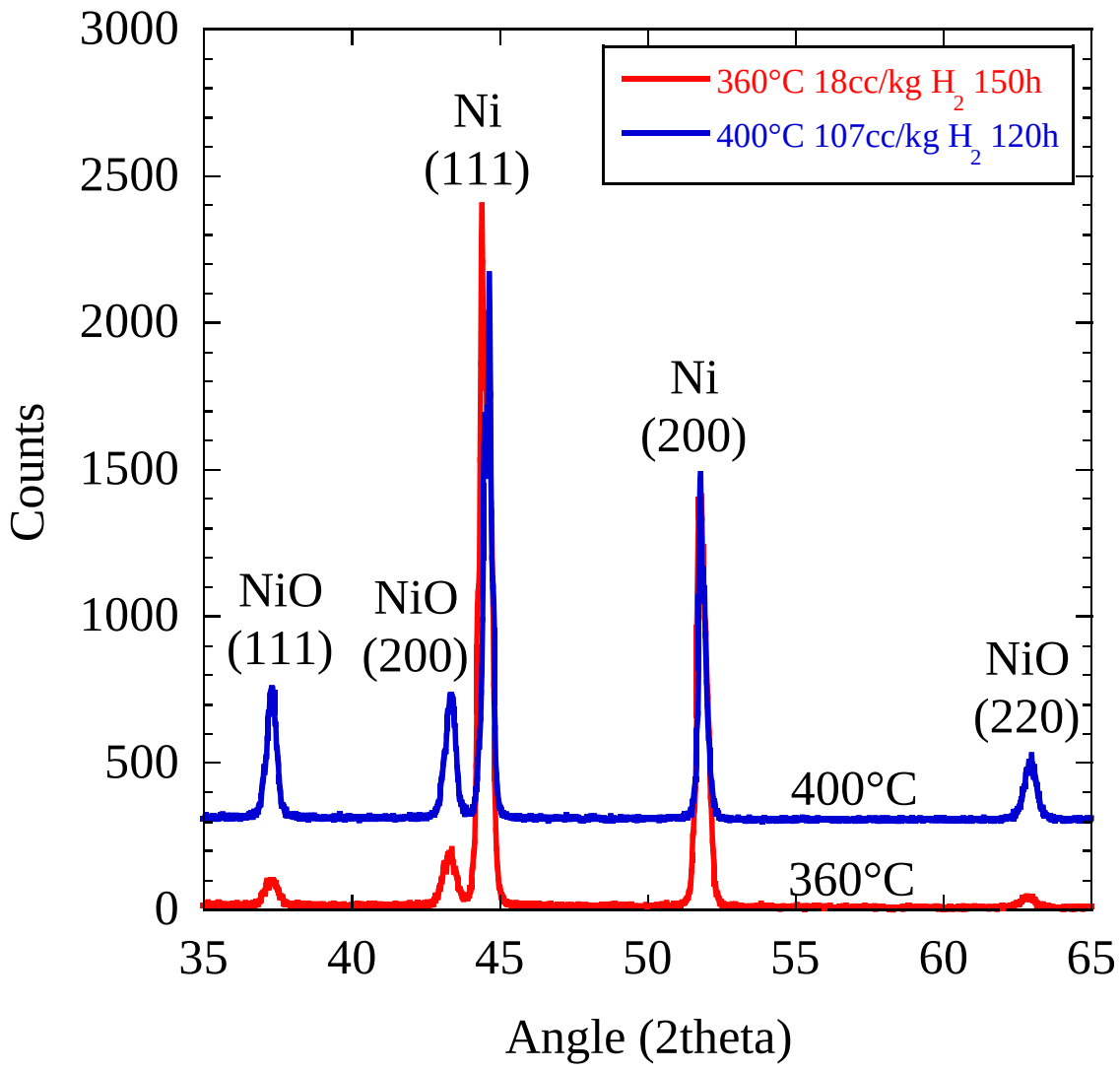

Figure 4.4. Grazing incidence X-ray diffraction of oxidized nickel coupons from subcritical and supercritical water showing NiO structured oxide for both conditions. The incident angle was 1.5° with a scan rate of 0.3°/min.

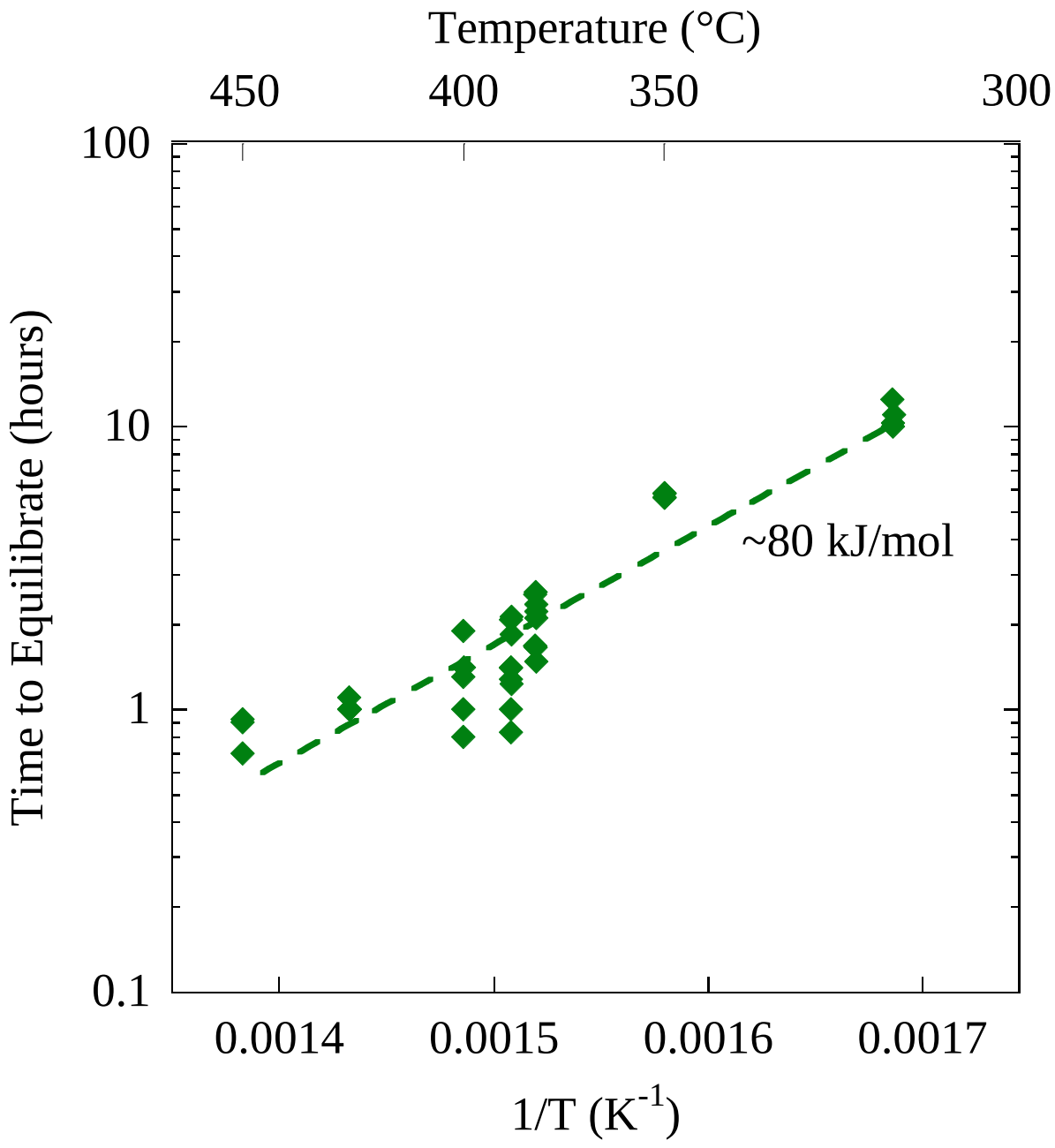

Figure 4.5. Time to equilibrate for hydrogen diffusion through Pd-Ag membrane as a function of inverse temperature.

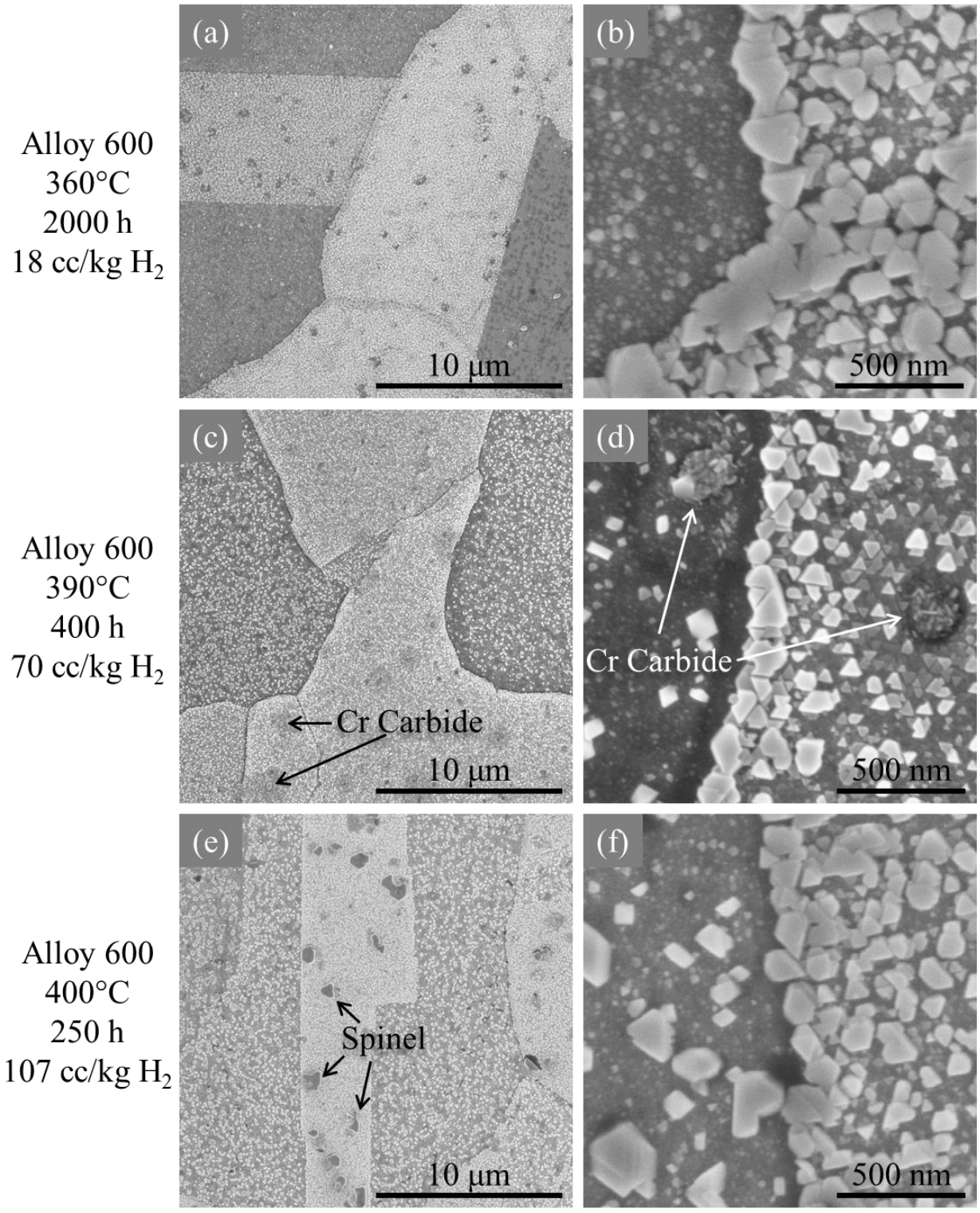
Alloy 600
360°C
2000 h
18 cc/kg H_2
(a)
10 μm
(b)
500 nm
Alloy 600
390°C
400 h
70 cc/kg H_2
(c)
Cr Carbide
10 μm
(d)
Cr Carbide
500 nm
Alloy 600
400°C
250 h
107 cc/kg H_2
(e)
Spinel
10 μm
(f)
500 nm

(a)

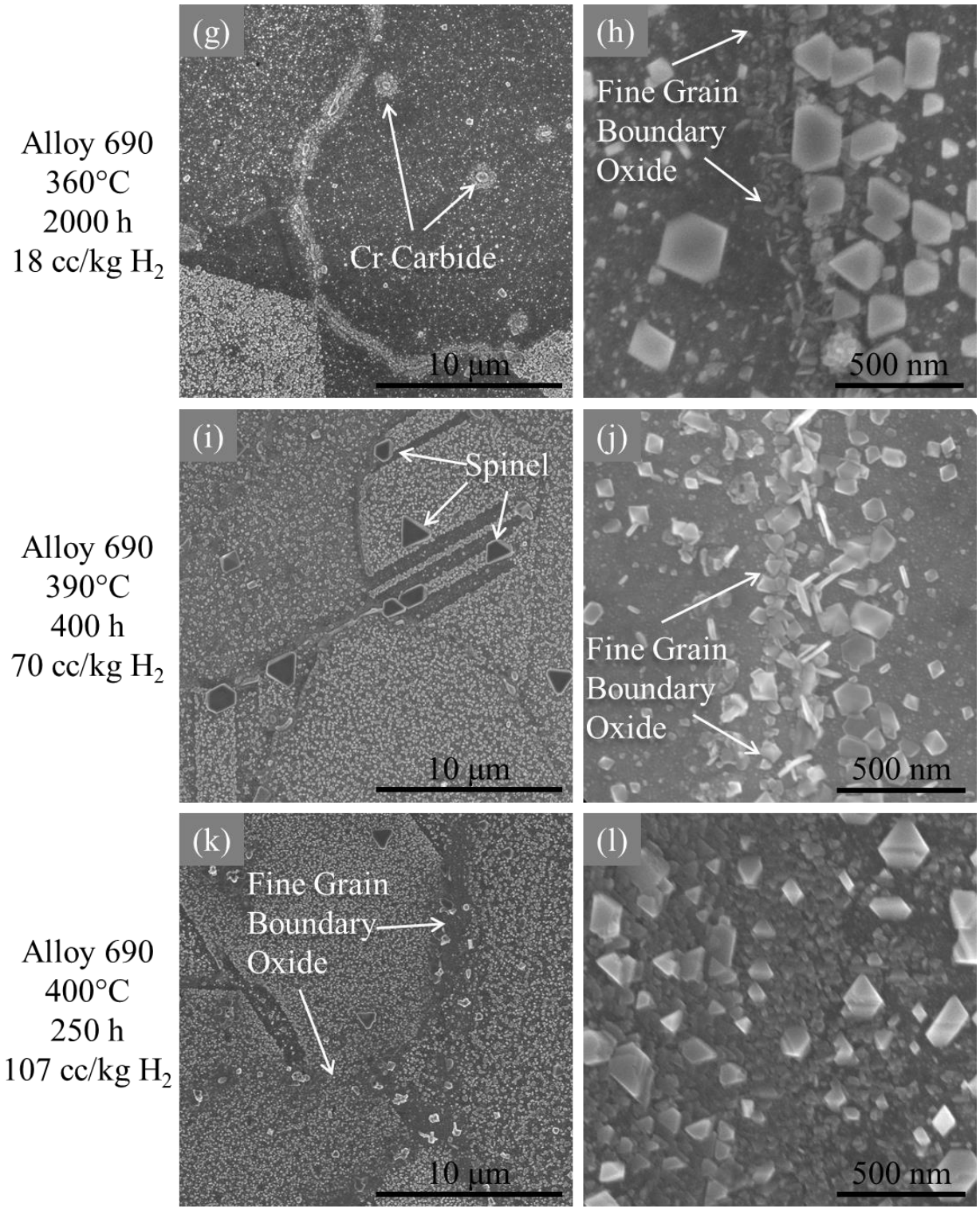

(b)

Figure 4.6. Low and high magnification SEM images taken at 5 keV of surface oxidation observed on Alloy 600 (a) and Alloy 690 (b).

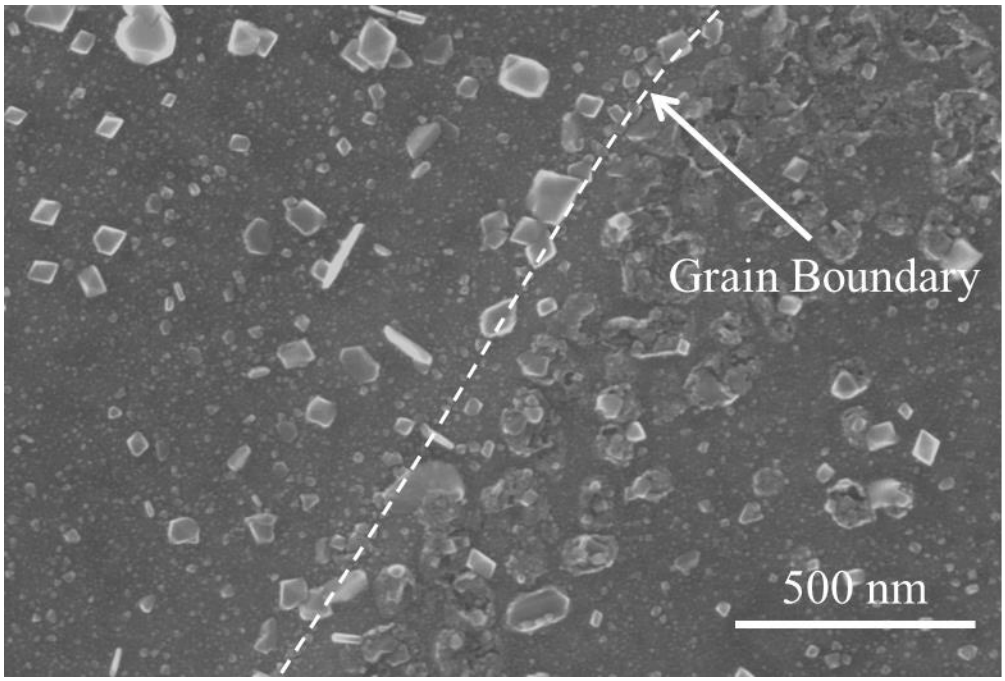

(a)

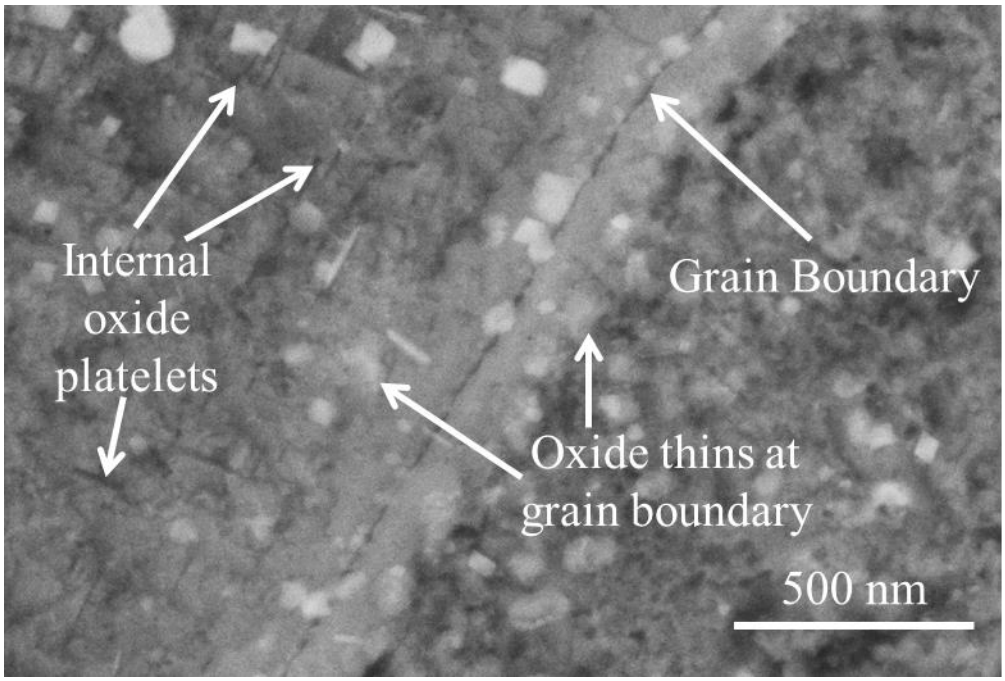

(b)

Figure 4.7. Surface micrographs of Alloy 690 exposed to 360°C water for 2000h imaged with (a) secondary electrons and (b) backscattered electrons at 15 keV.

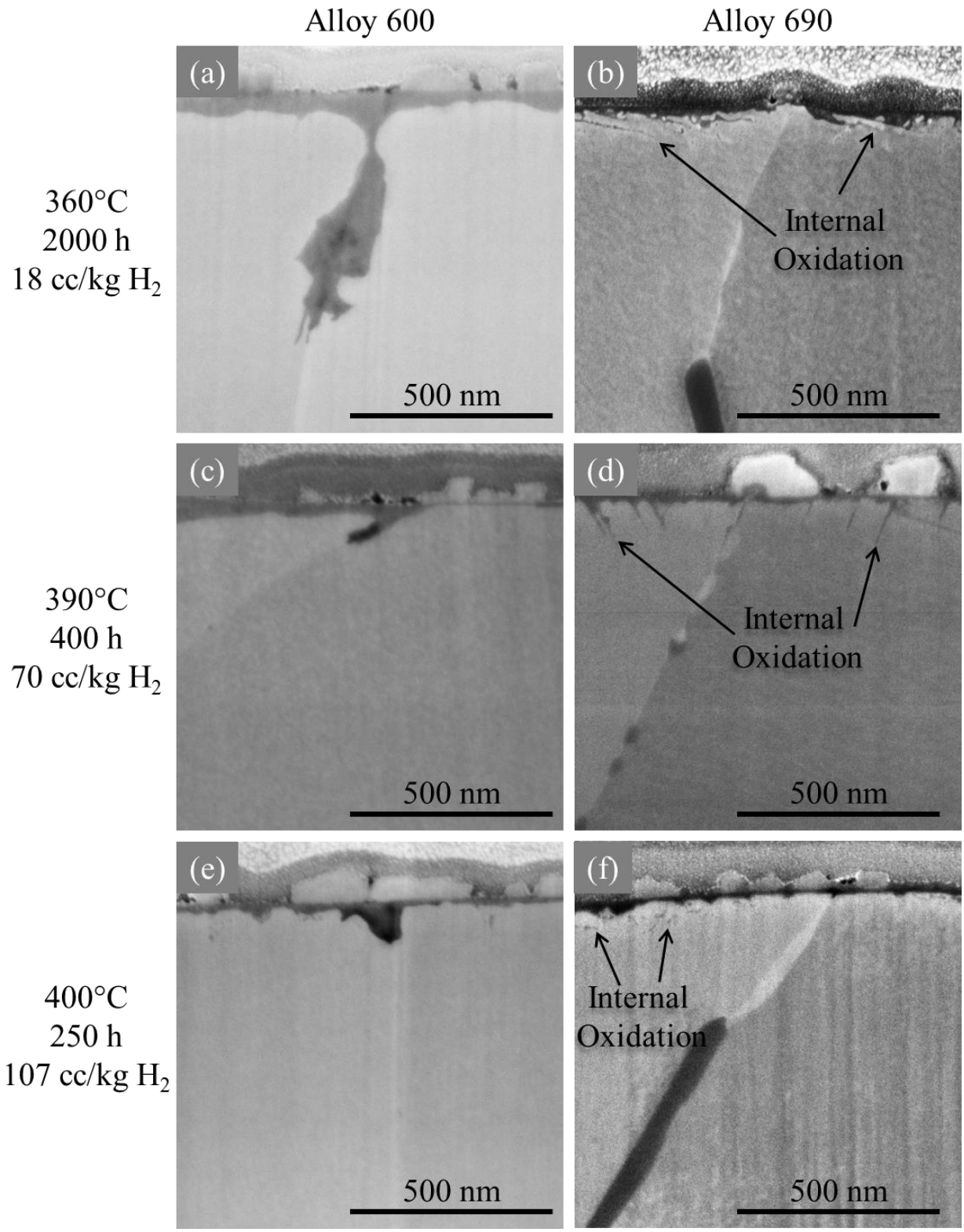

Figure 4.8. Cross section FIB-SEM images taken at 5 keV of grain boundary and surface oxidation on Alloy 600 and Alloy 690. Alloy 600 showed grain boundary oxidation while Alloy 690 intragranular internal oxidation and grain boundary migration in subcritical and supercritical water.

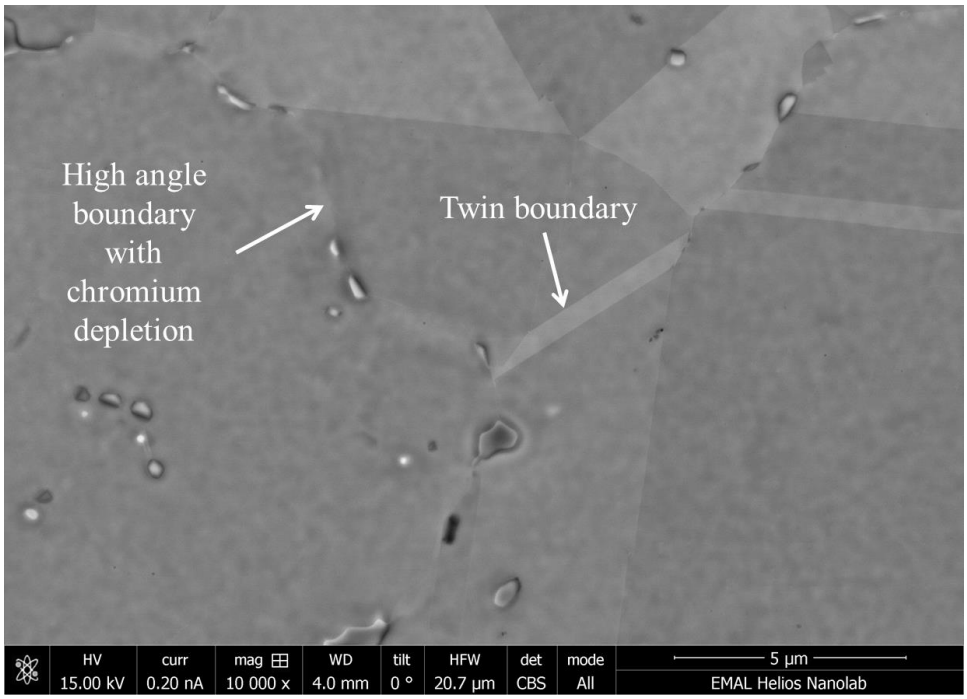

(a)

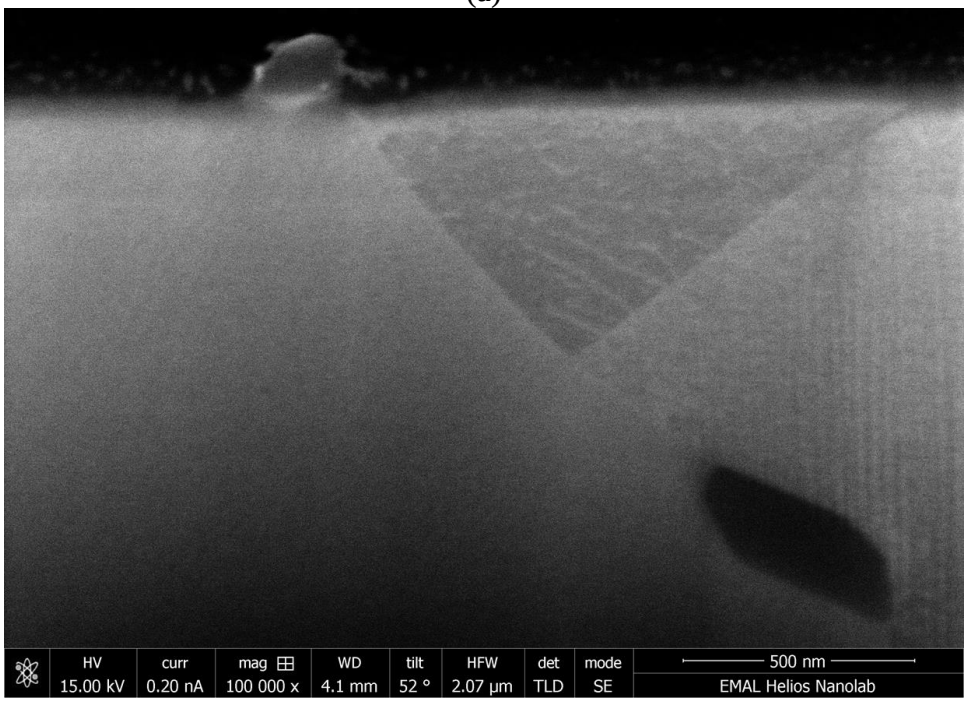

(b)

Figure 4.9. Micrographs of Alloy 690 prior to exposure showing no indication of grain boundary migration when observed (a) from the surface with backscattered electrons and (b) in cross section with secondary electrons.

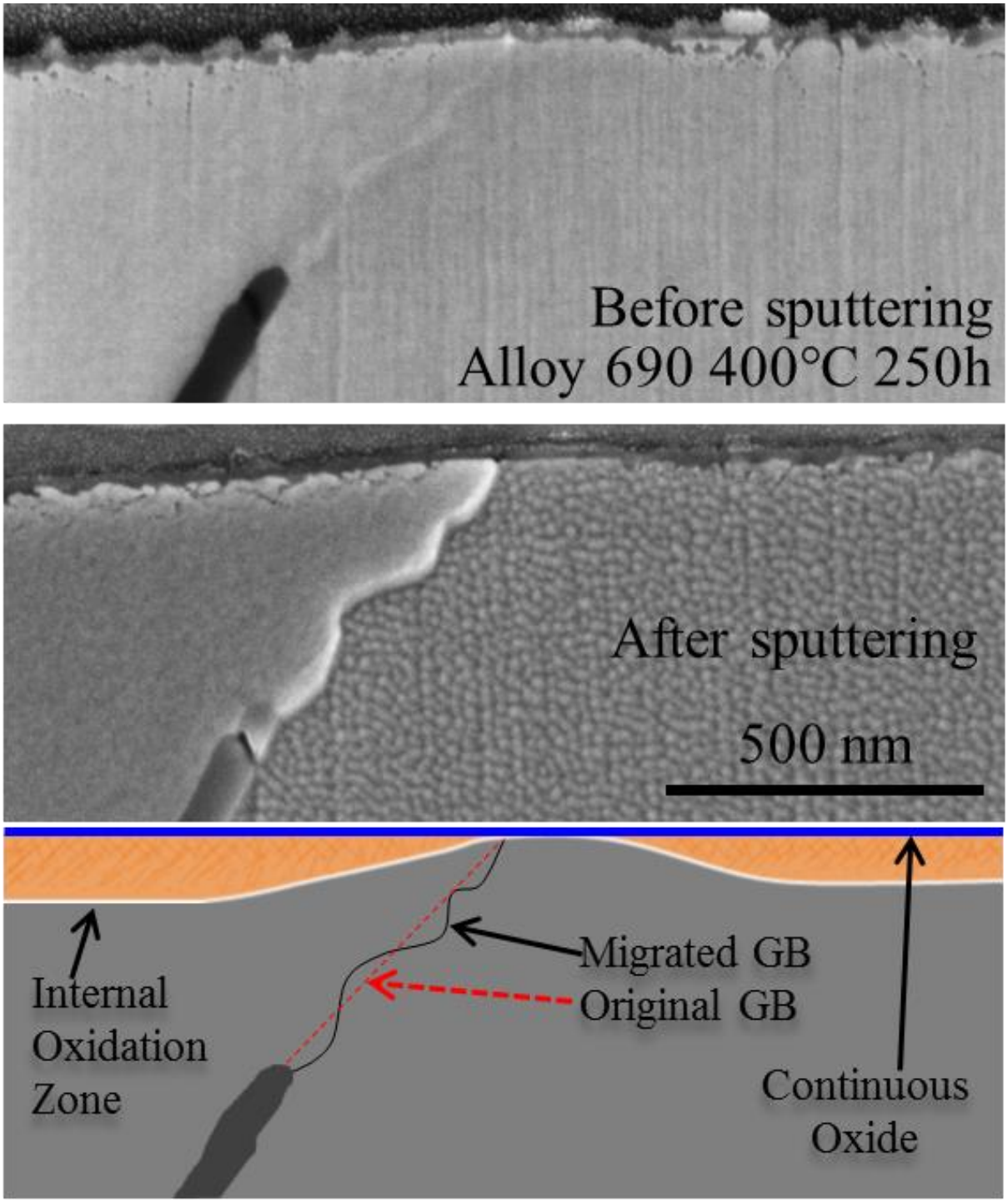

Figure 4.10. Grain boundary migration and chromium depletion observed in SEM at 5 keV in cross section of Alloy 690 exposed at 400°C for 250 hours. A lighter contrast indicated chromium depletion and the grain boundary location was revealed by sputtering with 2 keV argon at a current of 1 μA.

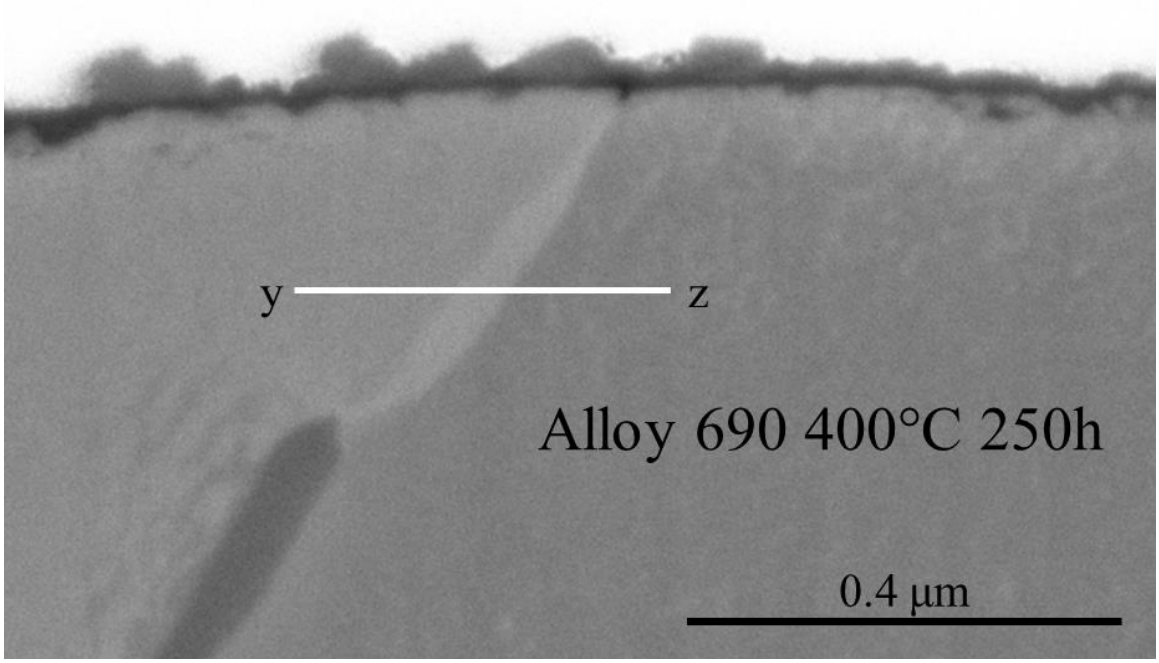

(a)

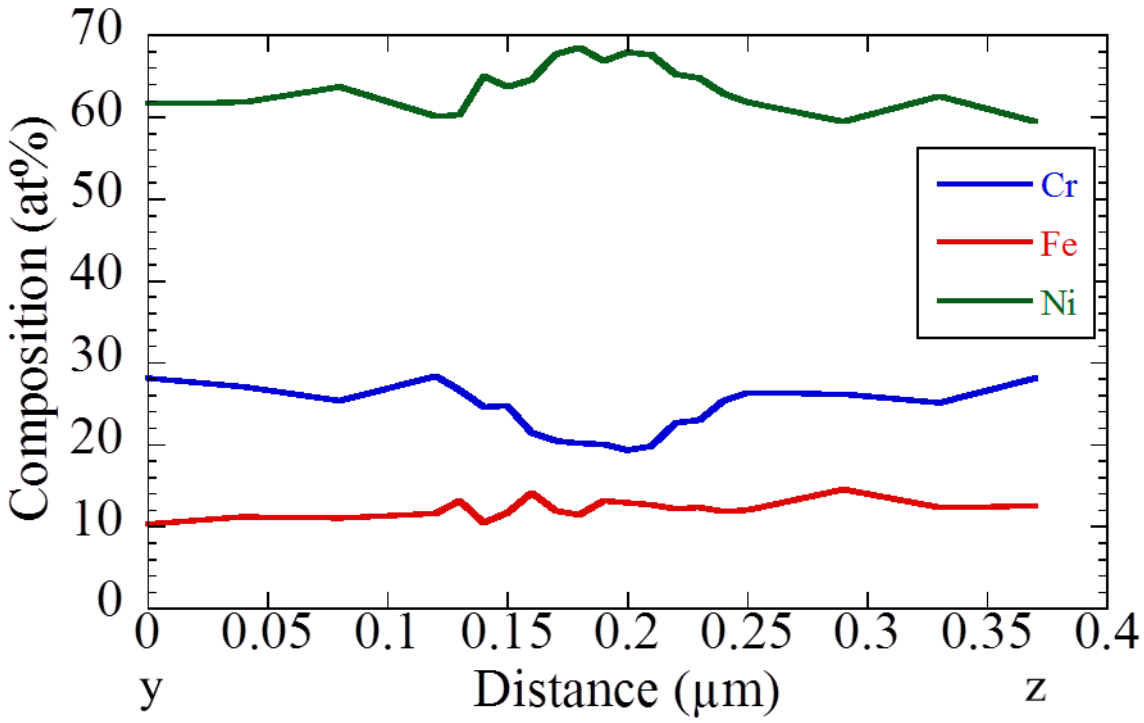

(b)

Figure 4.11. Cross section of Alloy 690 exposed to 400°C for 250h showing grain boundary migration when imaged with (a) secondary electrons at 5 keV and (b) chromium depletion from SAM measurements.

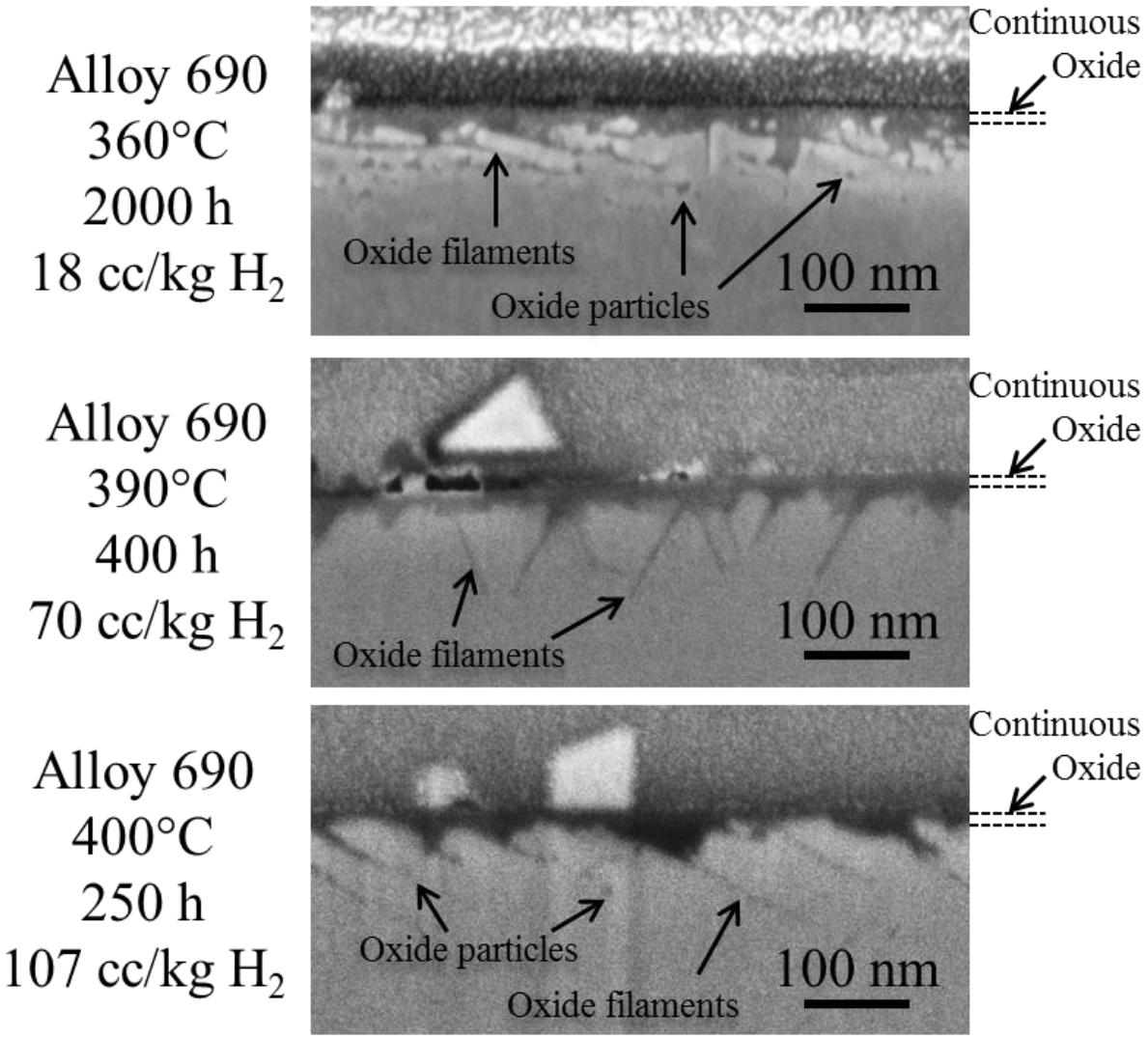

Figure 4.12. Cross section FIB-SEM images taken at 5 keV of internal and surface oxidation on Alloy 690 observed in subcritical and supercritical water.

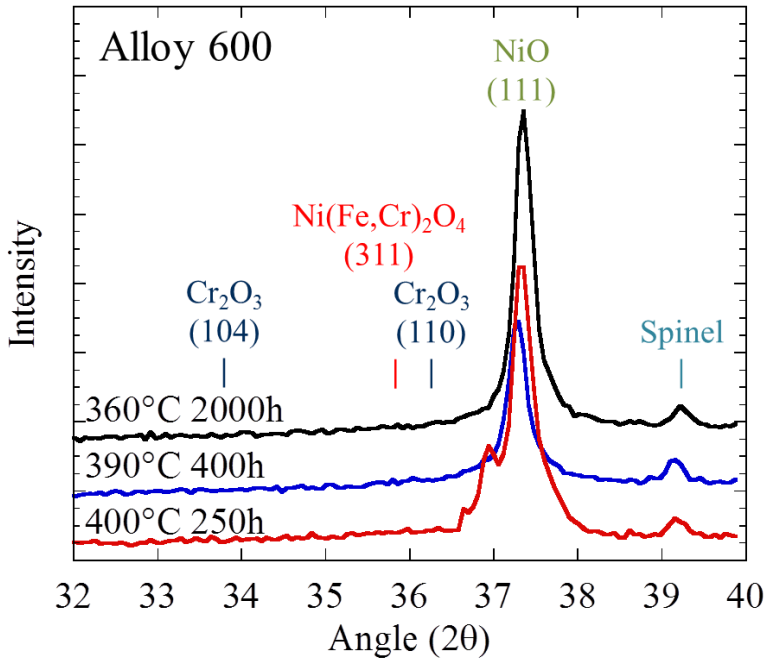

(a)

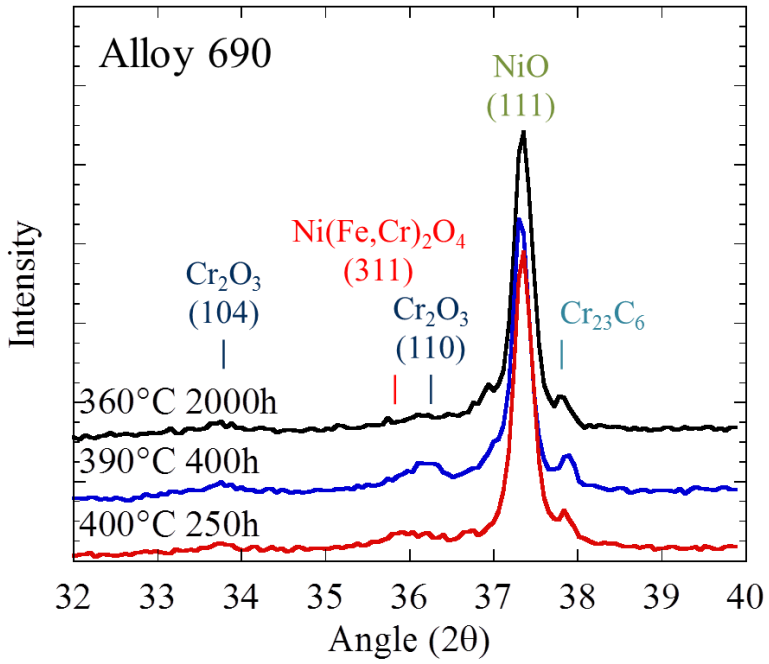

(b)

Figure 4.13. X-ray diffraction of Alloy 600 (a) and Alloy 690 (b) at an incident angle of 20°.

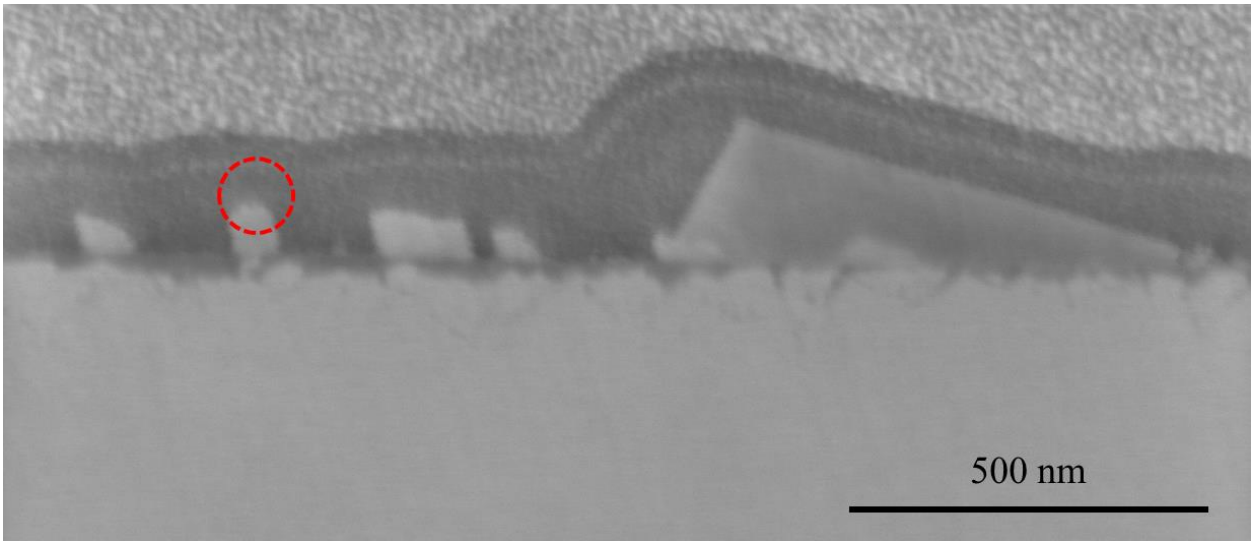

(a)

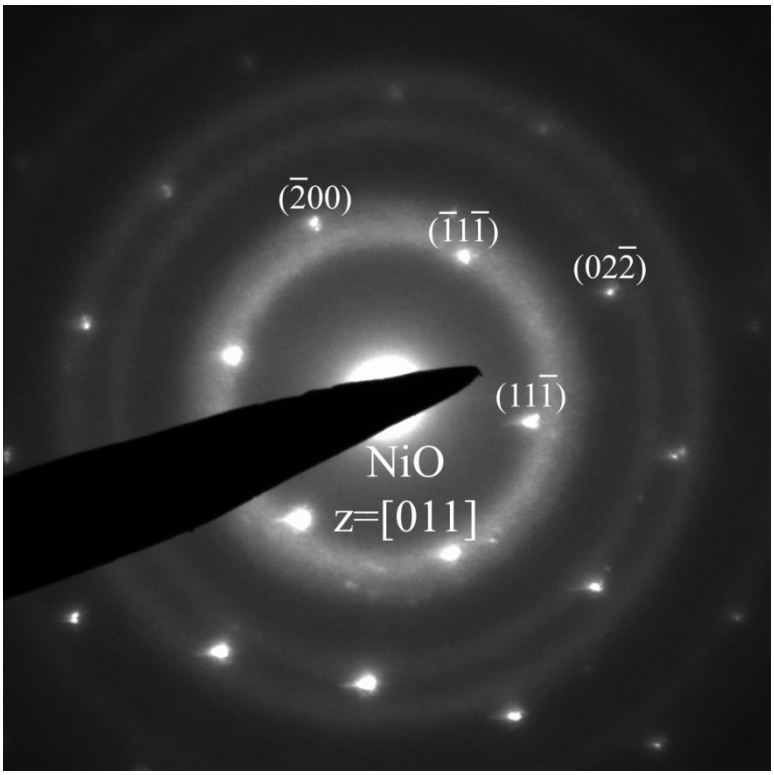

(b)

Figure 4.14. (a) 5 keV SEM micrograph and (b) selected area diffraction of NiO particle along [011] zone axis from surface of Alloy 690 exposed to 400°C for 250 hours with 107 cc/kg dissolved hydrogen.

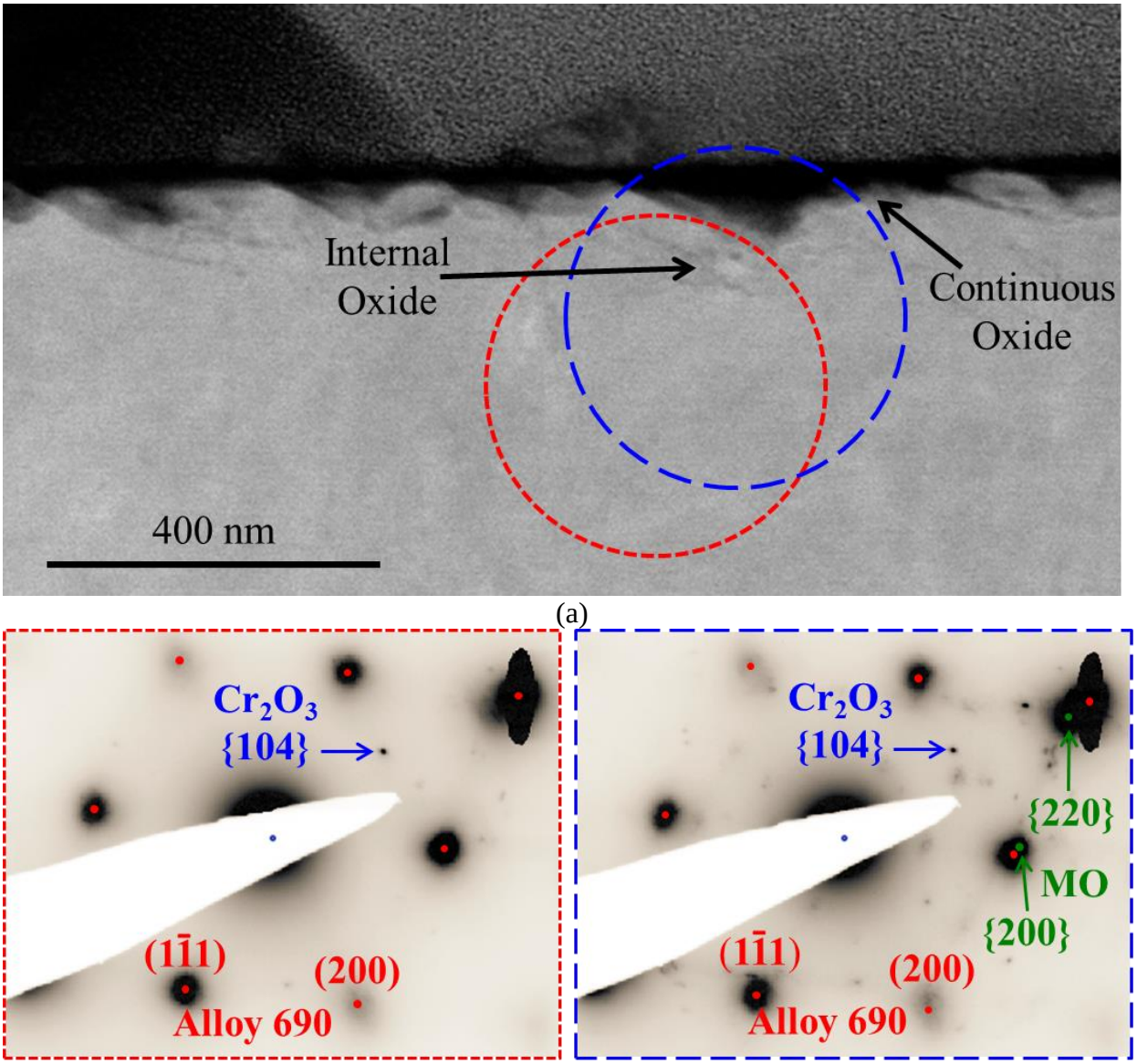

Figure 4.15. STEM (a) dark field micrograph of the cross section of Alloy 690 exposed at 400°C for 250 hrs, with selected area diffraction taken from (b) the area encircled with the fine dashed red line, and (c) the area encircled by the coarse dashed blue line.

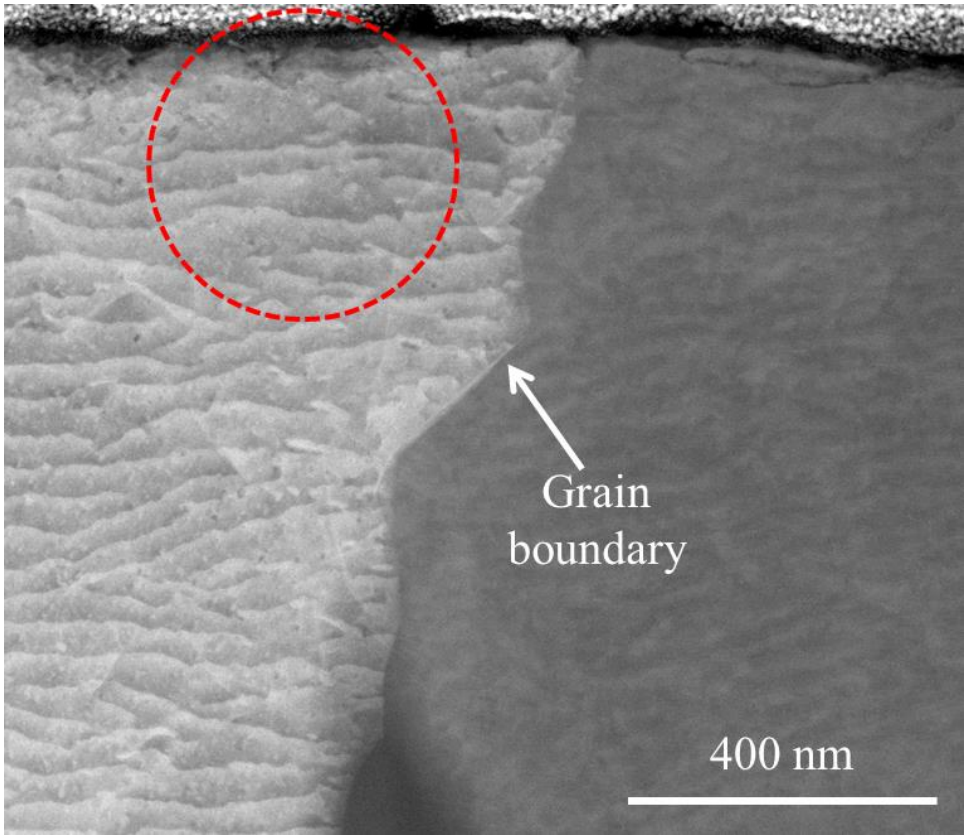

(a)

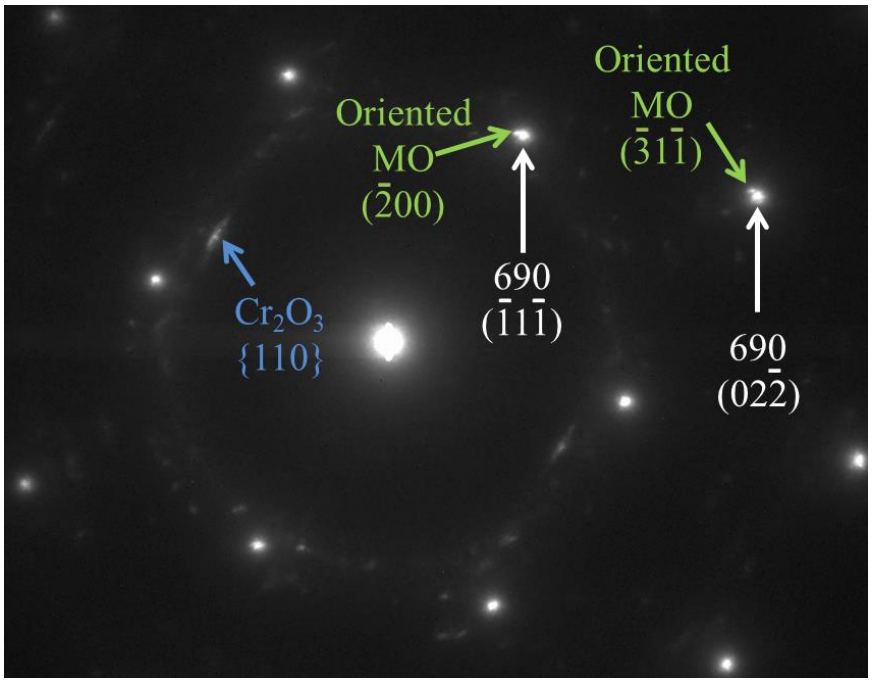

(b)

Figure 4.16. STEM (a) dark field micrograph of the cross section of Alloy 690 exposed at 360°C for 2000 hrs with a selected area diffraction pattern taken from the area encircled by the dashed red line matching Cr_2O_3 structure with MO oriented to the metal.

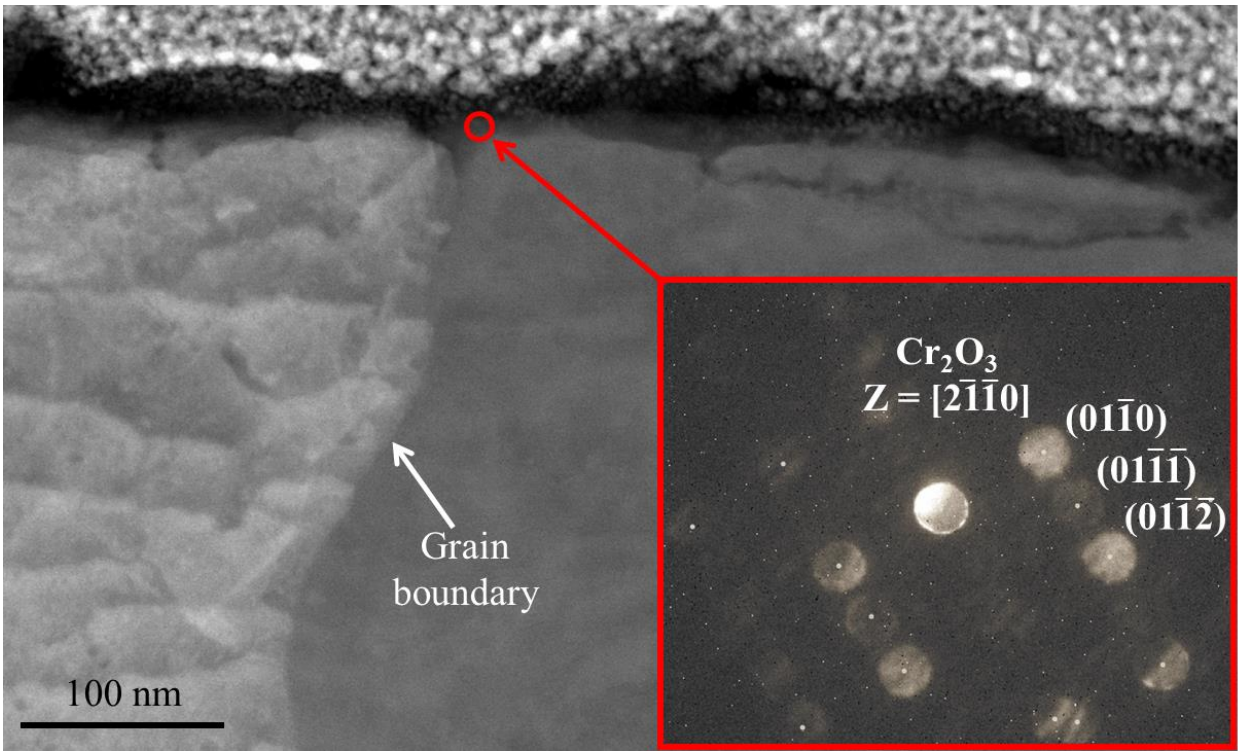

Figure 4.17. STEM (a) dark field micrograph of the cross section of Alloy 690 exposed at 360°C for 2000 hrs with a nano-diffraction pattern taken from the circled region matching Cr_2O_3 structure.

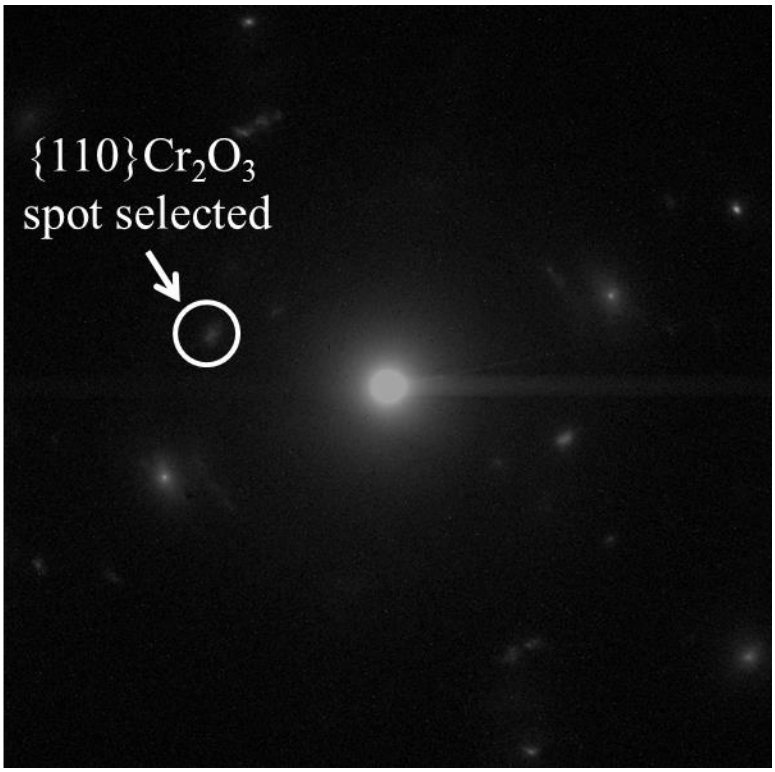

(a)

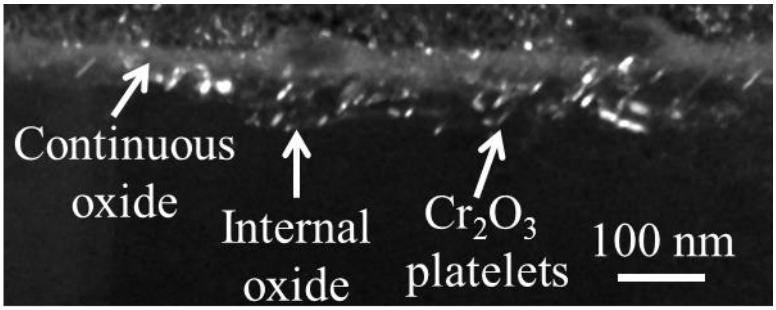

(b)

Figure 4.18. (a) Selected area diffraction of the surface oxide from a cross section of Alloy 690 exposed to 360°C for 2000 hrs. A Cr_2O_3 spot is selected and the (b) selected area dark field shows platelets of oriented oxide.

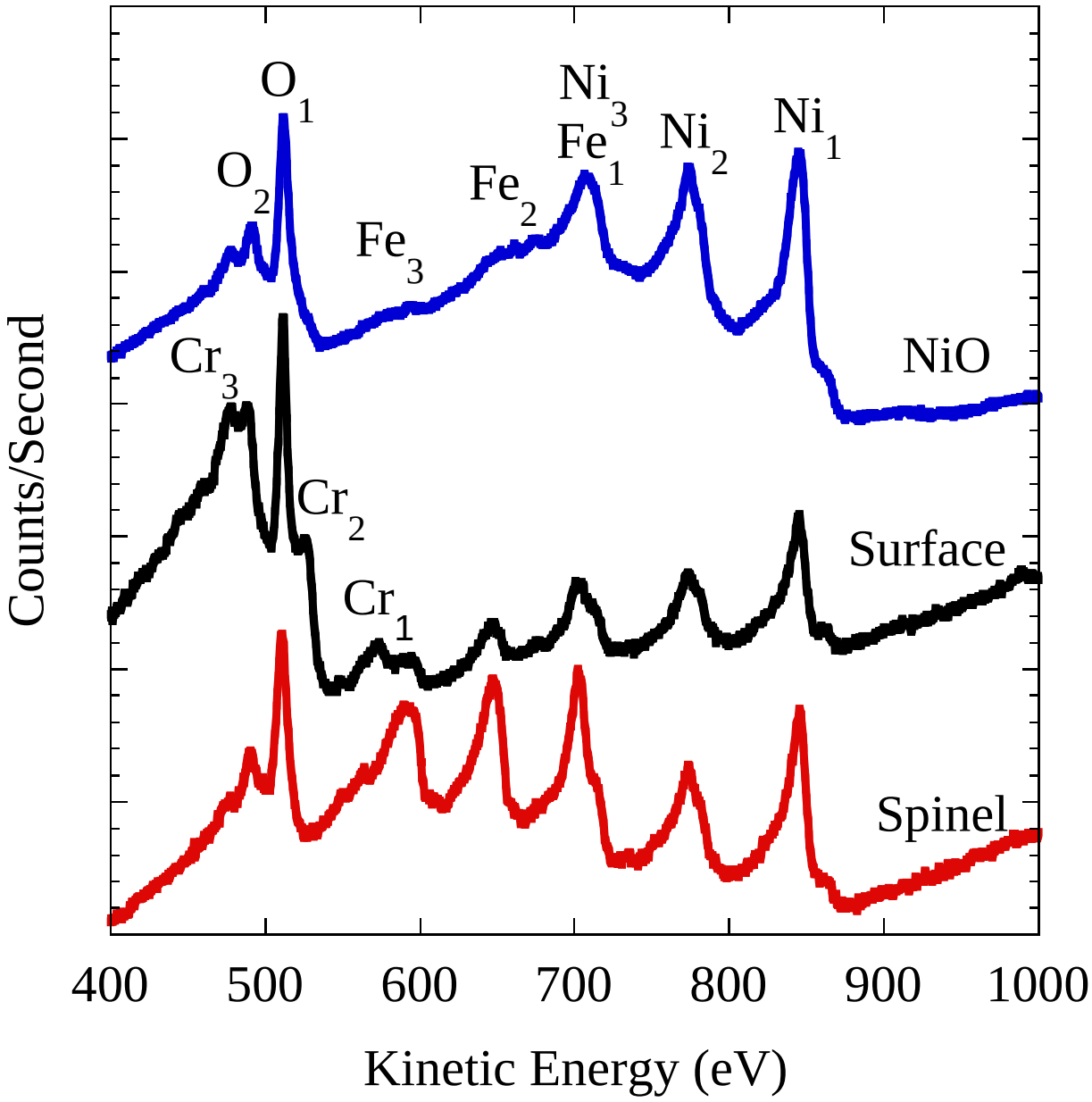

Figure 4.19. Representative Auger spectra taken from NiO, surface oxides, and spinel particles on Alloy 690 exposed to 400°C for 250 hrs.

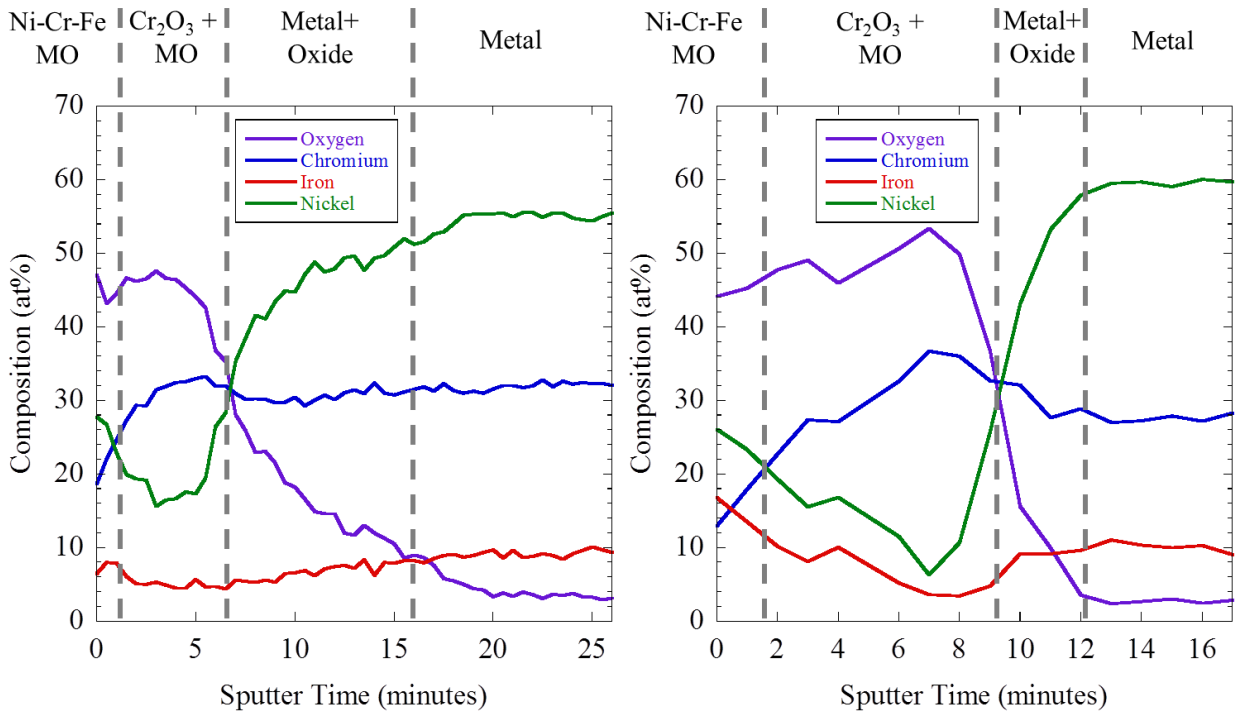

Figure 4.20. Depth profiling of grain boundary oxides on Alloy 690 exposed to (a) 360°C water for 2000 hrs and (b) 400°C supercritical water for 250 hrs performed by scanning Auger microscopy. Sputtering was performed with 2 keV argon at a current of 1 μA, yielding an approximate sputter rate of ~1nm/minute.

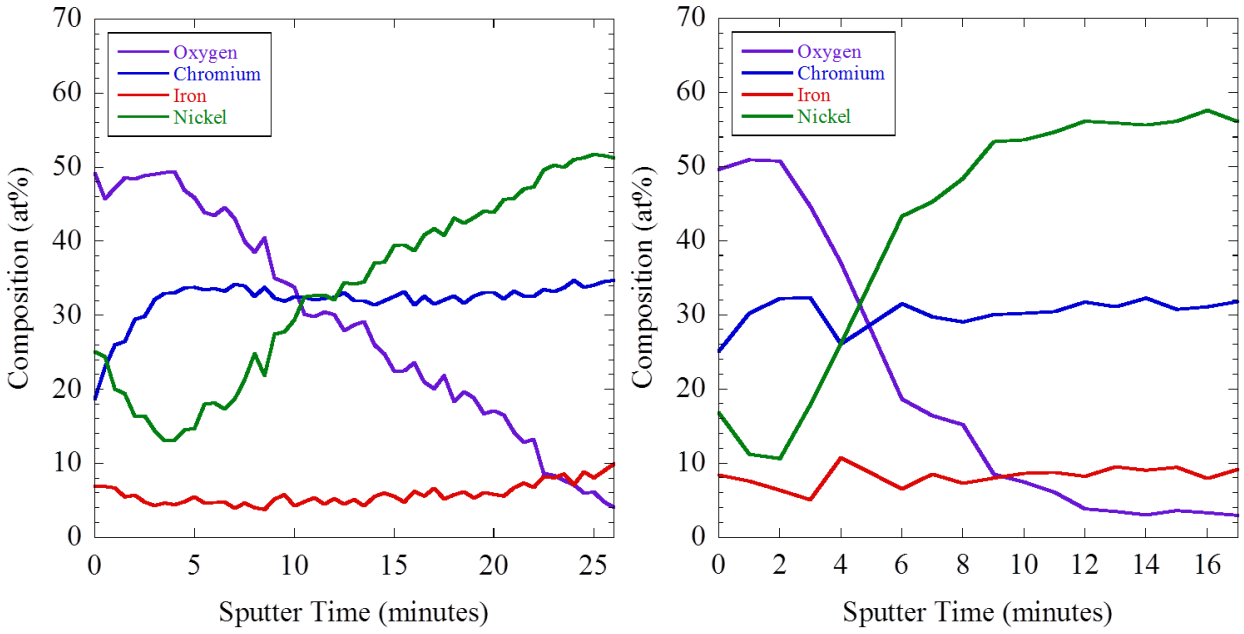

(a) (b)

Figure 4.21. Depth profiling of the inner oxide layer on Alloy 690 exposed to (a) 360°C water for 2000 hrs and (b) 400°C supercritical water for 250 hrs performed by scanning Auger microscopy. Sputtering was performed with 2 keV argon at a current of 1 μA, yielding an approximate sputter rate of ~1nm/minute.

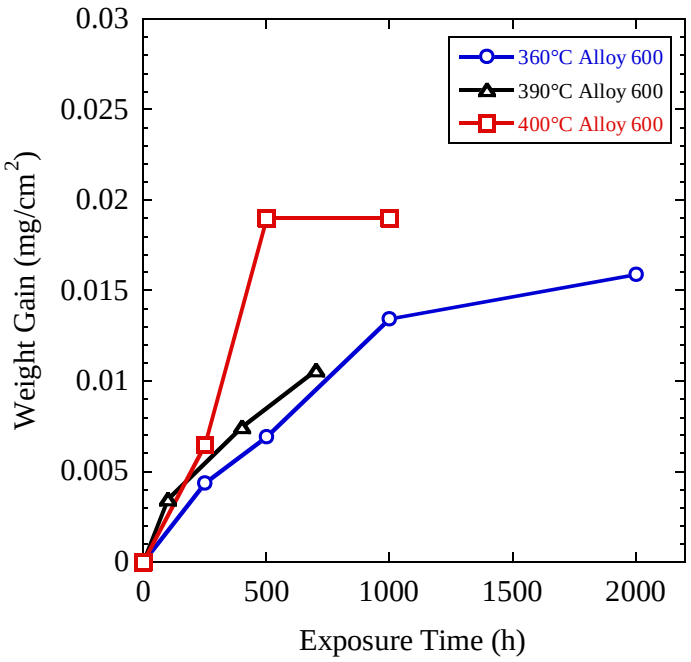

(a)

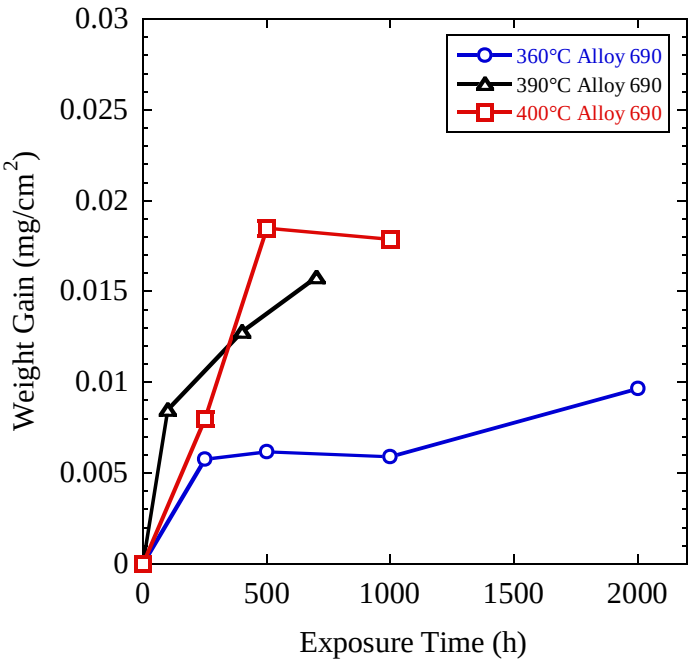

(b)

Figure 4.22. Weight gain of Alloy 600 (a) and 690 (b) exposed to 360, 390, and 400°C hydrogenated water.

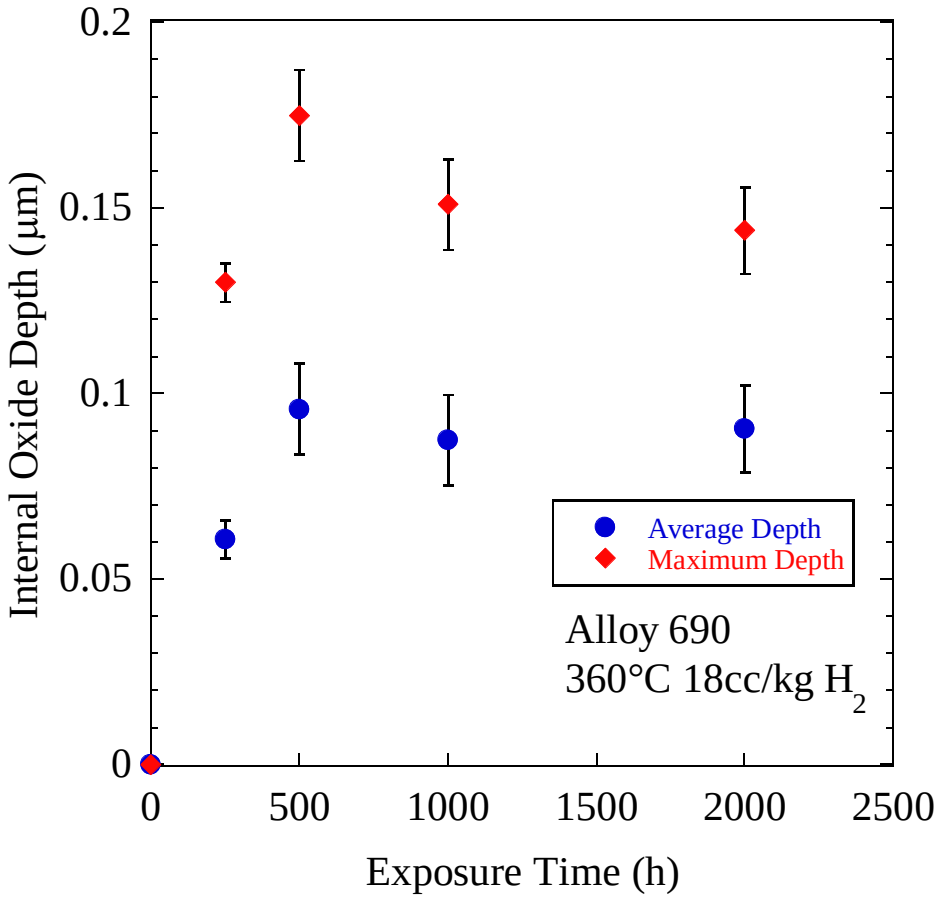

Figure 4.23. Average and maximum depth of internal oxidation as a function of time measured by cross section FIB-SEM for Alloy 690 exposed at 360°C for 2000 hours.

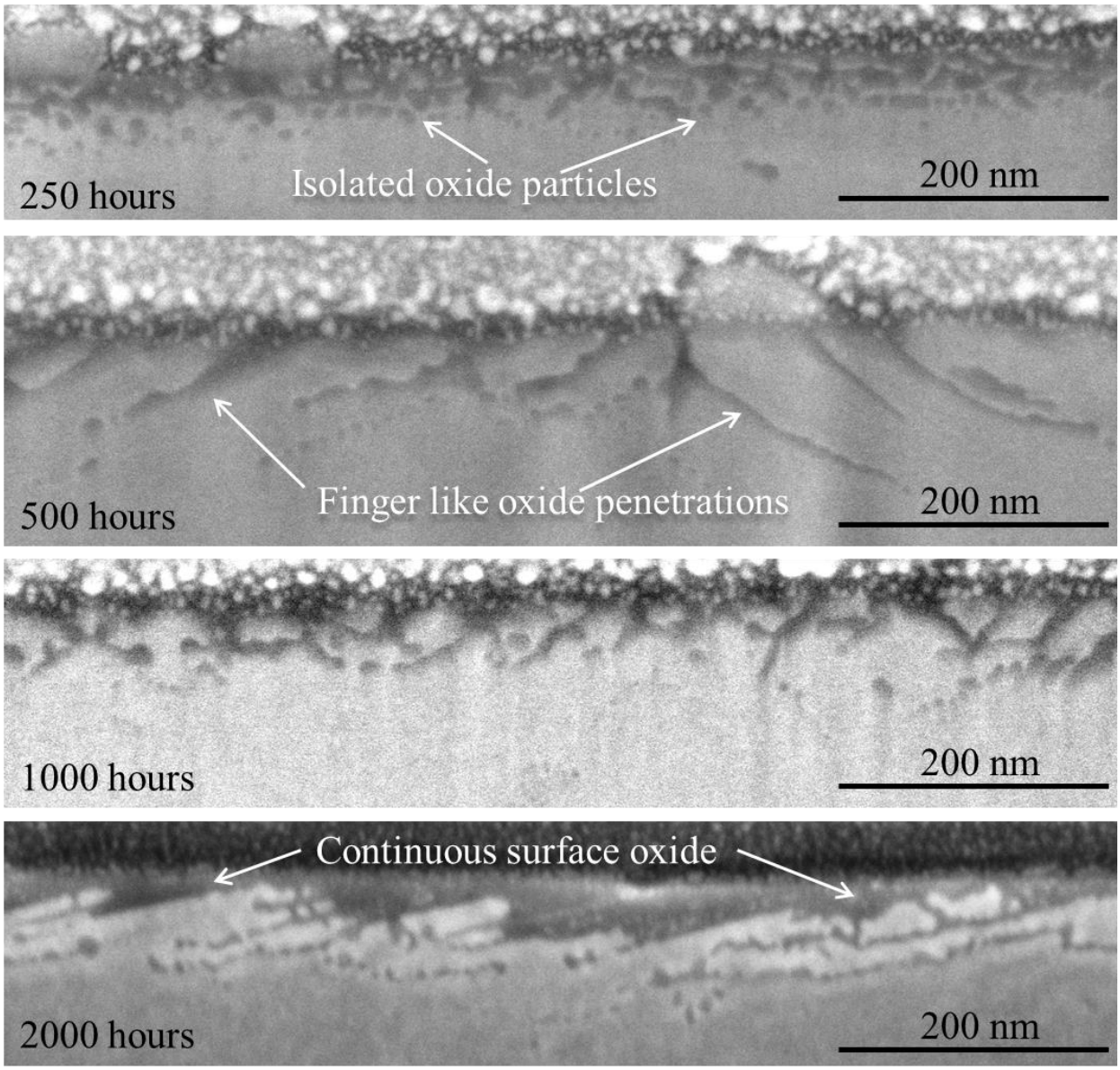

Figure 4.24. Representative internal oxidation cross section morphology observed in FIB-SEM at 5 keV on Alloy 690 exposed at 360°C for 2000 hours with 18 cc/kg dissolved hydrogen.

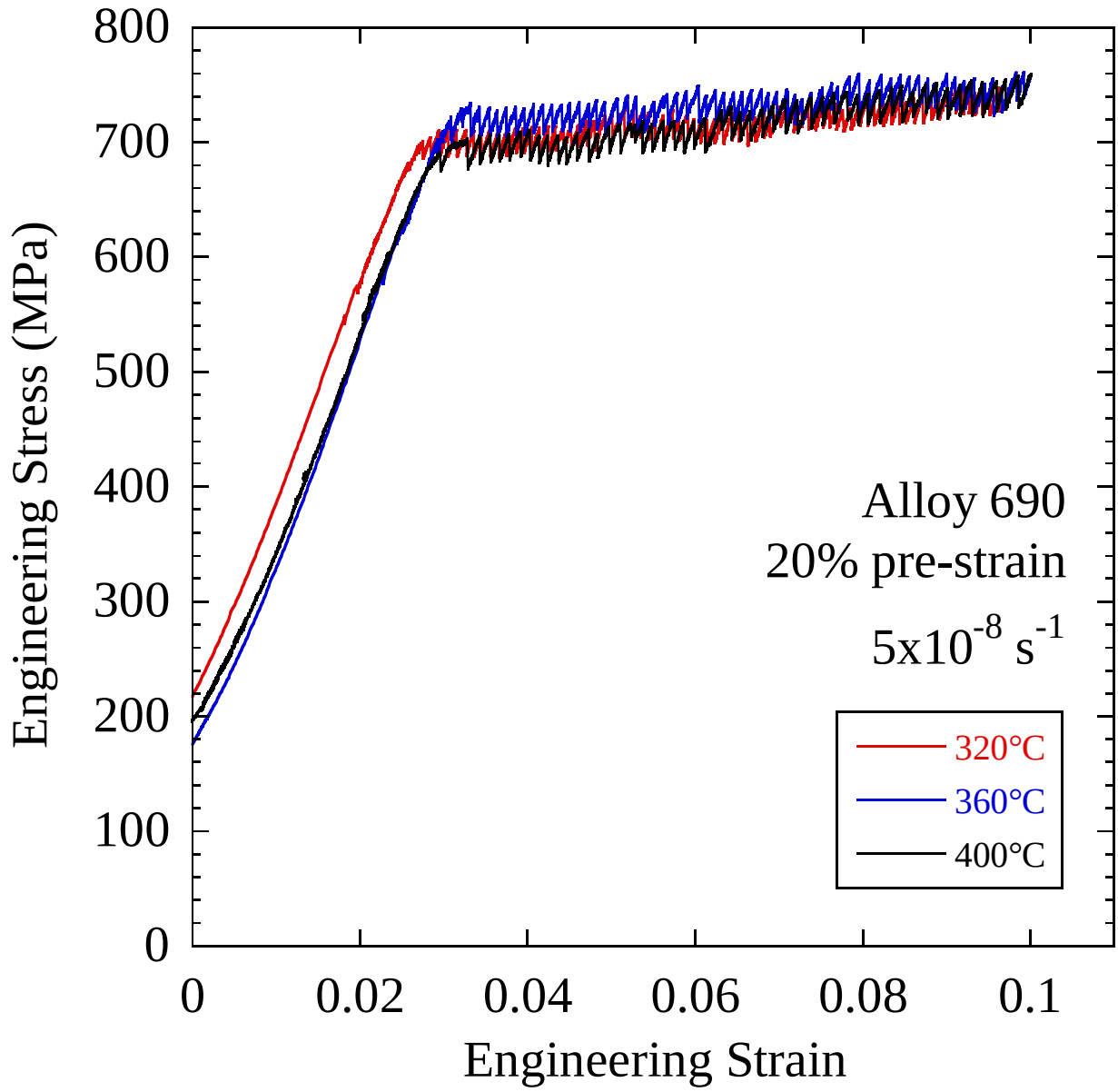

Figure 4.25. Engineering stress-strain curves for 20% pre-strained Alloy 690 strained to 7% at $5x10^{-8}$ s^{-1}.

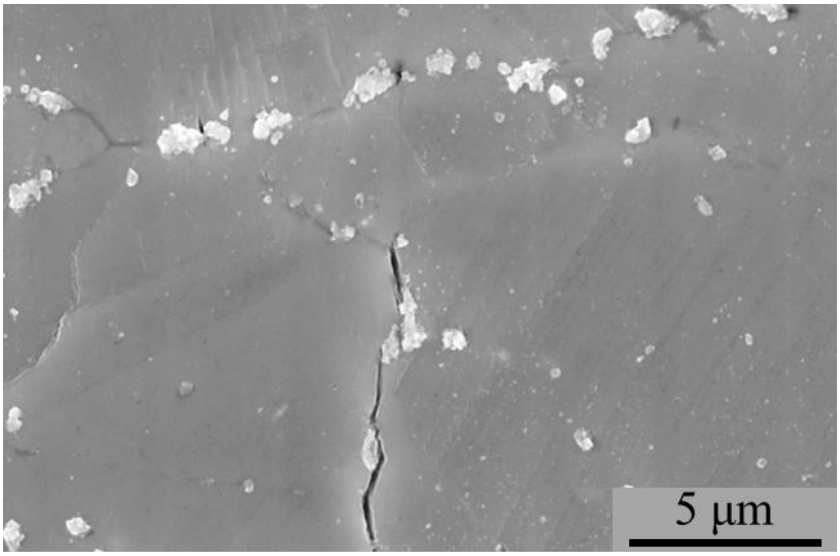

(a)

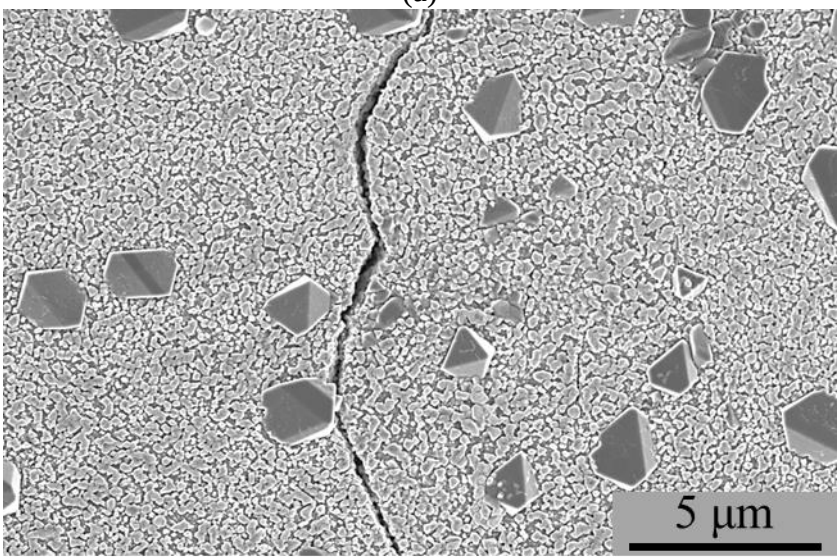

(b)

Figure 4.26. Representative examples of intergranular cracking observed in SEM at 5 keV strained in hydrogenated (a) 320°C water, and (b) 400°C supercritical water on 20% pre-strained Alloy 690 strained to 7% at $5x10^{-8}$ s^{-1}.

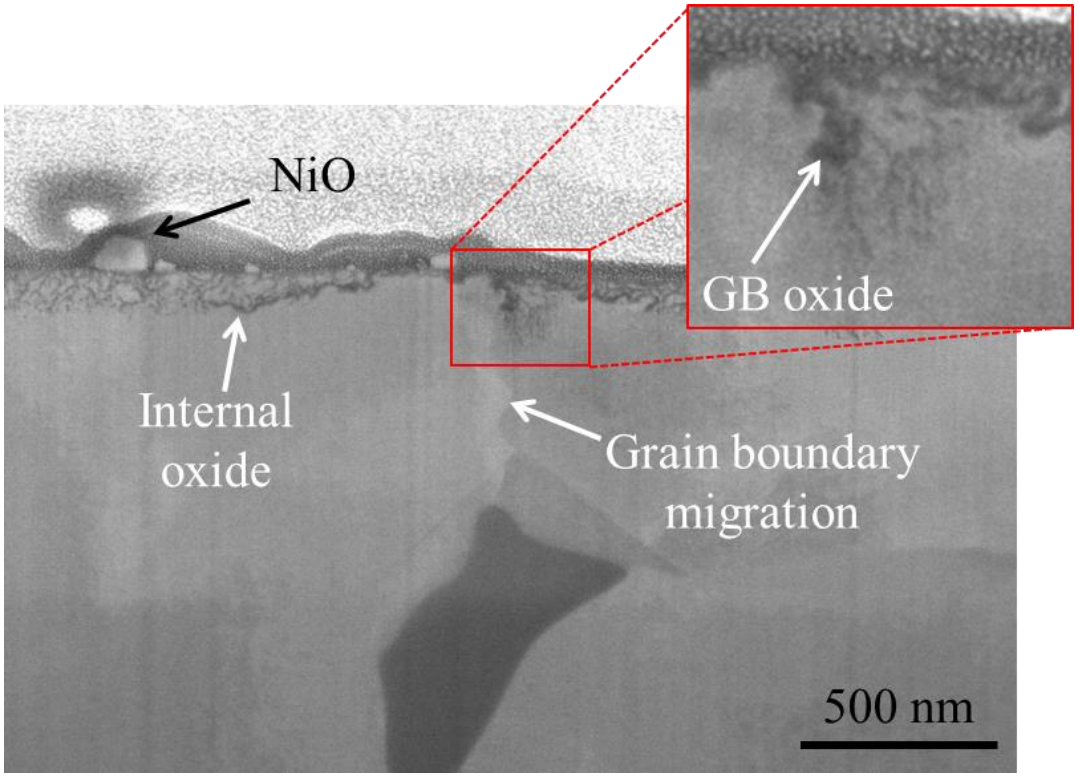

(a)

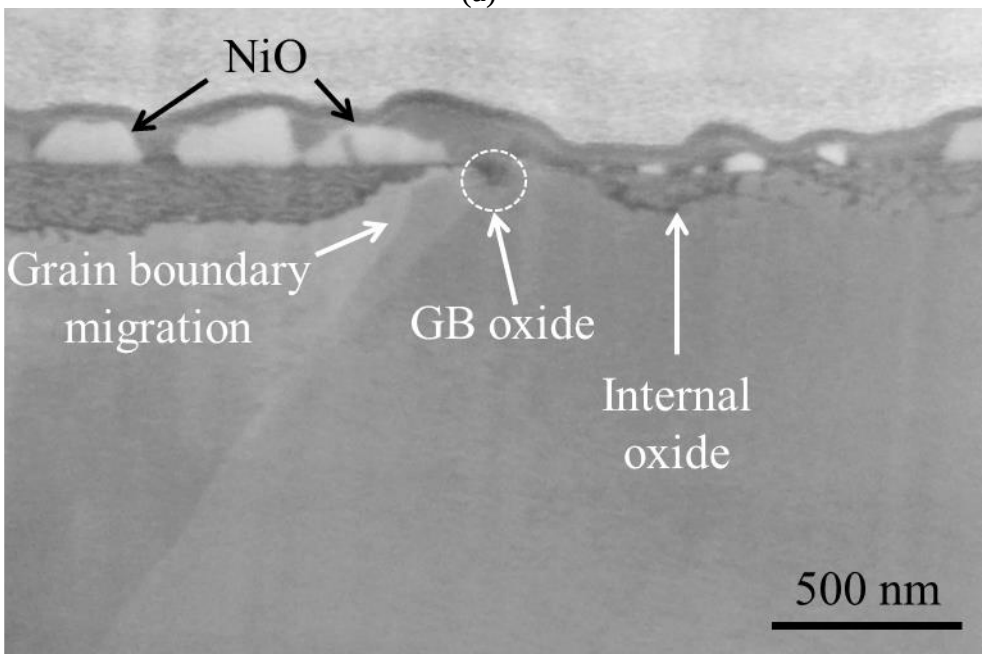

(b)

Figure 4.27. Examples of grain boundary oxidation of un-cracked grain boundaries observed in SEM at 5 keV strained in hydrogenated, (a) 320°C water, and (b) 400°C supercritical water on 20% pre-strained Alloy 690 strained to 7% at $5x10^{-8}$ s^{-1}.

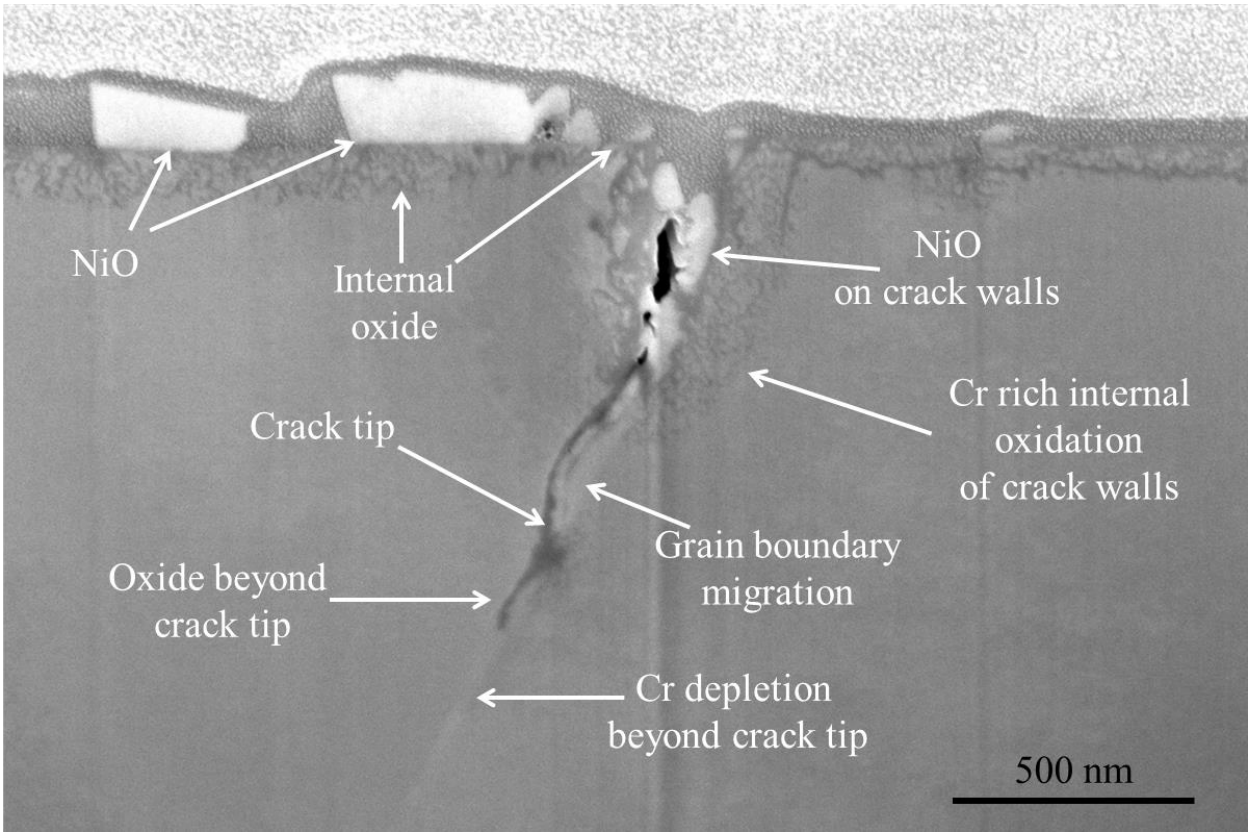

Figure 4.28. 5 keV SEM-FIB cross section of a crack in 20% pre-strained Alloy 690 strained in hydrogenated subcritical water at 360°C to 7% at $5x10^{-8}$ s^{-1}.

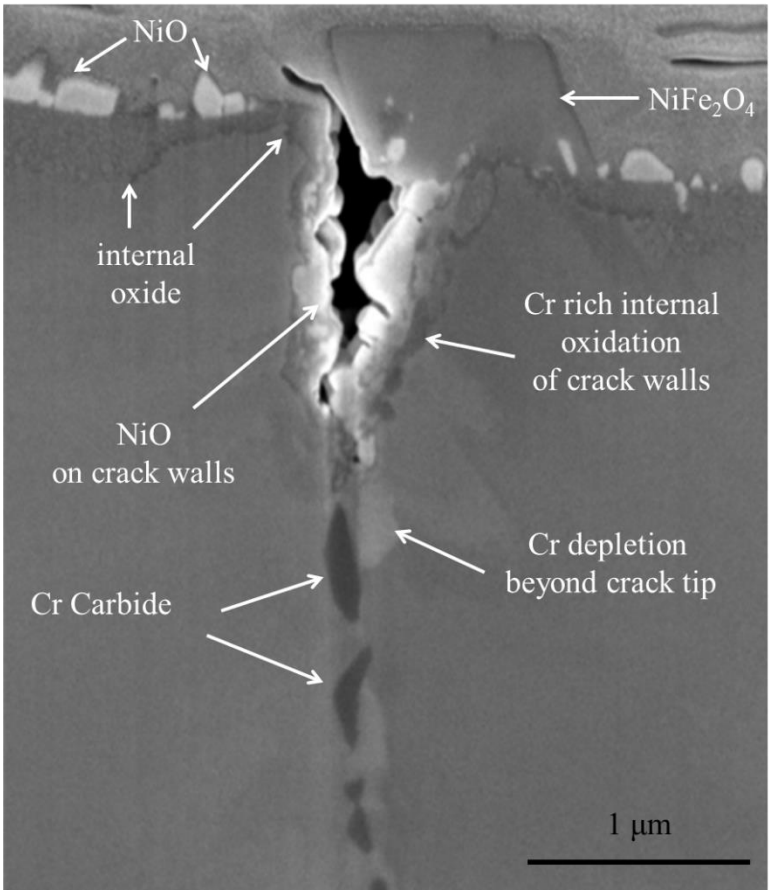

(a)

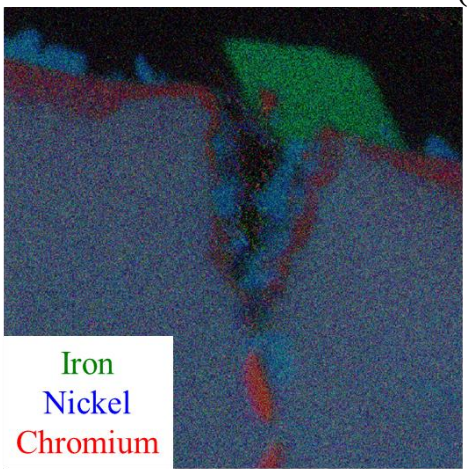

(b)

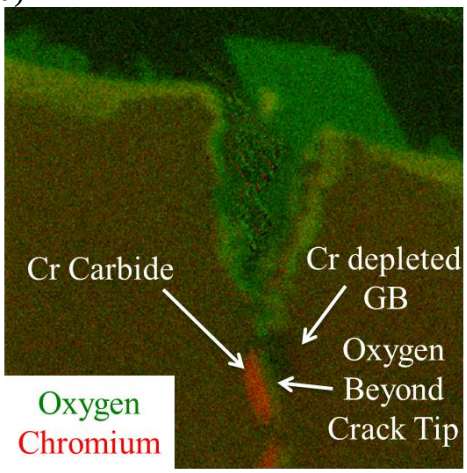

(c)

Figure 4.29. (a) 5 kev SEM-FIB cross section of a crack in 20% pre-strained Alloy 690 strained in hydrogenated supercritical water at 400°C to 7% at $5x10^{-8}$ s^{-1}. Scanning Auger microscopy maps highlighting (b) the metallic composition of oxides and (c) the presence of oxygen beyond the crack tip.

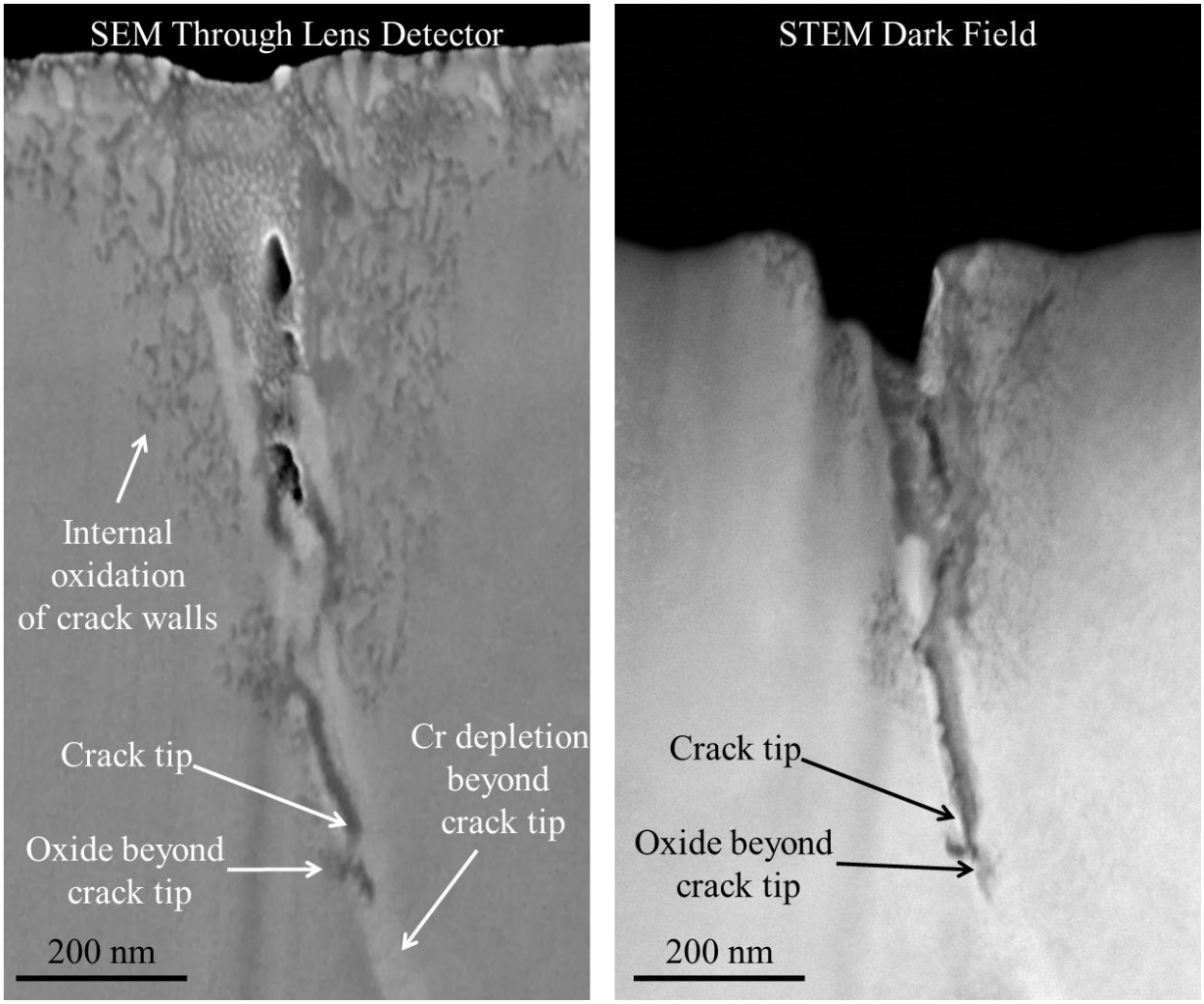

(a) (b)

Figure 4.30. FIB lift-out of a crack in 20% pre-strained Alloy 690 strained in hydrogenated subcritical water at 360°C to 7% at $5x10^{-8}$ s^{-1} imaged by (a) SEM secondary electrons at 5 keV and (b) STEM dark field.

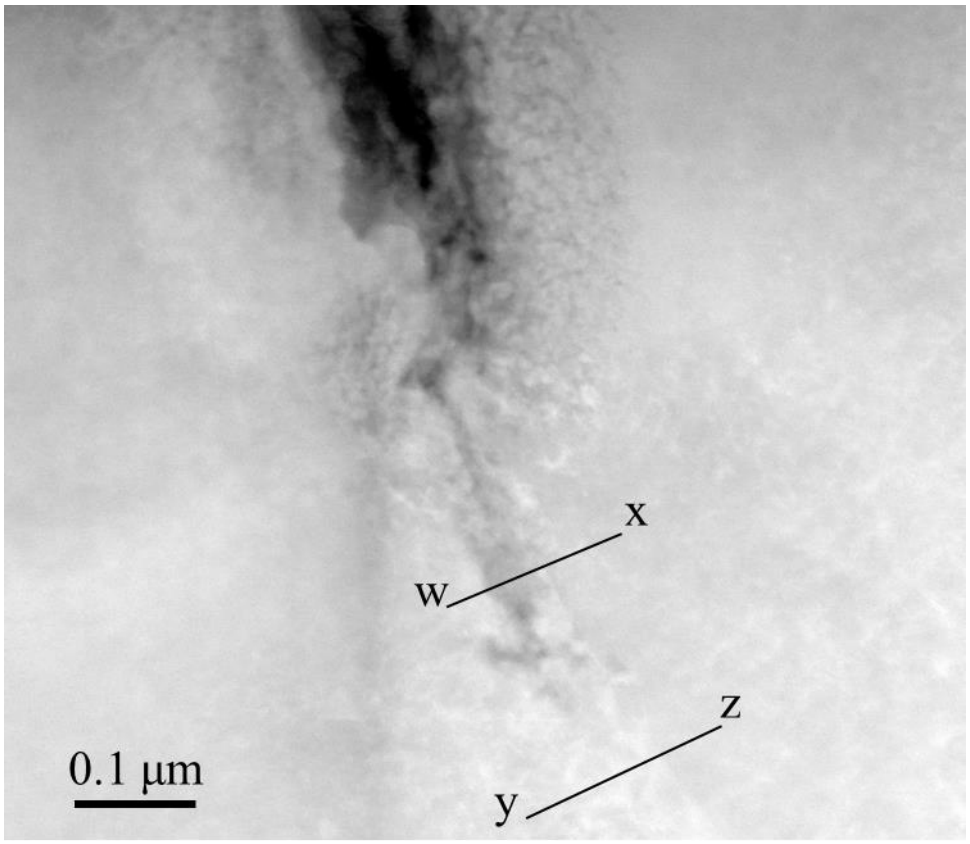

(a)

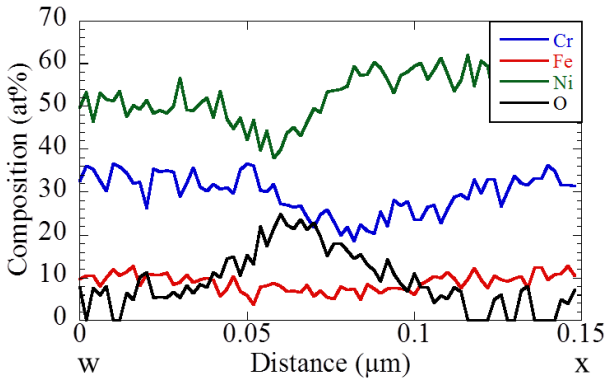

(b)

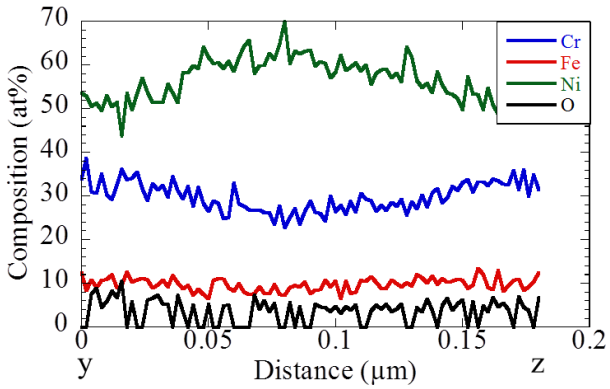

(c)

Figure 4.31. (a) STEM-EDS of the crack shown in Figure 4.30 (20% pre-strained Alloy 690 strained in hydrogenated subcritical water at 360°C to 7% at $5x10^{-8}$ s^{-1}) conducted at (b) the crack tip and (c) in the grain boundary beyond the crack tip.

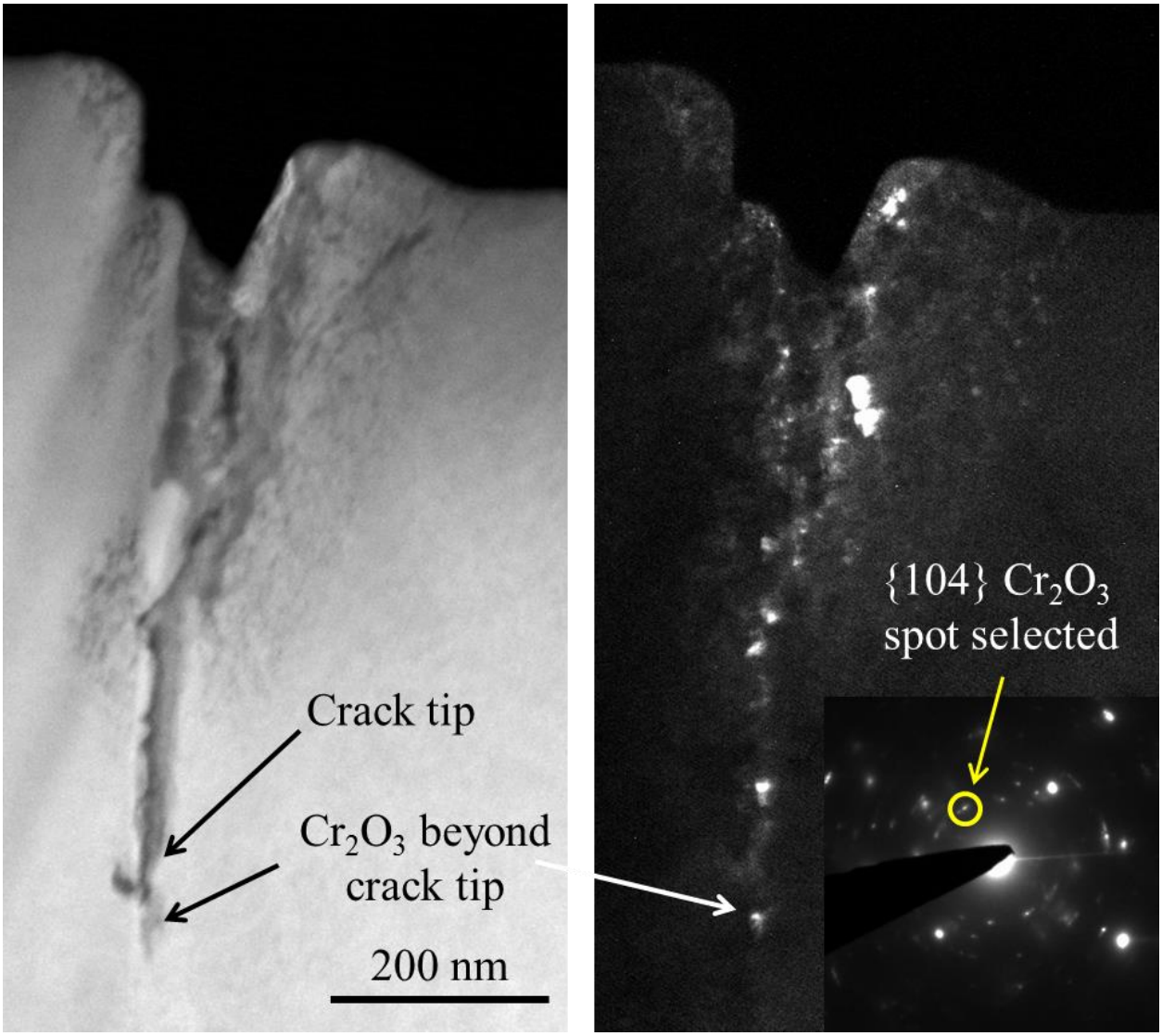

Figure 4.32. STEM dark field image (a), and selected area TEM dark field image (b) of the crack shown in Figure 4.30 (20% pre-strained Alloy 690 strained in hydrogenated subcritical water at 360°C to 7% at $5x10^{-8}$ s^{-1}) showing the presence of nanocrystaline Cr_2O_3 along crack walls and beyond the crack tip.

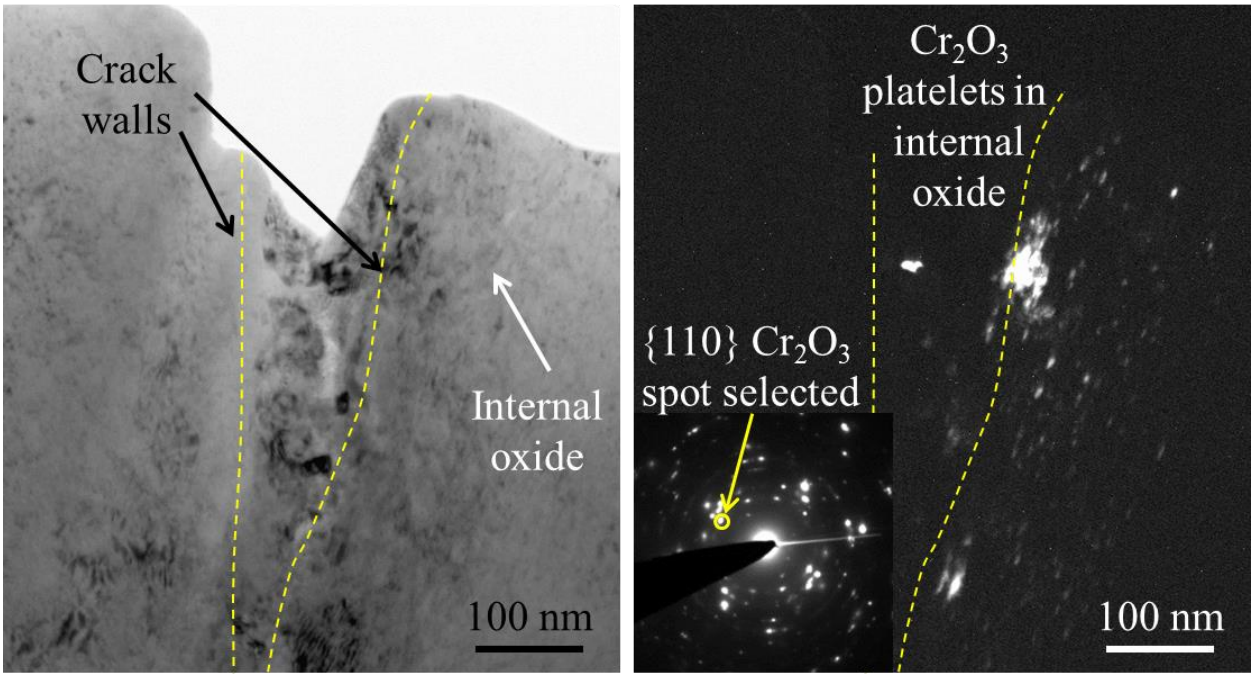

(a) (b)

Figure 4.33. Bright field image (a), and dark field image (b) of the crack shown in Figure 4.30 (20% pre-strained Alloy 690 strained in hydrogenated subcritical water at 360°C to 7% at $5x10^{-8}$ s^{-1}) showing the presence of Cr_2O_3 platelets in the internal oxide of the crack wall.

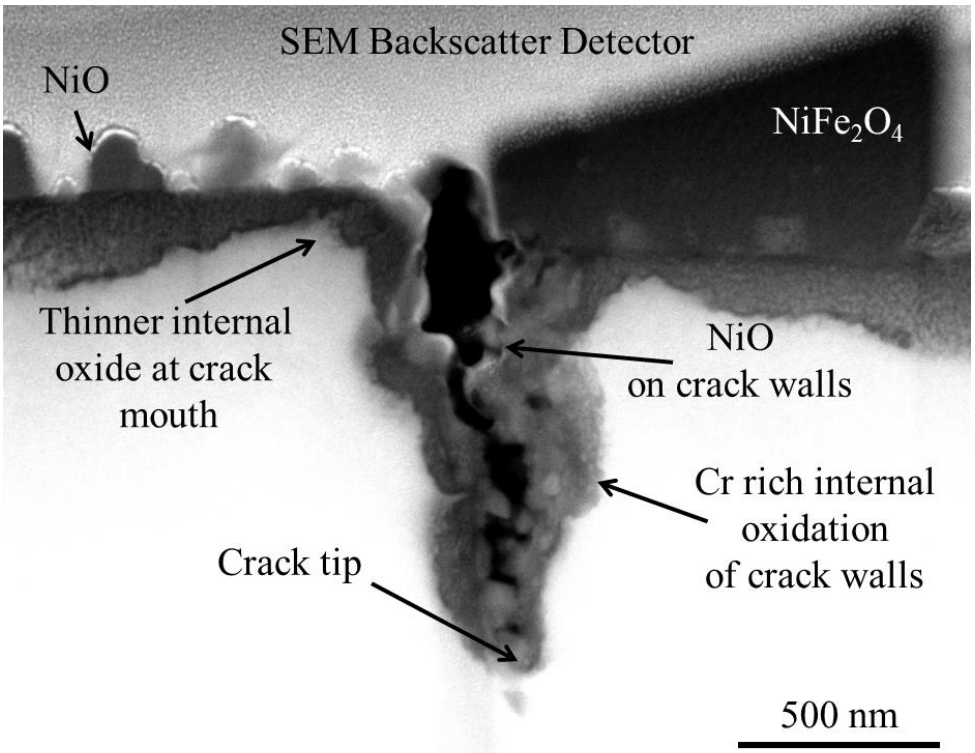

(a)

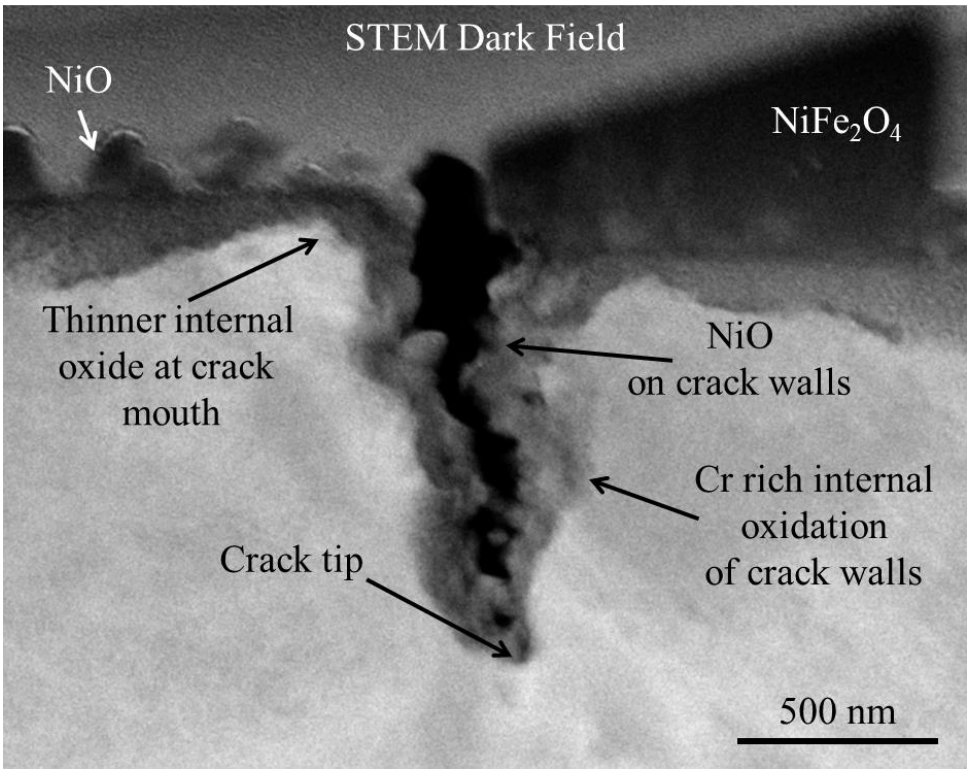

(b)

Figure 4.34. FIB lift-out of a crack in 20% pre-strained Alloy 690 strained in hydrogenated supercritical water at 400°C to 7% at $5x10^{-8}$ s^{-1} imaged by (a) 5 keV SEM backscattered electrons and (b) STEM dark field.

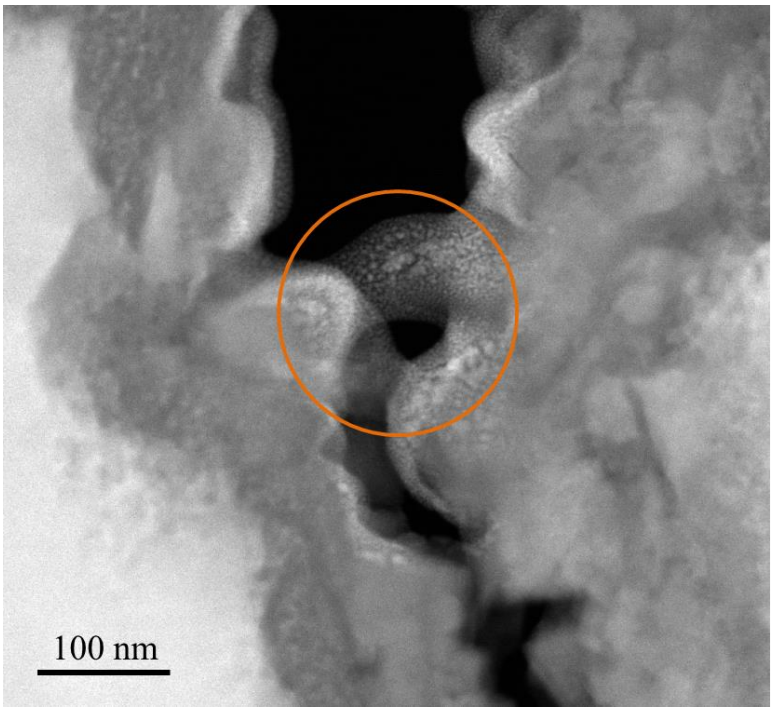

(a)

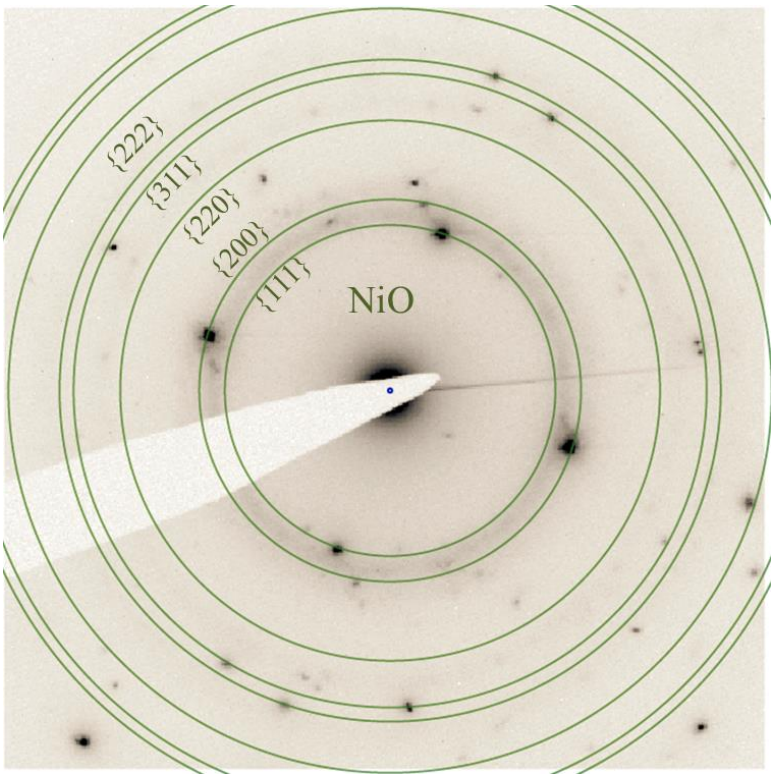

(b)

Figure 4.35. (a) Darkfield TEM and (b) selected area diffraction consistent with NiO from the crack walls of the same crack as in Figure 4.34 of Alloy 690 strained in hydrogenated supercritical water at 400°C to 7% at $5x10^{-8}$ s^{-1}.

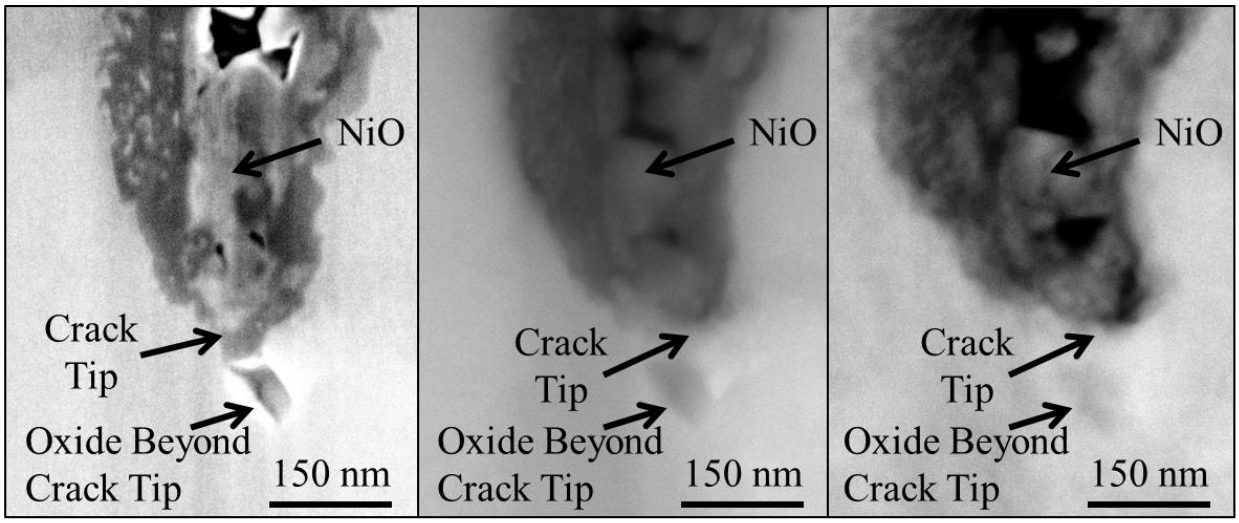

(a) (b) (c)

Figure 4.36. Crack tip of the same crack as in Figure 4.34 of Alloy 690 strained in hydrogenated supercritical water at 400°C to 7% at $5x10^{-8}$ s^{-1} imaged in SEM with (a) 5 keV secondary and (b) 5 keV backscattered electrons and (c) STEM dark field.

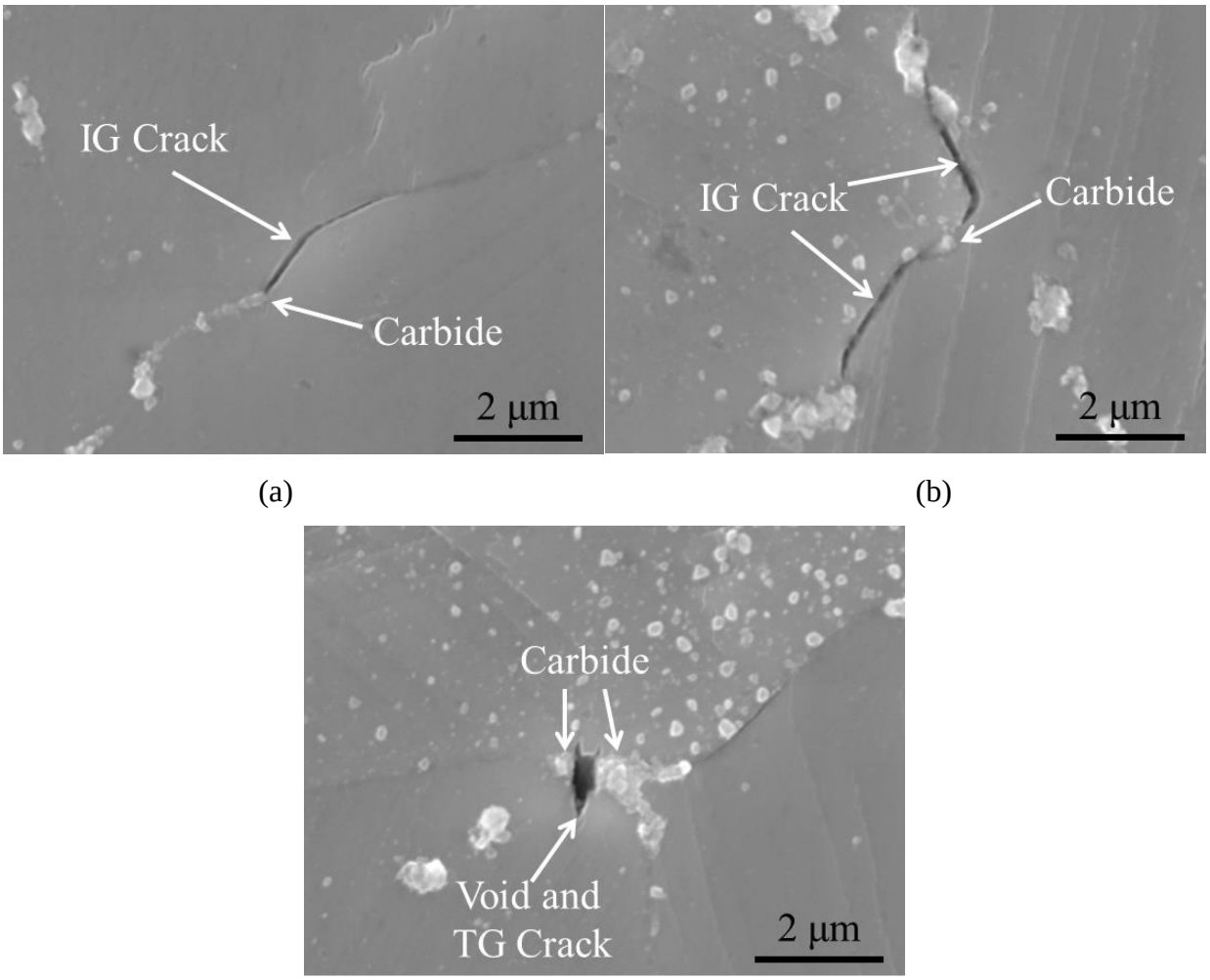

Figure 4.37. Gauge surface micrographs of 20% pre-strained Alloy 690 strained in hydrogenated subcritical water at 320°C to 7% at $5x10^{-8}$ s^{-1} showing (a, b) crack arrest at carbides and (c) short transgranular cracking from voids between carbides in SEM at 20 keV.

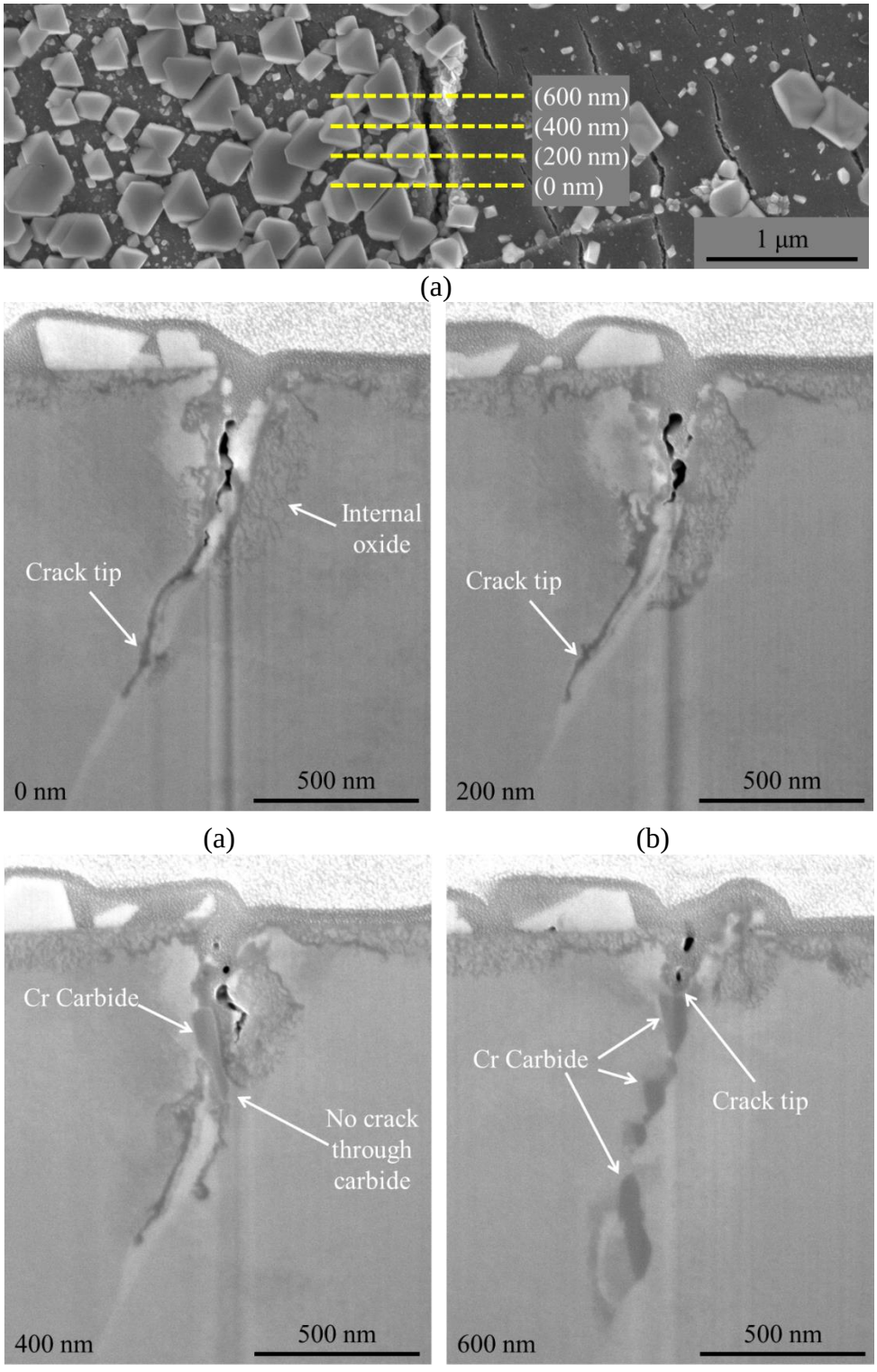

Figure 4.38. Serial sections of a crack imaged at 5 keV in 20% pre-strained Alloy 690 strained in hydrogenated subcritical water at 360°C to 7% at $5x10^{-8}$ s^{-1} showing shallower crack depths in the presence of carbides.

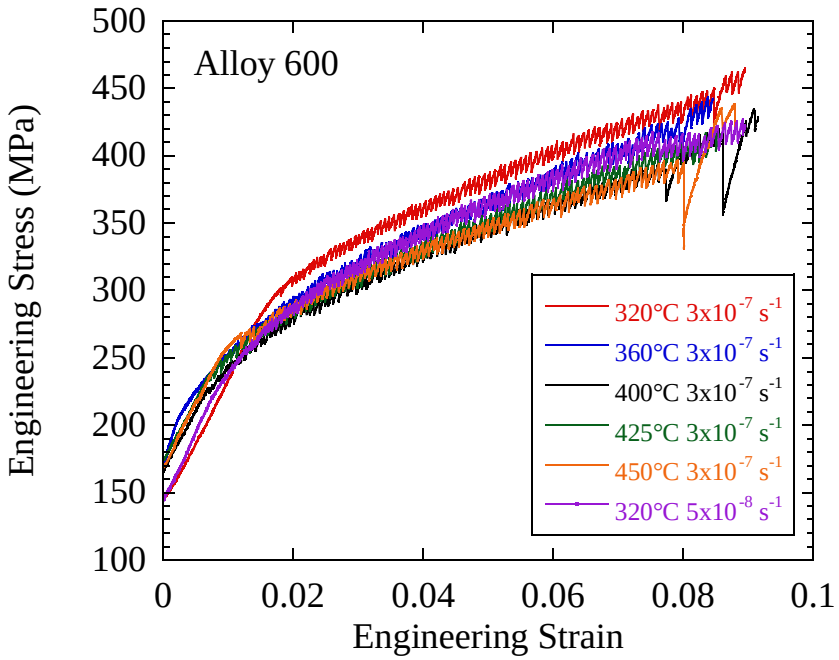

(a)

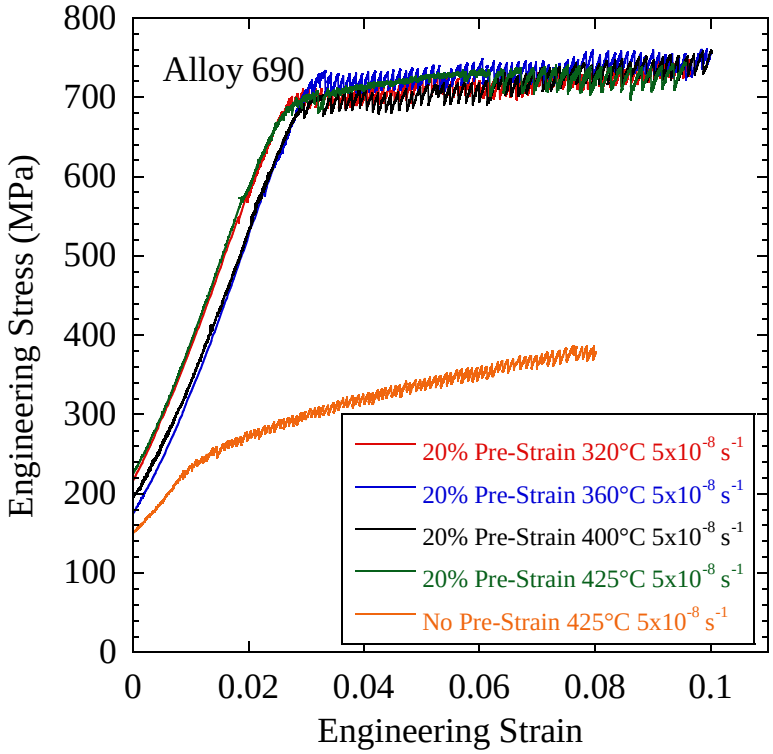

(b)

Figure 4.39. Representative engineering stress-strain curves for (a)Alloy 600 strained to 8% at and (b)Alloy 690 strained to 7% at $5x10^{-8}$ s^{-1}.

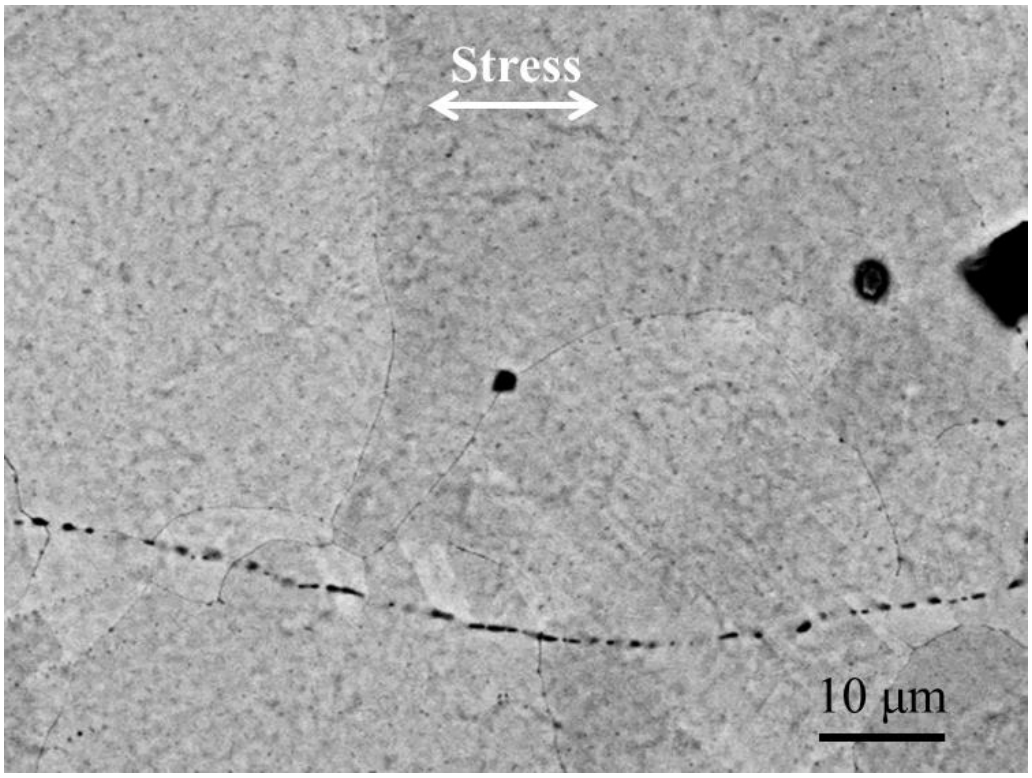

(a)

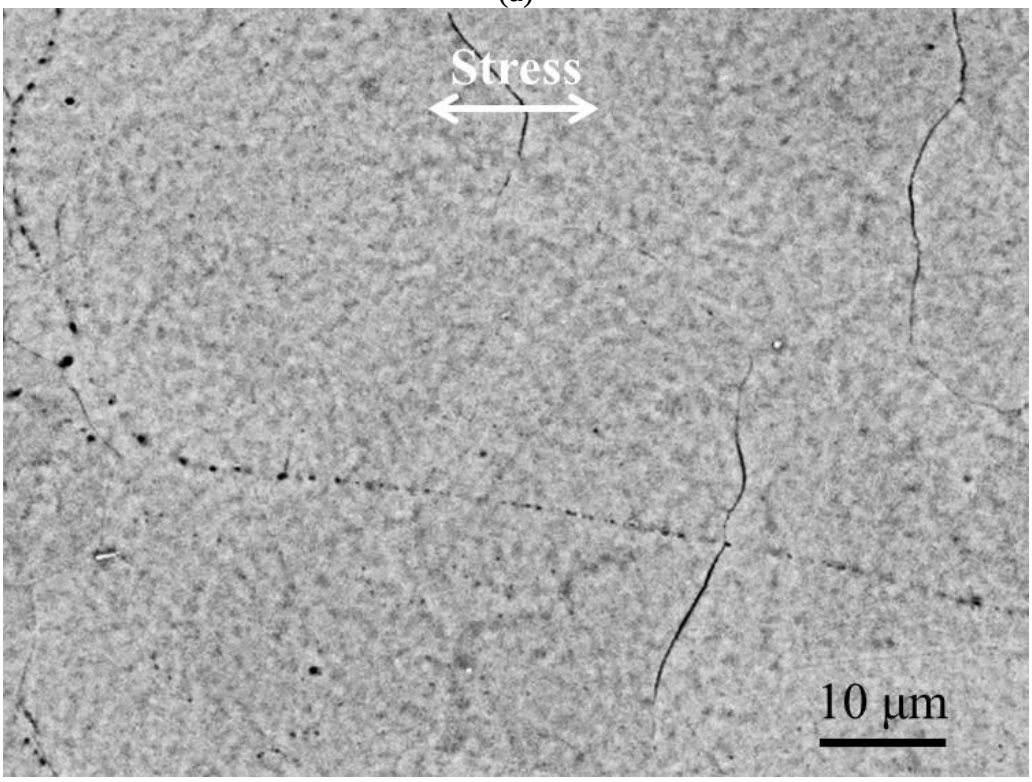

(b)

Figure 4.40. Micrographs of the gauge surfaces of Alloy 600 after CERT straining to 2% at (a)320°C and (b)425°C at $3x10^{-7}$ s^{-1} with the tensile axis oriented left to right imaged with 30 keV backscattered electrons.

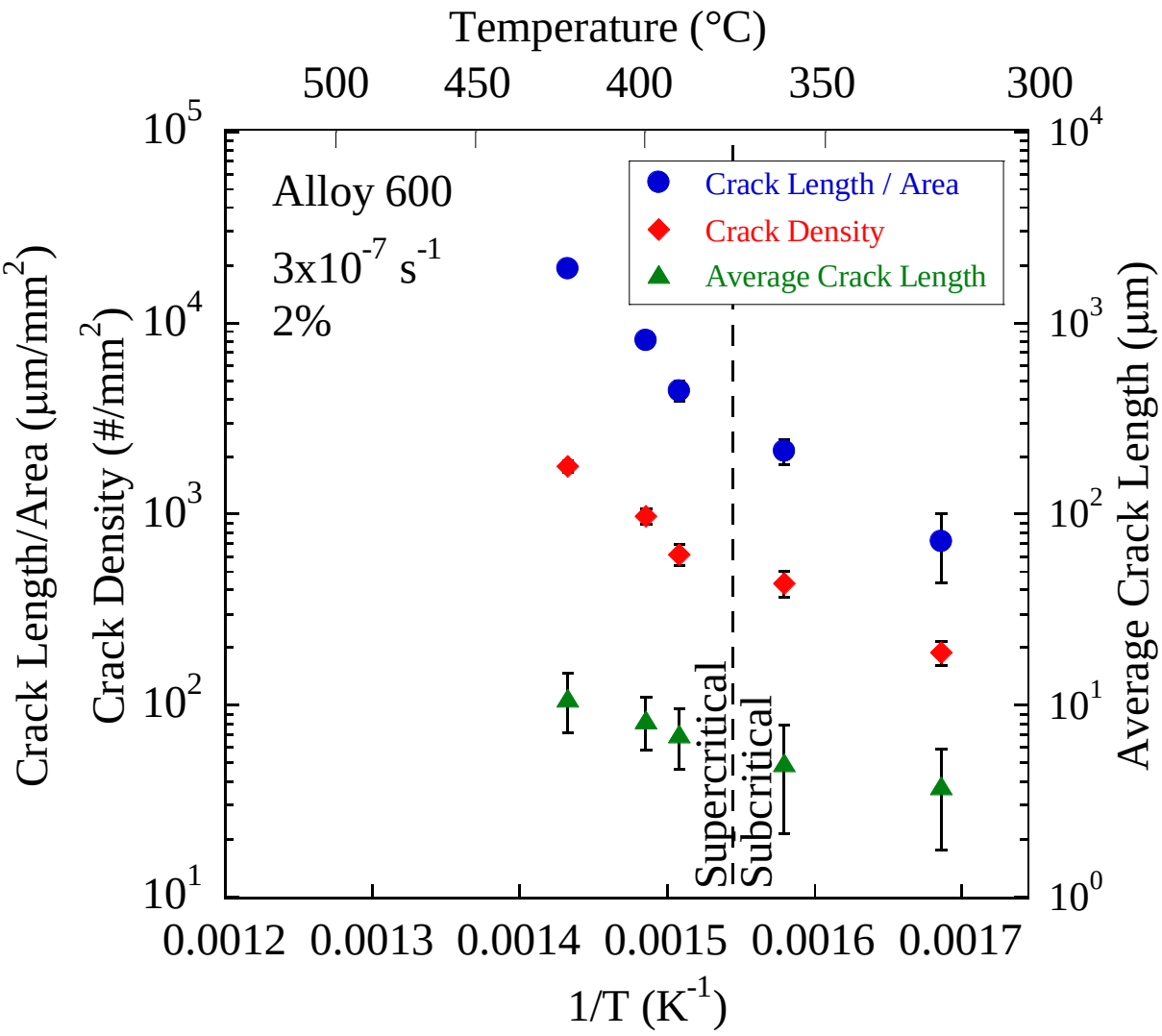

Figure 4.41. Cracking severity as a function of inverse temperature for Alloy 600 samples strained to 2% at a strain rate of $3x10^{-7}$ s^{-1}.

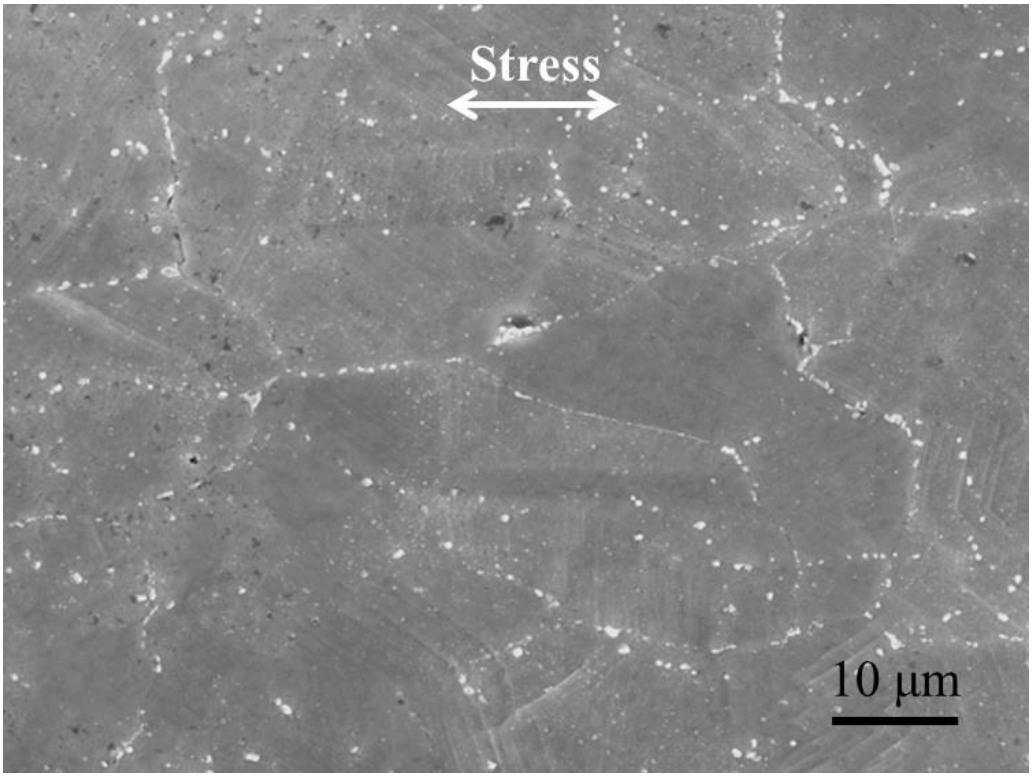

(a)

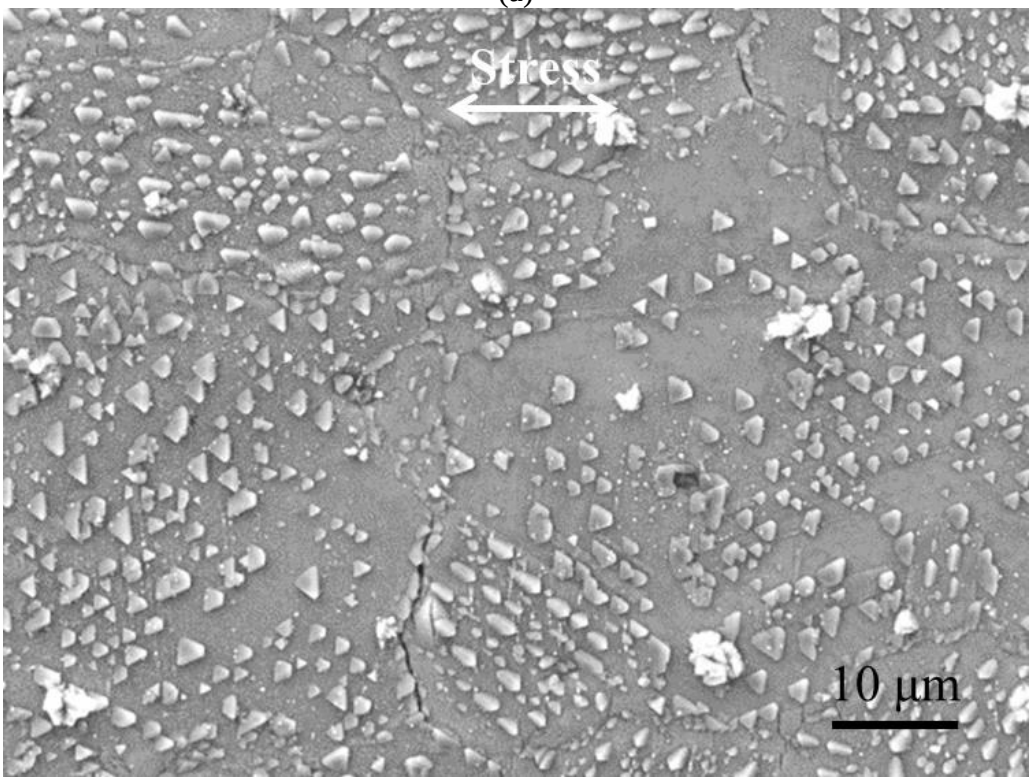

(b)

Figure 4.42. Micrographs of the gauge surfaces of 20% pre-strained Alloy 690 imaged with 20 keV secondary electrons after straining in CERT to 7% at $5x10^{-8}$ s^{-1} at (a)320°C and (b)450°C with the tensile axis oriented left to right.

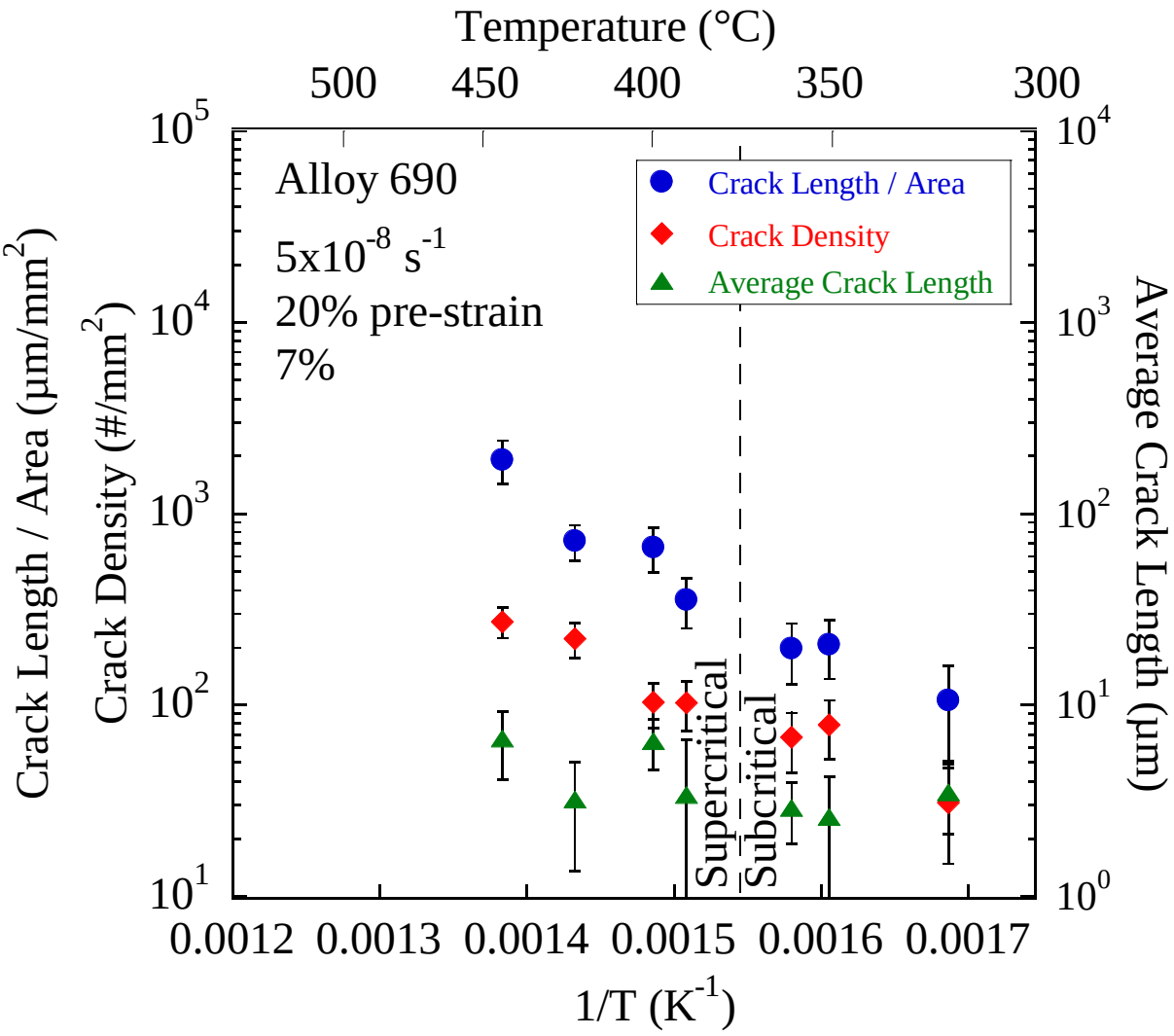

Figure 4.43. Cracking severity as a function of inverse temperature for Alloy 690 samples strained to 7% at a strain rate of $5x10^{-8}$ s^{-1} in hydrogenated subcritical and supercritical water.

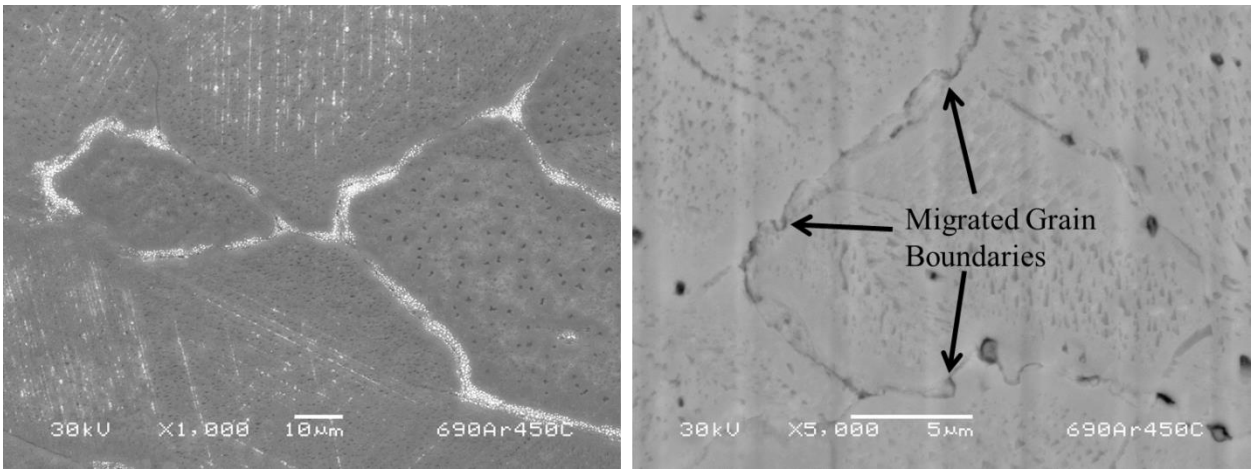

(a) (b)

Figure 4.44. Gauge surface of Alloy 690 strained in argon at 450°C to 7% at $5x10^{-8}$ s^{-1} showing (a) light oxidation and along grain boundaries and (b) grain boundary migration when imaged with backscattered electrons.

CHAPTER 5- DISCUSSION

5.1 Determination of Henry's constant and Ni/NiO phase transition

The exposure of nickel coupons to determine oxidation as a function of dissolved hydrogen concentration is summarized in Figure 4.1 for temperatures between 320°C to 450°C. The experimentally measured Ni/NiO transition in terms of dissolved hydrogen for each temperature is taken at the midpoint between the Ni stable sample with the lowest dissolved hydrogen concentration, and the NiO stable sample with the highest dissolved hydrogen concentration on a linear scale. Data from Attanasio and Morton[70] are also shown on the plot and are consistent with the observed oxidation behavior in subcritical water. The dissolved hydrogen is not a direct measure for the thermodynamic stability of nickel; instead the fugacity should exhibit a good correlation with the free energy for the oxidation of nickel in an ideal case. For a given fugacity the dissolved hydrogen concentration can vary due to changes in the solubility of hydrogen and the density of water. Knowing this, any trends in the measured oxidation of nickel in terms of dissolved hydrogen concentration cannot be fully interpreted without a further understanding of the hydrogen solubility in supercritical water.

The Henry's law constants from the measured fugacities are plotted as a function of temperature at 25MPa in Figure 5.1. The constants are plotted in solid red circles using the dissolved hydrogen concentration at 25°C. Error in the Henry's coefficient is due to error propagated from

the calculated dissolved hydrogen concentration. Also plotted are the measured Henry's law constants from work by Attanasio[70] and Kishima[16] at 25 MPa that agree with the constants measured in this study. The data from both sources were scaled to 25 MPa using the pressure relationship observed in Kishima's work. At temperatures up to 320°C, the Henry's constant decreases linearly until the critical temperature. In the temperature range of the supercritical water transition, the slope changes to become less temperature dependent. Note that beyond the critical temperature the Henry's constant approaches zero, indicating a high solubility of hydrogen.

The observed trends in the Henry's constant corresponds well with other water properties in this pressure and temperature range. Properties of water such as the molar volume, density, enthalpy, entropy, speed of sound, viscosity, and thermal conductivity have sharp behavior transitions at the critical point at low density, but not at high density [71]. The correlation to other water properties adds support to the sharp transition in the trend of Henry's constant observed near the critical temperature. This trend is also seen when comparing the measured values of Henry's constant in this study at 25 MPa to those of Kishima[16] at 62 MPa over the same temperature range as shown in Figure 5.2. There is a sharp transition during the phase change at 25 MPa. However, at higher pressure, there is not a sharp transition in the Henry's constant at the critical temperature. This dependence on pressure is also observed in the temperature dependence of the density of water at the same pressures. At 25 MPa the density decreases sharply at the critical temperature with an inflection point at 385°C. At 62 MPa, there is no sharp decrease in the density at the critical temperature.

The effect of vessel pressure on the Henry's law constant was measured at 385°C and 390°C as shown in Figure 5.3. The pressure dependence was measured between 24.1 to 25.2 MPa. Over this narrow pressure range, the dependence appears to be linear with the Henry's constant increasing with pressure. A larger deviation in the pressure dependence of the Henry's constant is expected as the temperature approaches the critical temperature. This is observed in the slopes of the pressure dependence at the two temperatures; there is greater pressure dependence at 385°C than at 390°C with slopes of 0.00074 and 0.00052 atm/[(cc/kg) MPa] respectively.

The fugacity of each exposure condition used to determine the stability of nickel is plotted in Figure 5.4. The fugacity was calculated by multiplying the average Henry's law constant (atm/(cc/kg)) by the dissolved hydrogen concentration (cc/kg), assuming a fugacity coefficient of unity. Also plotted is the fugacity of the phase transition measured by Attanasio [70] in subcritical water, denoted by the solid red curve. In subcritical water there is good agreement between the observed fugacity of hydrogen at the Ni/NiO transition and that of Attanasio. However, the trend into supercritical water displays more complicated behavior with a decrease in the fugacity at the SCW transition followed by an increase at a similar slope to that observed in subcritical water.

A thermodynamic model has been developed for the fugacity at the Ni/NiO transition from subcritical to supercritical water. This model is developed using the reaction of nickel with water as the basis for the reaction as follows:

$$\mathrm{Ni} + \mathrm{H_2O} = \mathrm{NiO} + \mathrm{H_2} \tag{5.1}$$

$$\Delta G^o(T) = \Delta H^o(T) - T\,\Delta S^o(T) = -RT\ln K_{eq} \tag{5.2}$$

where $\Delta G^o(T)$ is the standard Gibbs free energy, $\Delta H^o(T)$ and $\Delta S^o(T)$ are the enthalpy and entropy of formation for the phase transition, R is the universal gas constant, T is the temperature in Kelvin, and K_{eq} is the equilibrium constant for the reaction. The enthalpy and entropy can be calculated as a function of temperature by knowing the heat capacity of the reaction ($\Delta {C_p}^o(T)$) as follows:

$$\Delta H^o(T) = \Delta H^o_{298} + \int_{298}^{T} \Delta {C_p}^o(T) dT \tag{5.3}$$

$$\Delta S^o(T) = \Delta S^o_{298} + \int_{298}^{T} \frac{\Delta {C_p}^o(T)}{T} dT \tag{5.4}$$

$$\Delta {C_p}^o(T) = ({C_p}^{\mathrm{H_2}}(T) + {C_p}^{\mathrm{NiO}}(T)) - ({C_p}^{\mathrm{H_2O}}(T) + {C_p}^{\mathrm{Ni}}(T)) \tag{5.5}$$

where ${C_p}^i(T)$ is the heat capacity of species i as a function of temperature which is plotted in Figure 5.5. Heat capacities for hydrogen and water were taken from steam tables [71]. The heat capacity as a function of temperature for Ni was taken from work by Bronson et al.[72] from 100 to 500°C with data from Connelly et al.[73] for values near the Curie temperature. Values for the heat capacity for NiO were taken from work by Keem and Honig [74]. The equilibrium constant for the reaction is defined as follows:

$$K_{eq} = \frac{[\mathrm{NiO}][\mathrm{H_2}]}{[\mathrm{Ni}][\mathrm{H_2O}]} = \frac{f_{\mathrm{H_2}}}{\left(\frac{\rho_{\mathrm{H_2O}}}{\rho^o{}_{\mathrm{H_2O}}}\right)^k} \tag{5.6}$$

where brackets refer to the thermodynamic activities of the species involved, $f_{\mathrm{H_2}}$ is the fugacity of hydrogen in atmospheres, $\rho_{\mathrm{H_2O}}$ is the density of water, and k is the net change in the waters of solvation for the reaction. In most cases the activity of water is considered to be at unity, however, because of the transition from subcritical to supercritical a refinement is needed in the model. A pressure dependent equilibrium constant is suggested by Marshall [75] and is applied

with success by Ziemniak[76] to model the solubility of CuO in pure subcritical and supercritical water by assuming the activity of water is based more on the concentration than the fugacity. Taking the activity of water to be equal to the molar density ratio raised to the solvation of waters satisfies this condition. Substituting eqn (5.3), (5.4), and (5.6) into eqn (5.2) yields a relationship for the fugacity of hydrogen of the reaction as function of the thermodynamic properties and the density of water:

$$\ln f_{\mathrm{H_2}} = -\frac{\Delta H^o_{298}}{RT} + \frac{\Delta S^o_{298}}{R} - \frac{1}{RT}\int_{298}^{T} \Delta {C_p}^o(T)dT + \frac{1}{R}\int_{298}^{T} \frac{\Delta {C_p}^o(T)}{T}dT + k\ln\left(\frac{\rho_{\mathrm{H_2O}}}{{\rho^o}_{\mathrm{H_2O}}}\right). \quad (5.7)$$

The thermodynamic model is empirically fit to the measured fugacity of the Ni/NiO transition in Figure 5.6. The exposure conditions are plotted as $\ln(f_{\mathrm{H_2}})$ as a function of 1/T where NiO stable coupons are in solid black squares and Ni stable coupons are open black squares. Half-filled squares represent data for contact electrode resistance experiments conducted by Attanasio [70]. Regions of NiO and Ni stability are shaded, the unshaded region between represents the uncertainty in the location of the phase boundary. The fit to the data yields a ΔH^o_{298} of 48,119 J/mol, a ΔS^o_{298} of 65.6 J/mol K, and *k* of 0.488. These values are quite similar to those reported for the oxidation of nickel obtained from thermodynamic tables with a ΔH^o_{298} of 46,100 J/mol and a ΔS^o_{298} of 68.0 J/mol K [76]. The fit agrees very well with exposure data in subcritical water, but not as well in supercritical water. The decrease in the fugacity at the SCW transition and subsequent increase at higher temperature is captured by the thermodynamic model. However, the slope in supercritical water and the actual values for the fugacity do not match as well, suggesting additional corrections to the ideal thermodynamic model may be needed.

In conclusion, the location of the Ni/NiO phase boundary was experimentally determined in terms of the dissolved hydrogen concentration and hydrogen fugacity in subcritical and supercritical water. There is good agreement between the measurements in subcritical water. The Henry's law constant of hydrogen in water was calculated by in situ measurements between 320 and 450°C at 25 MPa. The Measurements show excellent repeatability and validate the use of Henry's law in this concentration range. A Thermodynamic model was developed to describe the fugacity of hydrogen at the Ni/NiO boundary as a function of temperature. Good agreement was found with thermodynamic data for the oxidation of nickel. The model captures what originally appeared to be anomalies in the measure fugacity at the phase transition and suggests that the activity of water plays an important role in the oxidation.

5.2 Corrosion of Alloy 600 and Alloy 690 across the subcritical-supercritical transition

The objective of this section is to determine whether the oxidation behavior of Alloys 600 and 690 is continuous across the subcritical/supercritical water transition, implying a consistent mechanism. Oxidation occurs by a sequence of reactions and is often characterized by the rate limiting step of the process. A reaction can have the same products but the path in which those products are created may be different, indicating a different mechanism is operating. For example, gaseous oxidation of pure nickel occurs by oxygen diffusion through the lattice to form NiO at high temperatures, but by pipe diffusion along dislocations at low temperatures[77]. In that case the change in mechanism is associated with a change in the activation energy and the morphology of oxide observed. Part of the challenge with the objective is that the mechanisms of oxidation for both alloys in PWR primary water are not well established. This makes

demonstrating whether there is a change in the mechanism dependent on correlating observations of the oxide character between subcritical and supercritical water. The oxide character was established by characterizing the oxide morphology, crystal structure of oxides, and the compositions of oxides.

The morphology of oxides in each water regime appears to be consistent for both alloys. In both environments, Alloy 600 and Alloy 690 form bi-layer oxides composed of surface oxide particles and a continuous inner oxide layer. In both environments the oxide particles have the same morphology, relative size, and Z contrast observed in SEM. Pitting of TiN particles is also observed for both alloys in both environments, and is especially apparent after the 500 hr exposure. In both environments, Alloy 600 forms a continuous oxide layer with thickness dependent on grain orientation, and grain boundaries are preferentially oxidized (Figure 4.8a,c,e). Furthermore, the morphology of oxides observed on Alloy 600 in both environments agree well with other investigations of oxidation of Alloy 600 in PWR primary water[24,27,30,31,35]. It should be noted that the depth of grain boundary oxidation for time-temperature equivalent samples of Alloy 600 decreases with temperature, suggesting that the activation energy for grain boundary oxidation is less than 180 kJ/mol. While measuring an activation energy of 125 kJ/mol for overall oxidation, Morton[31] measured a lower activation energy of 66±17 kJ/mol for the growth of the chromium rich surface oxide and suggested that the chromium rich layer growth may be controlled by oxygen ingress.

The morphology of oxides on Alloy 690 is consistent between exposures in subcritical and supercritical water and is illustrated in the Figure 5.7 schematic. A thin continuous surface oxide

is observed in both environments with sub-surface intragranular internal oxidation (Figure 4.12). In close proximity to grain boundaries, the internal oxide is thinner with only a raised continuous surface oxide observed above grain boundaries (Figure 4.8b,d,f) with corresponding chromium deletion in the subsurface in the migrated grain boundary (Figure 4.10). The bi-layer oxide structure observed in this work for both water environments is consistent with observations from the literature[23–26,32,33]. There is some variation in the morphologies observed within the literature. However if the surface preparation condition is taken into consideration, most of the discrepancies can be accounted for. Electropolished and vibratory polished samples exposed to PWR primary water all show a thin continuous surface oxide enriched in chromium with Cr_2O_3 at the metal-oxide interface and no observed chromium depletion in the metal. Recent exposures and high resolution SEM investigations of Alloy 690 and model alloy Ni-30Cr conducted by Olsza et al.[25,26] show markedly similar morphologies to this work.

The observation of intragranular internal oxidation was unexpected in Alloy 690 where it is commonly thought a continuous protective Cr_2O_3 layer forms in less than one sec.[30]. However there is precedence for internal oxidation of Alloy 690 and Ni-Cr alloys in water and gaseous environments with the potential fixed at the Ni-NiO boundary. The previously mentioned exposures in PWR primary water by Olsza showed evidence of internal oxidation, as did high temperature gas exposure of Ni-Cr alloys by Wood et al.[39] between 800°C and 1100°C in Ni-NiO Rhines packs. One interesting observation was that when the pack material was not in contact with the sample surface there was more extensive internal oxidation observed. Wood et al.[39] attributed this behavior to formation of fast growing NiO on the surface that was able to surmount, overgrow, and undercut slow growing Cr_2O_3 nuclei, suppressing initial lateral development of a protective Cr_2O_3 surface layer. This is likely the case for Alloy 690 exposures

in subcritical and supercritical water observed in this work. However, it appears that the internal oxidation is a transient state at these low temperatures in water, where eventual passivation of the surface is observed and internal oxide growth is halted after 500 hr of exposure at 360°C as shown in Figure 4.23. Wood et al.[39] also observed in low temperature exposures that there was no internal oxide formed around grain boundaries, where fast chromium diffusion to the surface resulted in a relatively substantial protective oxide layer. Our observations of Cr_2O_3 above grain boundaries in Alloy 690, thinning of the internal oxide layer at the intersection between grain boundary and surface, and chromium depletion in the sub surface boundary support the formation of a fast growing protective Cr_2O_3 layer above grain boundaries supplied by enhanced diffusion of chromium along the grain boundary.

The structure of oxides corresponds with the observed morphologies and is consistent between subcritical and supercritical water. XRD results are inconclusive as there are missing peaks for phases that are observed with SEM, such as the sparse, faceted spinel particles on Alloy 600, due to the limitations of the brightness of the X-ray source. However XRD is able to give some measure of the abundance of a phase. For example, spinel peaks are observed for Alloy 690 at higher temperatures where the density of surface spinel oxide particles is greater (Figure 4.13b). TEM analysis of oxides on Alloy 690 reveals that there is no change in the structure of oxides observed between subcritical and supercritical water. Selected area diffraction determined that the internal oxide is composed of platelets of Cr_2O_3 with a continuous, oriented surface oxide consisting of MO structured oxide. The same morphology of Cr_2O_3 is also observed in backscatter imaging of the surface (Figure 4.7b).

The composition of oxides corresponds well with the observed structures and morphologies. The composition of oxides measured in SAM is consistent between subcritical and supercritical water. However, all of the oxides are oxygen deficient. The deficiency in oxygen is likely due to the argon sputtering performed during the analysis. In previous studies using X-ray photoelectron spectroscopy, reduction of oxides has been observed by the presence of metallic nickel peaks during the initial sputtering of the surface with argon[78,79]. Because SAM was not used to collect valence information in this study it cannot be confirmed that reduction occurred.

The composition of the material caused dramatic changes in contrast observed when imaging with the through lens detector after FIB milling of the cross section samples, as shown in Figure 4.8d. NiO particles appeared bright, Cr rich internal oxide appeared dark, and the base metal was grey. This change in contrast corresponds well with the atomic mass of the metal constituent of the material, lighter elements had darker contrast. However, typically when imaging in back scatter mode and in STEM the oxygen in the oxide particles causes a much darker contrast, the oxygen presence dominates the change in contrast. This is expected, given that the average atomic mass of the oxide particles is much lighter than the base metal due to the presence of oxygen. However when imaging with the through lens detector, the NiO particle is behaving as if it has a *higher* average atomic mass than the base metal, which is not the case. One possible explanation is the mechanism reviewed by El-Gomati et al.[80] where contrast changes can occur because of metal-semiconductor surface contacts. The model supports their observations of changing contrast between p doped and n doped sections of semiconductors where they postulate that a thin metallic carbon layer is present on the surface. The junction between the metallic carbon and the semiconductor is able to change the surface polarity, varying with the band gap of

the semiconductor substrate. A similar phenomena may be occurring with the oxide particles in the FIB cross sections. The oxides act as semiconductors, and a thin layer of carbon is deposited when imaging the material in SEM. The various oxides have different band gaps, which may explain the difference in contrast between the oxides. The base metal may also show this effect somewhat due to a native oxide formed on the freshly milled surface in the SEM. Nevertheless, the contrast effect is consistent with concentration when viewed with the through lens detector across all observed samples and conventional backscatter shows the expected contrast.

The oxidation rate was measured by weight gain of samples and by measuring the depth of internal oxidation. Weight gain measurements of Alloy 690 show non-parabolic oxide growth with slight decreases in weight gain potentially indicating spallation or pitting of secondary phases. In aerated SCW conditions, Zhong et al.[79] observed decreases in weight gain and non-parabolic growth of Alloy 690, which they attributed to pitting of TiN particles which was also observed in this study. Measurements of the internal oxide depth on Alloy 690 in subcritical water are more conclusive, showing initial linear oxide growth that then appears to halt after 500 hr. The linear oxidation rate and high weight gain in the first 500 hr suggests that a protective layer was not formed initially, allowing internal oxidation. The halt in internal oxide growth coincides with observation of a coherent surface film MO structured oxide, which appears to be protective and coarsens after 500 hours at 360°C (Figure 4.24).

In conclusion, the mechanisms for oxidation of Alloy 600 and Alloy 690 are consistent between hydrogenated subcritical and supercritical water. The observed morphology, structure, and composition of oxides is consistent across the critical temperature. Oxidation of both alloys

results in a multi-layer oxide structure composed of particles of NiO and $NiFe_2O_4$ formed by precipitation on the outer surface, and a chromium rich inner oxide layer formed by diffusion of oxygen to the metal-oxide interface. The continuous oxide on Alloy 690 is more chromium rich than that observed on Alloy 600 and is composed of oriented MO with chromium and iron contents similar to that of the metal matrix. The inner oxide on Alloy 690 initially forms my internal oxidation before a protective layer of chromium rich MO is formed with Cr_2O_3 at the metal-oxide interface. Grain boundaries in Alloy 690 act as fast diffusion paths for chromium to form a protective Cr_2O_3 layer at the surface, preventing internal oxidation from occurring close to the boundary.

5.3 SCC initiation of Alloy 690 across the subcritical-supercritical transition

The objective of this section is to develop a mechanistic understanding of the stress corrosion crack initiation behavior Alloy 690 in hydrogenated subcritical and supercritical water. The proposed mechanism for initiation of stress corrosion cracks in Alloy 690 consists of three stages: 1) an oxidation stage in which a protective film of Cr_2O_3 is formed on the surface over the grain boundaries, 2) an incubation stage in which successive cycles of oxide film rupture and repair depletes the grain boundary of chromium, and 3) a nucleation stage in which the chromium depleted grain boundary is no longer able to support formation of a protective layer, exposing the grain boundary to the water environment and subsequent formation and rupture of oxides down the grain boundary. The following sections outline how each stage of the mechanism is supported by the oxidation and crack initiation morphology observed in this work

as well as observations from the literature. The morphology of initiated cracks and the effect of chromium carbides on cracking are discussed in both water environments.

5.3.1 Localized Oxidation

Oxidation proceeds first by formation of a protective Cr_2O_3 layer on the surface above the grain boundary. Chromium is supplied by diffusion along the grain boundary causing chromium depletion in the matrix adjacent to the boundary. Grain boundary migration accompanies chromium depletion. Away from the grain boundary region, the surface is unable to form a protective oxide layer, leading to internal oxidation. This internal oxidation region is much thinner at the grain boundary since the boundary is able to supply Cr to support formation of an oxide above it. Figure 5.8a shows a schematic of a high angle grain boundary in Alloy 690 prior to exposure to water. A short time after exposure, a protective Cr_2O_3 layer is formed on the surface above the grain boundary as shown in Figure 5.8b. Grain boundary migration and formation of Cr_2O_3 above grain boundaries has been observed on unstressed corrosion coupons of Alloy 690 with low surface damage. Olszta et al.[25] used a combination of TEM and atom probe tomography to show that the surface grain boundary oxide was composed of Cr_2O_3 on coupons of Alloy 600 exposed to PWR primary water. They also observed sub-surface grain boundary migration with the migrated area depleted of chromium to 7 at% a distance 50 nm from the surface, and to 18% a distance 200nm from the surface after exposure to PWR primary water at 360°C. Grain boundary migration and chromium depletion was also observed in the migrated region to 20 at% a distance of 200nm below the surface in this work (Figure 4.11). The inability to form a protective oxide layer away from the grain boundary region leads to internal oxidation as shown schematically in Figure 5.8c. Internal oxidation of Alloy 690 has been observed on

corrosion coupons and on crack walls in crack growth experiments conducted in PWR primary water. Olszta et al.[81] characterized the internal oxide layer as consisting of discrete Cr_2O_3 platelets like that in Figure 4.7, Figure 4.18, and Figure 4.33 surrounded by nanocrystaline MO. Both Olszta et al.[25] and this work (Figure 4.7, Figure 4.8, Figure 5.7) found that the internal oxidation zone thinned at the grain boundary on unstressed samples of Alloy 690.

5.3.2 Crack Incubation

Due to its brittle nature, the Cr_2O_3 layer ruptures during straining and the surface re-passivates by further diffusion of chromium along the grain boundary. Successive increments of strain further rupture the oxide layer, which then passivates by more chromium diffusion to the surface. If a constant load is applied before oxidizing the sample, the subsequently formed oxide above the grain boundary is under negligible stress. If a constant load is applied once an oxide layer is formed, it can cause rupture of the oxide layer, which is then passivated with a stress free oxide. This behavior explains why crack initiation is observed in CERT experiments and not in constant load testing conducted for over as much as 10 years[50–52]. The absence of crack initiation in samples subjected to a constant load is evidence of the repassivation behavior shown schematically in Figure 5.8d-f.

5.3.3 Crack Nucleation

After repeated cycles of oxide fracture followed by repair, the grain boundary becomes further depleted in chromium and migrates further form its original position. At some point the grain boundary region is no longer able to supply enough chromium to form a protective surface film, exposing the grain boundary to the water environment, resulting in grain boundary oxidation and

subsequent crack nucleation by fracture along the oxide-metal interface, shown schematically in Figure 5.8g-i. While extensive grain boundary oxidation of Alloy 690 has not been measured like it has for Alloy 600, the observation of Cr_2O_3 in grain boundaries ahead of the crack tip, and grain boundary oxidation of what appeared to be intact grain boundaries support the possibility. Grain boundary oxidation of Alloy 690 was observed following straining in both subcritical and supercritical water environments (Figure 4.27) along uncracked grain boundaries. Grain boundary oxidation was *not* observed in unstressed corrosion coupons of Alloy 690 (Figure 4.8) as the surface was able to maintain a protective film above grain boundaries. Fujii et al.[82] performed micro tensile tests on individual oxidized grain boundaries of Alloy 600 and found that the stress required to cause fracture of the grain boundary was as low as 180 MPa, whereas unoxidized grain boundaries did not fracture at 1000 MPa. Fracture occurred along the oxide-metal interface, and not through the oxide itself. The crack tip morphology of initiated cracks in this study shows that the crack propagates along the grain boundary instead of through the chromium depleted region (Figure 4.28), suggesting that active transport of oxygen along the grain boundary is required for crack propagation. The role of grain boundary migration on surface passivation by Cr_2O_3 is not known. If grain boundary migration is the source for chromium diffusion from the bulk to reach the surface by way of the grain boundary, there should be no breakdown in the passivation of the surface as long as there is room for the grain boundary to migrate. However, the grain boundary migration may be simply a *consequence* of chromium diffusion in the grain boundary from further into the sample. If this is the case, passivation could break down after the grain boundary is depleted to a critical depth where Cr_2O_3 can no longer be formed quickly enough to prevent grain boundary oxidation.

5.3.4 Crack initiation in subcritical and supercritical water

The crack morphology of intergranular stress corrosion crack initiation in Alloy 690 is consistent between subcritical and supercritical water as shown schematically in Figure 5.9. In both environments thinning of the internal oxide layer is observed at the crack mouth. Internal oxidation is observed on crack walls but is absent at the crack tip, suggesting that there is no direct water access and that internal oxidation is not directly involved in the crack nucleation process. In both environments, cracks are filled with NiO, and Cr_2O_3 is observed beyond the crack tip. Because the cracks are filled with oxide, the location of the crack tip is defined by the end of the internal oxidation zone and the end of the NiO that fills the crack. High resolution TEM examination of cracks grown in crack growth rate experiments on Alloys 600 and 690 have shown that NiO fills cracks and grows on crack walls[35,36,46]. Sennour et al.[35] observed the formation of Cr_2O_3 beyond the primary and secondary crack tips of Alloy 600, with greater depth of penetration observed on secondary cracks. A complication with CERT tests is that the stress state of the crack is unknown and it is not possible to determine whether a crack was growing or had arrested at the time the experiment was terminated. Therefore, it is possible that the analyzed cracks had arrested and the oxidation beyond the crack tip is not representative of an actively growing crack. However, the observation of Cr_2O_3 beyond the crack tip suggests that it is involved in crack propagation at some stage.

Intergranular $M_{23}C_6$ chromium carbides have been found to arrest crack growth on the gage surface. The crack depth is shallower when carbides are present as shown in Figure 4.37 and Figure 4.38. Bruemmer et al.[46] observed similar behavior in examinations of cracks grown in crack growth rate experiments on Alloy 690 where intergranular cracks often appeared to blunt

at cracked carbides. Carbides can potentially act to mechanically stabilize the grain boundary by acting as pinning points for dislocations[35] is supported by observation of intact carbides bridging open cracks in Figure 4.38c. Carbides could also act as preferential oxidation sites, preventing further metal oxidation is supported by the observation of oxygen along carbides beyond the blunted crack tip of Alloy 690 in Figure 4.29. Before cracks nucleate, intergranular chromium carbides could also act as chromium sources for the passivation of grain boundaries by supporting the formation of Cr_2O_3 on the surface, as observed for unstressed coupons (Figure 4.8, Figure 4.17)[25].

The proposed crack initiation mechanism is reliant on a dynamic strain to cause initiation of cracks on Alloy 690, which does not typically occur in an operating plant suggesting that crack initiation is unlikely to occur of Alloy 690 in an operating condition. Recent work by Bruemmer et al.[83] supports this by their observations during constant load testing with bursts of dynamic strain on Alloy 690. A sample of 31% cold rolled Alloy 690 was instrumented with DCPD potential drop leads to measure crack initiation in situ and subjected to a constant load in PWR primary water conditions. To accelerate the crack initiation, the load on the sample was periodically increased. Over the course of the experiment, the stress on the 31% cold rolled sample was increased to 810 MPa without any signs of initiation detected from the DCPD signal. After 9600 hours of exposure, the load was increased to 905 MPA which caused yielding (0.5% strain) of the sample. Shortly after, initiation was detected in the DCPD signal and the fracture surface showed pockets of intergranular cracking. Another set of experiments was conducted on blunt notch CT specimens using low frequency cyclic loading to initiate cracking. The samples were loaded from 27.5 to 44 MPa$\sqrt{m}$ over 200 hours, and then held at the higher load for another

200 hours repeatedly. After three cycles of this loading pattern, the sample appeared to show fast crack growth, suggesting that cracks initiated then grew to a stable crack growth condition. Investigation of the blunt notch after testing showed evidence of intergranular cracking on the surface. No crack initiation was observed in any samples of Alloy 690 without additional plastic strain occurring during the test, consistent with the proposed mechanism of crack initiation. Even though the conditions of the experiments conducted in this work are unlikely to occur in a nuclear reactor, setting the bound of safe operation of components to within the elastic regime.

An additional verification of the mechanism is its observed dependence on temperature. The crack density of Alloy 690 increases with temperature, as does the amount of oxidation. This behavior is supported by the proposed model. As the temperature is increased the rate of oxidation and diffusion also increases. The faster oxidation would lead to faster repassivation of the surface by growth of a Cr_2O_3 layer and faster depletion of the grain boundary of chromium. A higher rate of oxidation of the surface can also inject more vacancies into the matrix and grain boundary, further enhancing the chromium diffusion and depletion. For a given strain, the grain boundaries at a higher temperature would be more chromium depleted than the grain boundaries at lower temperature. The more severe chromium depletion would lead to a high susceptibility to crack initiation at higher temperatures. Another effect of the increase in temperature is possibly activating a creep process. No crack initiation was observed for samples of Alloy 600 and Alloy 690 strained in 450°C argon as described in Section 4.4, where the contribution of creep cracking would have been most severe. The lack of cracking in an inert high temperature environment, especially for a material as susceptible as Alloy 600, suggests that creep is not a controlling mechanism for crack initiation in the temperature ranged use in this study. Assuming a high

creep rate for Alloy 690 as suggested by Boursier et al.[84] of 10^{-10} s^{-1}, the samples strained in this study would have experienced approximately 0.03% strain due to creep over the course of a 700 hour experiment, which is negligible. However, even if moderately low rates creep were occurring, the model of crack initiation should be unaffected. There is little information about creep of commercial Alloy 690 at an operating temperature range, but the mechanism would likely be dominated by dislocation climb and glide instead of by point defect migration along grain boundaries. The dislocation climb and glides produces deformation that is not drastically different than the strain observed during CERT testing, suggesting that the proposed crack initiation mechanism would still operate. This would not be the case at higher temperatures where void nucleation due to diffusion creep (Nabarro-Herring or Coble) would be the driving force for cracking, but since diffusion creep is primarily limited to high homologous temperatures it is not expected to occur over the temperature range tested.

In conclusion, a SCC initiation mechanism was developed for Alloy 690 that produces the observed cracks of consistent morphology between subcritical and supercritical water. The mechanism is composed of three stages: 1) an oxidation stage in which a protective film of Cr_2O_3 is formed on the surface above grain boundaries, 2) an incubation stage in which successive cycles of oxide film rupture and repair depletes the grain boundary of chromium, and 3) a nucleation stage in which the chromium depleted grain boundary is no long able to form a protective film, exposing the grain boundary to the water environment and subsequent formation and rupture of oxides down the grain boundary. Cracks were observed to propagate along the grain boundary and not in the chromium depleted region, which is not susceptible to internal

oxidation. Oxides (Cr_2O_3) are observed ahead of crack tips. Surface crack growth and crack growth into the sample is hindered by chromium carbides.

5.4 Accelerated SCC initiation of Alloy 600 and Alloy 690 in supercritical water

The objective of this section is to determine whether the stress corrosion crack initiation behavior of Alloys 600 and 690 is continuous across the subcritical/supercritical water transition, implying a consistent mechanism. This is done by establishing that all the features that bear on and result from SCC initiation do not undergo abrupt transitions when traversing the critical point. The first part and second part of this section will focus on discussion of the results presented in Section 4.4. The last part will combine what is known about the corrosion and crack initiation behavior from Sections 5.2 and 5.3 and will establish that stress corrosion crack initiation in subcritical and supercritical water is occurring by the same mechanism.

5.4.1 Activation energy of crack initiation

Laboratory testing has shown that stress corrosion crack initiation follows an Arrhenius relationship with the mechanism of initiation defined by a single activation energy[13,60] which can be described as:

$$L_A = A\, e^{-Q/RT} \tag{5.8}$$

where L_A is the crack length per unit area, A is pre-exponential factor, and Q is the activation energy for crack initiation in CERT testing. The crack length per unit area as a function of 1/T is shown for Alloy 600 in Figure 5.10. There is good agreement between the activation energies measured for samples strained to 8% in subcritical water (123±16 kJ/mol) and samples strained

to 2% over the entire temperature range (121±13 kJ/mol). There is no discontinuity or change in slope across the supercritical - subcritical transition, suggesting a consistent mechanism for crack initiation of Alloy 600. The measured activation energy also agrees well with literature data for the crack initiation of Alloy 600 in constant load experiments where the hydrogen was controlled at the Ni/NiO phase boundary. Richey et al.[43] tested solution annealed Alloy 600 in constant load using in situ direct current potential drop to detect crack initiation and found the activation energy to be ~140±25 kJ/mol. Etien et al.[41] used the same method on high temperature annealed Alloy 600 and found an activation of 103±18 kJ/mol. The values in this work fall between those by Richey and Etien.

The crack length per unit area as a function of 1/T is plotted for Alloy 690 in Figure 5.11. Pre-strained Alloy 690 that was strained to 7% at $5x10^{-8}$ s^{-1} is shown in solid blue circles with a measured activation energy of 92±12 kJ/mol. There is no discontinuity or change in slope observed at the critical temperature and the trend is fit well with an Arrhenius relationship with low error, suggesting a consistent mechanism for crack initiation in subcritical and supercritical regimes. Crack initiation data from Teysseyre and Was[53] is also plotted in Figure 5.11 as purple diamonds for samples of Alloy 690 strained to failure in deaerated water at $3x10^{-7}$ s^{-1} with an activation energy of 87 kJ/mol, which is in good agreement with this work. Figure 4.43 shows the temperature dependence of the different metrics of crack initiation for Alloy 690. The average crack length is relatively independent of temperature, which implies that the measured activation energy is primarily capturing crack nucleation in CERT. Similar behavior is also observed for Alloy 600 in Figure 4.41, where the crack length is largely temperature independent. The cracking mode was intergranular for both alloys when observed from the gauge

surface for both water conditions. Quantitative analysis of crack initiation establishes that there is no discontinuity or change in slope across the subcritical/supercritical water transition.

The magnitudes of the activation energy are a measure of the rate limiting step in a complex reaction to cause the stress corrosion crack initiation. Table 5.1 shows select activation energies for diffusion of metal species in oxygen in bulk metal and through select oxides. The activation energy measured for Alloy 600 crack initiation is 121±13 kJ/mol and the popular mechanism for crack initiation involves a grain boundary oxidation process. There are several processes that have similar activation energies such as nickel diffusion through NiO, oxygen diffusion through Ni, and oxygen diffusion along the metal-oxide interface of intergranular internal oxidation of 617 by Gulsoy [85]. Out of those options, the diffusion of oxygen along the metal-oxide interface of grain boundary oxides also matches very well with the microstructural observations of crack initiation in Alloy 600. It is less clear what process would be occurring to match the activation energy for Alloy 690 crack initiation (92±12 kJ/mol). There are several cases that have similar values such as nickel diffusion along NiO grain boundaries, iron diffusion along Fe_3O_4 grain boundaries, and oxygen diffusion in Cr_2O_3 at high temperatures. However, these processes do not match as well with the proposed film rupture based mechanism for crack initiation of Alloy 690. One possible reason for the discrepancy may be due to a process occurring during the straining that would lower the activation energy required. For example, corrosion or high stresses can inject vacancies into the metal and grain boundary which could remove the vacancy creation barrier in a few of the diffusion processes, lowering the activation energy. Another possible reason for the difference in activation energy could be simply the composition difference between Alloy 600 and Alloy 690. This effect is highlighted by the change in chromium

diffusion along grain boundaries and the lattice of Alloy 600 vs 20Cr25NiFe shown in Table 5.1. Alloy 600 has a higher nickel and lower chromium content than the steel, which causes the activation energy of chromium diffusion along the grain boundaries and lattice to be higher by 60-70 kJ/mol. Alloy 600 also has a higher nickel content than Alloy 690, but a lower chromium concentration, which may account for the change in activation energy of crack initiation between the two alloys if the same mechanism is operating.

5.4.2 Comparison of crack initiation between Alloy 600 and Alloy 690

A comparison of the cracking severity between Alloy 600 strained to 8% and Alloy 690 strained to 7% is shown in Figure 5.12. Two additional factors have an effect on the cracking severity between the two alloys, the difference in strain rate and the difference in pre-strain. Alloy 690 without pre-strain is shown in hollow blue circles and on average shows 3 times less cracking than the samples with 20% pre-strain. Alloy 600 strained at $5x10^{-8}$ s^{-1} at 320°C is shown as a solid green triangle, whereas the samples strained at $3x10^{-7}$ s^{-1} are shown as hollow green triangles. A decrease in the strain rate by a factor of 6 yielded a 6.6 times higher crack length per unit area the Alloy 600 sample. A factor of improvement (F_I) of how much more crack initiation resistant Alloy 690 is than Alloy 600 can be calculated from the activation energy fits to the data and the acceleration factors as:

$$F_I = A_{Strain\,rate} * B_{Pre-strain} * \frac{Alloy\ 600_{3x10^{-7}s^{-1}}}{Alloy\ 690_{5x10^{-8}s^{-1}}} \qquad (5.9)$$

where F_I is the factor of improvement, $A_{Strain\ rate}$ is the acceleration factor due to the difference in strain rate, and $B_{Pre\text{-}strain}$ is the acceleration factor due to the difference in pre-strain. It is assumed that the acceleration due to pre-straining and decreasing the strain rate do not change the activation energy of crack initiation. The factor of improvement as a function of inverse

temperature is shown in Table 5.2 and plotted in Figure 5.13 for the crack length per unit area, crack density, and average crack length. Error bars are calculated by summing the error from the values of Alloy 600 and Alloy 690 for each measure and temperature. The F_I for the average crack length is approximately 3 and independent of temperature, indicating that the activation energy for the average crack length for both alloys is the same. The F_Is for the crack density and crack length per unit area increase with temperature, as expected from the difference in activation energies between the alloys. The factor of improvement for the crack density, which can be thought of as a measure of crack nucleation, increases exponentially from 130x at 320°C to 420x at 450°C. The factor of improvement for the crack length per unit area, an overall measure of the crack initiation, increases exponentially from 480x at 320°C to 1480x at 450°C.

The mechanisms of crack initiation appear to be different between Alloy 600 and Alloy 690. The proposed mechanism for Alloy 690 is essentially film rupture of a Cr_2O_3 layer above grain boundaries. Alloy 600 does not form a Cr_2O_3 layer above grain boundaries, instead it oxidizes along grain boundaries into the metal [35,36]. The measured activation energies for both alloys are primarily measurements of the crack nucleation, and support a difference in the crack nucleation mechanism. This difference in mechanism would suggest that Alloy 600 has a shorter incubation period than Alloy 690 because of the immediate access of the environment to the grain boundary. Even though the initiation mechanisms appear to be different, there are significant similarities in the morphology of crack tips in initiated cracks, suggesting a similar mechanism in the crack growth. However, there a large difference between the crack growth rate in Alloy 600 and Alloy 690. The difference in crack growth rate may be due to either the

strength of the oxide formed beyond crack tips or the crack tip oxide may be more passivating at the higher chromium concentrations in Alloy 690.

The proposed mechanism of Alloy 690 crack initiation brings up the question of what is the true accelerating method occurring in these experiments, the temperature effect or dynamic straining. As discussed earlier in Section 5.3.4, crack initiation of Alloy 690 requires a dynamic strain to occur as there have been no observation of crack initiation of Alloy 690 during constant load experiments. The effect of temperature in accelerating cracking is pretty clear, the crack length per unit area of Alloy 690 at 450°C is 18 times higher than that observed at 320°C for the same strain and time of exposure. Changing the strain rate has some interesting effect; as the strain rate is decreased for Alloy 600, the crack initiation increases approximately linearly. A decrease in the strain rate by a factor of 6 (from $3x10^{-7}$ s^{-1} to $5x10^{-8}$ s^{-1}) increased the cracking susceptibility by a factor of 6.6. However, this is the acceleration at a fixed strain instead of a fixed time. Assuming a moderately fast creep rate of 10^{-10} s^{-1}, these experiments were conducted at 500x the creep rate. If the acceleration due to strain rate change were applied in this case, the constant load case should have 500x more cracking than that observed in the CERT experiments, but it would take approximately 25 years to achieve the same amount of strain. A more reasonable measure of the acceleration due to changing the strain rate is based on a fixed experiment time instead of a fixed strain. Unfortunately this type of experiment was not conducted in this work. Boursier et al.[84] observed deeper cracking in an experimental heat of Alloy 690 strained at $2.5x10^{-7}$ s^{-1} than in a sample strained at $5x10^{-8}$ s^{-1} for a fixed time at 360°C. The difference in severity of cracking increased with time between the two strain rates, but was limited by the necking of the samples. This result suggests that increasing the strain rate accelerates crack initiation for a fixed time, which agrees with the observation of crack initiation during CERT but

not in constant load. However, it is difficult to quantify to what extent the cracking is accelerated due to the strain rate. The fact that cracking is observed at 320°C at all in this work suggests that the strain rate is the dominant accelerating factor.

5.4.3 Continuity of SCC initiation mechanism between subcritical to supercritical water

One of the primary challenges with this work was that the mechanisms of corrosion and crack initiation for Alloy 600 and Alloy 690 were not known. Because of this, the approach taken in this dissertation was to separate the SCC initiation behavior by studying the constituents that lead to crack initiation (oxidation) and the characteristics of the initiation itself (crack morphology and temperature dependence). The oxidation behavior in both environments was discussed in Section 5.2 and was found to have consistent oxide morphology, structure, and composition between subcritical and supercritical water. The crack initiation morphology was discussed in Section 5.3 and was found to be consistent between both environments. The continuity in the crack initiation temperature dependence was supported quantitatively by the excellent fit of a single activation energy for crack initiation in each alloy across the critical temperature.

The density of the water environment does not appear to impact the susceptibility to stress corrosion cracking for Alloy 600 and Alloy 690. The density of water changes dramatically over the range of temperatures tested, shown in Figure 2.5. A change in water density is able to affect the thermodynamic stability of oxides as demonstrated in Section 5.1. Watanabe et al. [65] measured the susceptibility of 316 stainless steel to stress corrosion cracking in supercritical water as a function of density. The measurement was made using CERT testing and comparing the strain at failure to the dielectric constant of water. Watanabe found that as the density of

SCW increased, the strain to failure decreased, suggesting an effect of the diffusivity of ionic species in the water is the controlling factor. From this result, it was proposed that dissolution of metal plays an essential role in SCC of stainless steel. While the density does appear to have a large effect in the case of Watanabe's work, it does not seem to affect the SCC susceptibility of Alloy 600 or Alloy 690, evidenced by the consistent activation energy in subcritical and supercritical water. This result suggests that a similar dissolution mechanism to what Watanabe observed is not occurring for the nickel based alloys, which is consistent with the proposed mechanism for Alloy 690 crack initiation in Section 5.3. Another factor to consider is the corrosion potential relative to oxide stability of this work versus Watanabe's. This work was conducted at a constant potential from the Ni/NiO boundary in the NiO stable regime, essentially neglecting any effect of the density on the oxide phase formation. However, Watanabe's work was conducted in the same environment (8ppm dissolved oxygen), which could potentially cause a change in the stability of oxides as density is changed.

However, a mechanism for stress corrosion crack initiation of Alloy 690 is proposed in Section 5.3 which allows the components of the mechanism to be compared between subcritical and supercritical water. The mechanism consists of three stages; 1) an oxidation stage in which a protective film of Cr_2O_3 is formed on the surface over the grain boundaries, 2) an incubation stage in which successive cycles of oxide film rupture and repair depletes the grain boundary of chromium, and 3) a nucleation stage in which the chromium depleted grain boundary is no longer able to support formation of a protective layer, exposing the grain boundary to the water environment and subsequent formation and rupture of oxides down the grain boundary. Stage 1 (oxidation) is consistent between subcritical water and supercritical water. A protective oxide is

observed above grain boundaries evidenced by thinning of the internal oxide in both environments (Figure 4.7, Figure 4.8, Figure 5.7) that is composed of Cr_2O_3 (Figure 4.17, Figure 4.20). Stage 2 (incubation) is observed in both environments, evidenced by the thinning of the internal oxide at crack mouths of Alloy 690 (Figure 4.28, Figure 4.29, Figure 4.34) and the lack of crack initiation from constant load testing [50–52]. Stage 3 (nucleation) is consistent between subcritical and supercritical water, evidenced by observation of chromium depletion and grain boundary migration in both environments (Figure 4.10, Figure 4.11) and by grain boundary oxidation in CERT strained samples in both environments (Figure 4.27). The temperature dependence across the transition from subcritical to supercritical water shows no discontinuity or kink and is fit well with a single activation energy (Figure 5.11). All available evidence supports a consistent mechanism of stress corrosion crack initiation in both hydrogenated subcritical and supercritical water.

Table 5.1. Activation energy values of select diffusion data.

Diffusion Process	Activation Energy (kJ/mol)	Temperature Range (°C)	Reference
Nickel in NiO Lattice	165	500 - 1400	[86]
Nickel in NiO Dislocation	112	500 - 1400	[86]
Nickel in NiO Grain Boundary	91	500 - 1400	[86]
Nickel in 20Cr25NiFe grain boundary	200	840 - 1290	[87]
Nickel in 20Cr25NiFe Lattice	282	840 - 1290	[87]
Iron in Fe_3O_4 Bulk	238	350 - 1200	[88]
Iron in Fe_3O_4 Grain Boundary	87.9	0 - 80	[89]
Chromium in Cr_2O_3 Bulk	230-245	1100 - 1300	[90]
Chromium in 20Cr25NiFe grain boundary	187	840 - 1290	[87]
Chromium in 20Cr25NiFe Lattice	246	840 - 1290	[87]
Chromium in Alloy 600 Grain Boundary	227	585 - 1151	[91]
Chromium in Alloy 600 Lattice	300	585 - 1151	[91]
Oxygen in Cr_2O_3	101	1100 - 1450	[92]
Oxygen in Ni	158.7	227 - 1453	[93]
Oxygen in Ni	239.8	350 - 1000	[94]
Oxygen in 617 along grain boundary oxide	149.9-154.4	750 - 850	[85]

Table 5.2. Factor of improvement of Alloy 600 over Alloy 690.

Temperature (°C)	1/T (K^{-1})	Crack Length/ Area	Crack Density	Average Crack Length	Error Crack Length/ Area	Error Crack Density	Error Average Crack Length
320	0.00169	476.2	129.1	3.3	135.6	36.8	0.9
330	0.00166	528.3	143.9	3.3	133.9	36.5	0.8
340	0.00163	584.2	159.8	3.2	131.7	36.0	0.7
350	0.00161	643.9	177.0	3.2	129.1	35.5	0.6
360	0.00158	707.5	195.3	3.2	126.2	34.8	0.6
370	0.00156	775.1	214.8	3.2	122.9	34.1	0.5
380	0.00153	846.8	235.6	3.2	119.5	33.2	0.5
390	0.00151	922.7	257.7	3.2	115.8	32.3	0.4
400	0.00149	1002.8	281.1	3.2	112.0	31.4	0.4
410	0.00146	1087.2	305.9	3.2	108.0	30.4	0.3
420	0.00144	1175.9	332.0	3.2	103.9	29.3	0.3
430	0.00142	1269.1	359.6	3.2	99.7	28.3	0.3
440	0.0014	1366.8	388.5	3.2	95.5	27.2	0.2
450	0.00138	1468.9	418.9	3.2	91.3	26.0	0.2

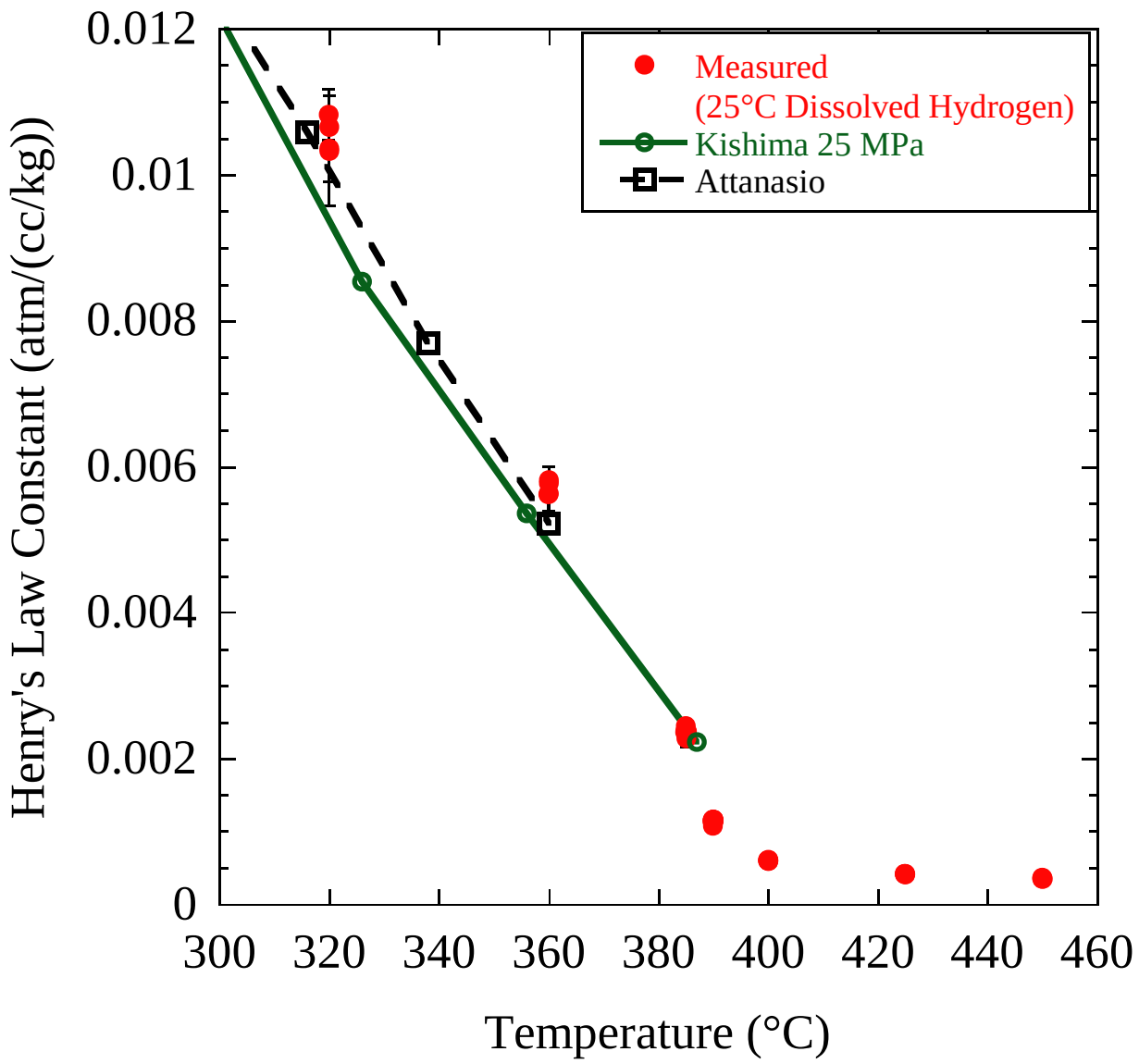

Figure 5.1. Henry's law constant measured at 25 MPa. Red circles indicate measurements where the dissolved hydrogen at 25°C was used to calculate the Henry's law constant. Data in subcritical and low supercritical water was obtained from Attanasio et al.[70] and Kishima et al.[16] for comparison.

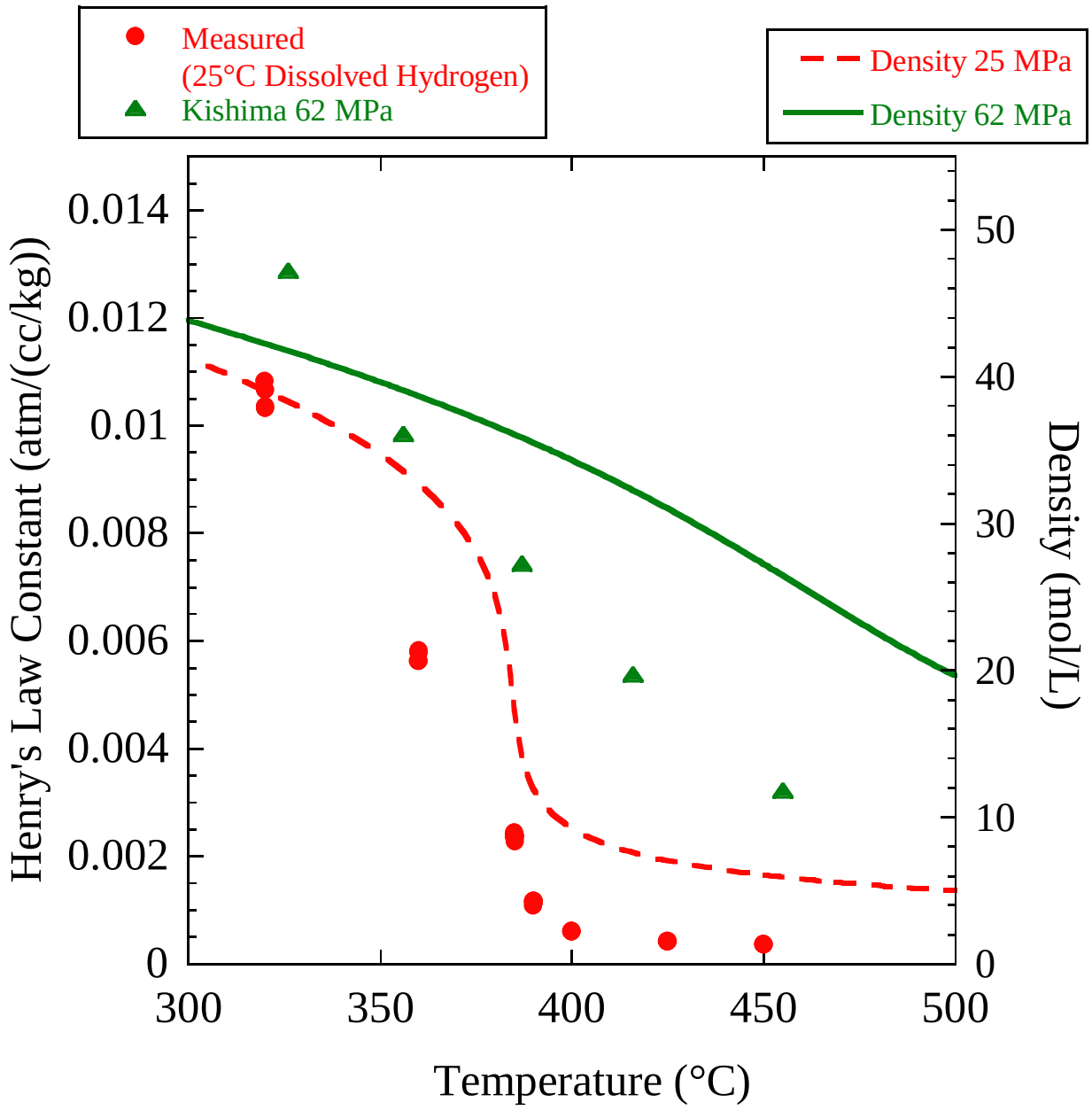

Figure 5.2. Demonstration of the effect of vessel pressure on the behavior of Henry's law constants and density at the critical temperature. In the data measure at 25 MPa in red circles, there is a sharp change in slope in both the Henry's law constant and the density. In the data from Kishima [16] at 62 MPa in green triangles, there is no change in the slope of the Henry's constant or the density at the critical temperature. Density values are taken from steam tables [71].

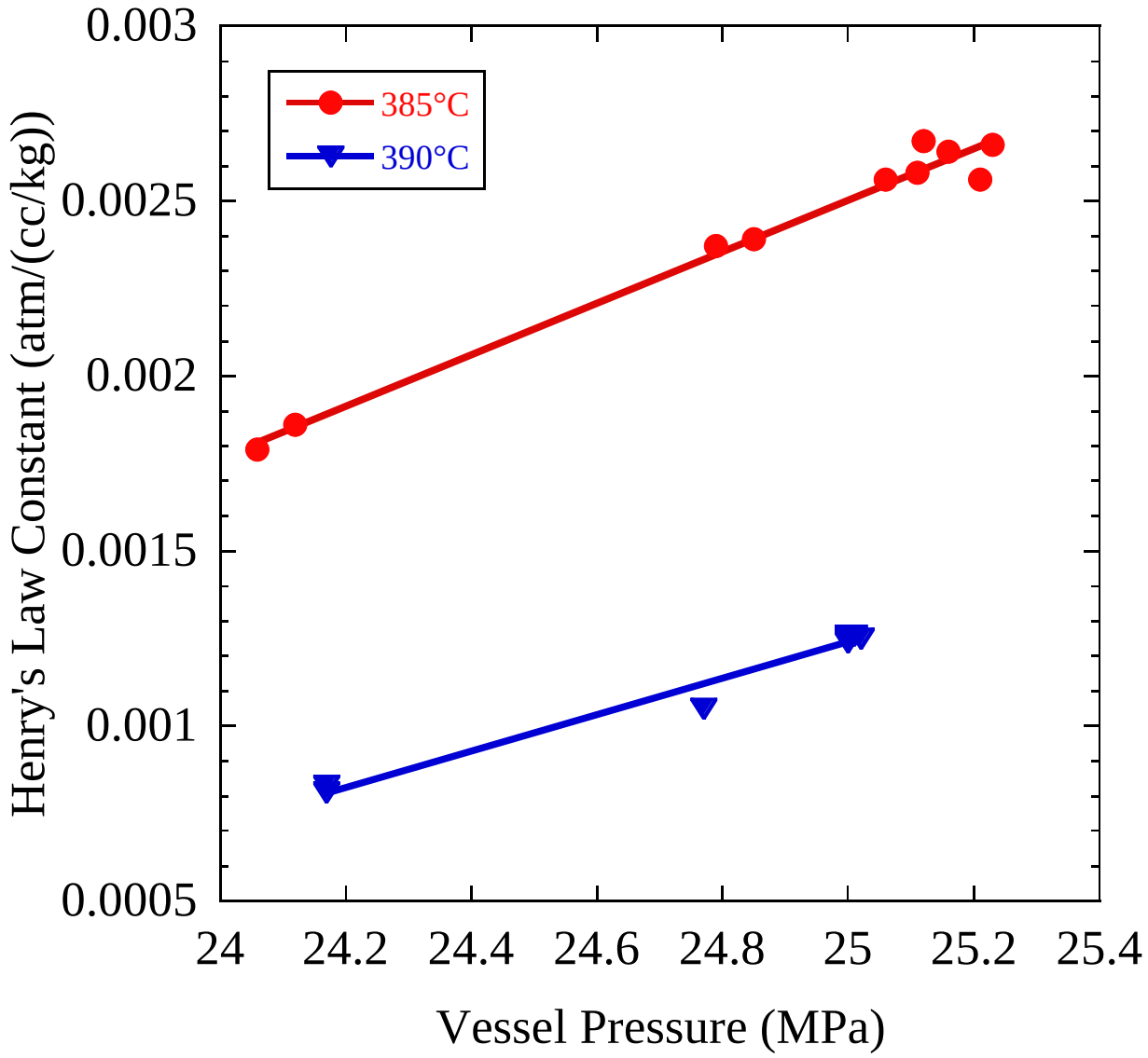

Figure 5.3. Effect of vessel pressure on the Henry's law constant was measured at 385°C and 390°C. Data taken at 385°C is shown in red circles and data taken at 390°C is shown in blue triangles.

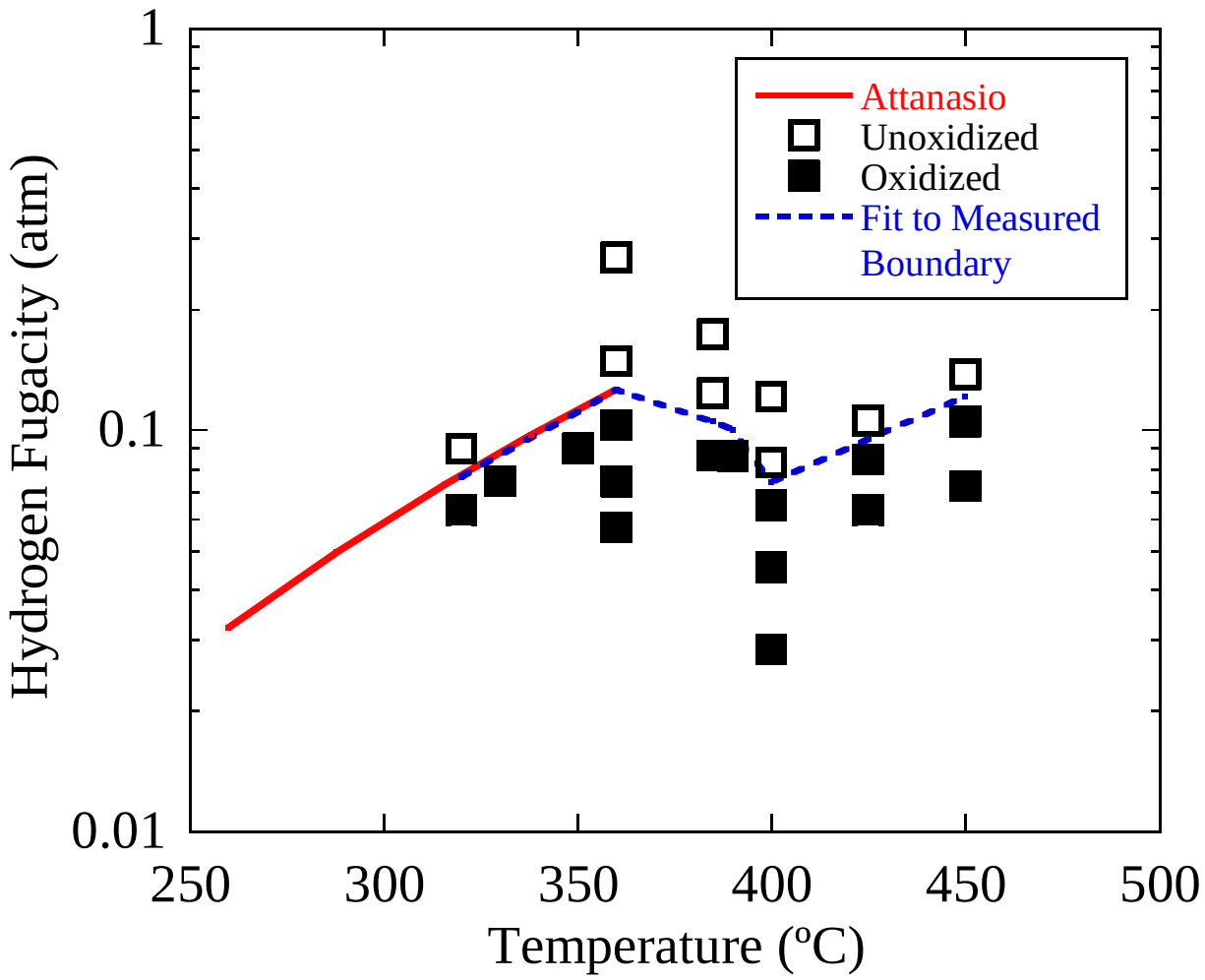

Figure 5.4. Summary of Ni coupon exposures to determine the location of the Ni/NiO boundary in supercritical water in terms of temperature and hydrogen fugacity. Open squares indicate no oxide formation and filled squares indicate conditions where oxide was found. A Fit to the measured boundary was taken as the midpoint between Ni stable and NiO stable conditions. Subcritical data was obtained from Attanasio and Morton[70].

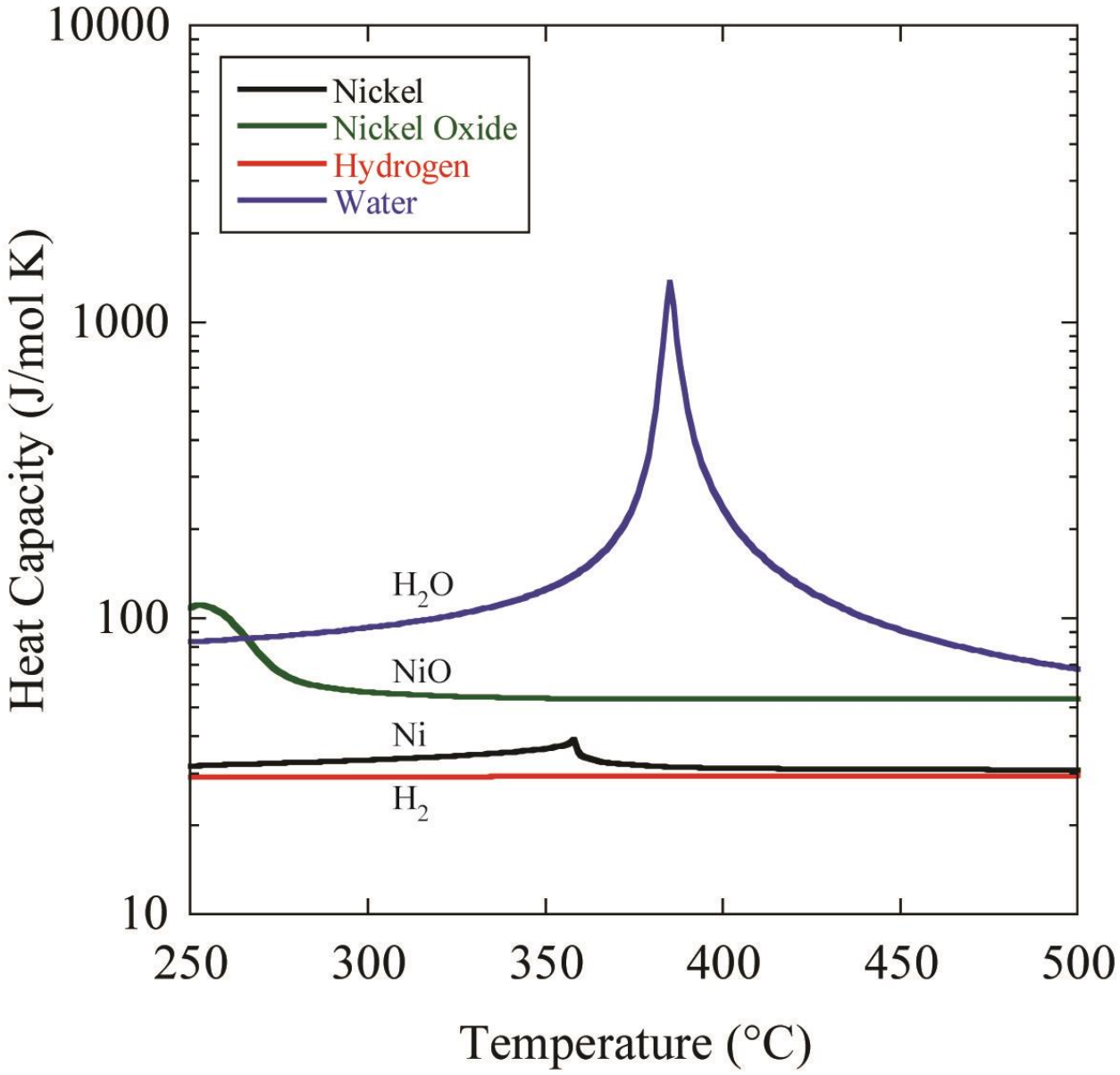

Figure 5.5. Heat capacity of nickel, nickel oxide, hydrogen, and water as a function temperature at 25 MPa [71–74].

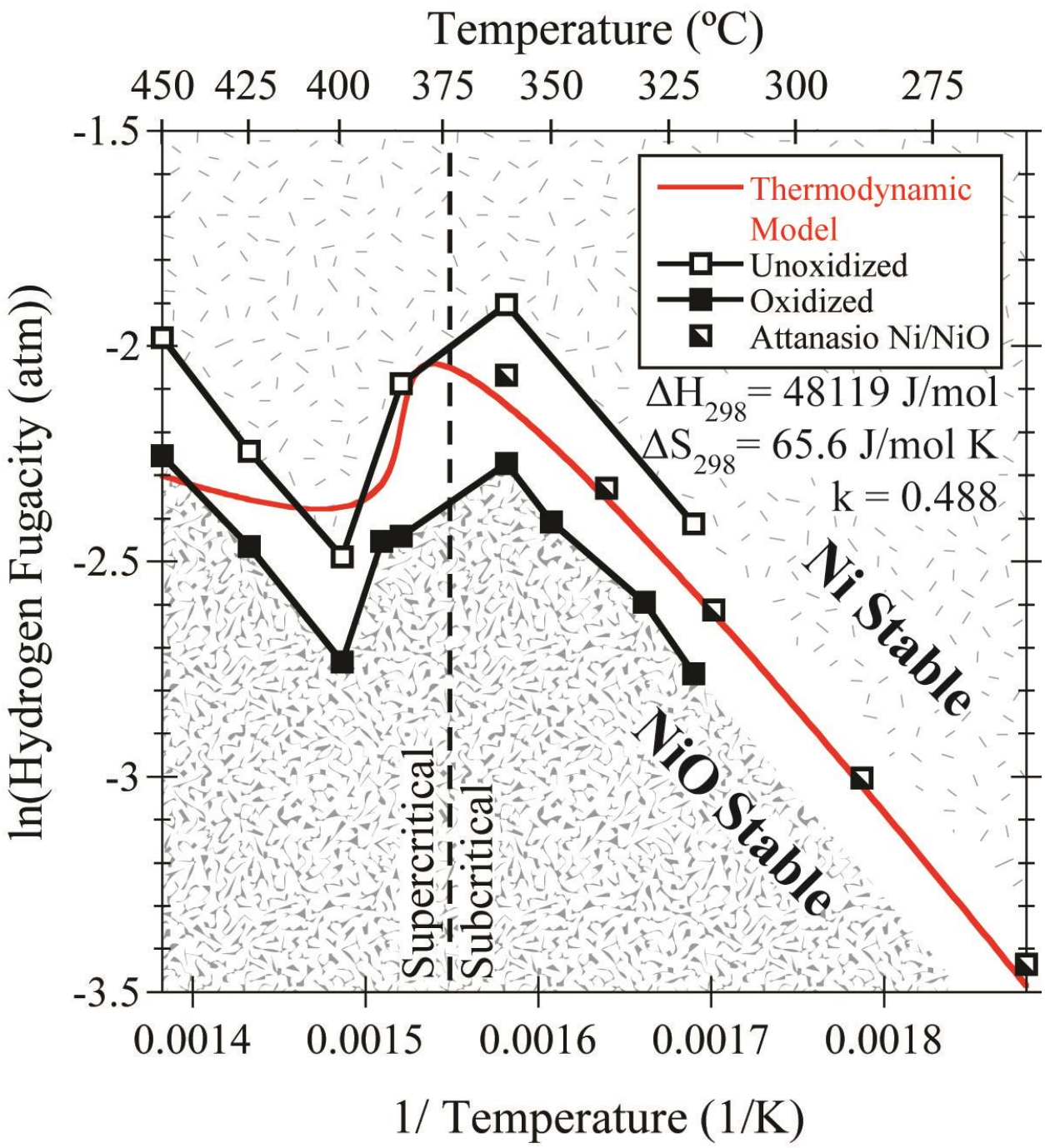

Figure 5.6. Measured fugacity of the Ni/NiO transition plotted in $\ln(f_{H_2})$ as a function of 1/T where NiO stable coupons are in black squares and Ni stable coupons are open squares. Half-filled squares represent data for contact electrode resistance experiments conducted by Attanasio et al.[70] The fit from equation 5.7 is shown as the smooth red line. Regions of NiO and Ni stability are shaded, the unshaded region between represents the uncertainty in the location of phase boundary.

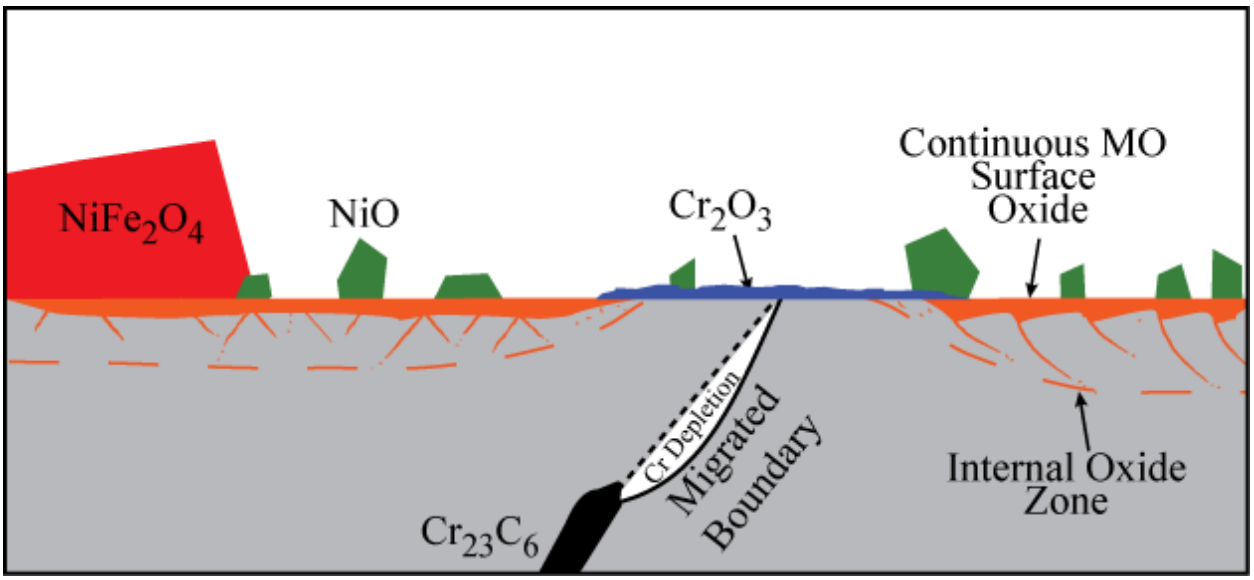

Figure 5.7. Schematic of oxidation behavior observed on Alloy 690 in hydrogenated subcritical and supercritical water.

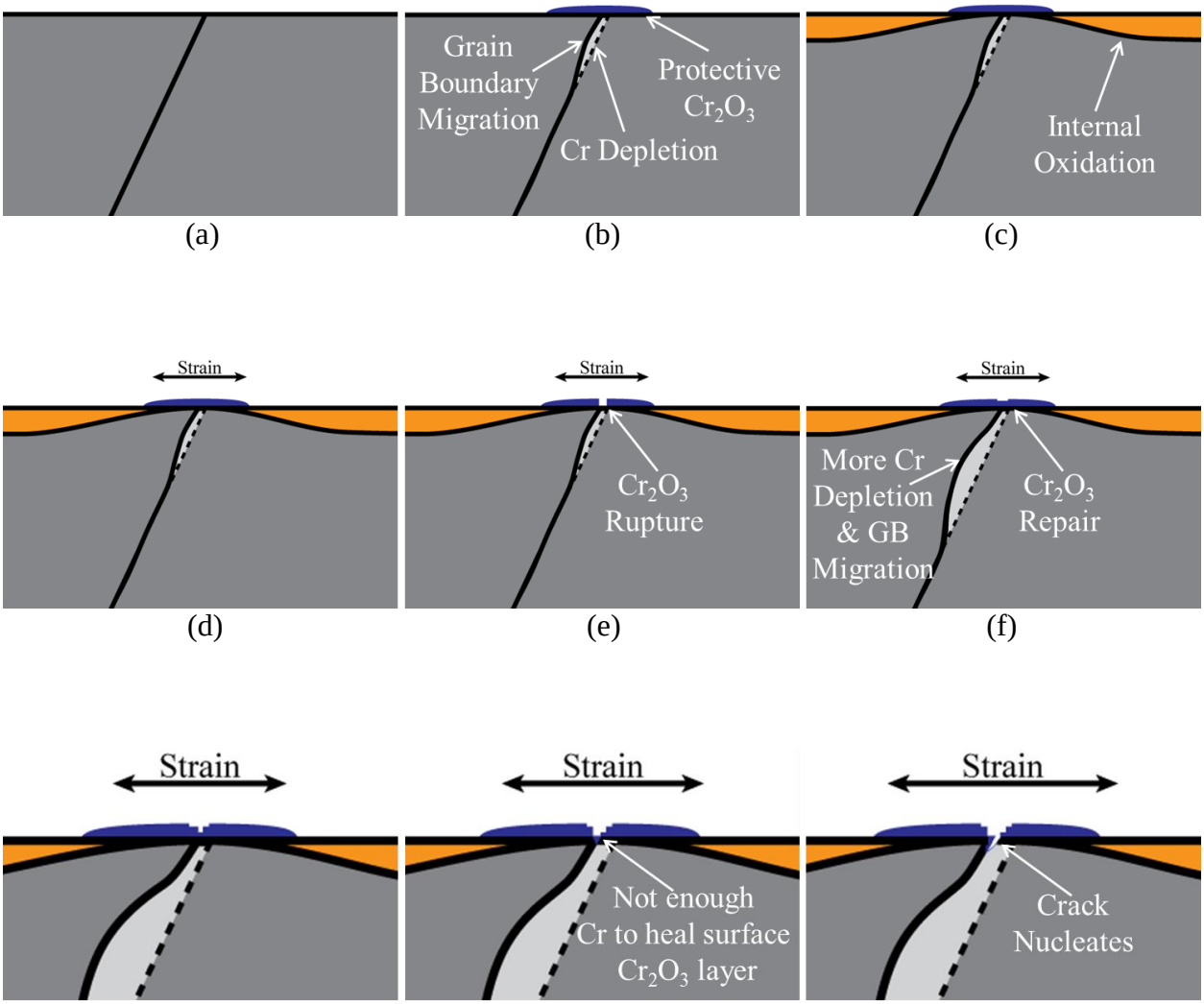

Figure 5.8. Schematic of the proposed SCC initiation mechanism of Alloy 690 subjected to dynamic stress; surface oxidation accompanied by grain boundary chromium depletion and grain boundary migration, and internal oxidation away from the grain boundary (a-c), rupture and repair of oxide by dynamic straining (d-f), and crack initiation along the boundary when a Cr_2O_3 is no long able to form (g-i).

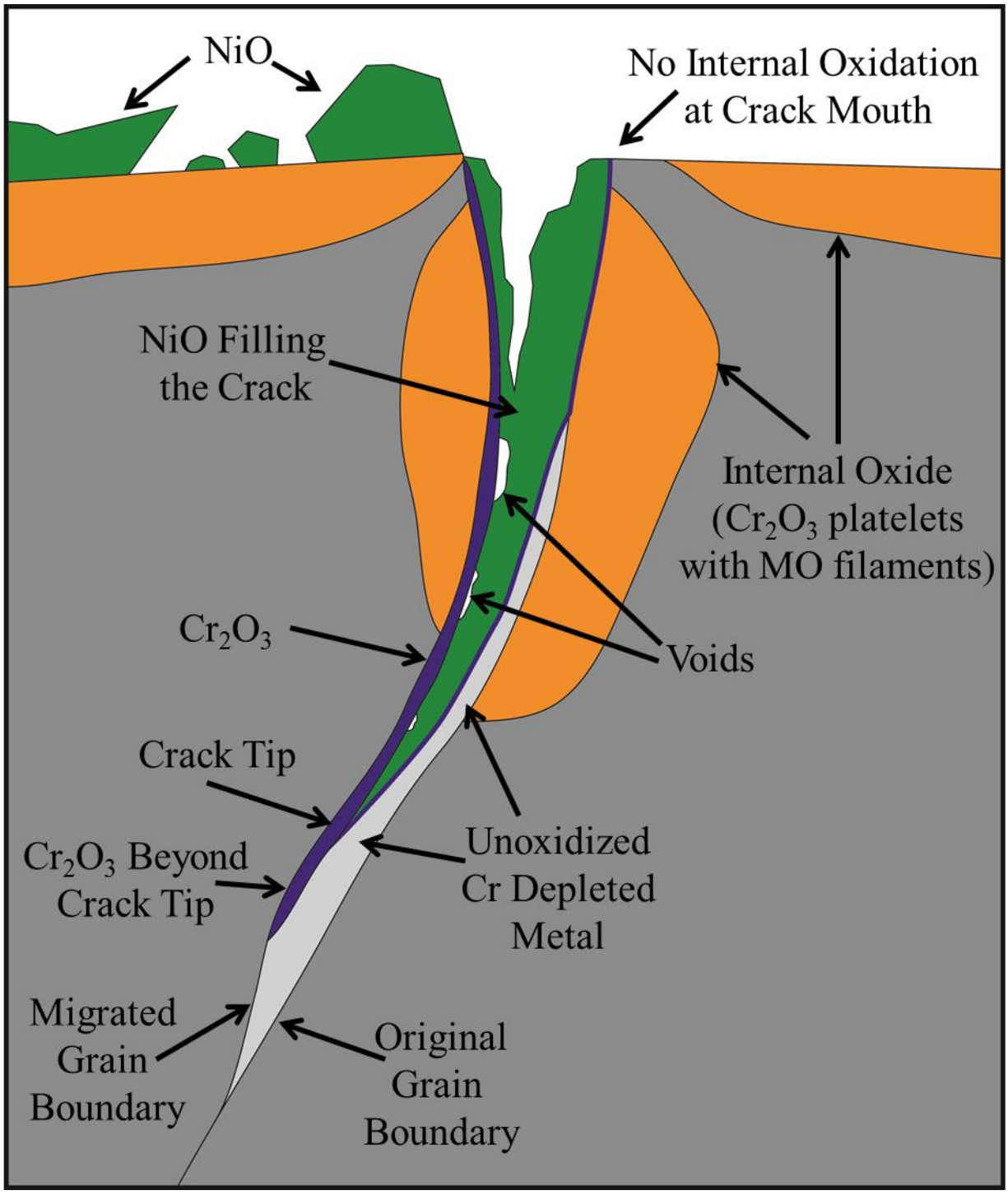

Figure 5.9. Schematic of cracking observed in 20% pre-strained Alloy 690 strained to 7% at $5x10^{-8}$ s^{-1} in hydrogenated subcritical and supercritical water.

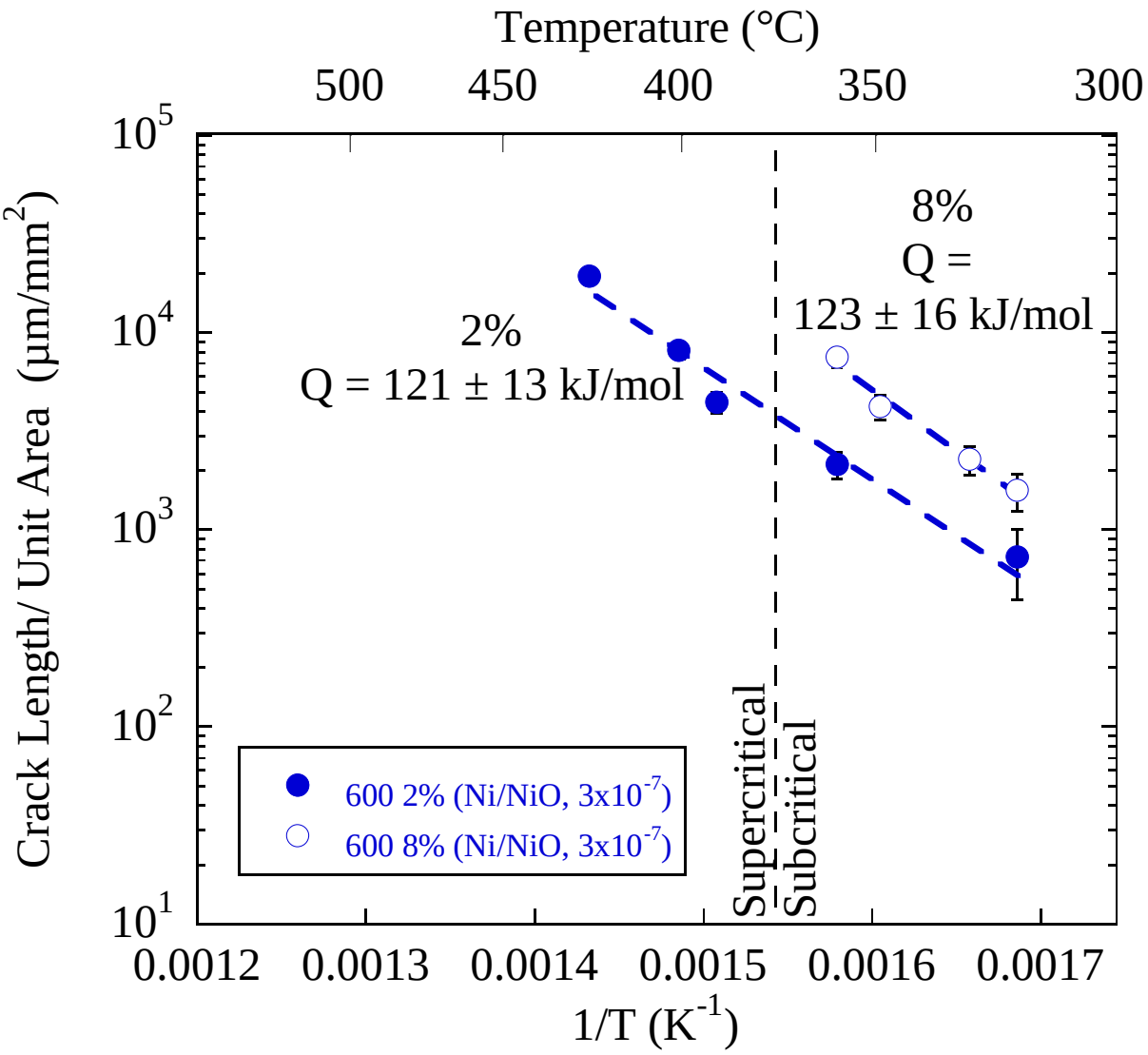

Figure 5.10. Activation energy with 95% confidence intervals for crack initiation of Alloy 600 strained to 2% in supercritical and subcritical water shown in blue filled circles. Samples strained to 8% in subcritical are shown as hollow blue circles for comparison.

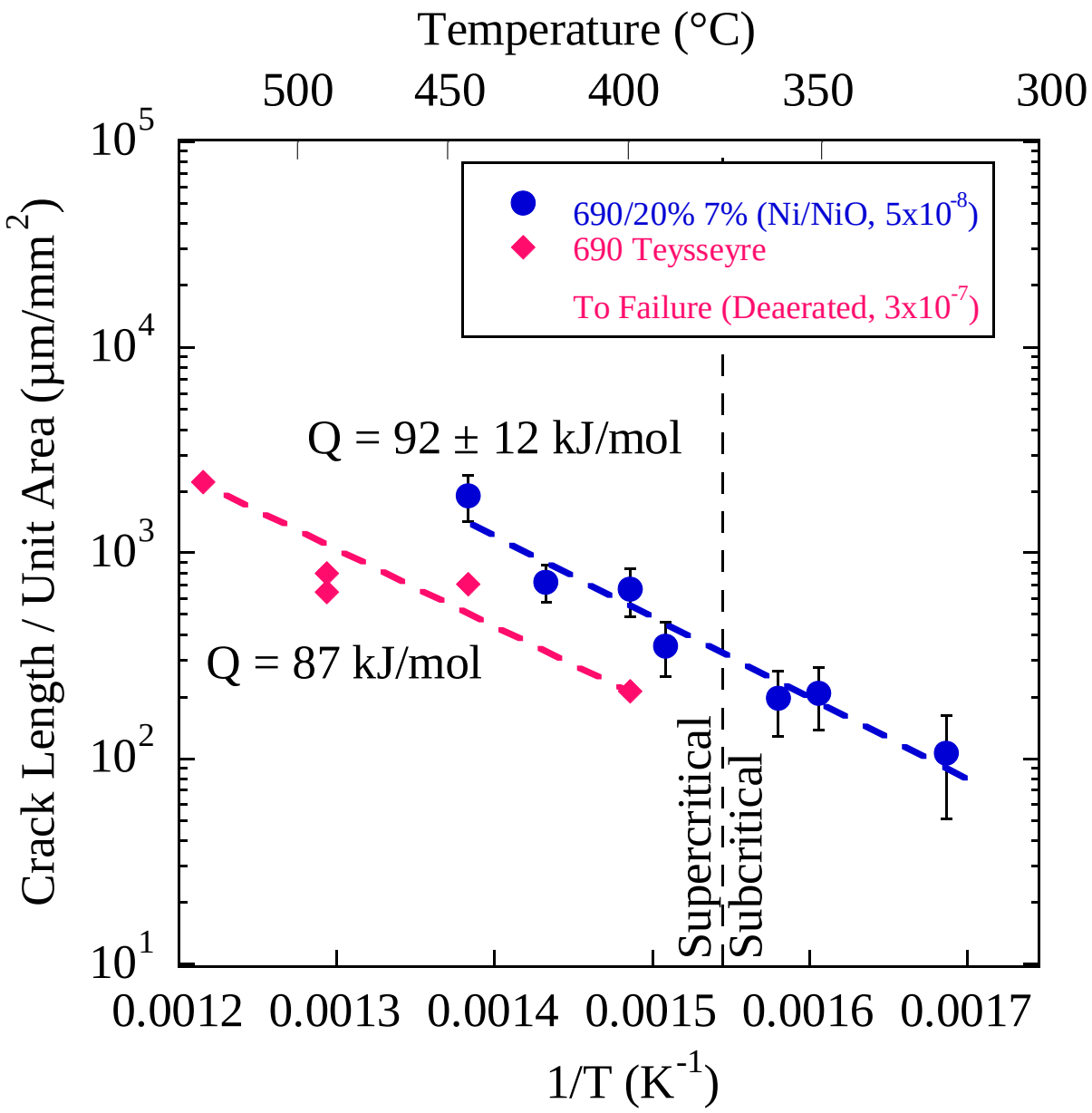

Figure 5.11. Activation energy with 95% confidence intervals for crack initiation of Alloy 690 strained to 7% in hydrogenated supercritical and subcritical water shown in blue filled circles. The cracking severity of Alloy 690 strained to failure in deaerated water at a faster strain rate of $3x10^{-7}$ s^{-1} is shown for comparison[53].

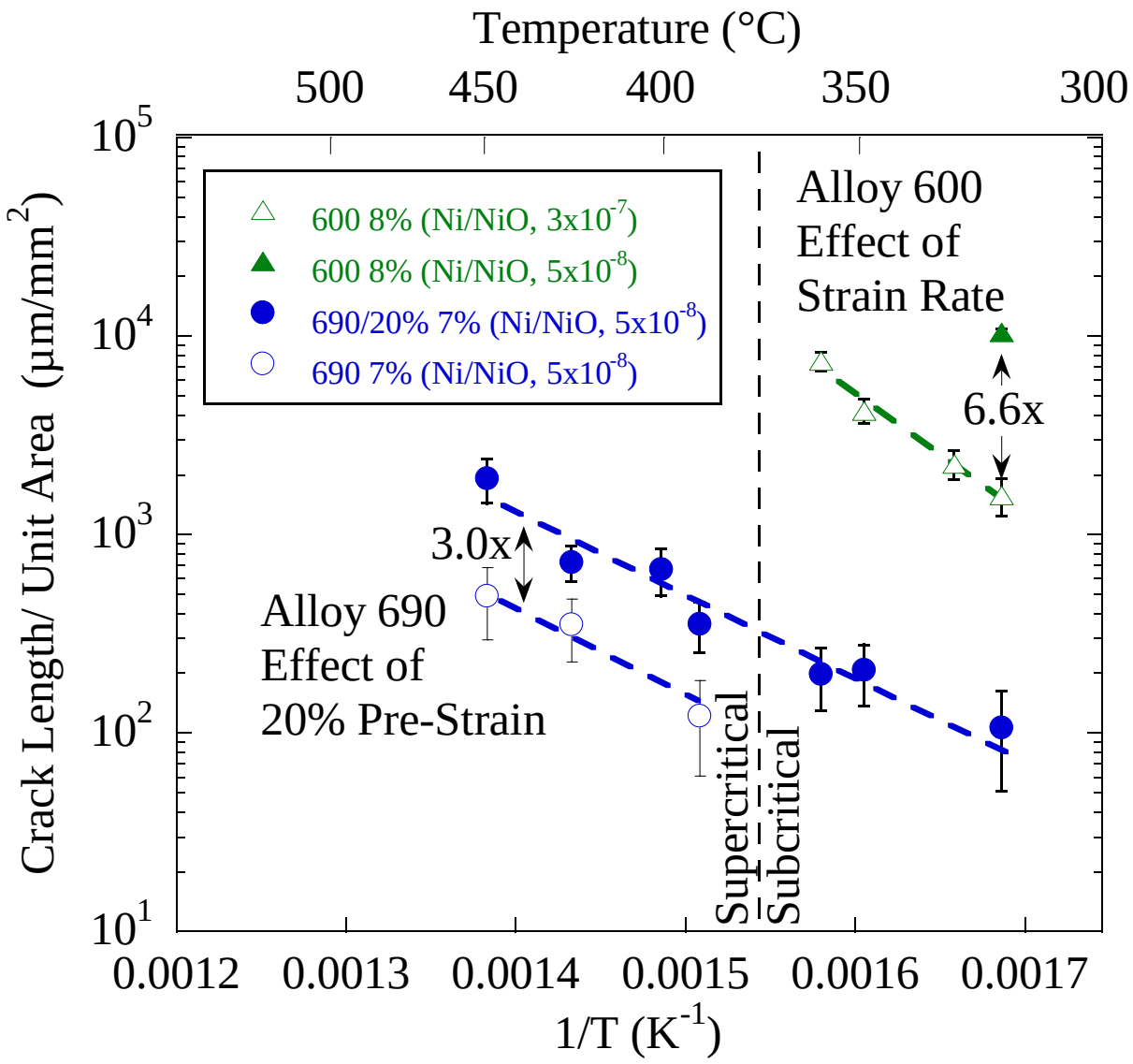

Figure 5.12 Comparison of cracking severity between Alloy 600 strained to 8% at $3x10^{-7}$ s^{-1} and Alloy 690 strained to 7% at $5x10^{-7}$ s^{-1} highlighting the effect of 20% pre-strain and strain rate.

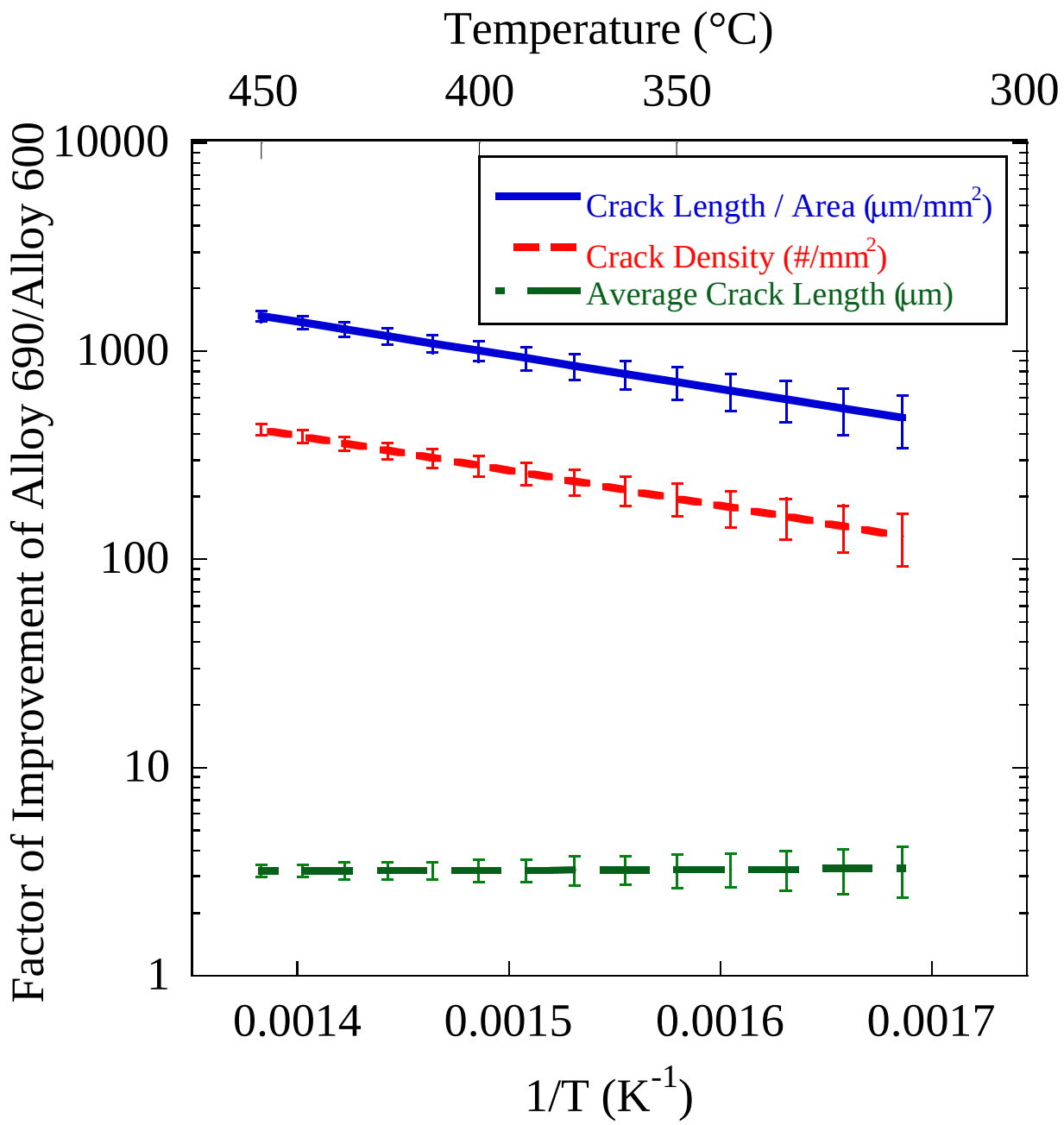

Figure 5.13 Factor of improvement of Alloy 690 over Alloy 600.

CHAPTER 6 - CONCLUSIONS

The major conclusions of this dissertation are as follows:

1. The mechanisms for stress corrosion crack initiation and corrosion of Alloy 600 and Alloy 690 are consistent between hydrogenated subcritical and supercritical water, supporting the use of accelerated SCC testing in supercritical water for simulating subcritical conditions.
2. The location of the Ni/NiO boundary was experimentally determined in terms of dissolved hydrogen concentration and hydrogen fugacity in subcritical and supercritical water with good agreement to literature data in subcritical water. Measurement of the phase transition will allow for future corrosion potential controlled SCC experiments in supercritical water conditions.
3. The Henry's law constant of hydrogen in water was calculated by in situ measurements of the fugacity for temperatures between 320 and 450°C at 25MPa. Measurements showed excellent repeatability and validated the use of Henry's law for hydrogen in this concentration range. Henry's constant was found to decrease linearly with temperature below the critical point. In supercritical water the Henry's constant was nearly temperature independent and approached zero, indicating high miscibility of supercritical water with hydrogen.
4. A thermodynamic model was developed to describe the fugacity of hydrogen at the Ni/NiO boundary as a function of temperature. Good agreement was found with

thermodynamic data for the oxidation of nickel. The model captures what originally appeared to be anomalies in the measured fugacity of hydrogen at the phase transition, and suggests that the activity of water plays an important role in the oxidation.

5. Oxidation results in a multi-layer oxide structure composed of particles of NiO and $NiFe_2O_4$ formed by precipitation on the outer surface, and a chromium rich inner oxide layer formed by diffusion of oxygen to the metal-oxide interface. The inner oxide on Alloy 600 is less chromium rich than that observed on Alloy 690. The inner oxide on Alloy 690 initially forms by internal oxidation before a protective layer of chromium rich MO is formed with Cr_2O_3 at the metal-oxide interface.
6. Grain boundaries in Alloy 690 act as fast diffusion paths for chromium to form a protective Cr_2O_3 layer at the surface, preventing internal oxidation from occurring. The underlying grain boundary migrates and is depleted in chromium.
7. The mechanism of SCC initiation of Alloy 690 is composed of three stages; 1) an oxidation stage in which a protective film of Cr_2O_3 is formed on the surface over the grain boundaries, 2) an incubation stage in which successive cycles of oxide film rupture and repair depletes the grain boundary of chromium, and 3) a nucleation stage in which the chromium depleted grain boundary is no longer able to support formation of a protective layer, exposing the grain boundary to the water environment and subsequent formation and rupture of oxides down the grain boundary.
8. The initiated crack propagates along the grain boundary and not in the chromium depleted region, which is not susceptible to grain boundary oxidation like that observed in Alloy 600 or internal oxidation like that observed on the Alloy 690 surface. Cr_2O_3 is observed in the grain boundary ahead of crack tips.

9. Surface crack growth and crack growth into the sample is hindered by chromium carbides, which are able to halt crack propagation due to a combination of mechanical and chemical effects.
10. The activation energy of crack initiation in CERT testing of mill annealed Alloy 600 does not change across the critical temperature and has a value of 121±13 kJ/mol. The activation energy of crack initiation in CERT testing of mill annealed Alloy 690 is dominated by the temperature dependence of crack nucleation, is fit well with a single activation energy across the critical temperature, and has a value of 92±12 kJ/mol.

CHAPTER 7 - FUTURE WORK

This dissertation was focused on building a body of evidence to determine if the mechanisms of crack initiation of Alloy 600 and Alloy 690 are the same in supercritical and subcritical water. While pursuing this objective there were several additional questions raised that warrant further study.

The most relevant to this work is a missing piece of evidence that was not addressed, *whether the oxidation rate of Alloy 600 and Alloy 690 is continuous between subcritical and supercritical water*. Answering this would serve to complete the body of evidence to determine if the corrosion of Alloy 600 and Alloy 690 occurs by the same mechanisms in subcritical and supercritical water. However this work has revealed subtleties in the oxidation that may make it difficult to determine if the rate is continuous. For both alloys there are several oxidation mechanisms occurring at different rates and at different stages of the process. Alloy 600 oxidation occurs by three processes: oxidation of the surface by inward oxygen diffusion to form matrix oriented MO, grain boundary oxidation, and precipitation of metallic species from the water to form NiO and $NiFe_2O_4$ particles on the surface. Alloy 690 oxidation may occur by four separate processes: internal oxidation of the matrix, passivation of the internal oxide by formation of matrix oriented MO, formation of Cr_2O_3 above grain boundaries which prevents internal oxidation, and precipitation of metallic species from the water to form NiO and $NiFe_2O_4$ particles on the surface. Each of these processes is occurring at a different rate, which

complicates the objective of determining a single rate of oxidation for the sample's oxidation. A further complication for Alloy 690 is the transition from linear internal oxidation to parabolic oxidation after the surface is passivated by the formation of MO.

There are facets of the proposed mechanism for crack initiation of Alloy 690 that warrant further study. One unknown in the mechanism is *what is the criteria for breakdown of Cr_2O_3 repassivation*. Knowing the case that causes Cr_2O_3 film breakdown would give further insight into how the mechanism operates and potentially provide clues as to how cracking could be mitigated. One way to approach this problem is to look more closely at why certain grain boundaries crack and others do not. For example, no cracking was observed along twin boundaries and it is not yet clear what property of those boundaries makes them immune to crack initiation. Digital image correlation may give some insight as to how strain is accommodated at different grain boundaries, possibly providing a link to a critical strain required to cause crack initiation. The proposed mechanism also relies on diffusion of chromium to the surface, which could potentially vary with the stress state of a grain boundary or the type of grain boundary. Determining the diffusion rates of species along certain grain boundaries is a difficult problem in a polycrystalline system with precipitates along grain boundaries and different grain boundary inclinations. Moving to a simple system such as a bi-crystal of model alloy 690 may be able to help with answering that question. The role of grain boundary migration on the diffusion of chromium is also unknown, or whether it is important to the breakdown of the Cr_2O_3 film. Is the diffusion of chromium to the surface fed by the migration of the grain boundary? If so, why would there be a decrease in the flux of chromium to the surface if there is more room for the boundary to migrate?

There are two additional issues raised that have more of an engineering focus. The more important issue to the nuclear power industry is the question of *will Alloy 690 will eventually crack in constant load due to creep*. This is a good application of the accelerated testing method in supercritical water, where the creep rate would be higher. There are challenges with the current setup to running a long term constant load experiment, but the experimental method is fairly straight forward. The other issue with more of an engineering focus is *what is the optimal carbide coverage along grain boundaries to help mitigate crack initiation and growth*. Answering this question is complicated by competing effects of carbides in cold worked material. Bruemmer et al.[46,83] found that thermally treated material had higher crack growth rates in heavily cold rolled material, but cracks were also seen to arrest at carbides. In this work, cracks were also observed to arrest at carbides and carbides appeared to act as sinks for oxygen, potentially preventing grain boundary oxidation. It is not clear if a higher carbide coverage would aid in arresting cracks or if it would help initiate cracks earlier due to enhanced chromium deletion at the grain boundaries.

APPENDICES

APPENDIX A:
INDEXING OF ELECTRON DIFFRACTION PATTERNS

Phase identification using electron diffraction patterns was conducted by comparing d-spacings of Cr_2O_3, $NiFe_2O_4$ (same as $NiCr_2O_4$), NiO, and 690 metal. In most cases selected area diffraction was performed on nanocrystaline oxides which yielded multiple spots for each lattice plane, necessitating use of ring patterns to index patterns. During each TEM session, a diffraction pattern of the base metal was taken to calibrate the camera length used in oxide diffraction. The lattice parameter of Alloy 690 was measured by X-ray diffraction (Figure 0.1) and the lattice parameter was measured at 3.5773Å. The following images show the indexing of TEM diffraction patterns used in this dissertation.

Table 0.1. Lattice spacing used for phase identification

Cr_2O_3		$NiCr_2O_4$		NiO		690 Metal	
d (Å)	plane	d (Å)	plane	d (Å)	plane	d (Å)	Plane
3.633	102	2.9374	200	2.412	111	2.06534	111
2.666	104	2.5043	311	2.089	200	1.78864	200
2.48	110	2.405	222	1.4768	220	1.26476	220
2.264	600	2.0849	400	1.2594	311	1.07859	311
2.176	113	1.6965	422	1.2058	222	1.03267	222
2.048	202	1.5997	333	1.0443	400	0.89432	400
1.816	204	1.4733	440	0.9583	331	0.82068	331
1.672	116	1.4063	531	0.934	420	0.7999	420
1.579	122	1.3173	620				
1.465	214	1.2685	533				
1.4314	300	1.2582	622				
1.2961	10 10	1.2008	444				
1.2398	220	1.1649	711				
1.2101	306	1.1118	642				
1.1731	312	1.0836	731				
1.1488	2010	1.0409	800				
1.1239	134	0.98	822				
1.0874	226	0.9604	751				
1.0422	21 10						
0.9462	324						
0.937	410						
0.8957	13 10						
0.8883	30 12						
0.8658	416						
0.8425	40 10						
0.8331	12 14						
0.8263	330						
0.7977	32 10						

Table 0.2. Indexed diffraction spots.

Figure	Phase	Diffraction spot	Measured Plane Spacing (Å)	Ideal Plane Spacing (Å)	% Deviation
4.13	NiO	-2 0 0	2.023	2.089	3.162
		2 0 0	2.080	2.089	0.442
		1 1 -1	2.412	2.412	0.011
		1 -1 1	2.412	2.412	0.011
		-1 1 -1	2.343	2.412	2.859
		1 -1 1	2.373	2.412	1.614
4.14b	Alloy 690	1 -1 1	2.092	2.065	1.268
		1 1 -1	2.068	2.065	0.136
		-1 -1 1	2.103	2.065	1.843
		-1 1 -1	2.165	2.065	4.821
		-2 0 0	1.898	1.789	6.140
		2 0 0	1.948	1.789	8.933
	Cr2O3	1 0 4	2.722	2.666	2.103
4.14c	Alloy 690	1 -1 1	2.080	2.065	0.699
		1 1 -1	2.191	2.065	6.061
		-1 -1 1	2.068	2.065	0.136
		-1 1 -1	2.103	2.065	1.843
		-2 0 0	1.889	1.789	5.598
		2 0 0	2.012	1.789	12.485
		0 2 -2	1.313	1.265	3.796
	Cr2O3	1 0 4	2.683	2.666	0.623
	MO	2 2 0	1.469	1.477	0.524
		2 0 0	2.128	2.089	1.871
4.15b	Alloy 690	1 -1 1	2.080	2.065	0.699
		1 1 -1	2.068	2.065	0.136
		-1 -1 1	2.068	2.065	0.136
		-1 1 -1	2.068	2.065	0.136
		-2 0 0	1.780	1.789	0.494
		2 0 0	1.780	1.789	0.494
	Cr2O3	1 1 0	2.485	2.480	0.184
		-1 -1 0	2.501	2.480	0.861
	MO	3 1 1	1.285	1.259	2.065
		2 0 0	2.092	2.089	0.145
4.16	Cr2O3	1 1 0	2.485	2.480	0.184

		1 1 3	2.140	2.176	1.660
		1 1 6	1.668	1.672	0.265
4.17	Cr2O3	1 1 0	2.702	2.480	1.357
		-1 -1 0	2.663	2.480	0.101
4.31	Cr2O3	1 0 4	2.683	2.666	0.623
		1 0 4	2.702	2.666	1.357
		1 0 4	2.644	2.666	0.814
		1 0 4	2.644	2.666	0.814
		1 1 0	2.501	2.480	0.861
4.32	Cr2O3	1 0 2	3.629	3.633	0.099
		-1 0 -2	3.629	3.633	0.099
		1 0 4	2.644	2.666	0.814
		1 0 4	2.626	2.666	1.518
		1 0 4	2.683	2.666	0.623
		1 1 0	2.485	2.480	0.184
		1 1 0	2.485	2.480	0.184

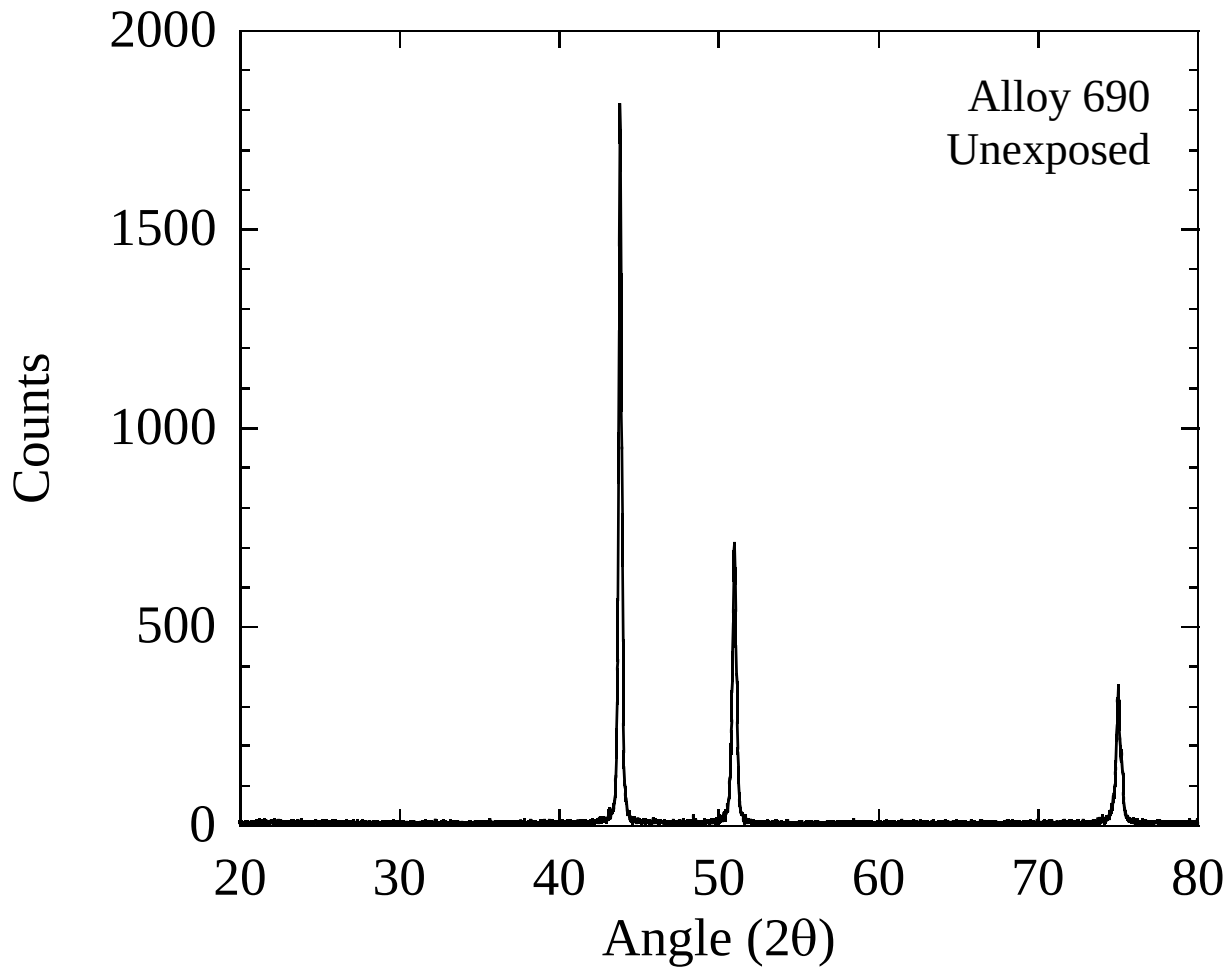

Figure 0.1. XRD of unexposed Alloy 690.

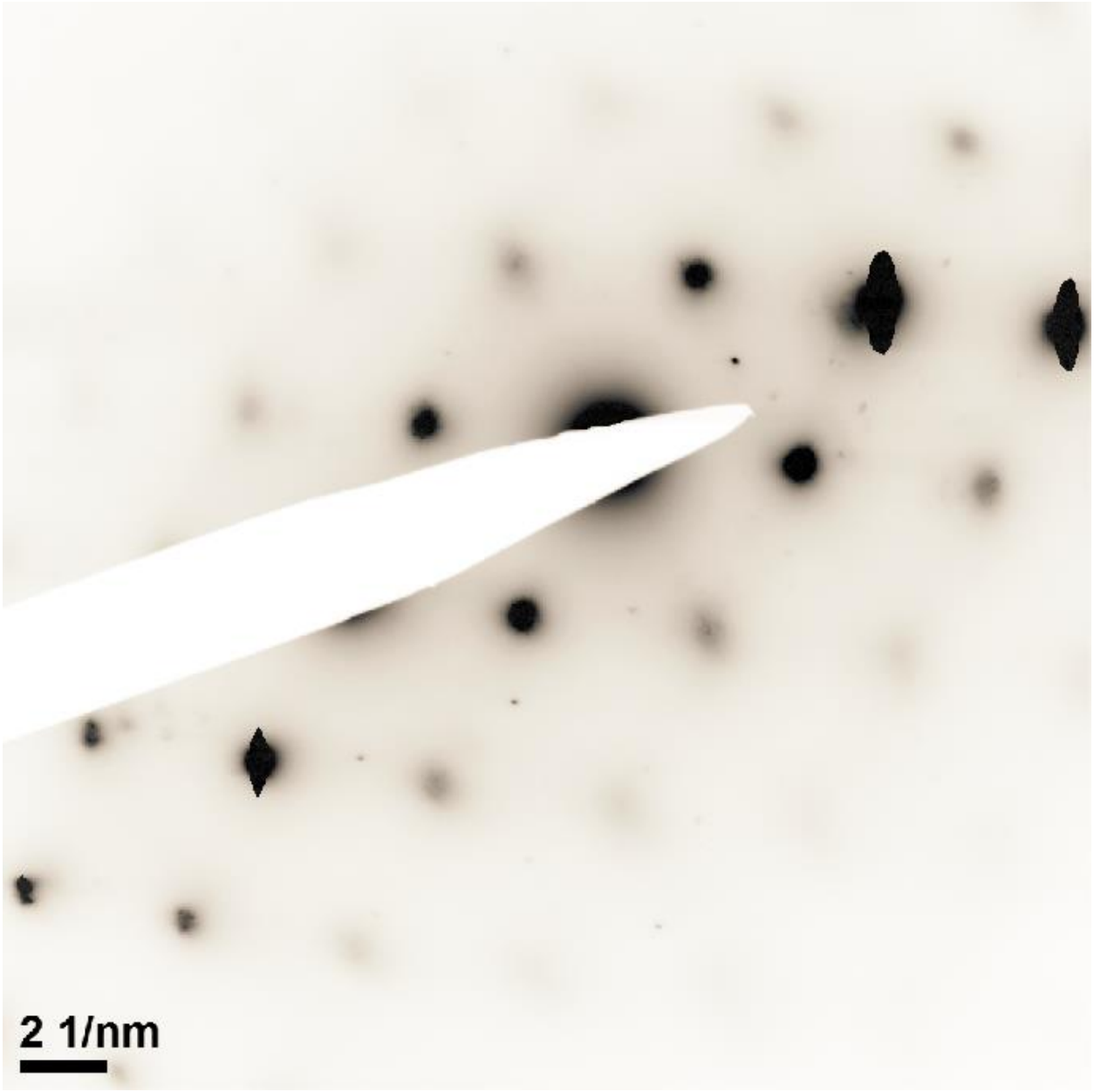

Figure 0.2. Diffraction pattern from Alloy 690 exposed at 400°C for 250 hrs of internal oxide (Figure 4.15b).

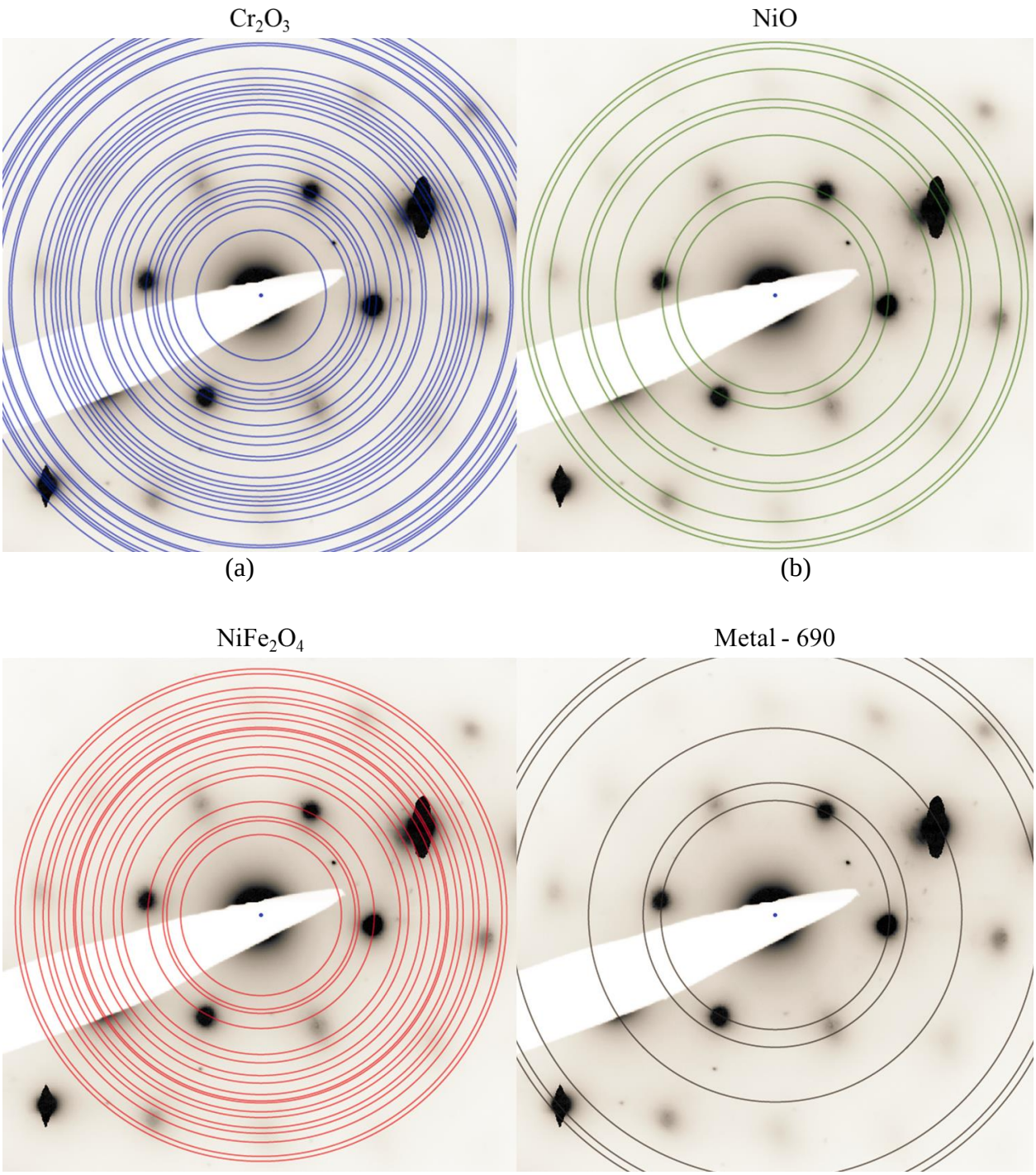

Figure 0.3. Indexing of Figure 0.2 with rings indicating plane spacing for (a) Cr_2O_3, (b) NiO, (c) $NiFe_2O_4$, and Alloy 690 metal.

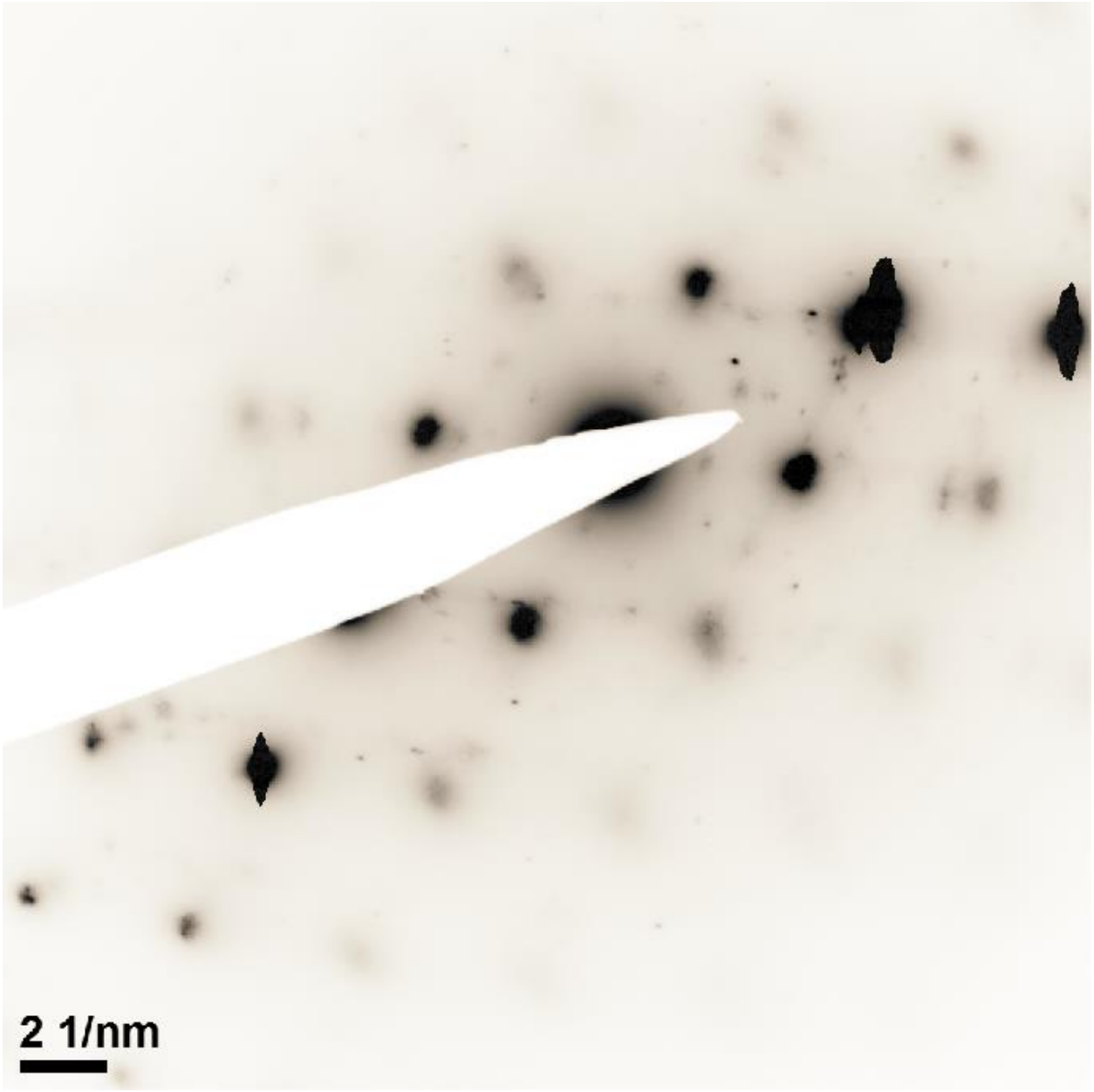

Figure 0.4. Diffraction pattern from Alloy 690 exposed at 400°C for 250 hrs of surface and internal oxide (Figure 4.15c).

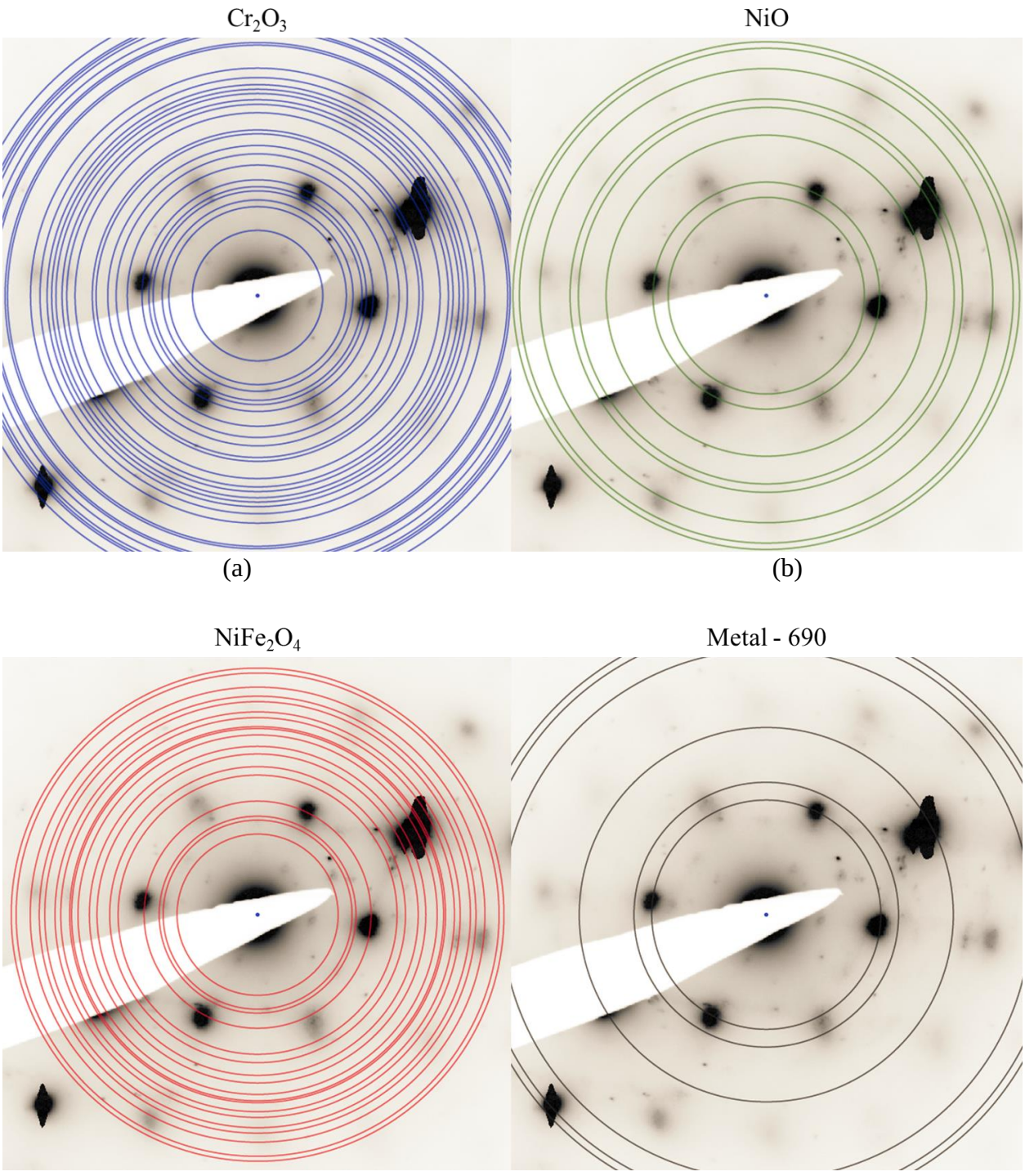

Figure 0.5. Indexing of Figure 0.4 with rings indicating plane spacing for (a) Cr_2O_3, (b) NiO, (c) $NiFe_2O_4$, and Alloy 690 metal.

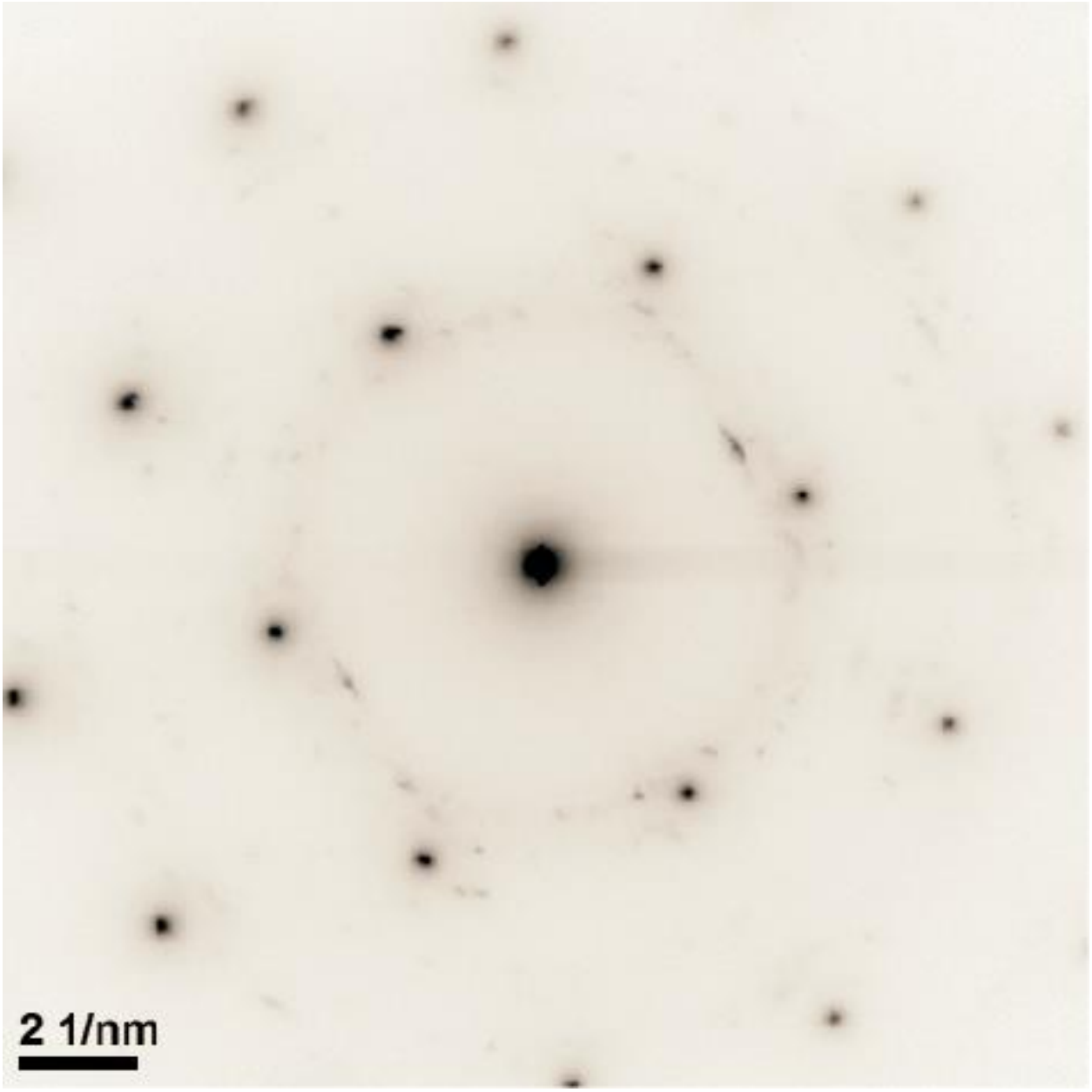

Figure 0.6. Diffraction pattern from Alloy 690 exposed at 360°C for 2000 hrs of surface and internal oxide (Figure 4.16b).

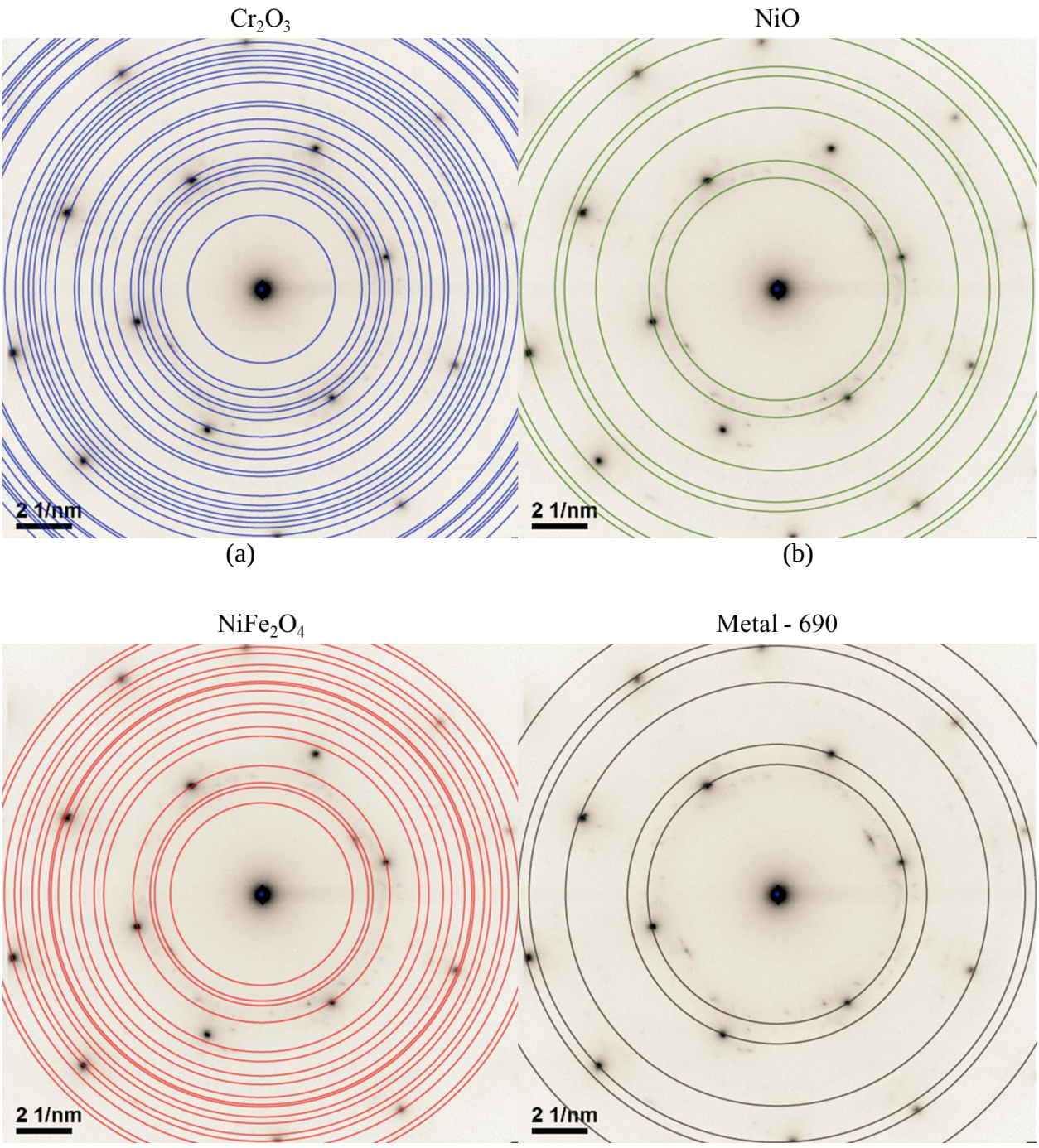

Figure 0.7. Indexing of Figure 0.6 with rings indicating plane spacing for (a) Cr_2O_3, (b) NiO, (c) $NiFe_2O_4$, and Alloy 690 metal.

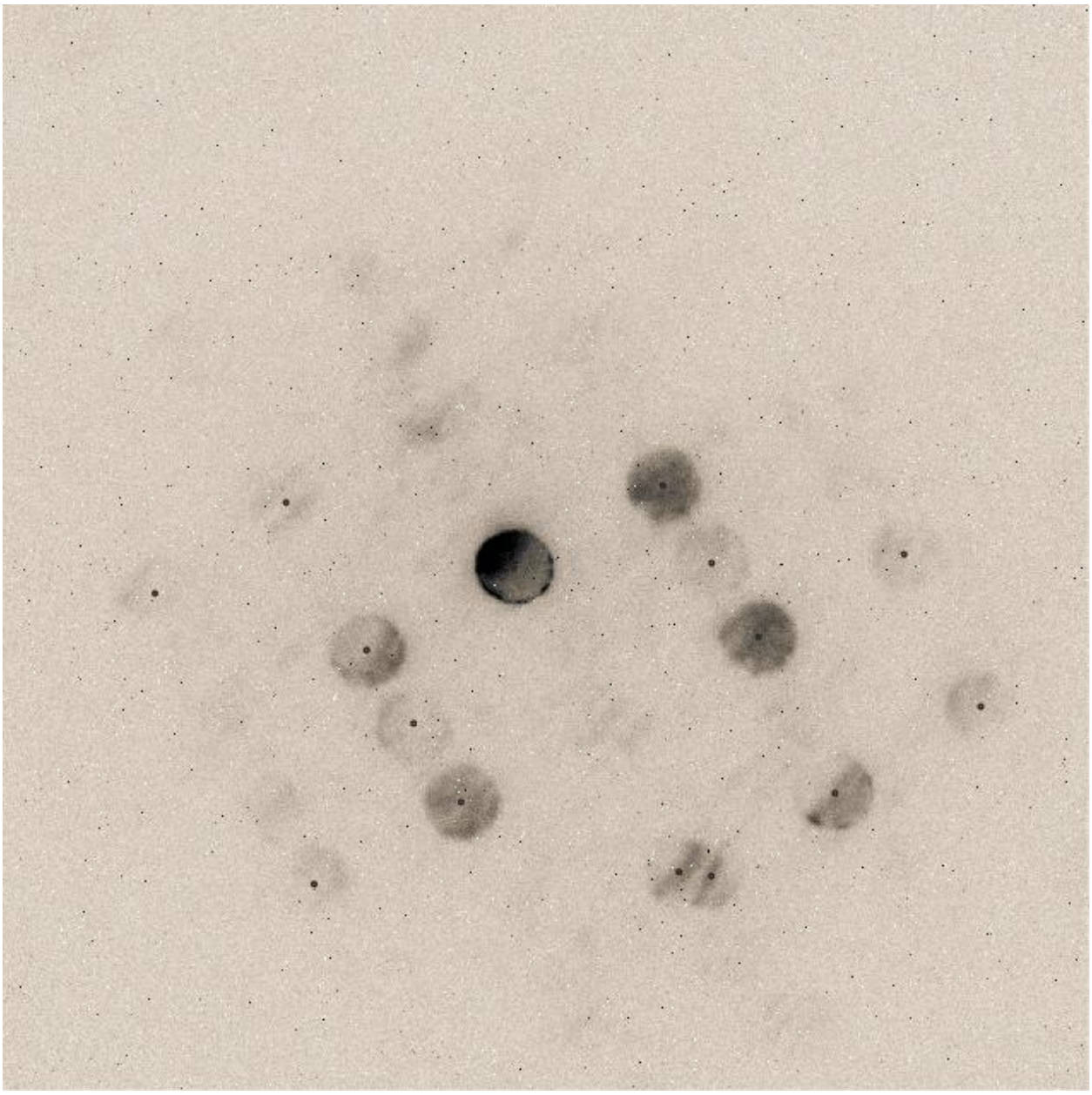

Figure 0.8. Nano-diffraction pattern from Alloy 690 exposed at 360°C for 2000 hrs of the surface oxide above a grain boundary (Figure 4.17).

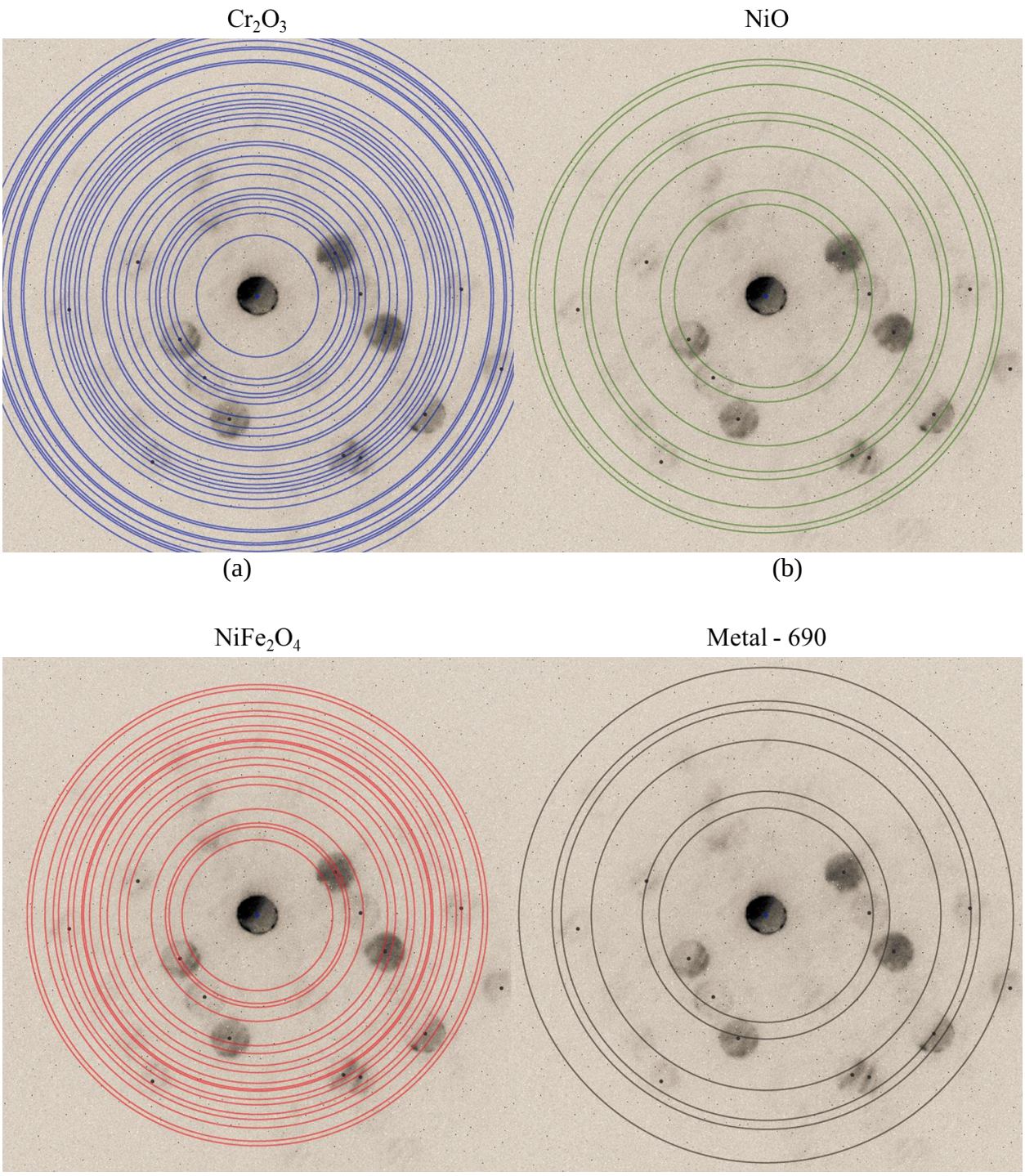

Figure 0.9. Indexing of Figure 0.8 with rings indicating plane spacing for (a) Cr_2O_3, (b) NiO, (c) $NiFe_2O_4$, and Alloy 690 metal.

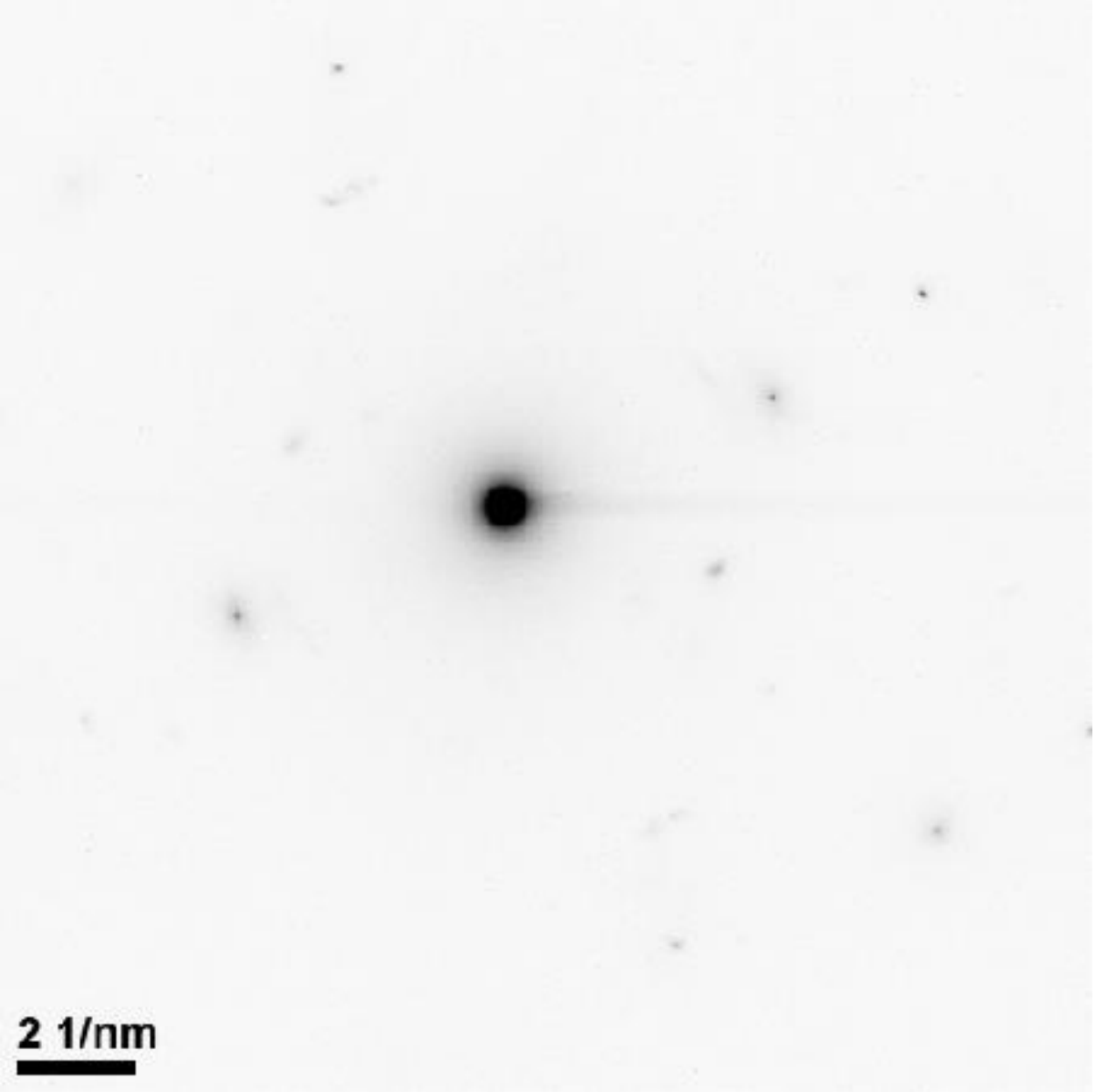

Figure 0.10. Diffraction pattern from Alloy 690 exposed at 360°C for 2000 hrs of surface and internal oxide (Figure 4.18a).

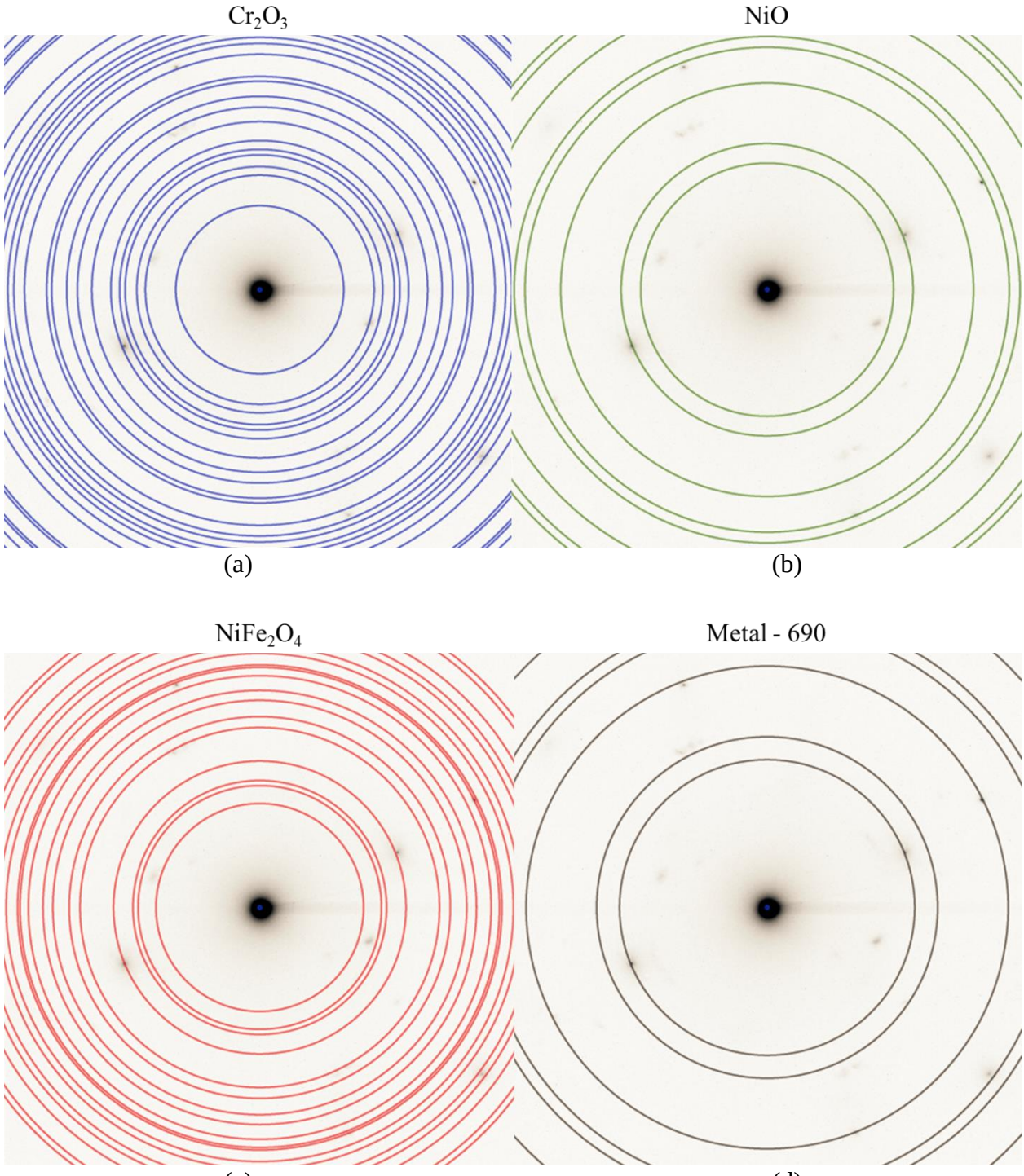

Figure 0.11. Indexing of Figure 0.10 with rings indicating plane spacing for (a) Cr_2O_3, (b) NiO, (c) $NiFe_2O_4$, and Alloy 690 metal.

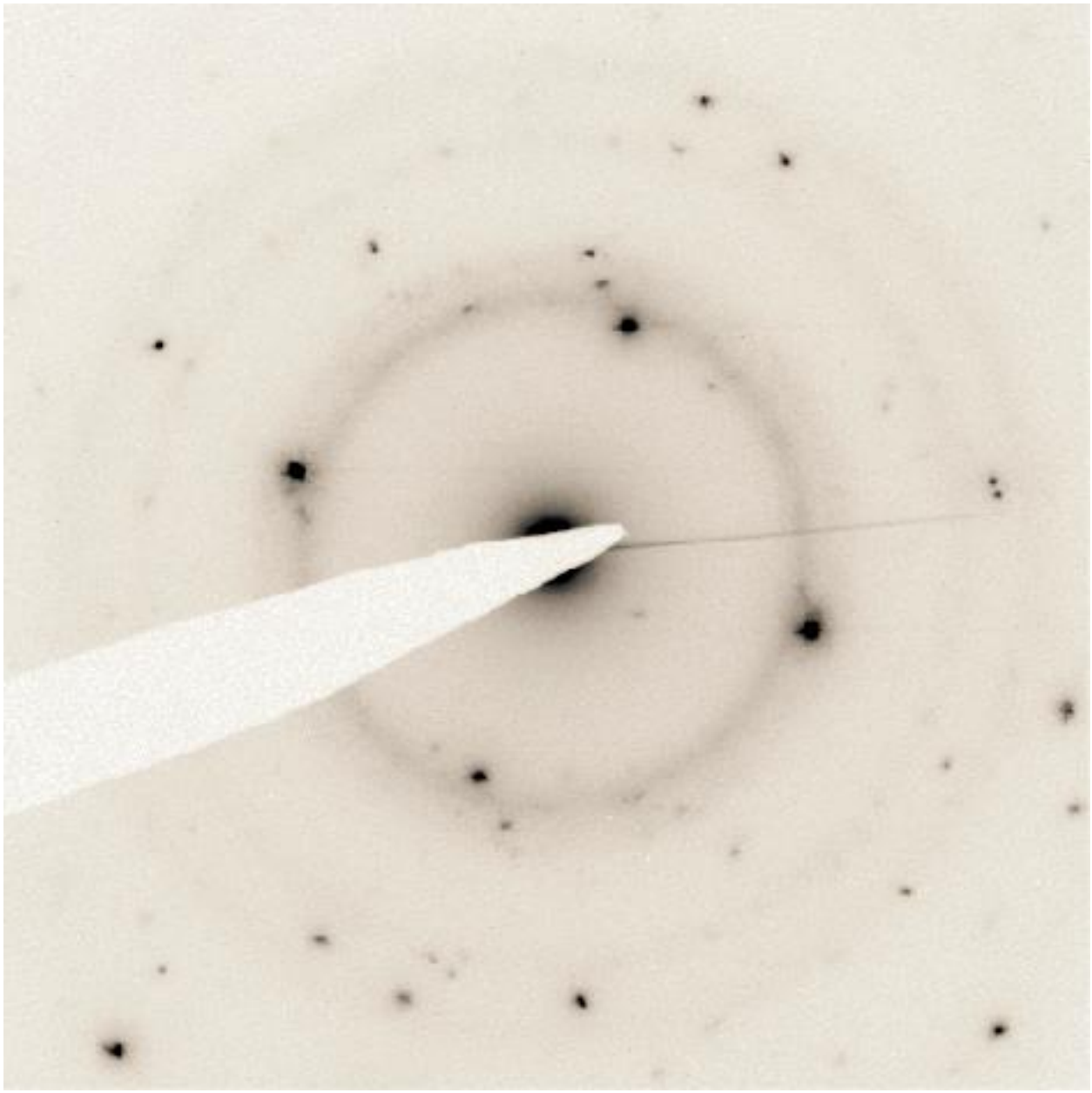

Figure 0.12. Diffraction pattern from a crack in Alloy 690 strained at 400°C of oxides filling the crack (Figure 4.35b).

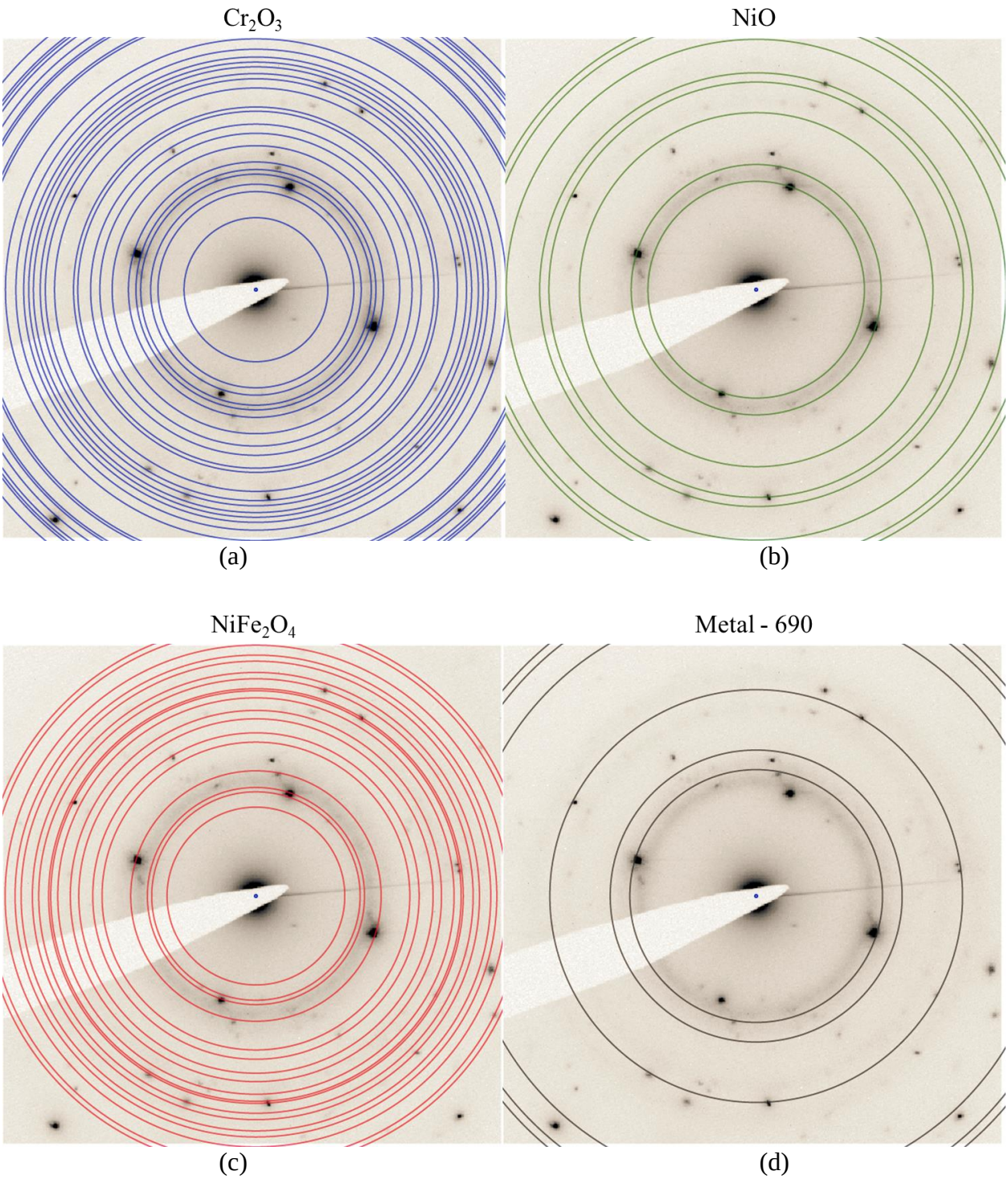

Figure 0.13. Indexing of Figure 0.12 with rings indicating plane spacing for (a) Cr_2O_3, (b) NiO, (c) $NiFe_2O_4$, and Alloy 690 metal.

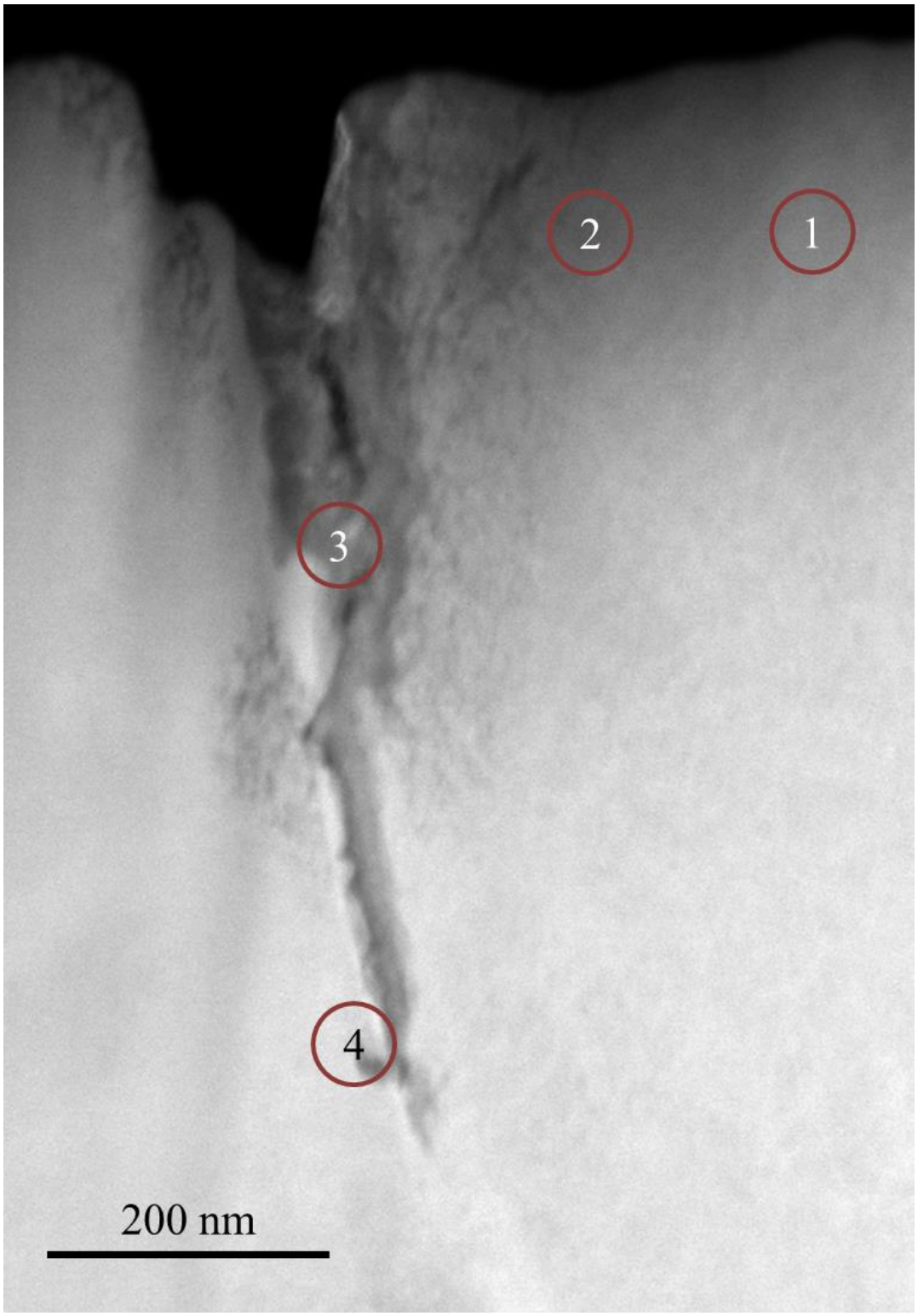

(a)

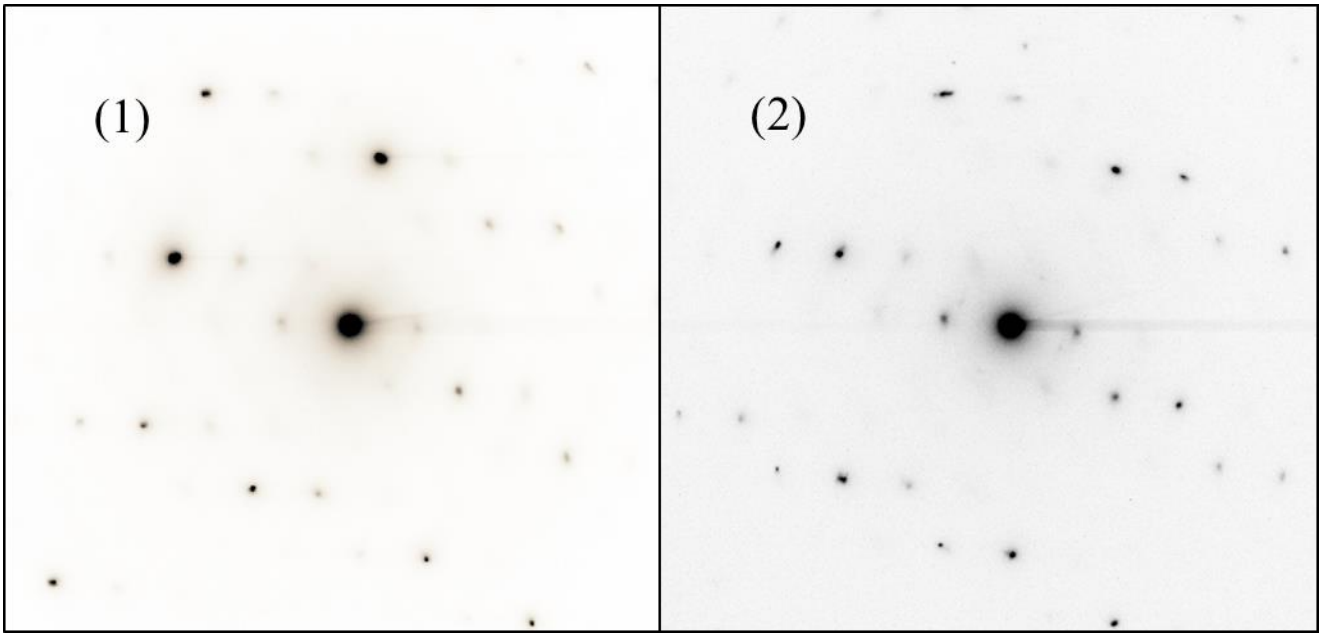

(b) (c)

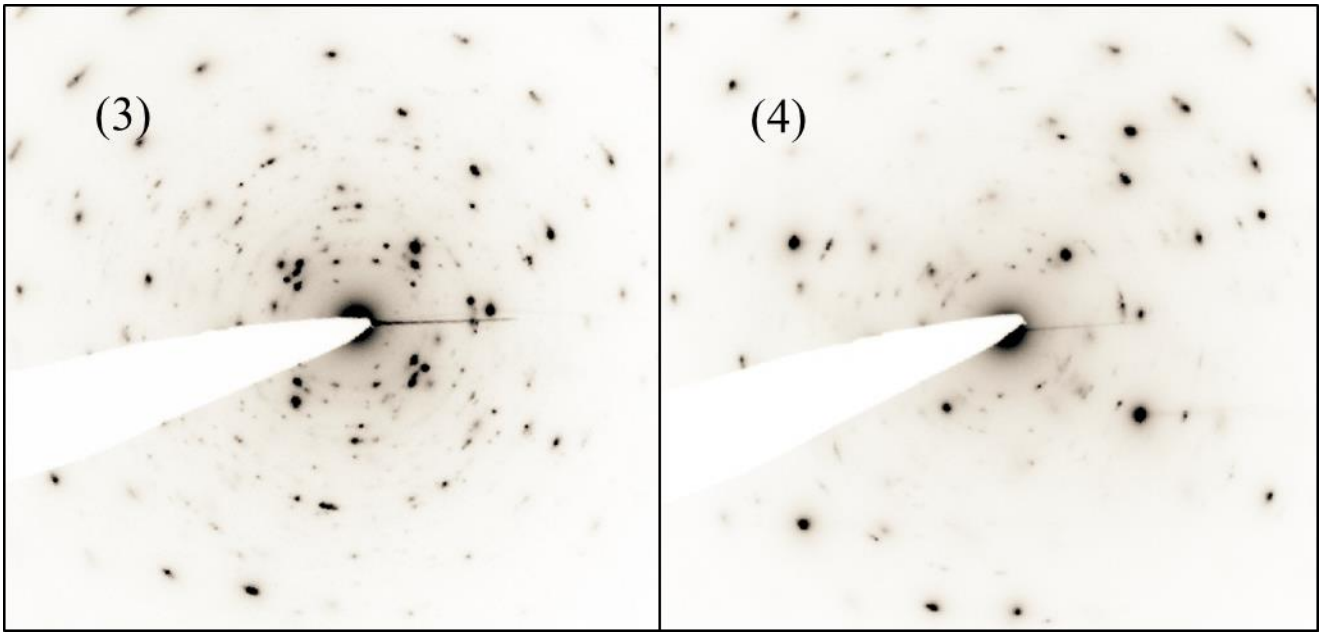

(d) (e)

Figure 0.14. (a) STEM image of a crack in Alloy 690 strained at 360°C with diffraction patterns taken from area (b) 1, (c) 2, (d) 3 - Figure 4.33c, and (e) 4 - Figure 4.33b.

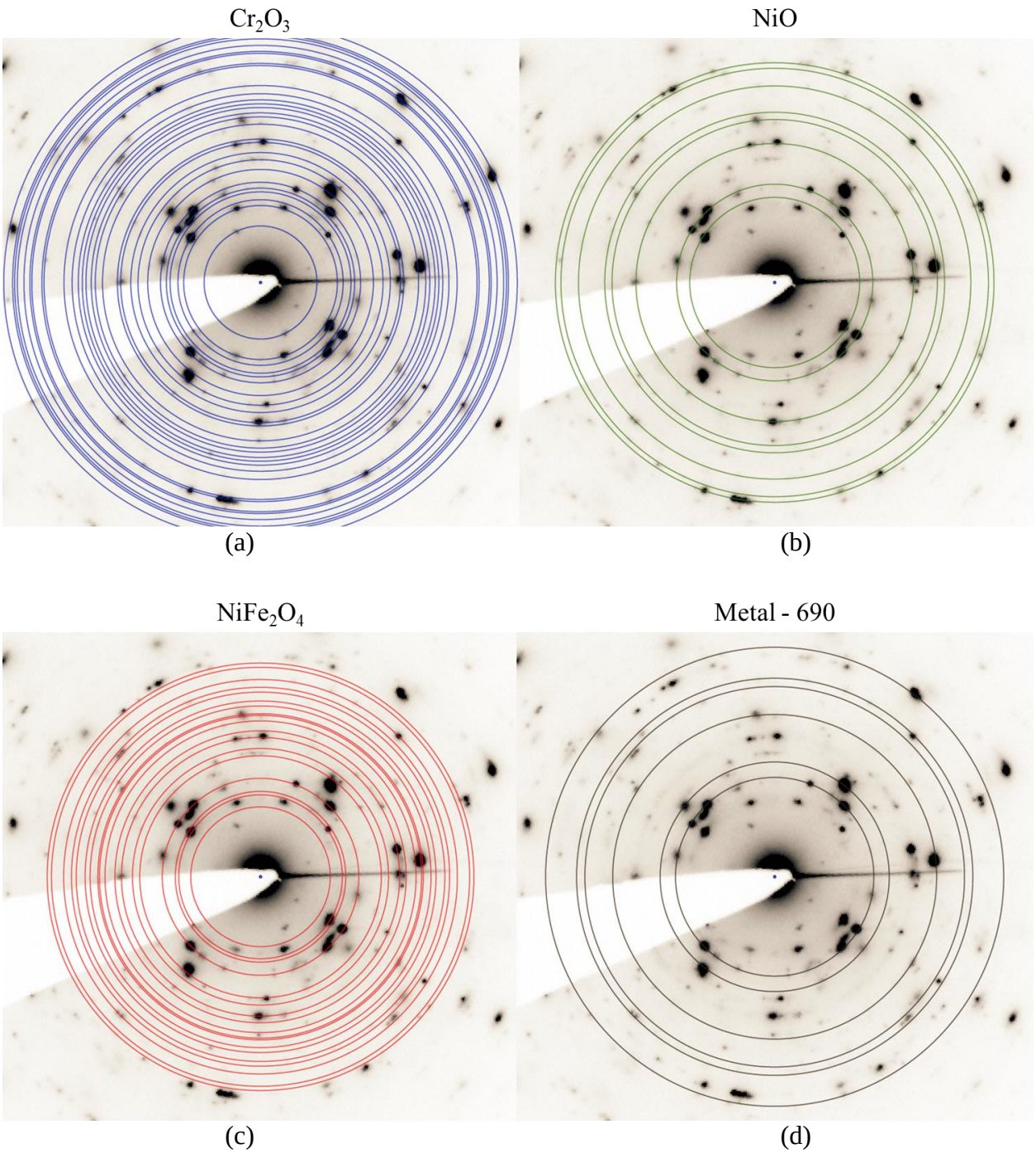

Figure 0.15. Indexing of Figure 0.14d with rings indicating plane spacing for (a) Cr_2O_3, (b) NiO, (c) $NiFe_2O_4$, and Alloy 690 metal.

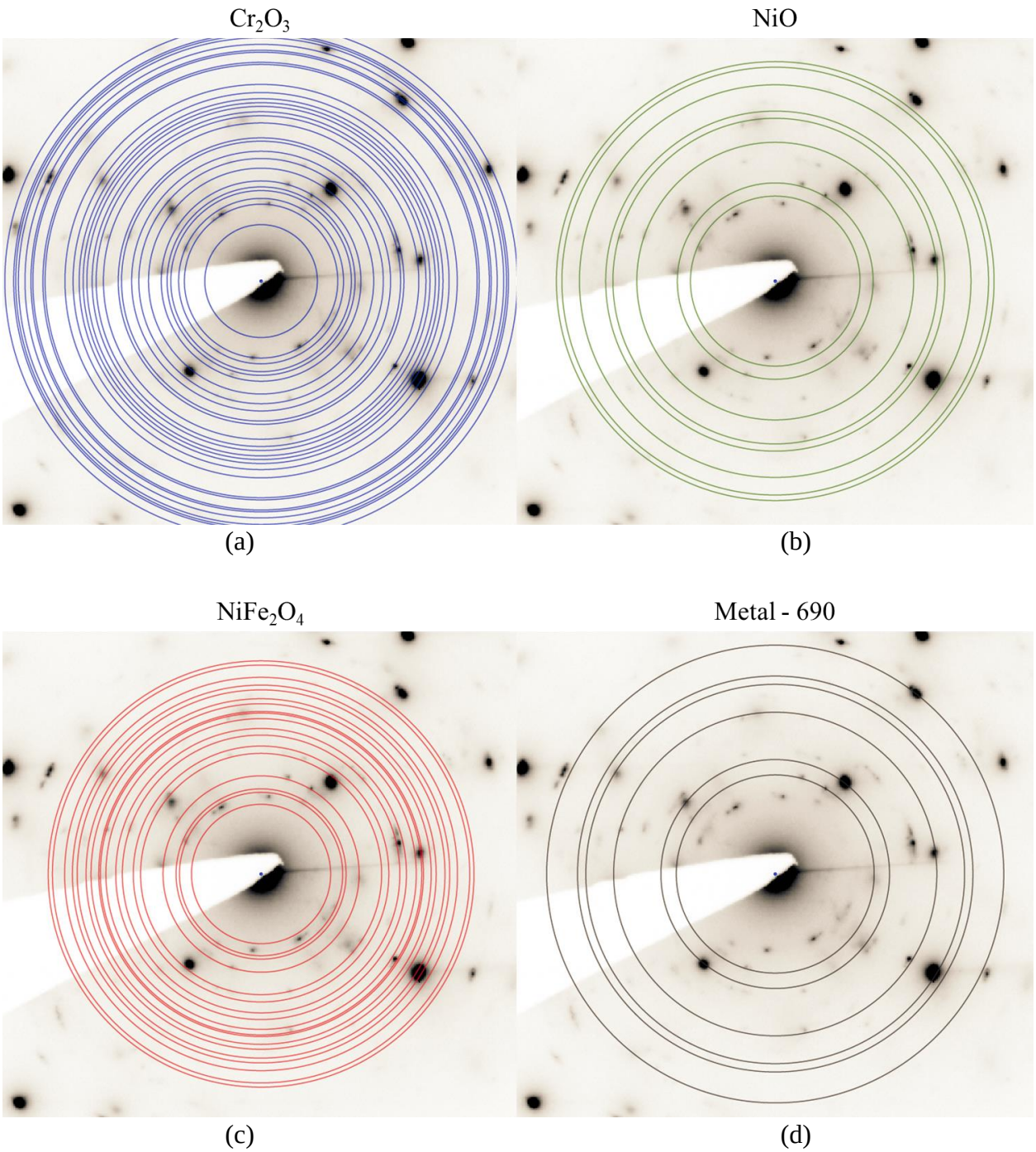

Figure 0.16. Indexing of Figure 0.14e with rings indicating plane spacing for (a) Cr_2O_3, (b) NiO, (c) $NiFe_2O_4$, and Alloy 690 metal.

APPENDIX B:
SUPPLEMENTARY CRACK INITIATION IMAGES

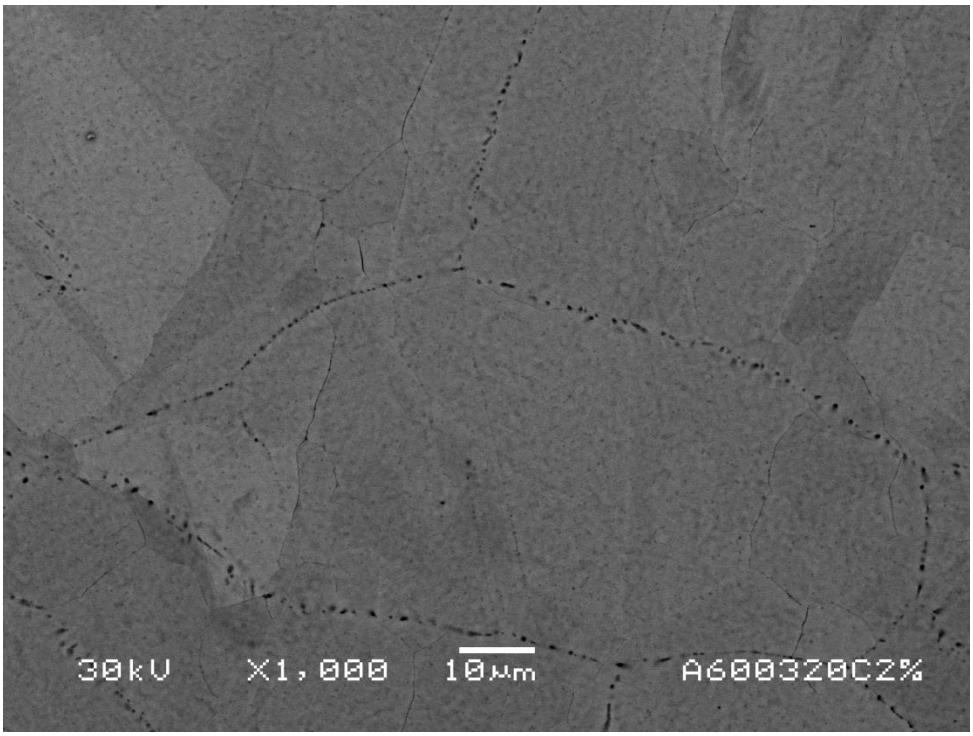

(a)

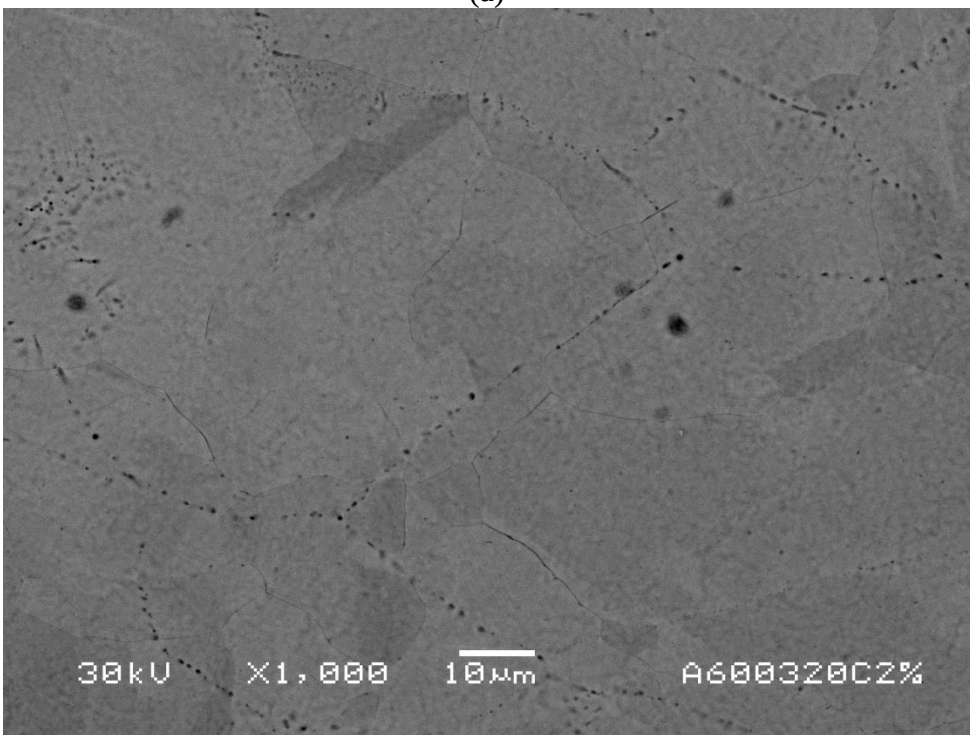

(b)

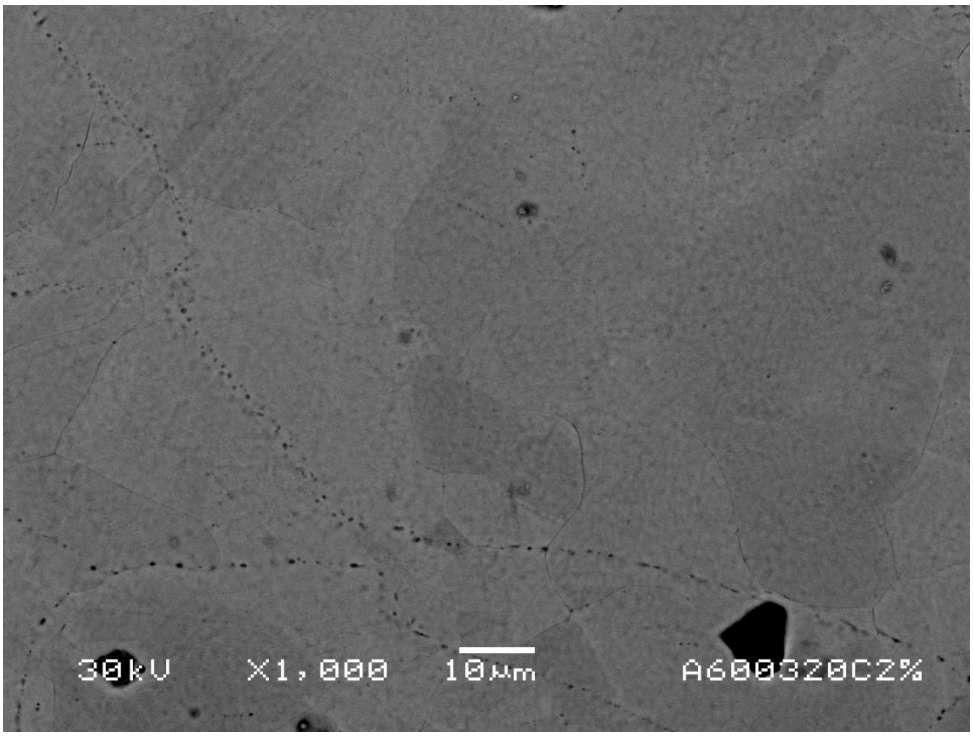

(c)

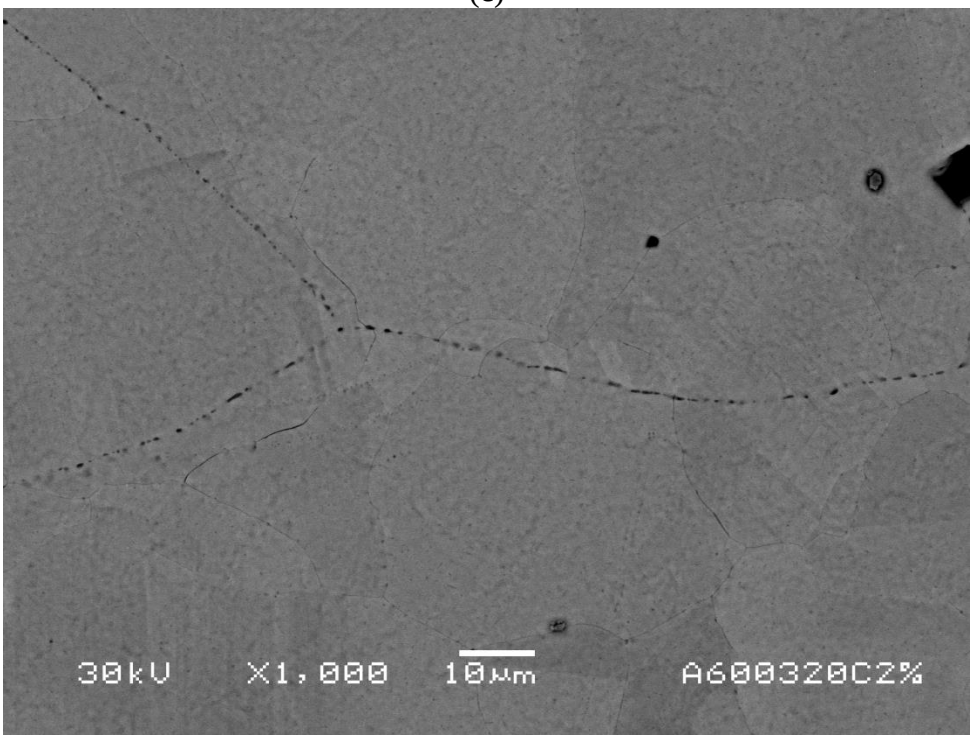

(d)

Figure 0.17. (a-d) Gauge surface of Alloy 600 strained to 2% in 320°C water at $3x10^{-7}$ s^{-1}.

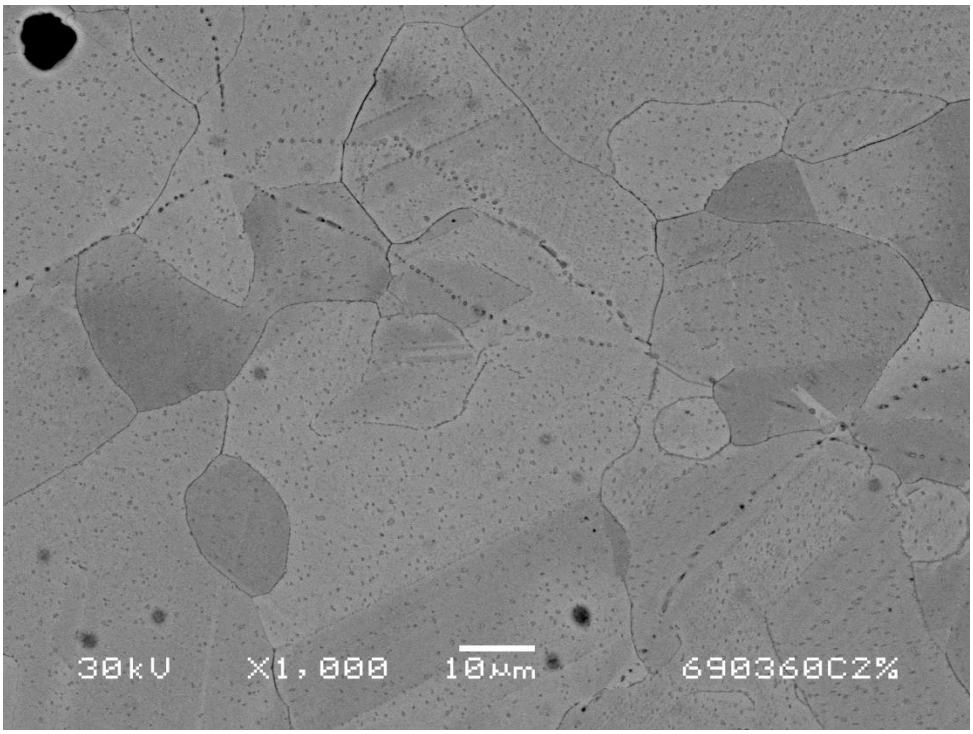

(a)

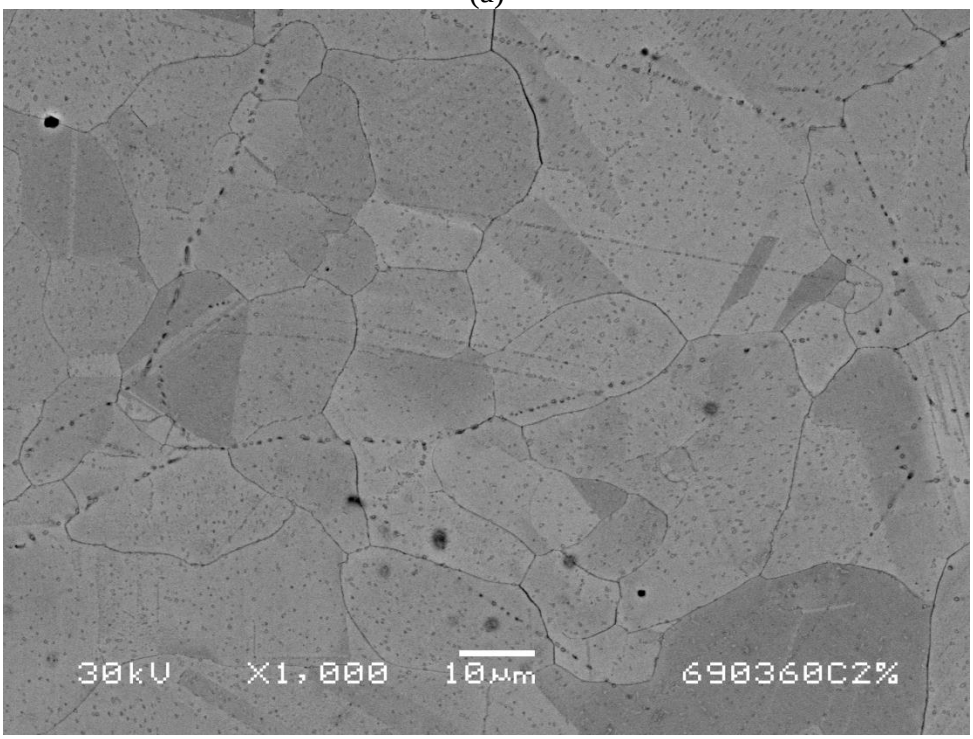

(b)

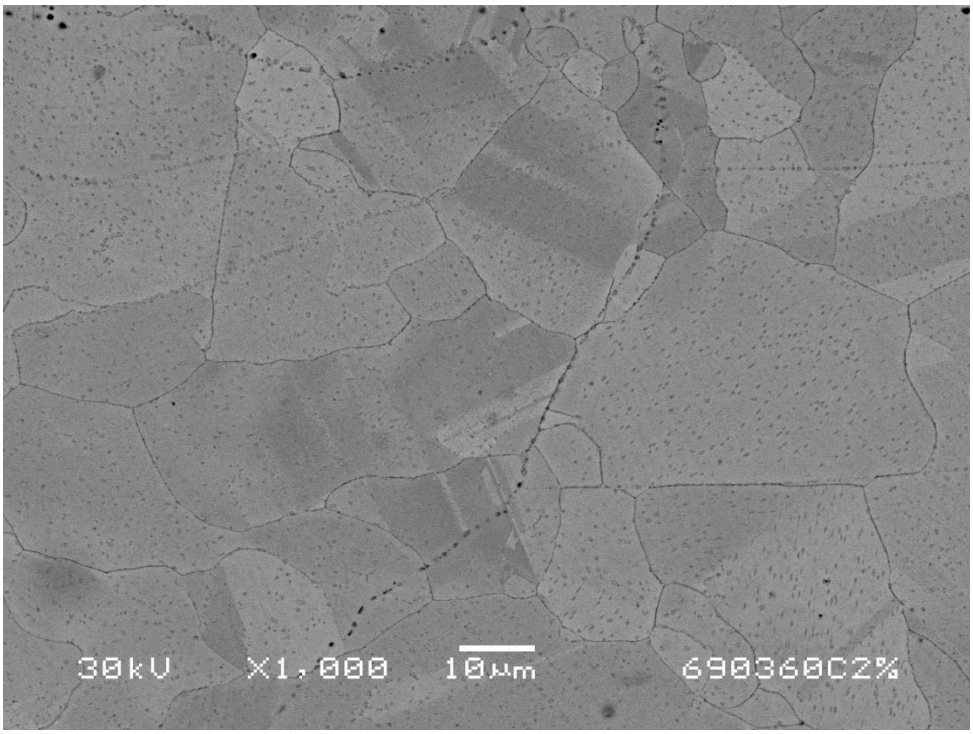

(c)

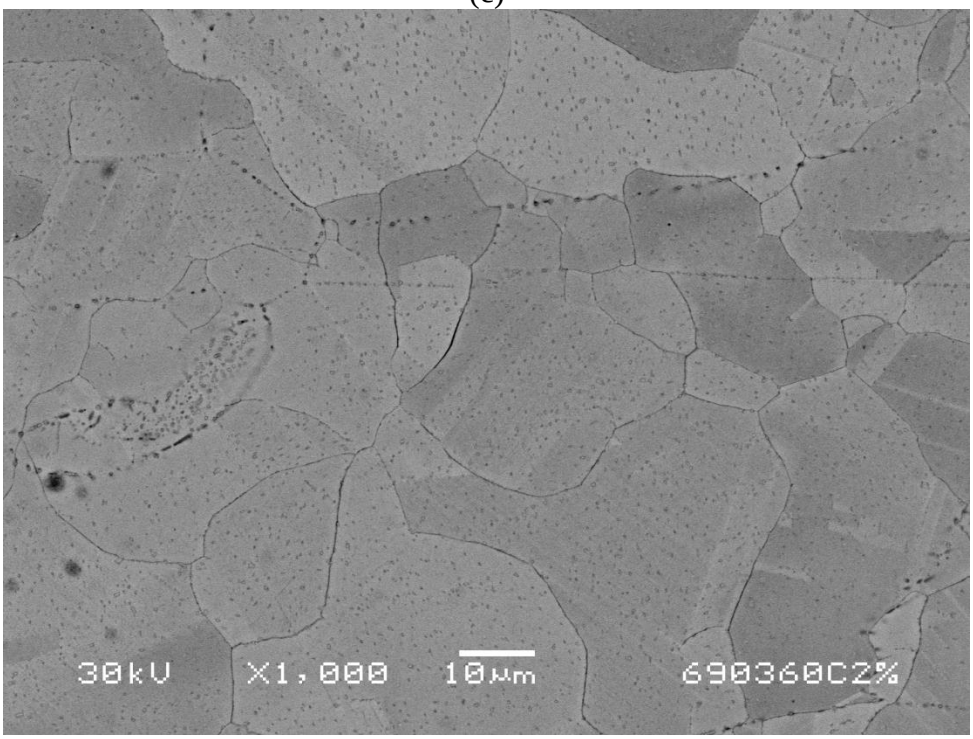

(d)

Figure 0.18. (a-d) Gauge surface of Alloy 600 strained to 2% in 360°C water at $3x10^{-7}$ s^{-1}.

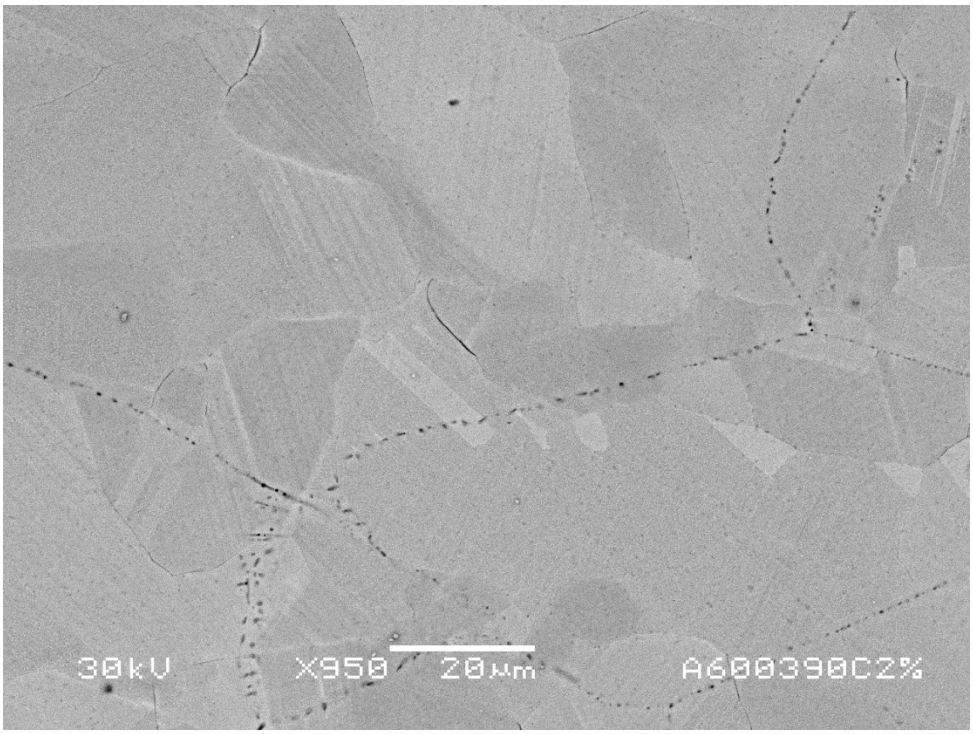

(a)

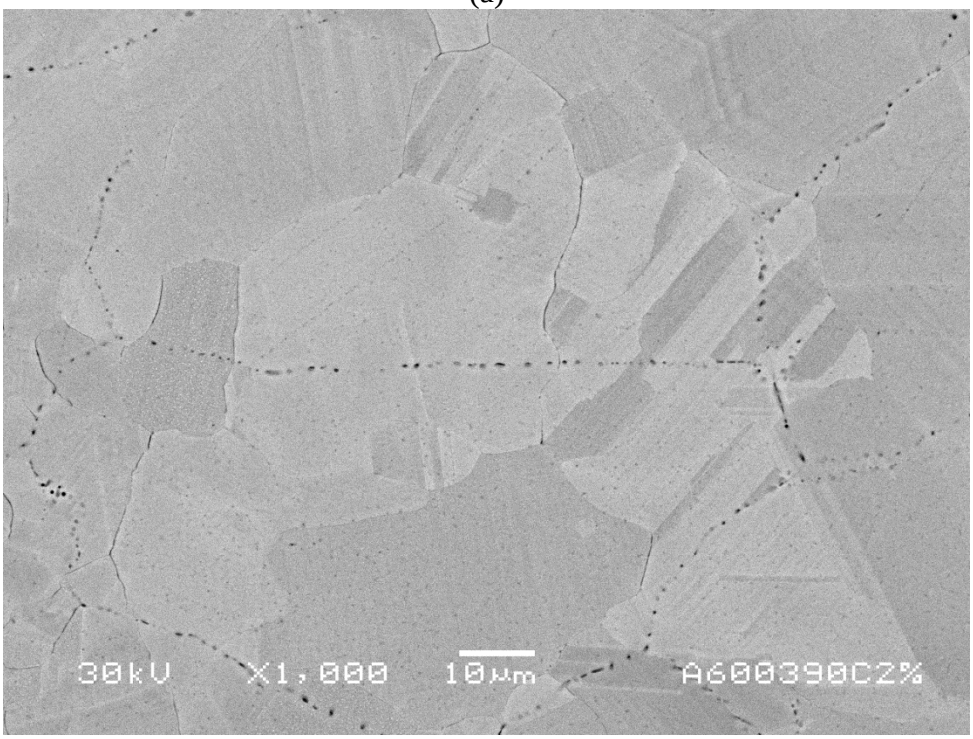

(b)

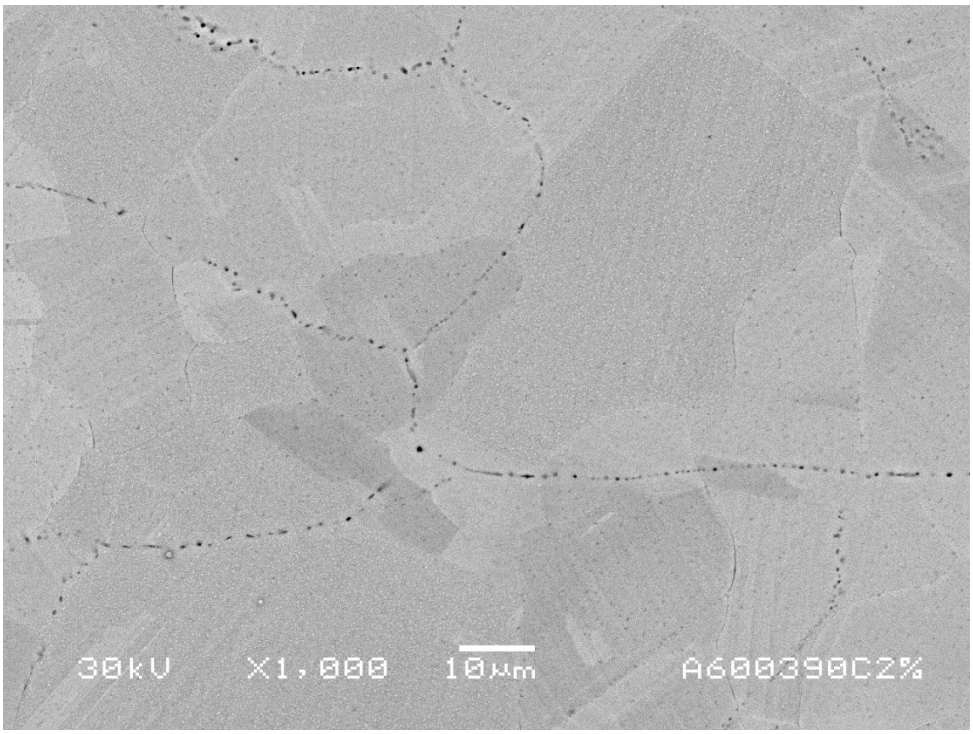

(c)

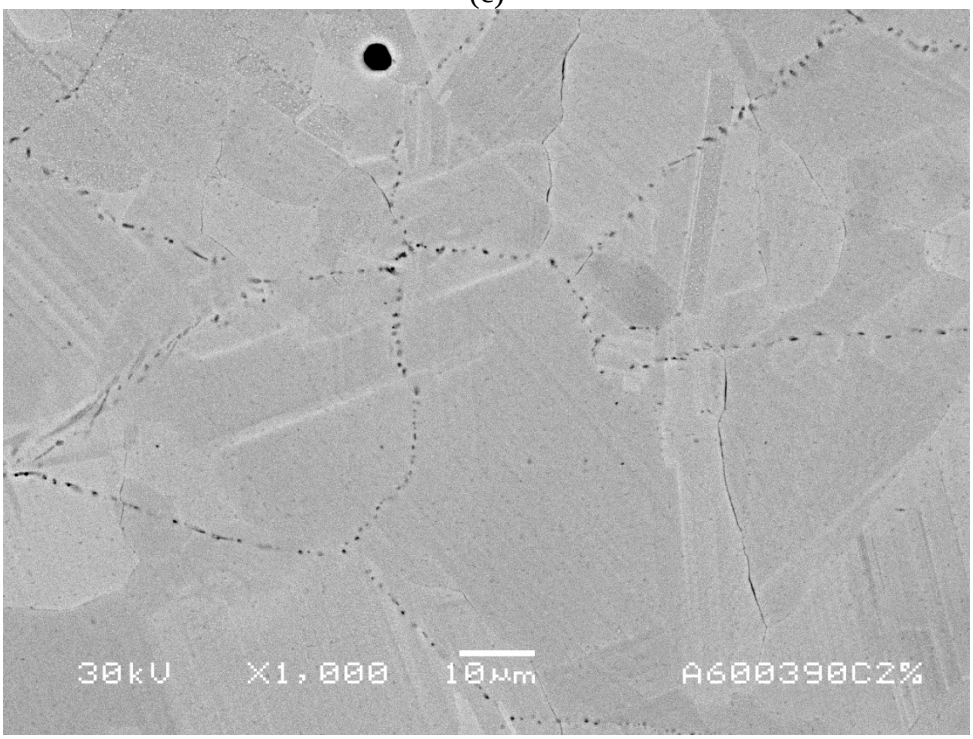

(d)

Figure 0.19. (a-d) Gauge surface of Alloy 600 strained to 2% in 390°C water at $3x10^{-7}$ s^{-1}.

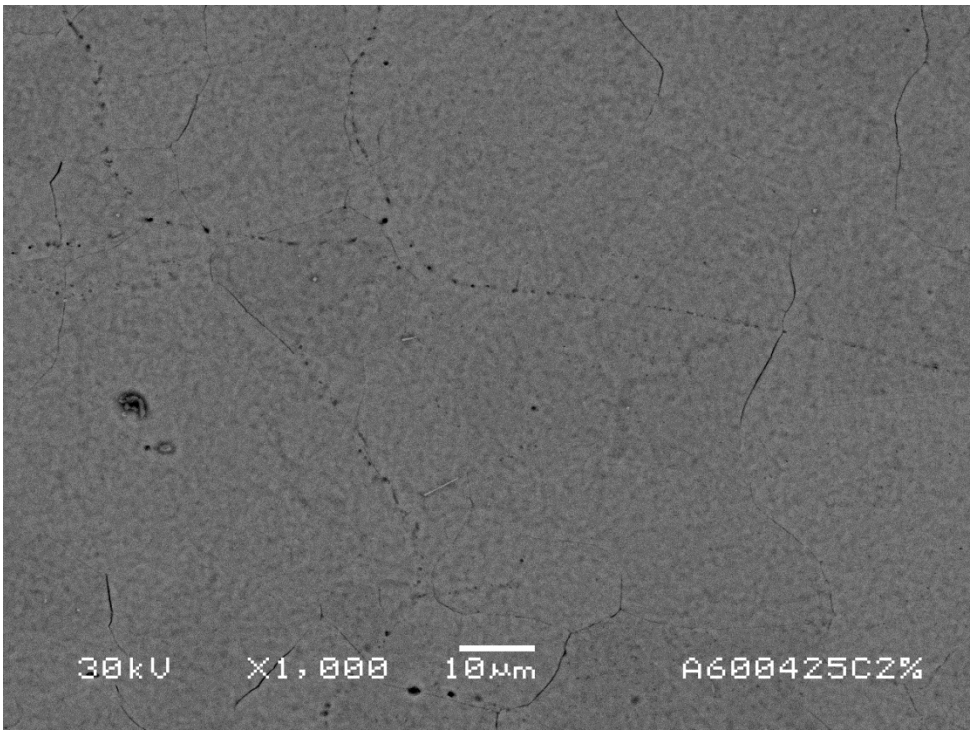

(a)

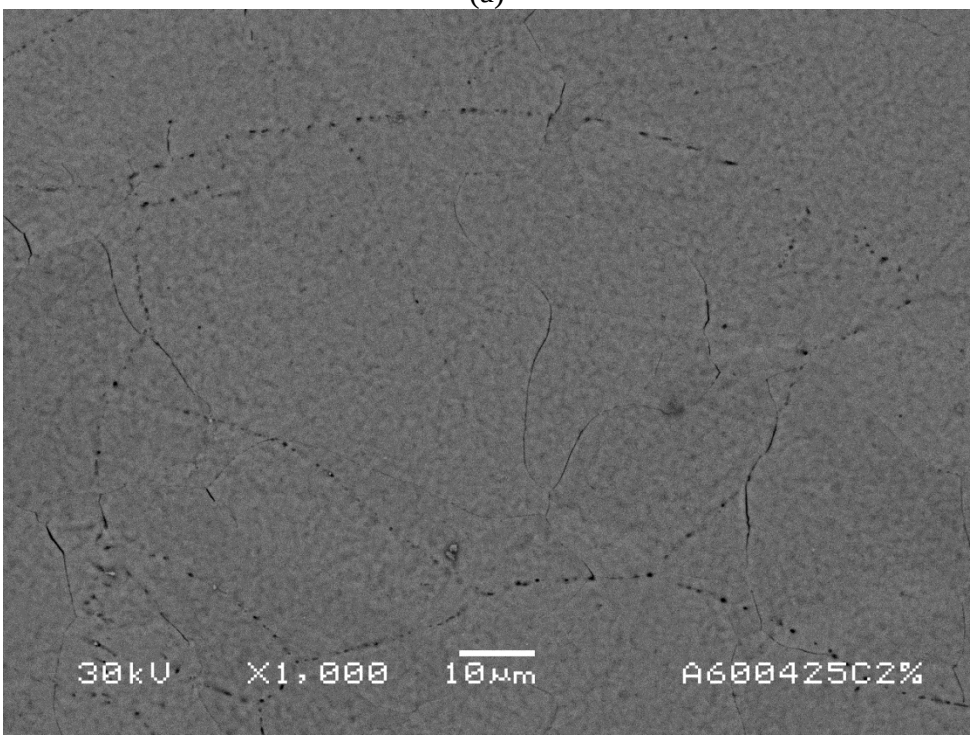

(b)

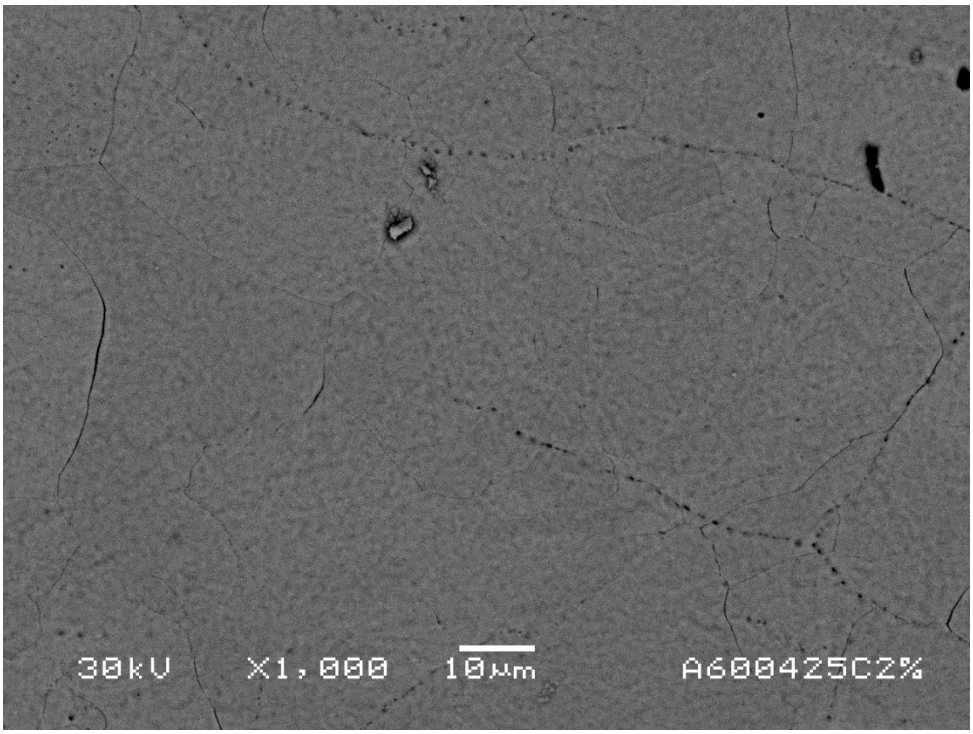

(c)

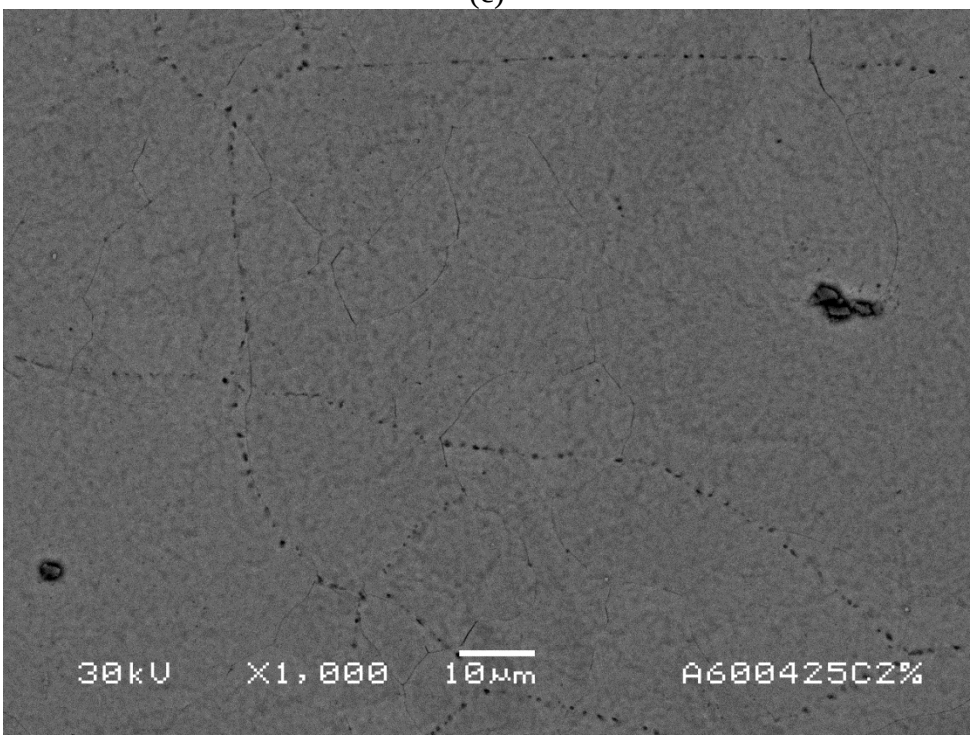

(d)

Figure 0.20. (a-d) Gauge surface of Alloy 600 strained to 2% in 425°C water at $3x10^{-7}$ s^{-1}.

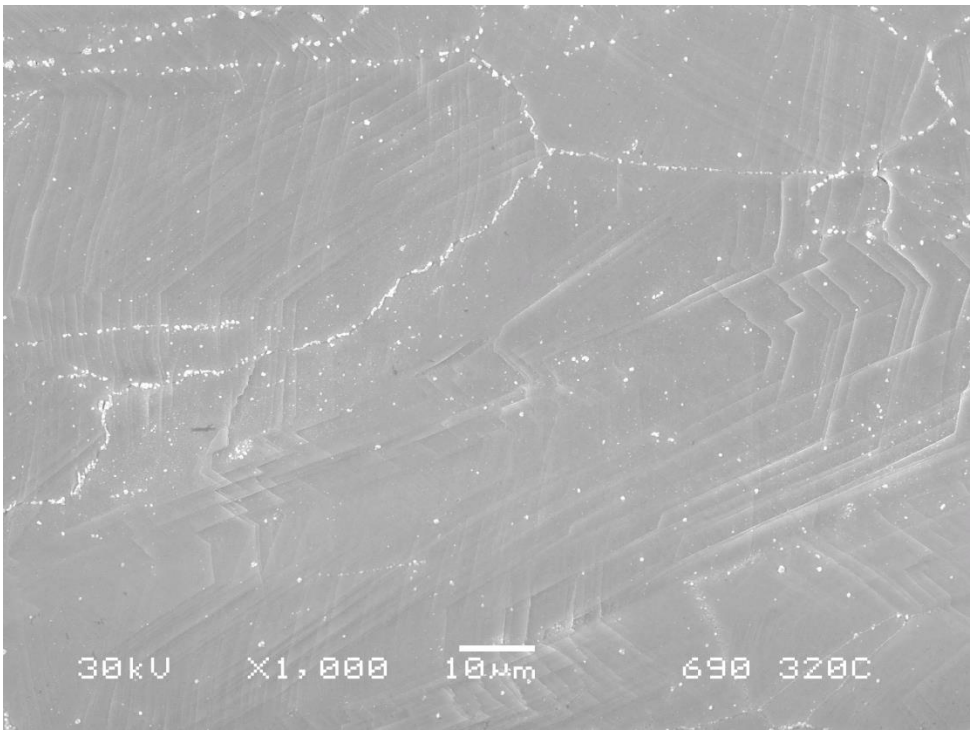

(a)

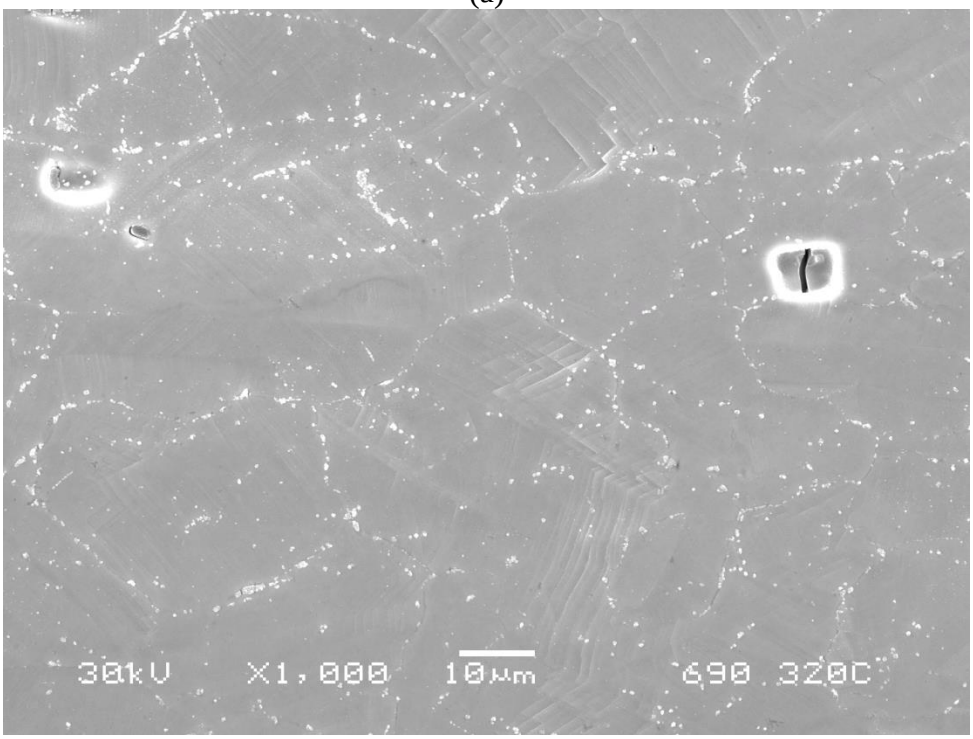

(b)

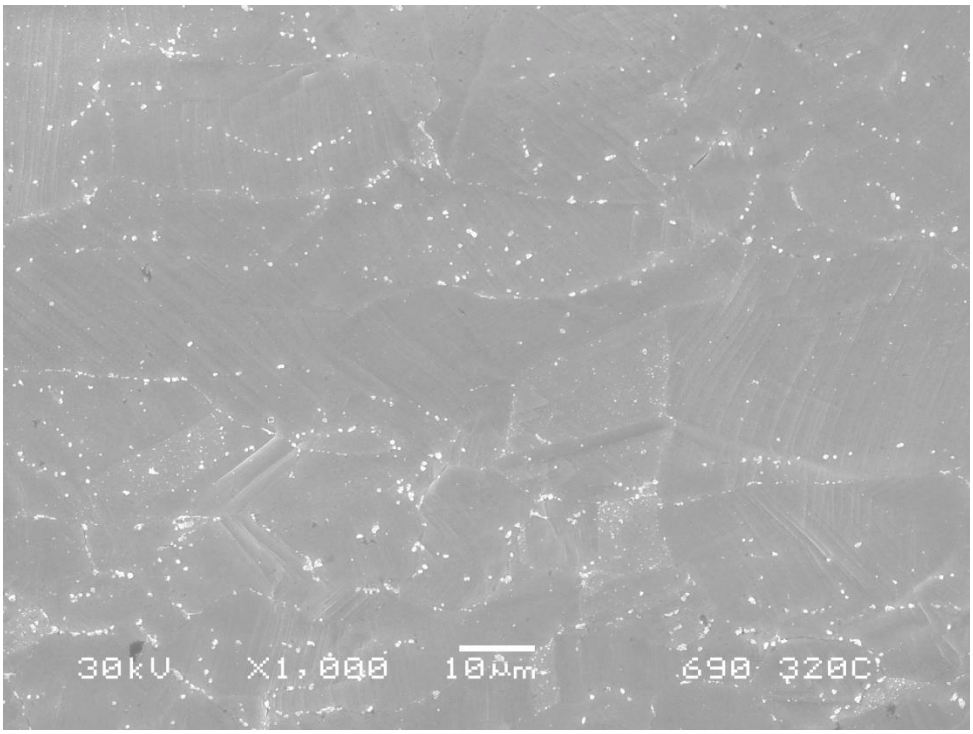

(c)

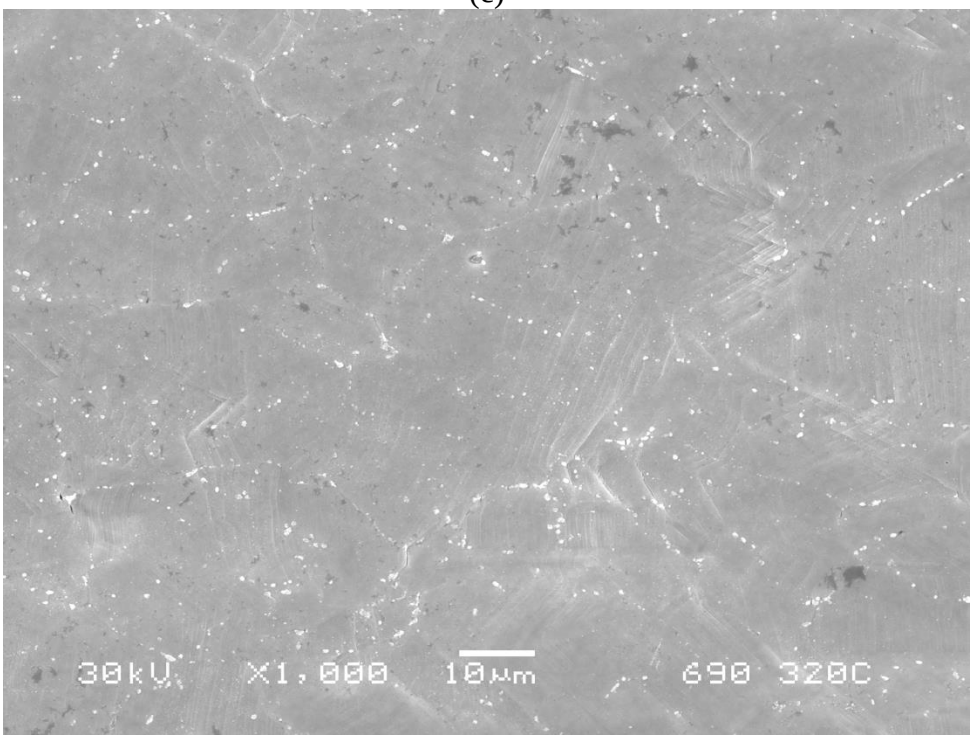

(d)

Figure 0.21. (a-d) Gauge surface of pre-strained Alloy 690 strained to 7% in 320°C water at $5x10^{-8}$ s^{-1}.

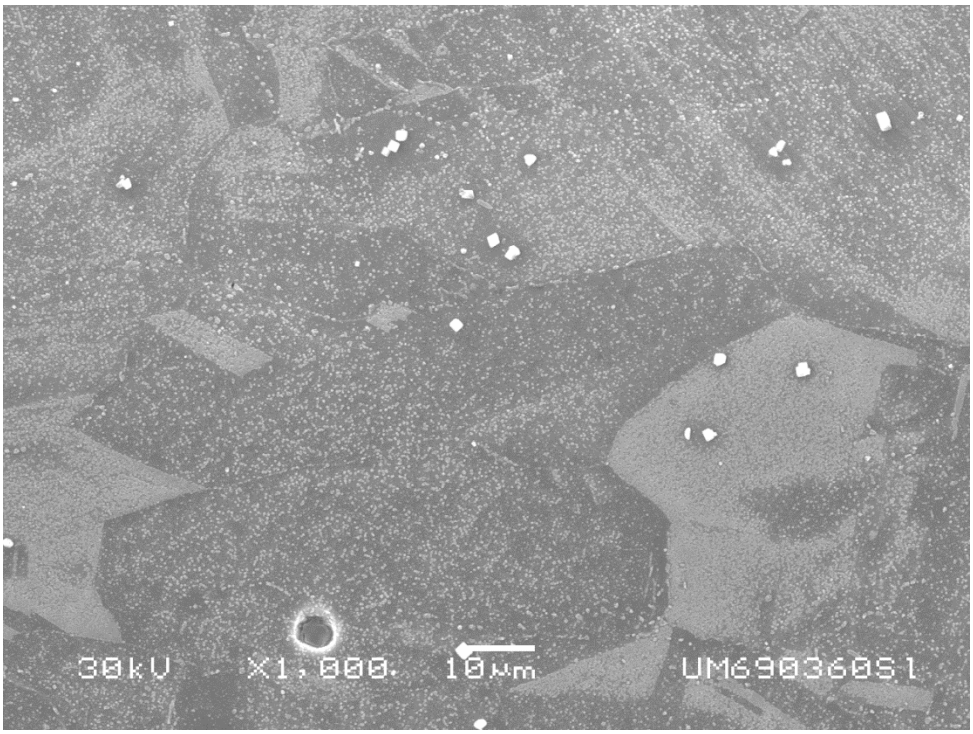

(a)

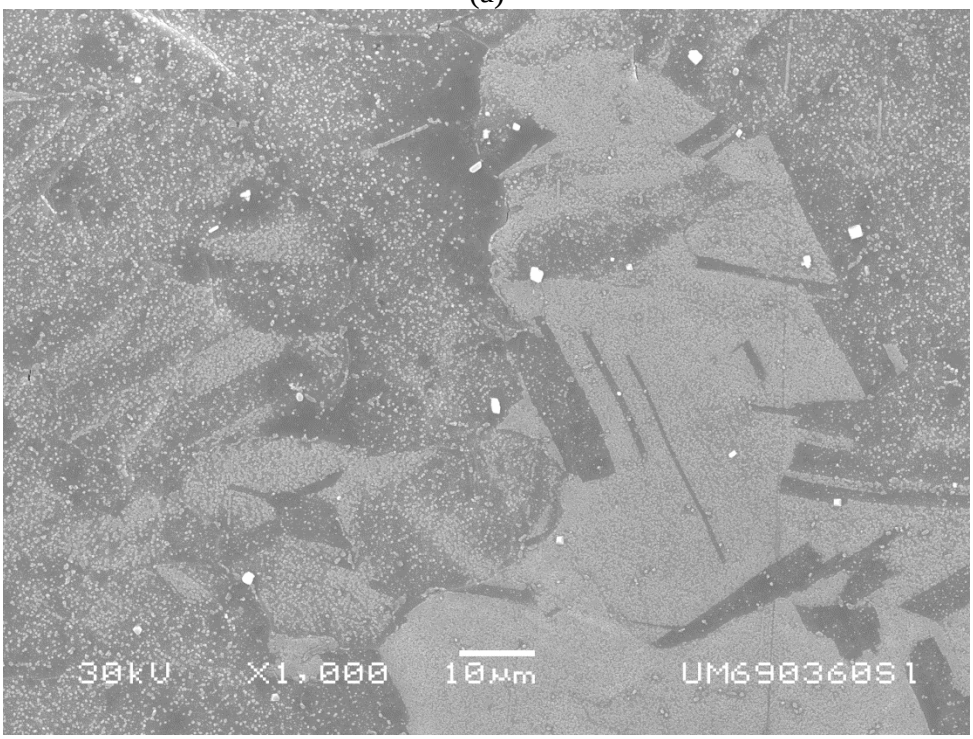

(b)

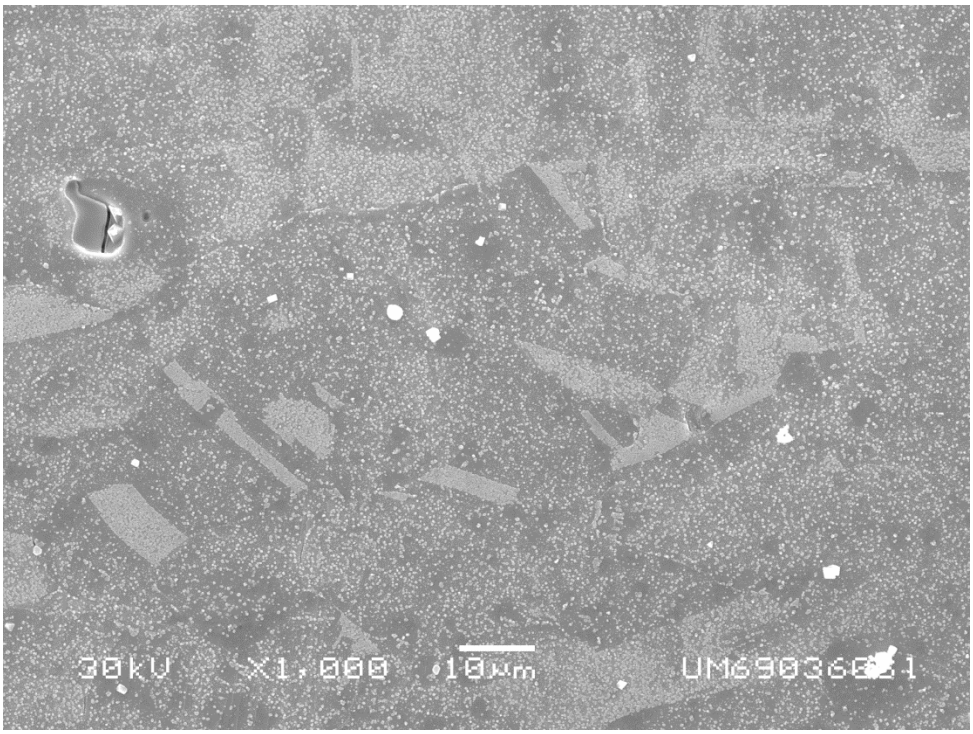

(c)

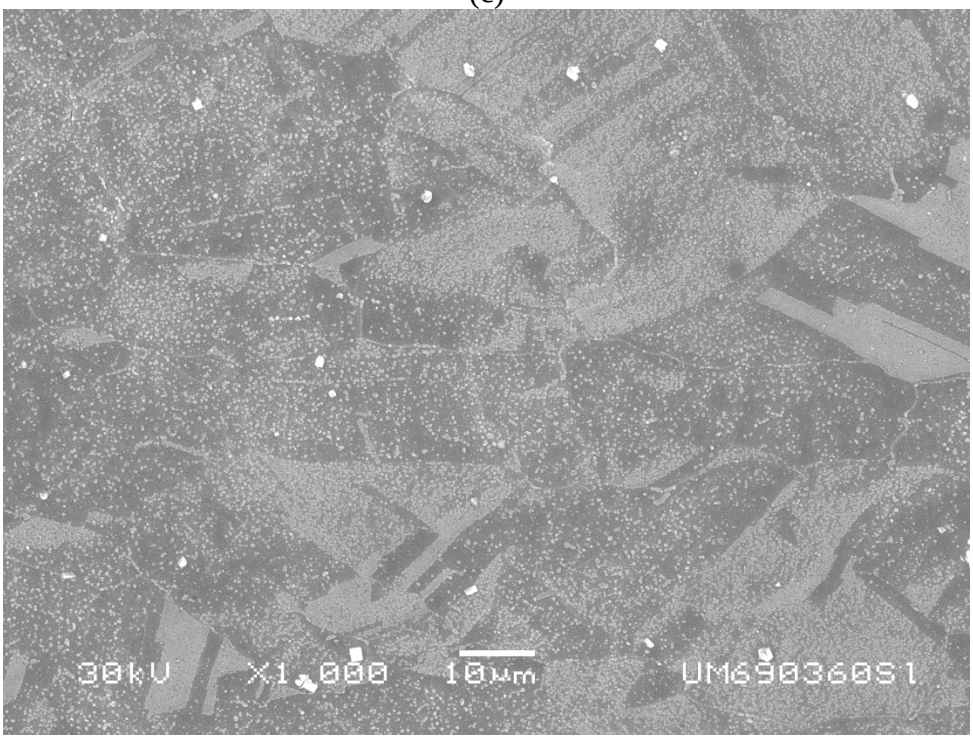

(d)

Figure 0.22. (a-d) Gauge surface of pre-strained Alloy 690 strained to 7% in 360°C water at $5x10^{-8}$ s^{-1}.

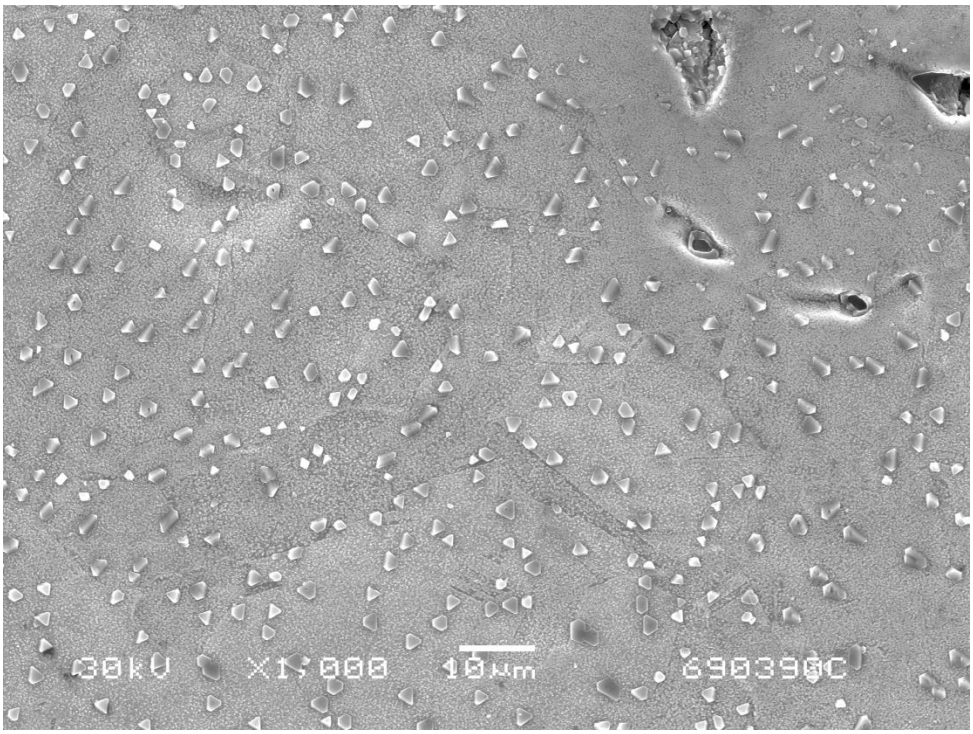

(a)

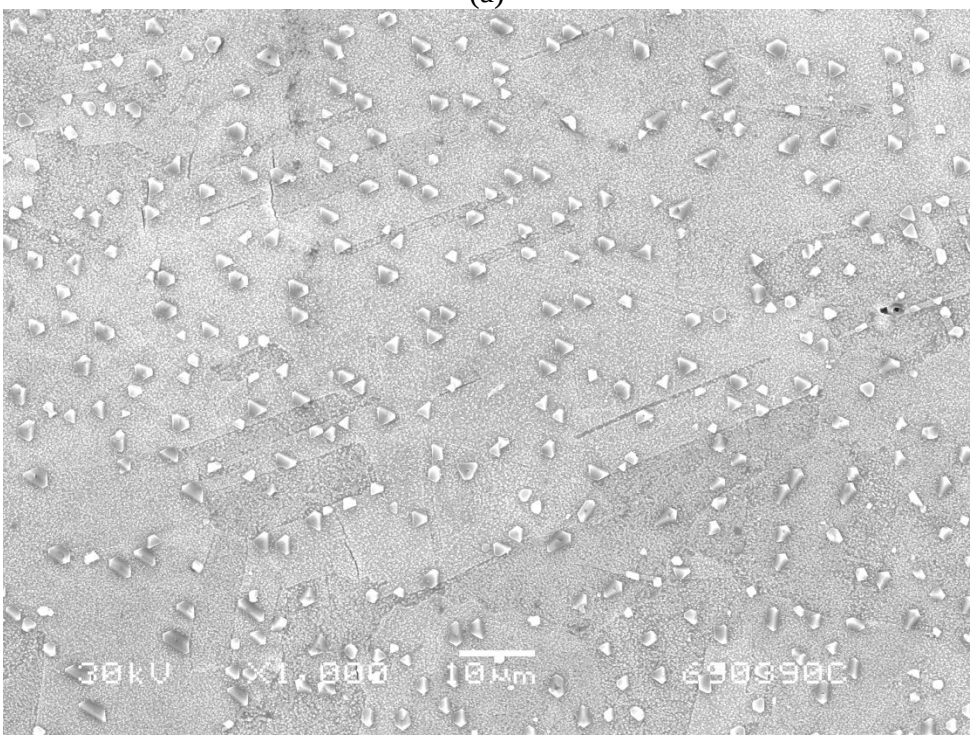

(b)

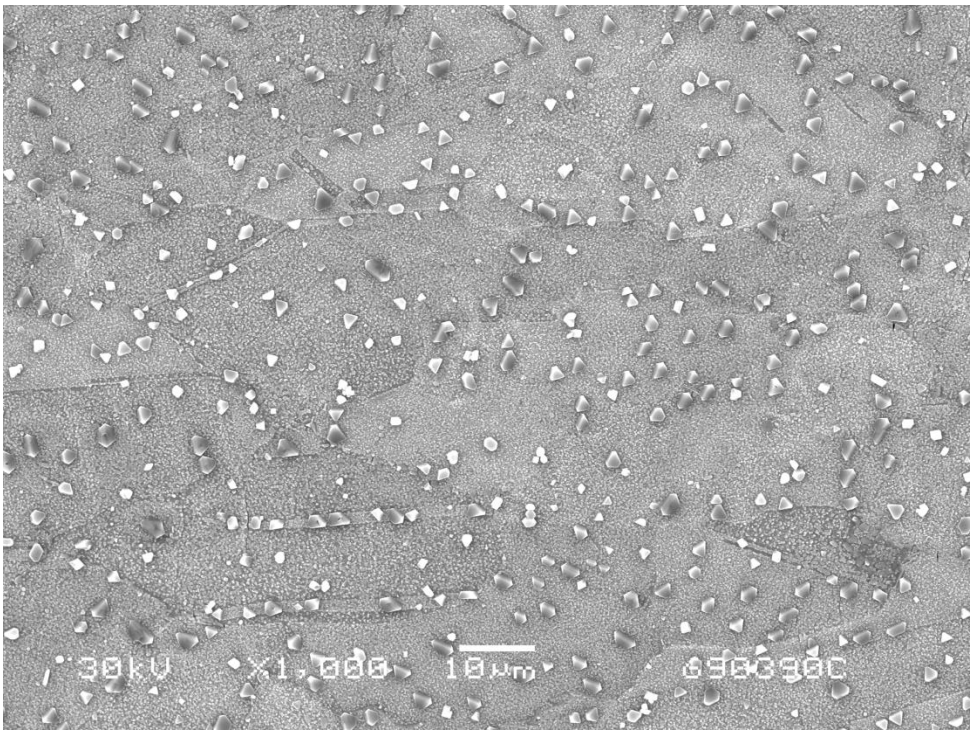

(c)

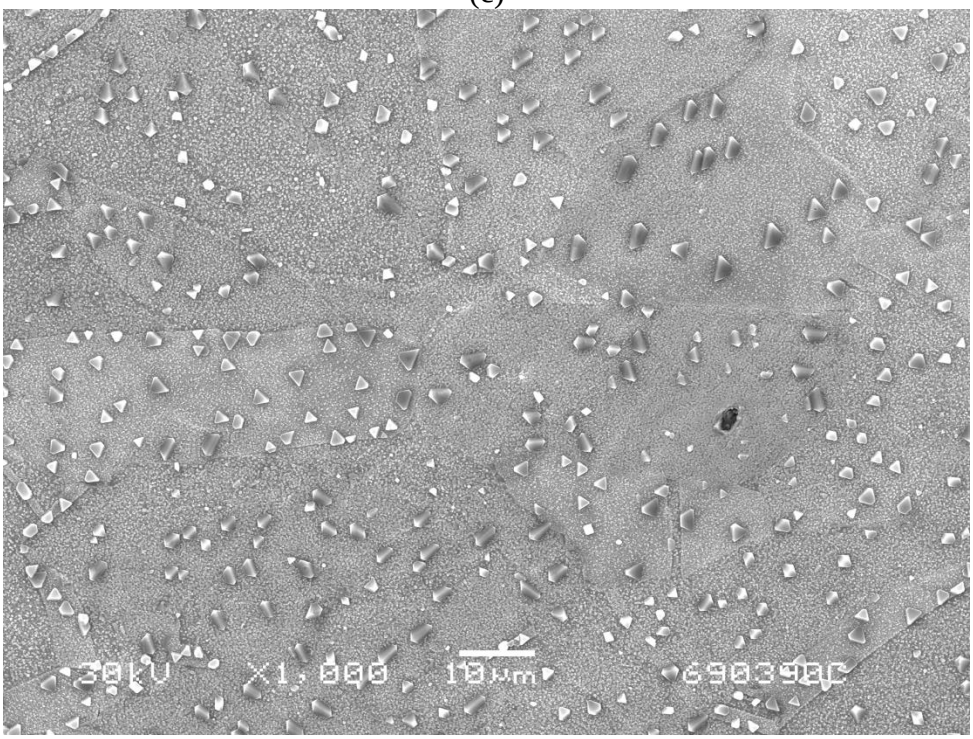

(d)

Figure 0.23. (a-d) Gauge surface of pre-strained Alloy 690 strained to 7% in 390°C water at $5x10^{-8}$ s^{-1}.

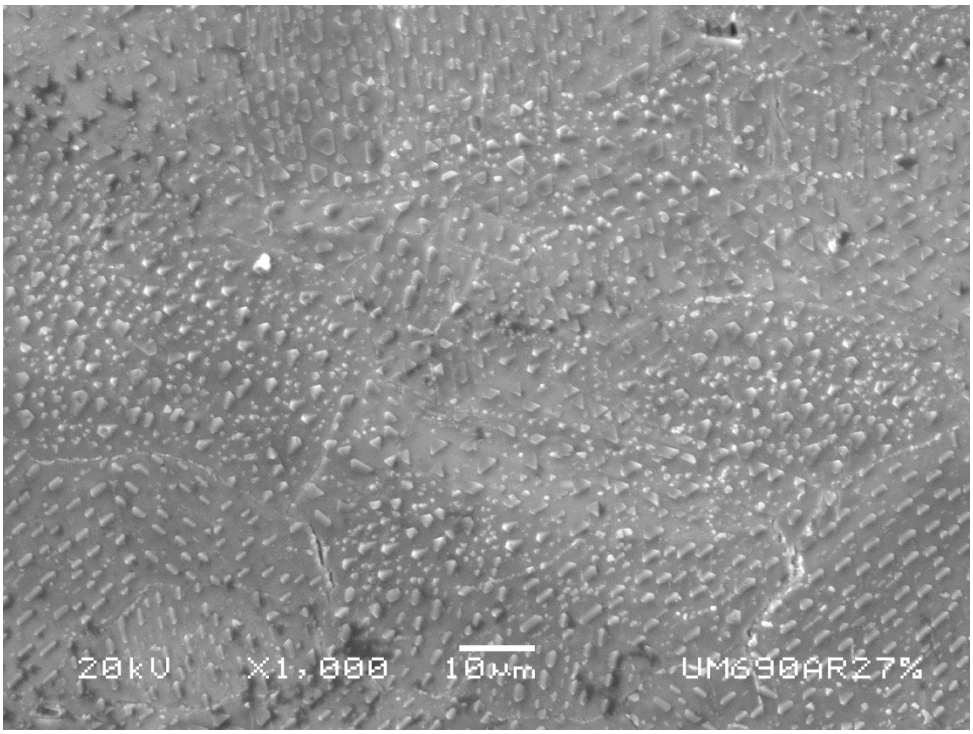

(a)

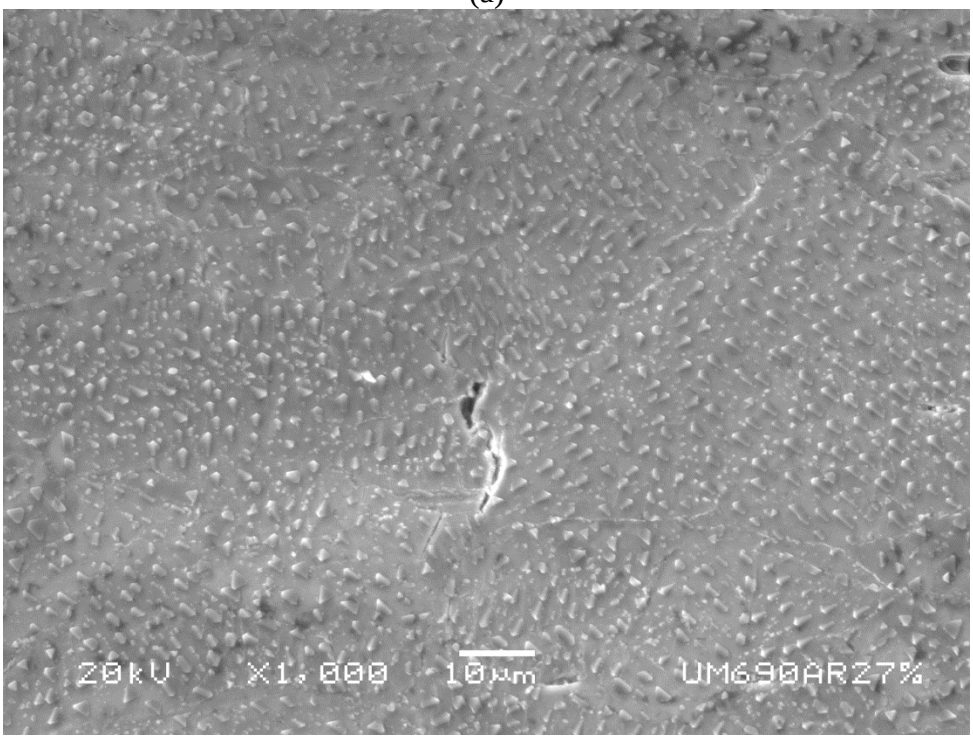

(b)

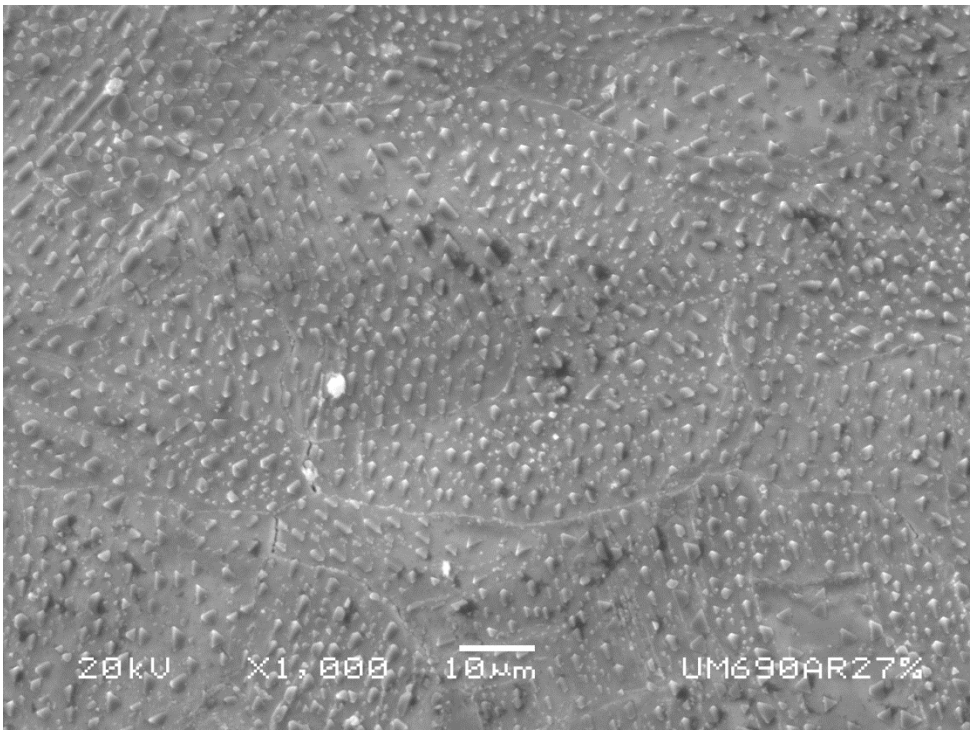

(c)

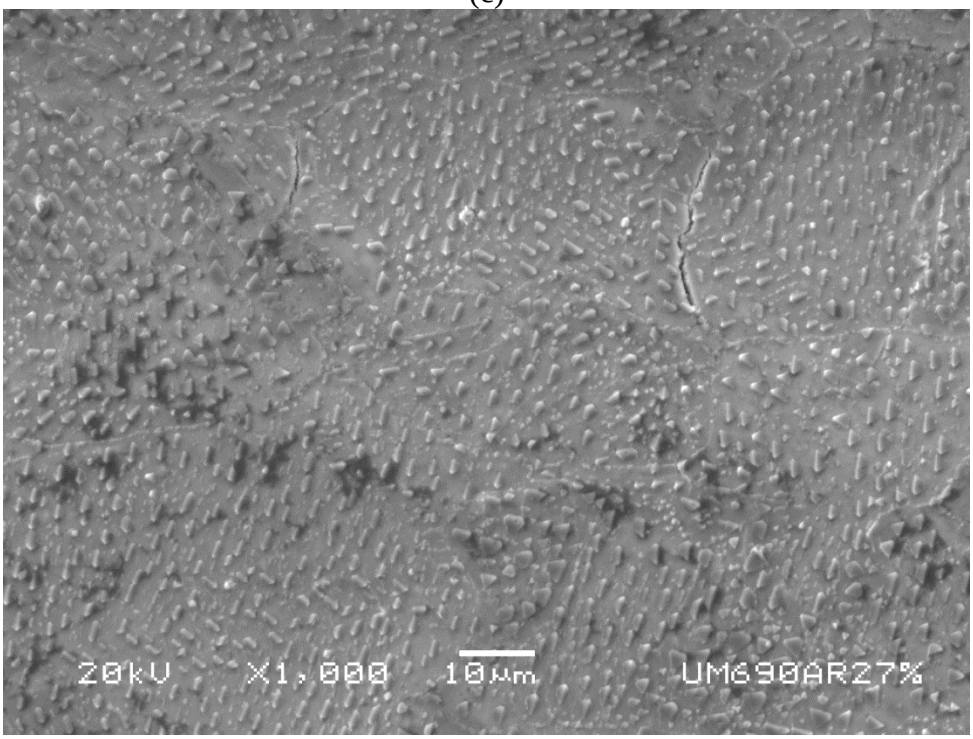

(d)

Figure 0.24. (a-d) Gauge surface of pre-strained Alloy 690 strained to 7% in 450°C water at $5x10^{-8}$ s^{-1}.

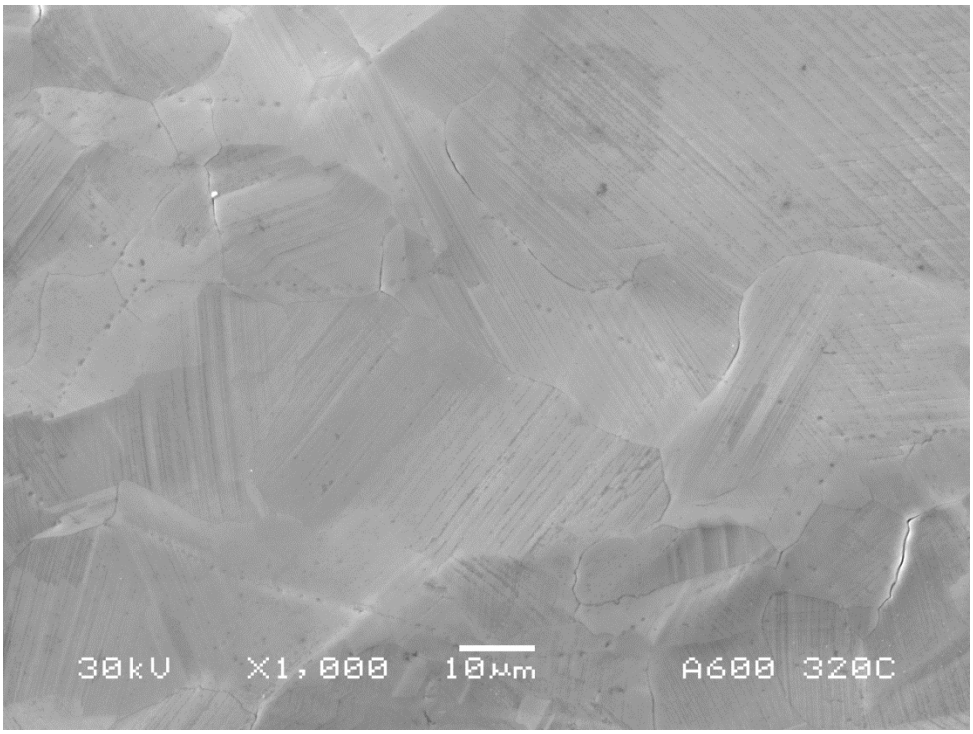

(a)

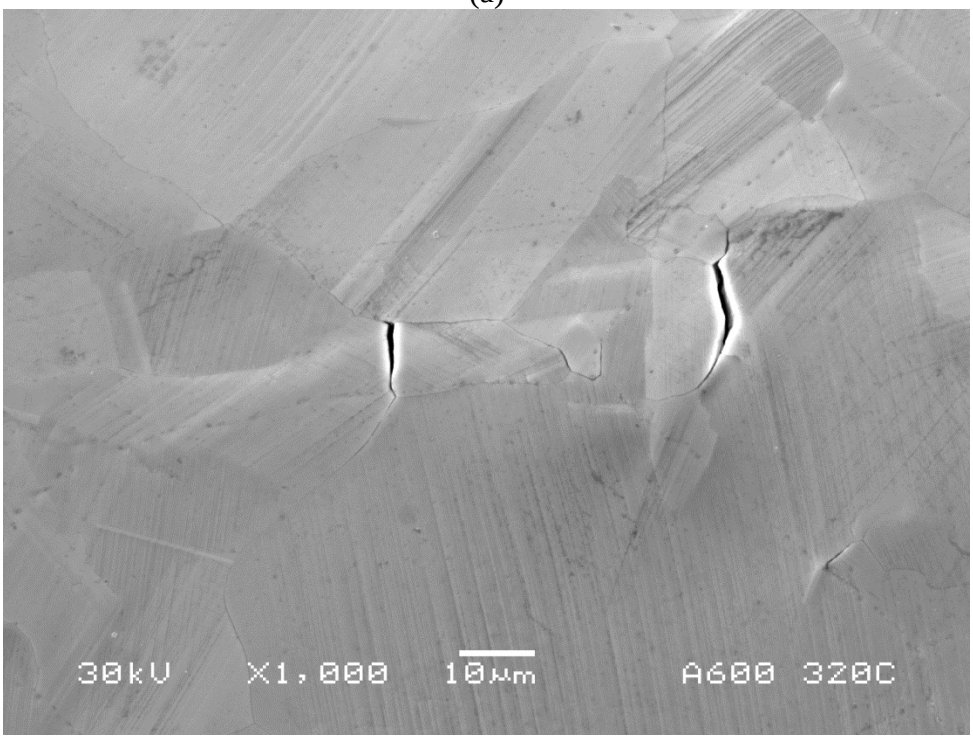

(b)

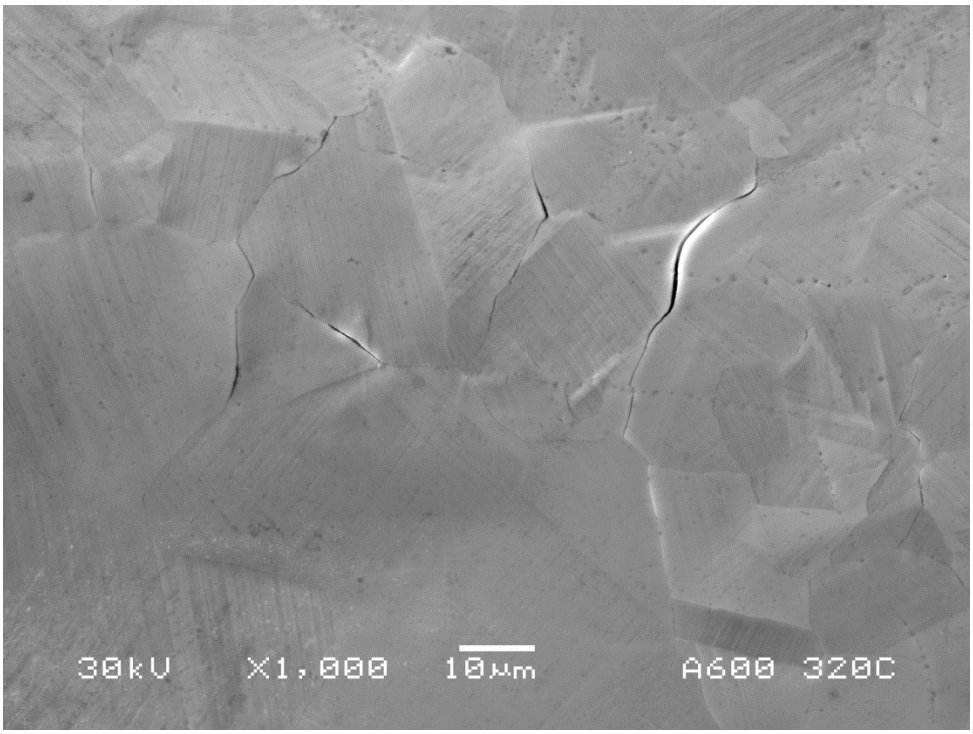

(c)

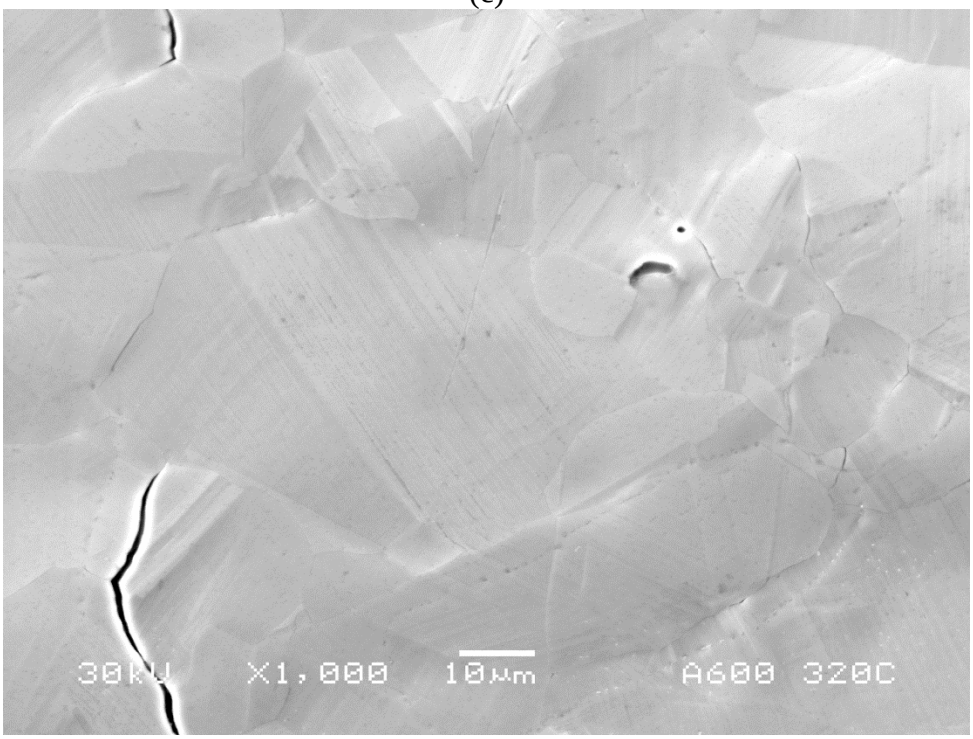

(d)

Figure 0.25. (a-d) Gauge surface of Alloy 600 strained to 8% in 320°C water at $3x10^{-7}$ s^{-1}.

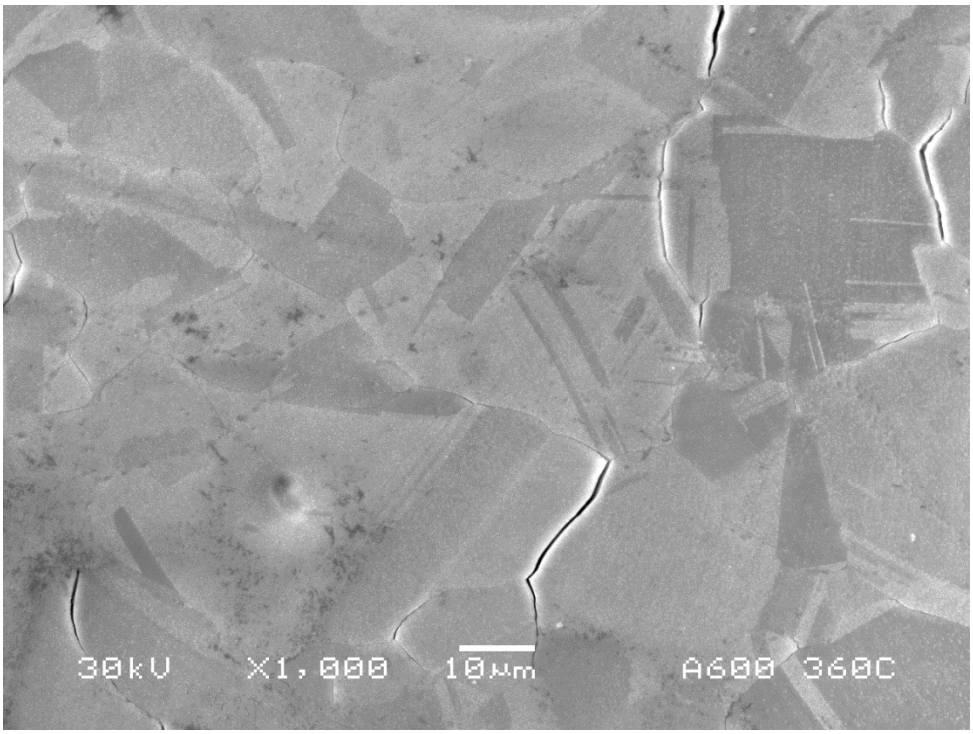

(a)

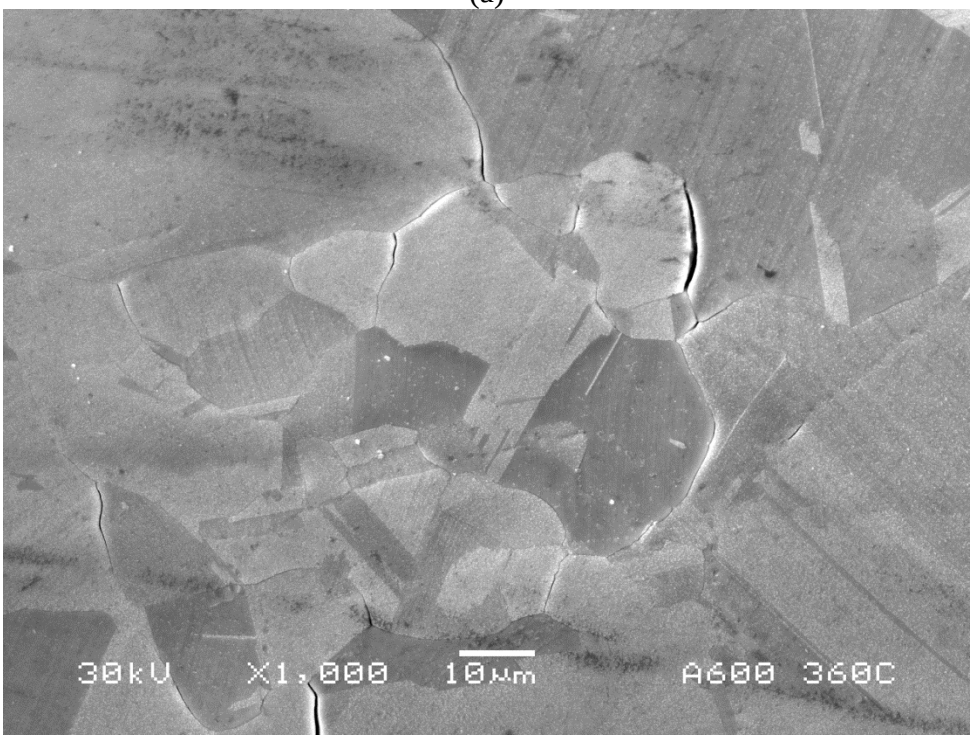

(b)

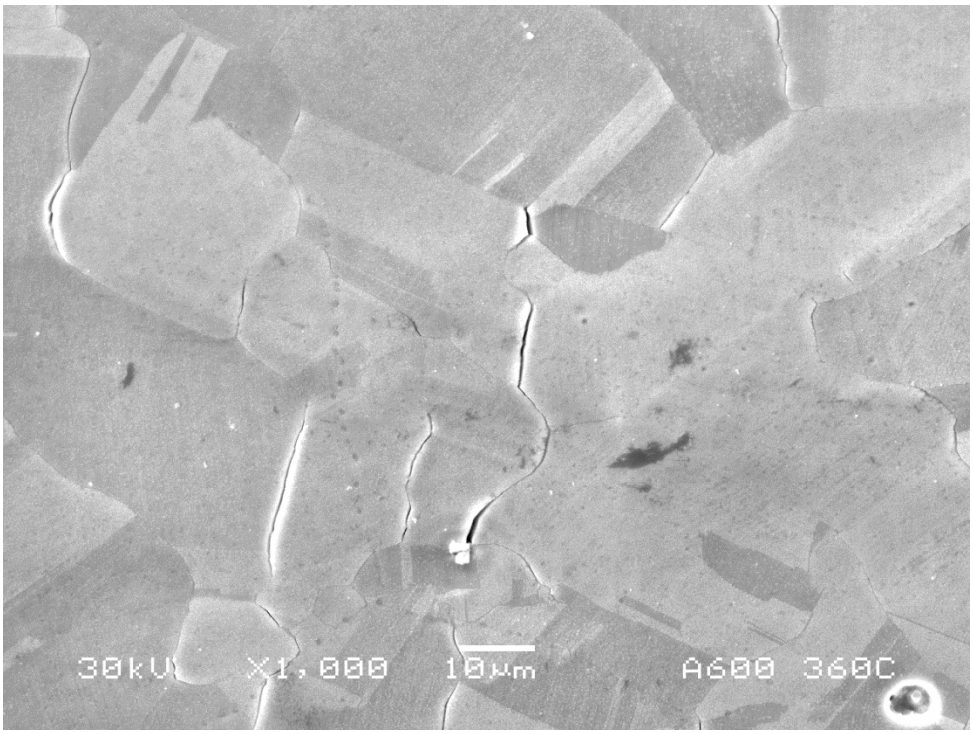

(c)

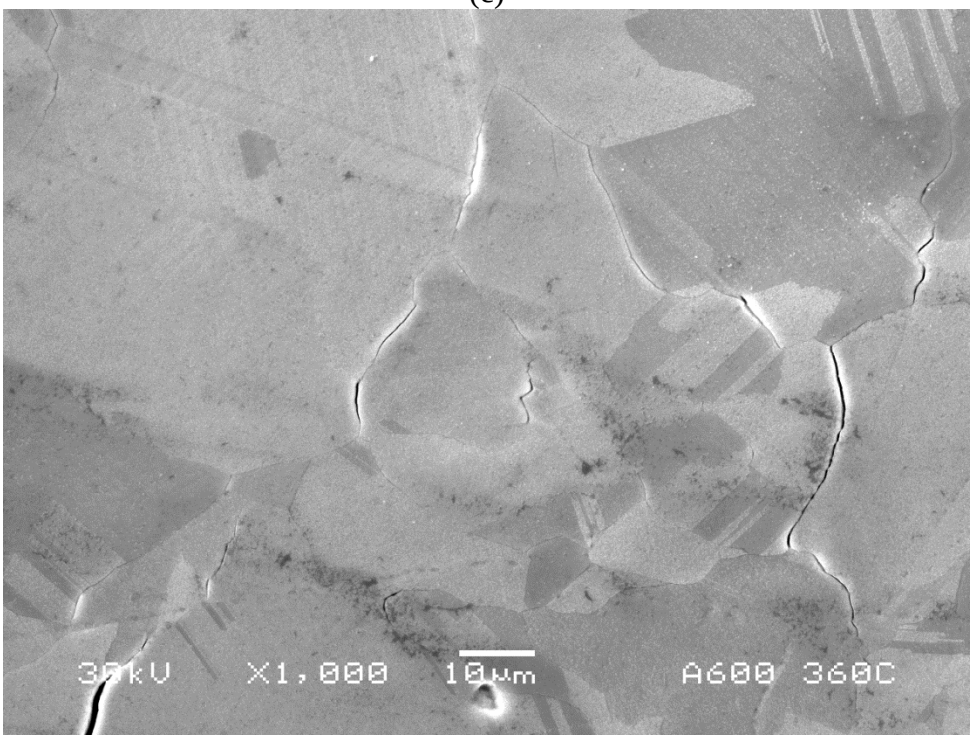

(d)

Figure 0.26. (a-d) Gauge surface of Alloy 600 strained to 8% in 360°C water at $3x10^{-7}$ s^{-1}.

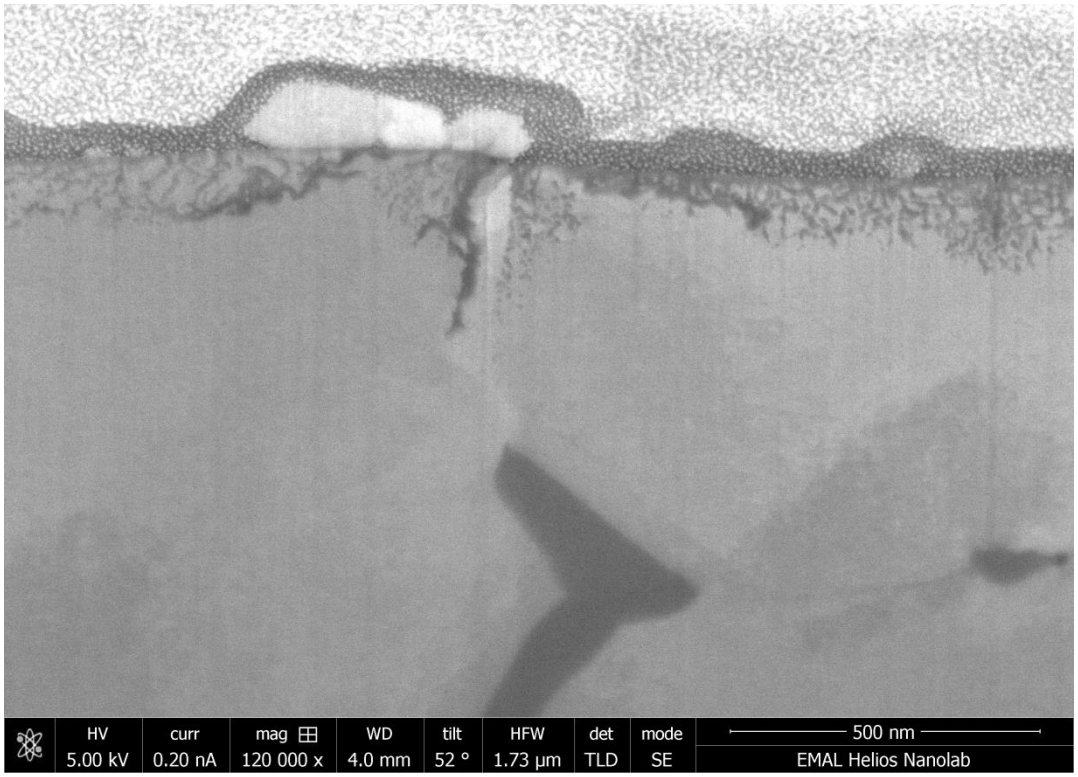
HV
5.00 kV
curr
0.20 nA
mag
120 000 x
WD
4.0 mm
tilt
52 °
HFW
1.73 µm
det
TLD
mode
SE
500 nm
EMAL Helios Nanolab

(a)

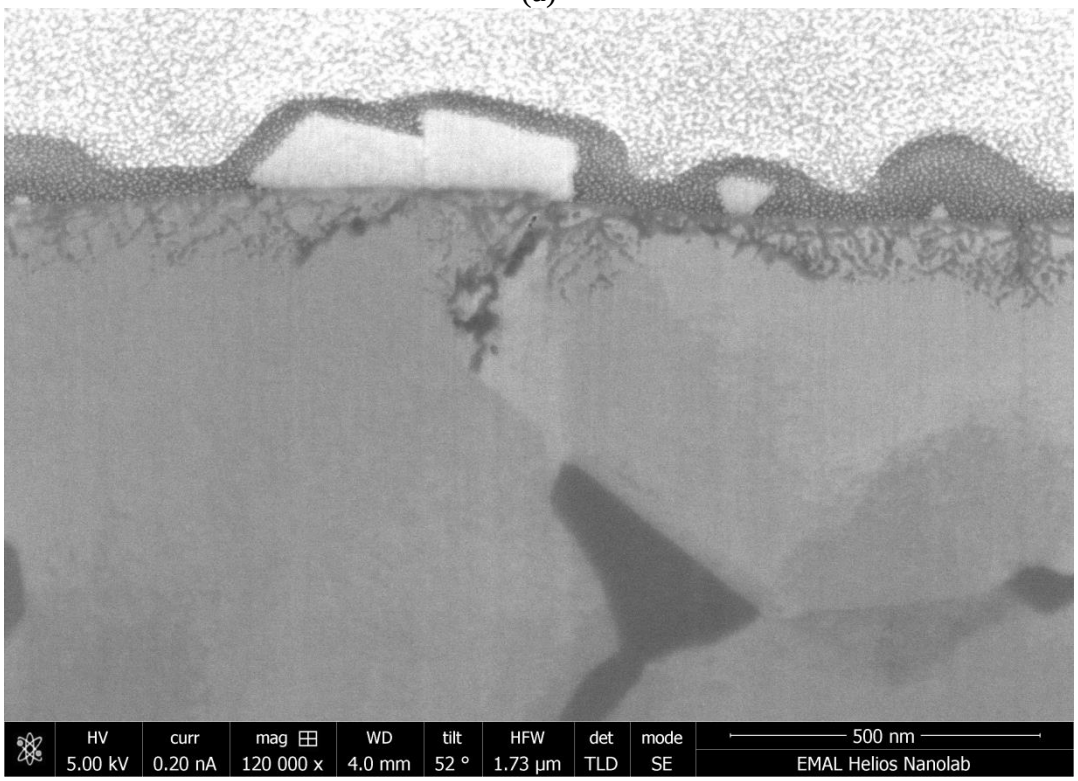
HV
5.00 kV
curr
0.20 nA
mag
120 000 x
WD
4.0 mm
tilt
52 °
HFW
1.73 µm
det
TLD
mode
SE
500 nm
EMAL Helios Nanolab

(b)

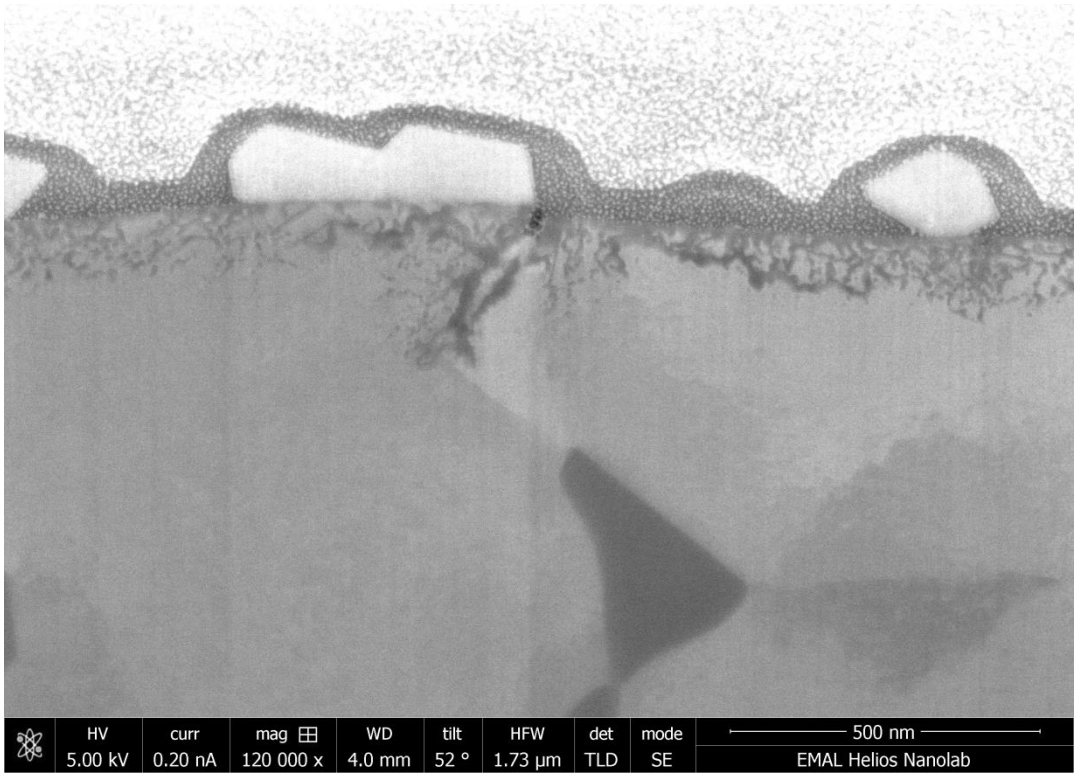
HV
5.00 kV
curr
0.20 nA
mag
120 000 x
WD
4.0 mm
tilt
52 °
HFW
1.73 µm
det
TLD
mode
SE
500 nm
EMAL Helios Nanolab

(c)

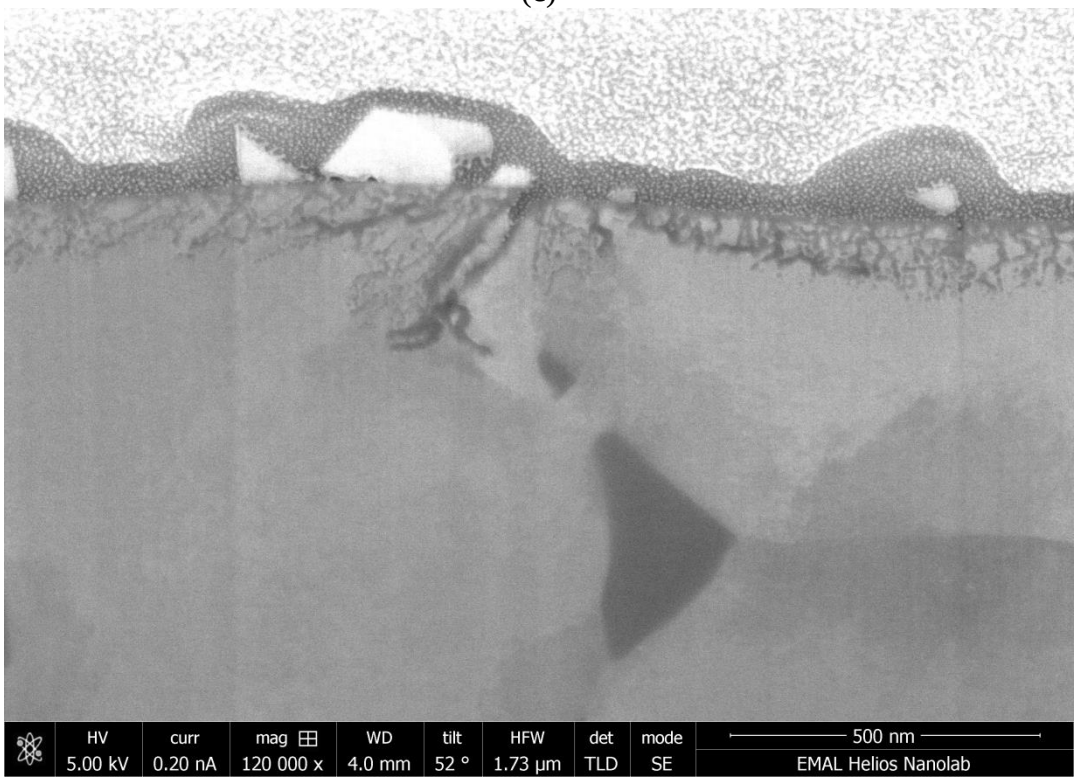
HV
5.00 kV
curr
0.20 nA
mag
120 000 x
WD
4.0 mm
tilt
52 °
HFW
1.73 µm
det
TLD
mode
SE
500 nm
EMAL Helios Nanolab

(d)

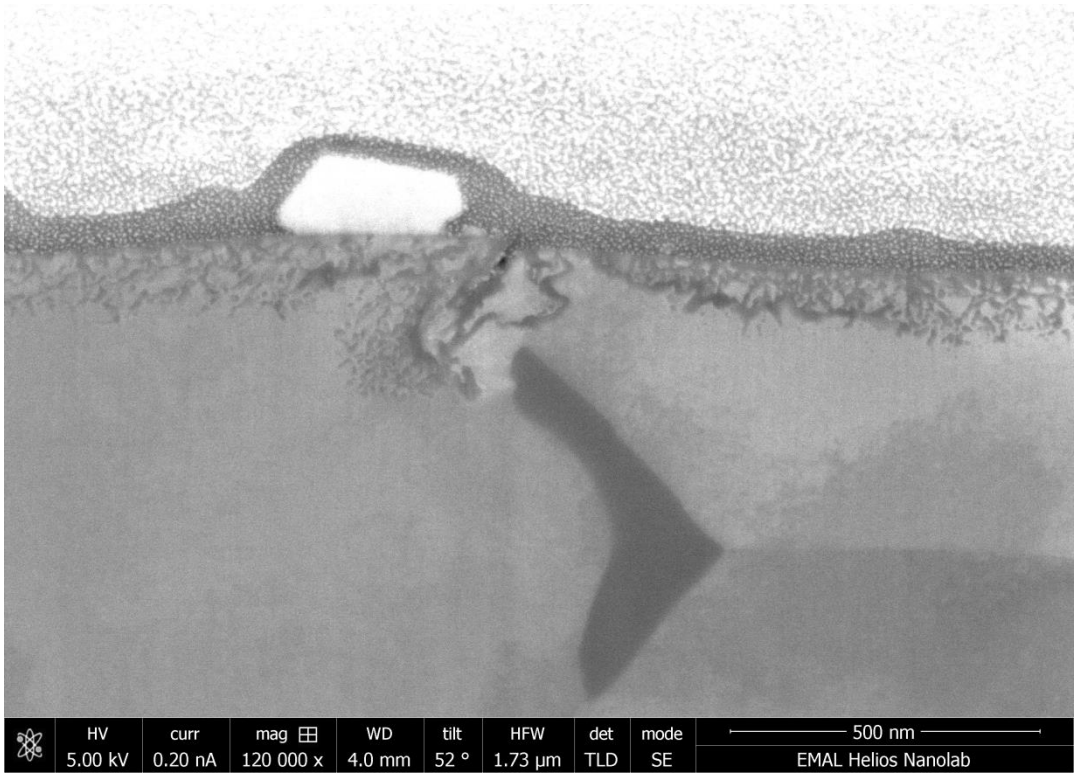
HV
5.00 kV
curr
0.20 nA
mag
120 000 x
WD
4.0 mm
tilt
52 °
HFW
1.73 µm
det
TLD
mode
SE
500 nm
EMAL Helios Nanolab

(e)

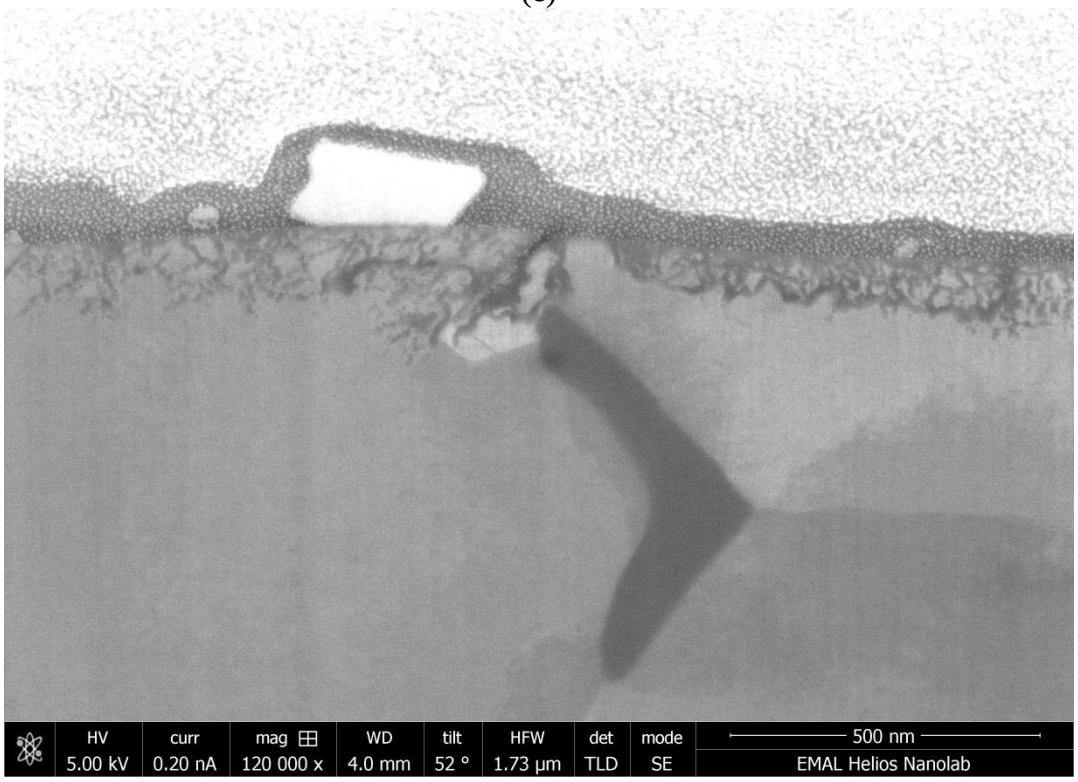
HV
5.00 kV
curr
0.20 nA
mag
120 000 x
WD
4.0 mm
tilt
52 °
HFW
1.73 µm
det
TLD
mode
SE
500 nm
EMAL Helios Nanolab

(f)

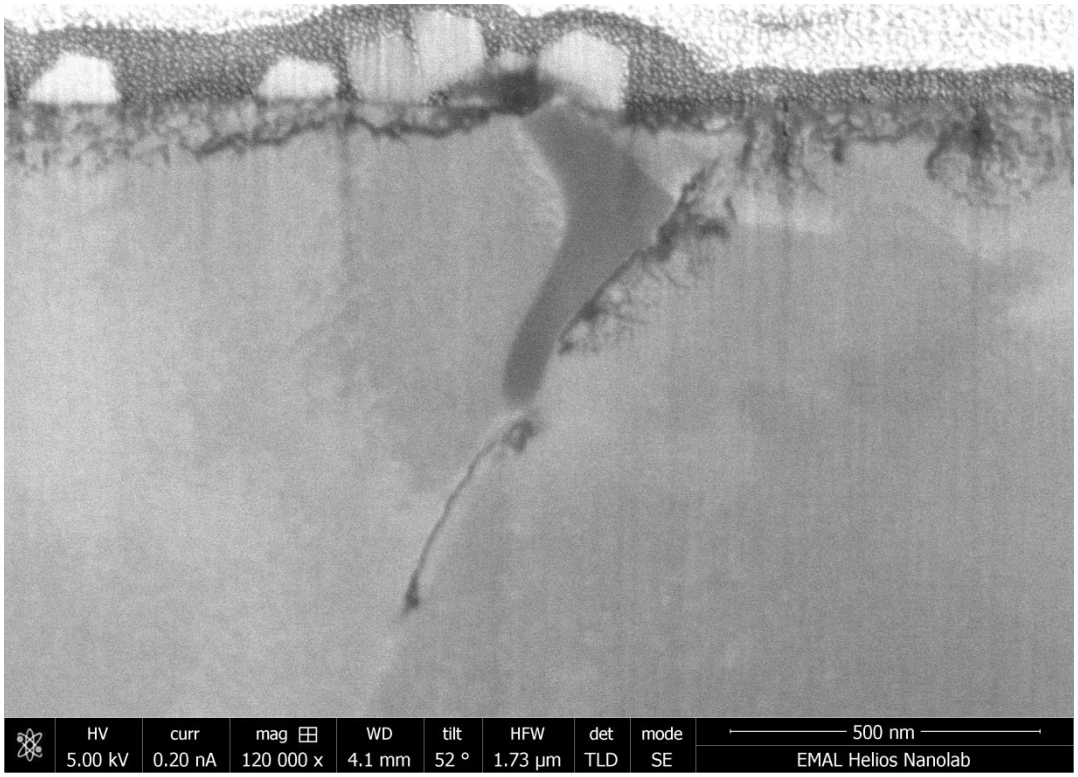

(g)

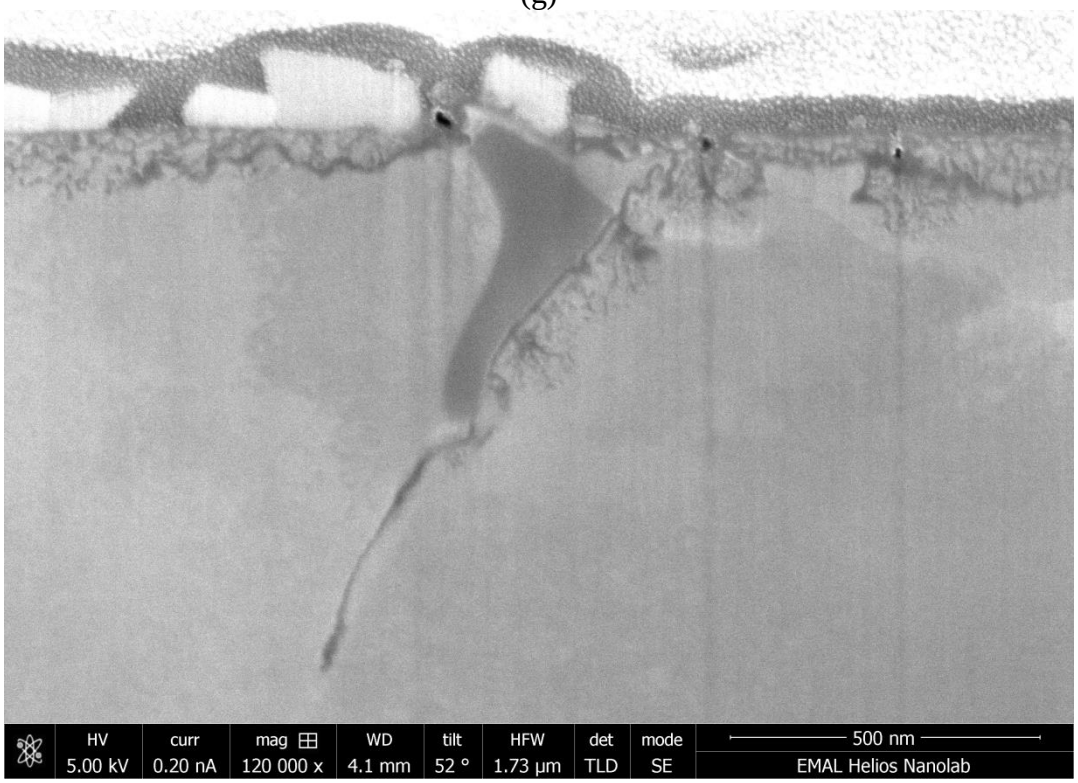

(h)

Figure 0.27. (a-h) FIB serial sectioning of a single grain boundary in Alloy 690 strained to 7% in 360°C water at $5x10^{-8}$ s^{-1}. Each image is ~ 100nm apart.

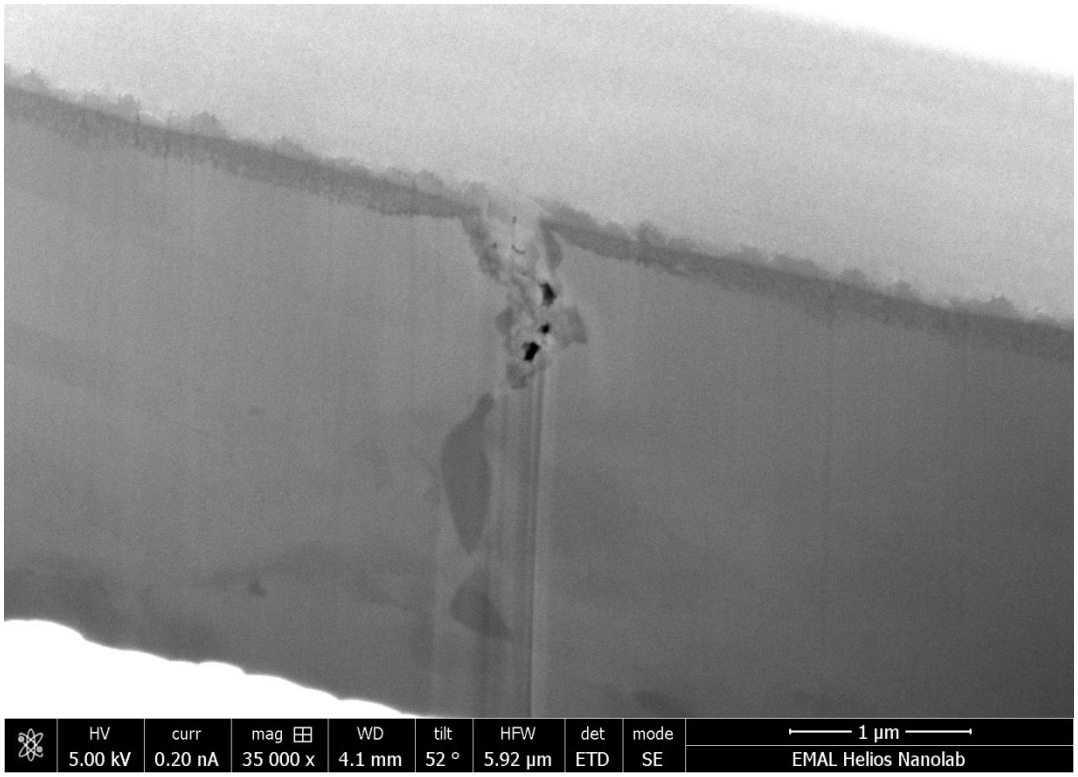
HV
5.00 kV
curr
0.20 nA
mag
35 000 x
WD
4.1 mm
tilt
52 °
HFW
5.92 µm
det
ETD
mode
SE
1 µm
EMAL Helios Nanolab

(a)

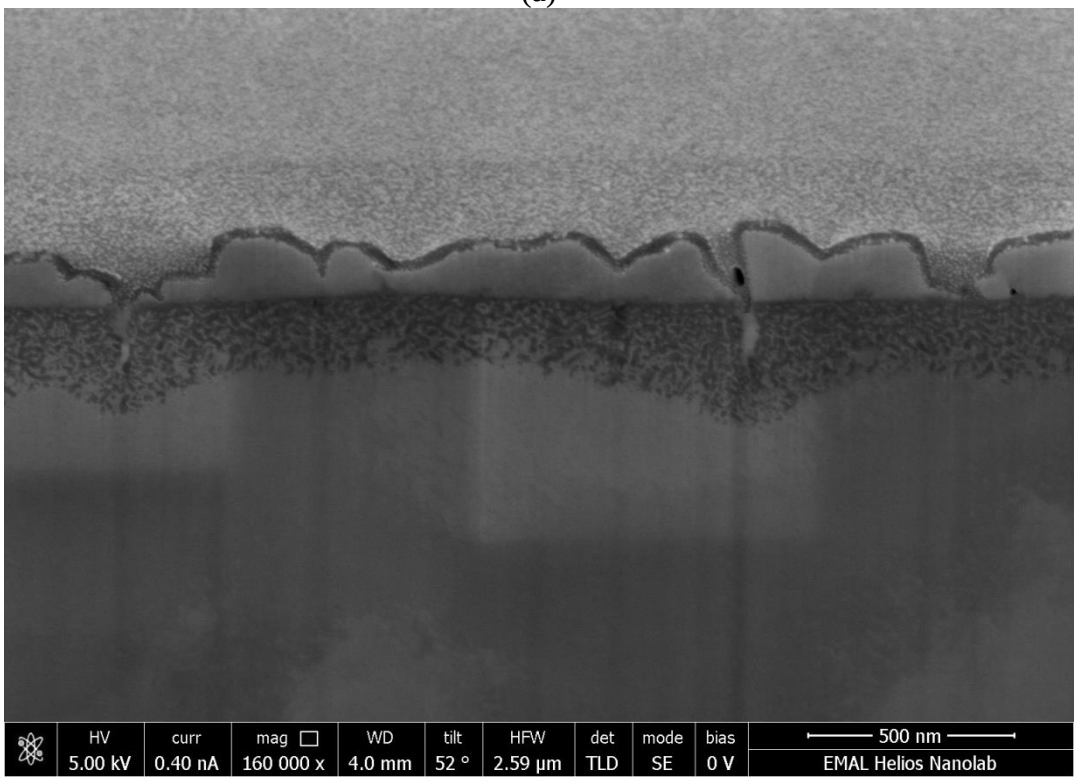
HV
5.00 kV
curr
0.40 nA
mag
160 000 x
WD
4.0 mm
tilt
52 °
HFW
2.59 µm
det
TLD
mode
SE
bias
0 V
500 nm
EMAL Helios Nanolab

(b)

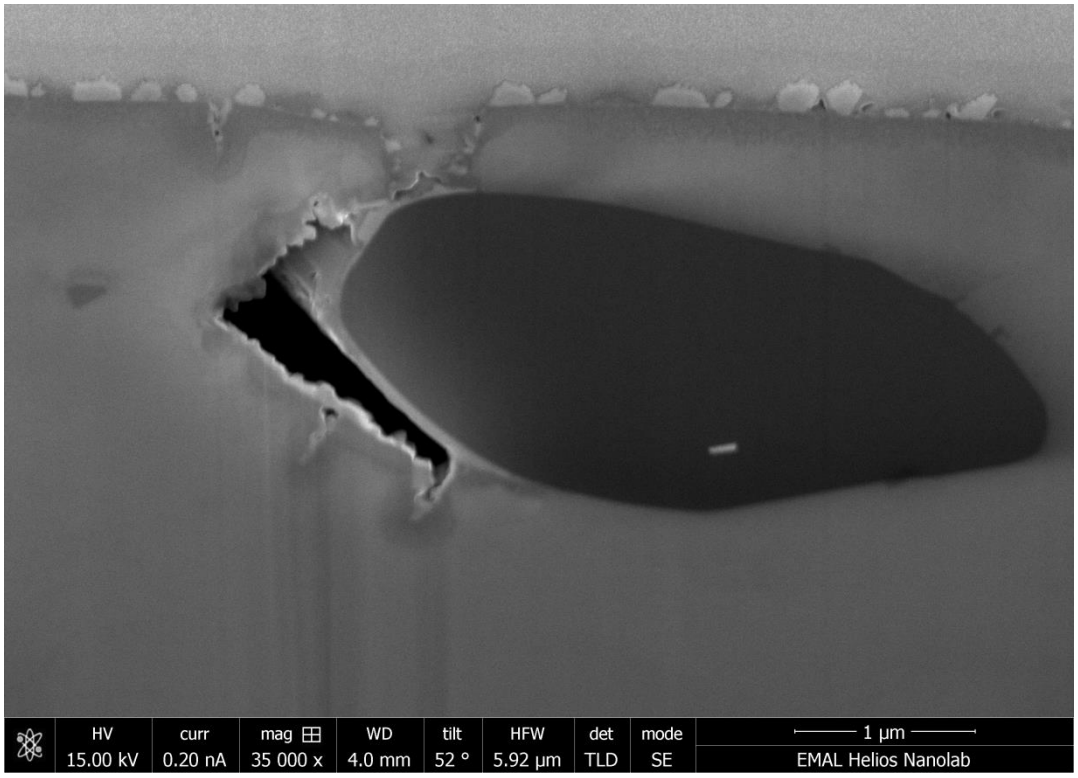
HV
15.00 kV
curr
0.20 nA
mag
35 000 x
WD
4.0 mm
tilt
52 °
HFW
5.92 µm
det
TLD
mode
SE
1 µm
EMAL Helios Nanolab

(c)

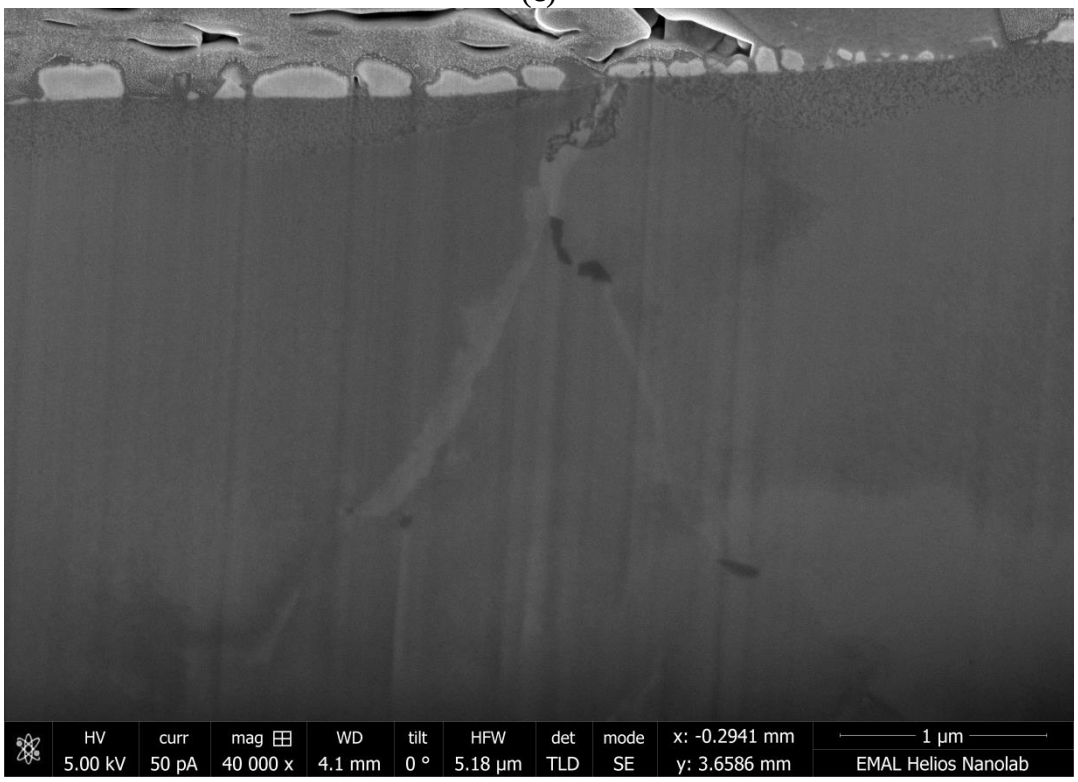
HV
5.00 kV
curr
50 pA
mag
40 000 x
WD
4.1 mm
tilt
0 °
HFW
5.18 µm
det
TLD
mode
SE
x: -0.2941 mm
y: 3.6586 mm
1 µm
EMAL Helios Nanolab

(d)

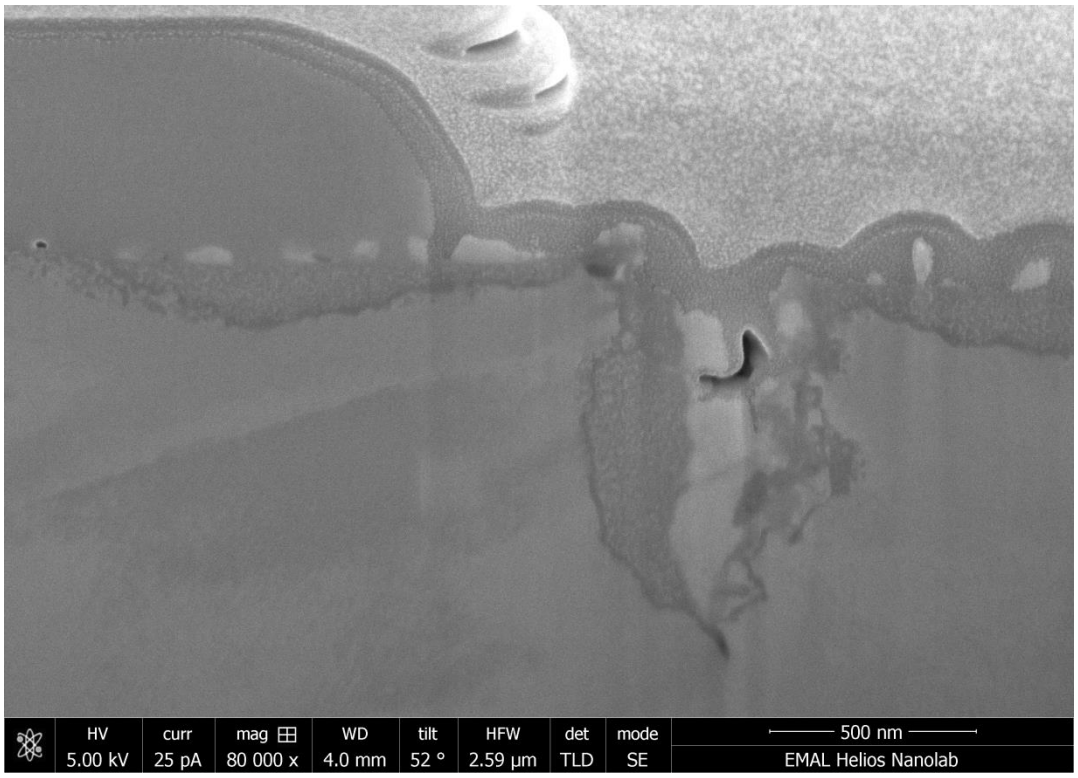
HV
5.00 kV
curr
25 pA
mag
80 000 x
WD
4.0 mm
tilt
52 °
HFW
2.59 µm
det
TLD
mode
SE
500 nm
EMAL Helios Nanolab

(e)

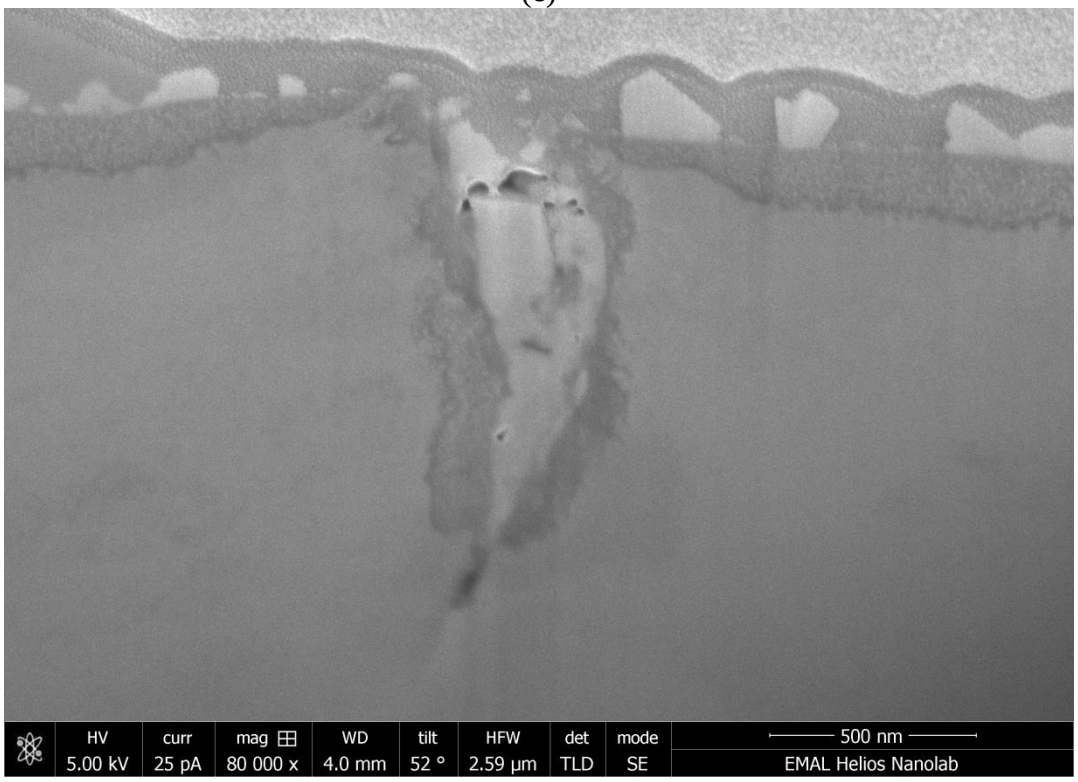
HV
5.00 kV
curr
25 pA
mag
80 000 x
WD
4.0 mm
tilt
52 °
HFW
2.59 µm
det
TLD
mode
SE
500 nm
EMAL Helios Nanolab

(f)

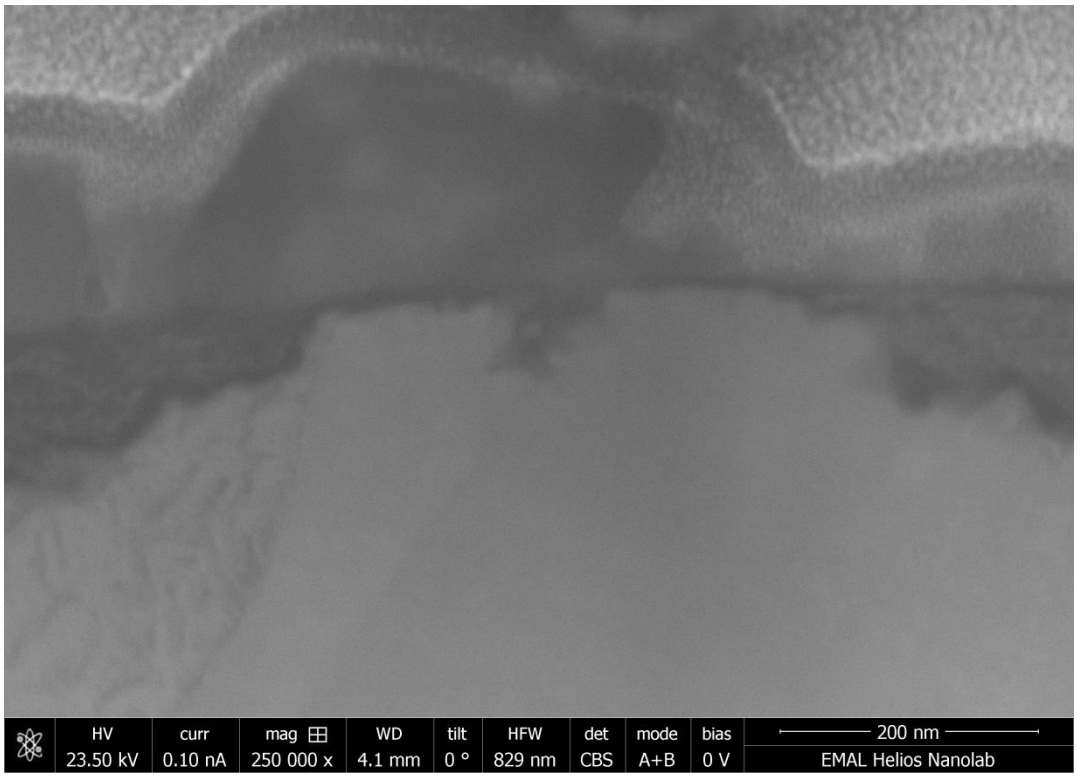

(g)

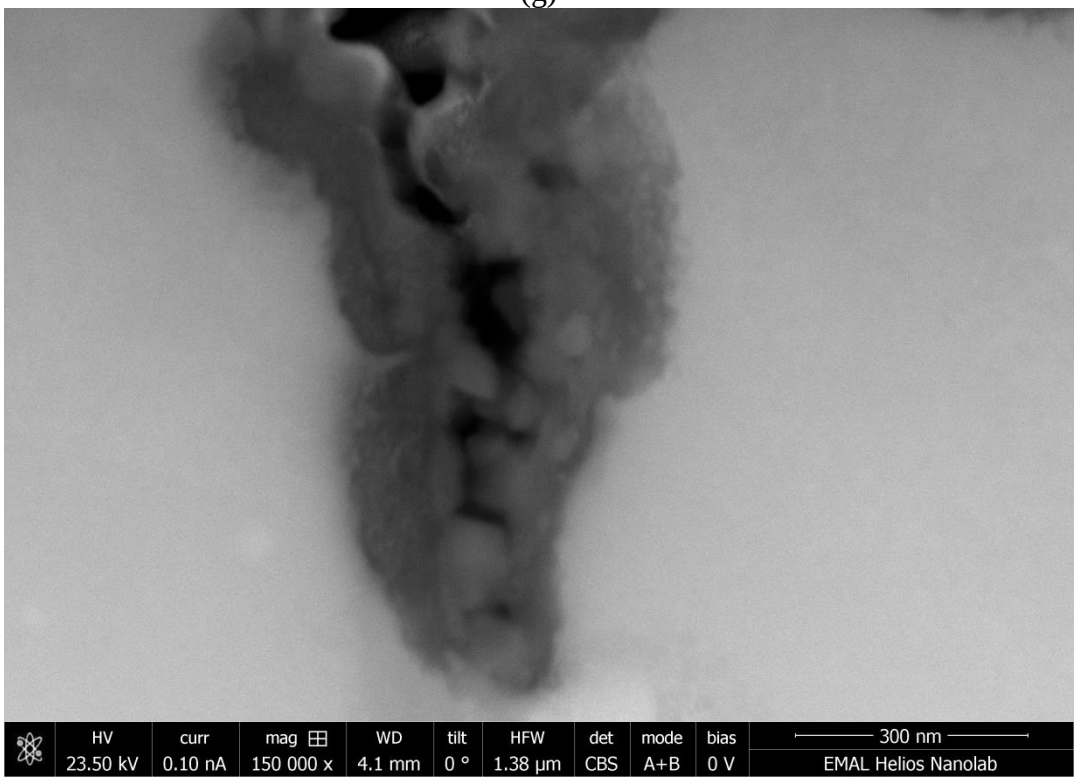

(h)

Figure 0.28. (a-h) Cross section micrographs taken from a sample of Alloy 690 strained to 7% in 400°C water at $5x10^{-8}$ s^{-1}.

BIBLIOGRAPHY

[1] Dutta RS. Corrosion aspects of Ni–Cr–Fe based and Ni–Cu based steam generator tube materials. J Nucl Mater 2009;393:343–9.

[2] Rodriguez P, Venkadesan S. Serrated Plastic Flow Revisited. Solid State Phenom 1995;42-43:257–66.

[3] Mulford RA, Kocks UF. New observations on the mechanisms of dynamic strain aging and of jerky flow. Acta Metall 1979;27:1125–34.

[4] Hänninen H, Ivanchenko M, Yagodzinskyy Y, Nevdacha V, Ehrnstén U, Aaltonen P. Dynamic Strain Aging of Ni-Base Alloys Inconel 600 and 690. 12th Int. Conf. Environ. Degrad. Mater. Nucl. Power Sytems - Water React., TMS; 2005, p. 1423–30.

[5] Samuel K, Mannan S, Rodriguez P. Serrated yielding in AISI 316 stainless steel. Acta Metall 1988;36:2323–7.

[6] Almeida LH De, May I Le, Emygdio PRO. Austenitic Stainless Steels M echanistic Modeling of Dynamic Strain Aging in. Science (80-) 1998;150:137–50.

[7] Hale C, Rollings W, Weaver M. Activation energy calculations for discontinuous yielding in Inconel 718SPF. Mater Sci Eng A 2001;300:153–64.

[8] Moss T, Was G. Dynamic Strain Aging of Nickel-Base Alloys 800H and 690. Metall Mater Trans A 2012;43:3428–32.

[9] Attanasio SA, Morton DS, Ando MA. Measurement and Calculation of Electrochemical Potentials in Hydrogenated High Temperature Water , including an Evaluation of the Yttria- Stabilized Zirconidiron-Iron Oxide (Fe / Fe304) Probe as a Reference Electrode. 2001.

[10] Attanasio S, Morton D, Young G. Measurement of the Nickel/Nickel Oxide Transition in Ni-Cr-Fe Alloys and Updated Data and Correlations to Quantify the Effect of Aqueous Hydrogen on Primary Water SCC. 11th Int Conf Environ Degrad Mater Nucl Power Syst — Water React 2003:143–55.

[11] Morton D, Fish J, Schurman MK, Attanasio SA. Influence of Dissolved Hydrogen on Nickel Alloy SCC in High Temperature Water. Corros. 99, San Antonio, Texas: NACE International; 1999.

[12] Scott PM, Combrade P. On the mechanism of stress corrosion crack initiation and growth in Alloy 600 exposed to PWR primary water. 11th Int. Conf. Environ. Degrad. Mater. Nucl. Power Syst. — Water React. Int. Symp. Environ. Degrad. Mater. Nucl. Power Syst. – Water React., La Grange Park, IL: American Nuclear Society; 2003, p. 29–38.

[13] Economy G, Jacko RJ, Pement FW. IGSCC Behavior of Alloy 600 Steam Generator Tubing in Water or Steam Tests Above 360 C. Corrosion 1987;43:727–34.

[14] Attanasio SA, Morton DS, Ando MA, Panayotou NF, Thompson CD. Measurement of the Nickel/Nickel Oxide Phase Transition in High Temperature Hydrogenated Water Using the Contact Electric Resistance (CER) Technique. 10th Int. Conf. Environ. Degrad. Mater. Nucl. Power Syst. — Water React., Lake Tahoe, Nevada: 2001.

[15] Moshier WC, Witt RC. Unpublished Data. 2002.

[16] Kishima N, Sakai H. Fugacity-concentration relationship of dilute hydrogen in water at elevated temperature and pressure. Earth Planet Sci Lett 1984;67:79–86.

[17] Kritzer P. Corrosion in high-temperature and supercritical water and aqueous solutions: a review. J Supercrit Fluids 2004;29:1–29.

[18] Ikushima Y. Physical and Chemical Properties of Supercritical Water 2000.

[19] Macdonald DD, Kriksunov LB. Probing the chemical and electrochemical properties of SCWO systems. Electrochim Acta 2001;47:775–90.

[20] Cook WG, Olive RP. Pourbaix diagrams for chromium, aluminum and titanium extended to high-subcritical and low-supercritical conditions. Corros Sci 2012;58:291–8.

[21] Cook WG, Olive RP. Pourbaix diagrams for the iron–water system extended to high-subcritical and low-supercritical conditions. Corros Sci 2012;55:326–31.

[22] Cook WG, Olive RP. Pourbaix diagrams for the nickel-water system extended to high-subcritical and low-supercritical conditions. Corros Sci 2012;58:284–90.

[23] Sennour M, Marchetti L, Martin F, Perrin S, Molins R, Pijolat M. A detailed TEM and SEM study of Ni-base alloys oxide scales formed in primary conditions of pressurized water reactor. J Nucl Mater 2010;402:147–56.

[24] Devine TM. Influence of Primary Water Chemistry on Oxides Formed on Alloy 600 and Alloy 690. 15th Int. Conf. Environ. Degrad. Mater. Nucl. Power Syst. React., John Wiley & Sons, Inc.; 2012, p. 967–92.

[25] Olszta MJ, Schreiber DK, Toloczko MB, Bruemmer SM. Alloy 690 Surface Nanostructures During Exposure to PWR Primary Water and Potential Influence on Stress

Corrosion Crack Initiation. Proc. 16th Int. Conf. Environ. Degrad. Mater. Nucl. Power Syst. React., Asheville, NC: 2013.

[26] Olszta MJ, Schreiber DK, Thomas LE, Bruemmer SM. Penetrative Internal Oxidation from Alloy 690 Surfaces and Stress Corrosion Crack Walls during Exposure to PWR Primary Water. 15th Int. Conf. Environ. Degrad. Mater. Nucl. Power Syst. React., Colorado Springs, CO: The Minerals, Metals and Materials Society.; 2011, p. 331–42.

[27] Ziemniak SE, Hanson M. Corrosion behavior of NiCrFe Alloy 600 in high temperature, hydrogenated water. Corros Sci 2006;48:498–521.

[28] Peng Q, Hou J, Sakaguchi K, Takeda Y, Shoji T. Effect of dissolved hydrogen on corrosion of Inconel Alloy 600 in high temperature hydrogenated water. Electrochim Acta 2011;56:8375–86.

[29] TERACHI T, TOTSUKA N, YAMADA T, NAKAGAWA T, DEGUCHI H, HORIUCHI M, et al. Influence of Dissolved Hydrogen on Structure of Oxide Film on Alloy 600 Formed in Primary Water of Pressurized Water Reactors. J Nucl Sci Technol 2003;40:509–16.

[30] Combrade P, Scott P. M., Foucault M., Andrieu E, Marcus P. Oxidation of Ni base alloys in PWR water: Oxide layers and associated damage to the base metal. In: Allen TR, King PJ, Nelson L, editors. Proc. 12th Int. Conf. Environ. Degrad. Mater. Nucl. Power Syst. React., Salt Lake City, UT: The Minerals, Metals and Materials Society.; 2005, p. 883–90.

[31] Morton D, Lewis N, Hanson M, Rice S, Sander P. Nickel alloy primary water bulk surface and SCC corrosion film analytical characterization and SCC mechanistic implications. 13th Int Conf Environ Degrad Mater Nucl Power Syst Can Nucl Soc 2007:1–31.

[32] Kuang W, Wu X, Han E-H, Rao J. The mechanism of oxide film formation on Alloy 690 in oxygenated high temperature water. Corros Sci 2011;53:3853–60.

[33] Carrette F, Lafont MC, Legras L, Guinard L, Pieraggi B. Analysis and TEM examinations of corrosion scales grown on alloy 690 exposed to PWR environment. Mater High Temp 2003;20:581–91.

[34] Zhang Z, Wang J, Han E-H, Ke W. Characterization of Different Surface States and Its Effects on the Oxidation Behaviours of Alloy 690TT. J Mater Sci Technol 2012;28:353–61.

[35] Sennour M, Laghoutaris P, Guerre C, Molins R. Advanced TEM characterization of stress corrosion cracking of Alloy 600 in pressurized water reactor primary water environment. J Nucl Mater 2009;393:254–66.

[36] Thomas LE, Bruemmer SM. High-Resolution Characterization of Intergranular Attack and Stress Corrosion Cracking of Alloy 600 in High-Temperature Primary Water. Corrosion 2000;56:572.

[37] Parsi A, Byers A, DeVito RL. Surface Analysis of Pressurized Water Reactor Steam Generator Tubing Specimens: Results of Surface and Microstructural Analysis of Tubes from Diablo Canyon 1, Onconee 2, Seabrook, and Vogtle 1 and 2 PWRs. EPRI Rep. 1018721, 2009.

[38] Cattant F. Surface Analysis of Pressurized Water Reactor Steam Generator Tubing Specimens: Updated Review of Results Obtained from the ID surfaces of EDF Tubes Pulled between 1985-1990. EPRI Rep. 1018593, 2009.

[39] Wood G, Stott F, Whittle D, Shida Y, Bastow B. The high-temperature internal oxidation and intergranular oxidation of nickel-chromium alloys. Corros Sci 1983;23:9–25.

[40] Totsuka N, Nishikawa Y, Nakajima N. Influence of Dissolved Hydrogen and Temperature on Primary Water Stress Corrosion Cracking of Mill Annealed Alloy 600. Corros. 2002, Denver, Colorado: NACE International; 2002.

[41] Etien RA, Richey E, Morton DS, Eager J. SCC Initiation Testing of Alloy 600 in High Temperature Water. 15th Int. Conf. Environ. Degrad. Mater. Nucl. Power Syst. React., John Wiley & Sons, Inc.; 2012, p. 2407–17.

[42] Morton DS, Attanasio SA, Richey E, Young GA. IN SEARCH OF THE TRUE TEMPERATURE AND STRESS INTENSITY FACTOR DEPENDENCIES FOR PWSCC. 12th Int. Conf. Environ. Degrad. Mater. Nucl. Power Sytems - Water React., The Minerals, Metals and Materials Society.; 2005, p. 977–88.

[43] Richey E, Morton DS, Etien RA. SCC initiation testing of nickel-based alloys in high temperature water. 13th Int. Conf. Environ. Degrad. Mater. Nucl. power Syst., Whistler, BC (Canada): Canadian Nuclear Society; 2007.

[44] Fournier L, Calonne O, Combrade P, Scott P, Chou P, Pathania R. Grain Boundary Oxidation and Embrittlement Prior to Crack Initiation in Alloy 600 in PWR Primary Water. 15th Int. Conf. Environ. Degrad. Mater. Nucl. Power Syst. React., John Wiley & Sons, Inc.; 2012, p. 1491–501.

[45] Andresen PL, Morra MM, Ahluwalia K. SCC of Alloy 690 and its Weld Metals. 15th Int. Conf. Environ. Degrad. Mater. Nucl. Power Syst. React., John Wiley & Sons, Inc.; 2012, p. 161–76.

[46] Bruemmer SM, Olszta MJ, Toloczko MB, Thomas LE. High-Resolution Characterizations of Grain Boundary Damage and Stress Corrosion Cracks in Cold-Rolled Alloy 690. 15th Int. Conf. Environ. Degrad. Mater. Nucl. Power Syst. React., John Wiley & Sons, Inc.; 2012, p. 301–14.

[47] Tsutsumi K, Couvant T. Evaluation of the Susceptibility to SCC Initiation of Alloy 690 in Simulated PWR Primary Water. 15th Int. Conf. Environ. Degrad. Mater. Nucl. Power Syst. React., John Wiley & Sons, Inc.; 2012, p. 41–52.

[48] Peng Q, Shoji T, Hou J, Takeda Y, Yonezawa T. Environmentally Assisted Crack Growth in Cold Worked Alloy 690TT in Primary Water at Low and High Temperatures. 15th Int. Conf. Environ. Degrad. Mater. Nucl. Power Syst. React., John Wiley & Sons, Inc.; 2012, p. 149–58.

[49] Arioka K, Yamada T, Miyamoto T, Terachi T. Dependence of Stress Corrosion Cracking of Alloy 690 on Temperature, Cold Work, and Carbide Precipitation—Role of Diffusion of Vacancies at Crack Tips. Corrosion 2011;67:35006–18.

[50] Hickling J, Ahluwalia K. Materials Reliability Program: Resistance of Alloys 690, 52 and 152 to Primary Water Stress Corrosion Cracking (MRP-237, Rev. 1): Summary of Findings From Completed and Ongoing Test Programs Since 2004, 1018130. Palo Alto, CA: 2008.

[51] Ahluwalia K. Materials Reliability Program: Resistance of Alloys 690, 152, and 52 to Primary Water Stress Corrosion Cracking (MRP-237, Rev.2): Summary of Findings Between 2008 and 2012 from Completed and Ongoing Test Programs, 3002000190. Palo Alto, CA: 2013.

[52] Toloczko MB, Olszta MJ, Bruemmer S. Update on SCC Initiation Testing of Cold-Worked Alloy 690 in PWR Primary Water. EPRI MRP PWSCC Expert Panel Meet., Tampa, FL: 2013.

[53] Teysseyre S, Was GS. Stress Corrosion Cracking of Austenitic Alloys in Supercritical Water. Corrosion 2006;62:1100.

[54] Medway S. AMEC A690 Summary. EPRI MRP PWSCC Expert Panel Meet., Tampa, FL: 2012.

[55] Rebak RB, Xia Z, Szklarska-Smialowska Z. Effect of Temperature and Cold Work on the Crack Growth Rate of Alloy 600 in Primary Water. Corrosion 1995;51:689.

[56] Andresen PL, Morra MM. Stress Corrosion Cracking of Stainless Steels and Nickel Alloys in High-Temperature Water. Corrosion 2008;64:15–29.

[57] Scott PM. 2000 F.N. Speller Award Lecture: Stress Corrosion Cracking in Pressurized Water Reactors—Interpretation, Modeling, and Remedies. Corrosion 2000;56:771.

[58] Panter J, Viguier B, Cloue J, Foucault M, Combrade P, Andrieu E. Influence of oxide films on primary water stress corrosion cracking initiation of alloy 600. J Nucl Mater 2006;348:213–21.

[59] Rebak RB, Szklarska-Smialowska Z. Technical Note: Effect of Specimen Thickness on Cracking Susceptibility of Alloy 600 in High-Temperature Water. Corrosion 1995;51:376.

[60] Bandy R, Rooyen D Van. Stress Corrosion Cracking of Inconel Alloy 600 in High Temperature Water—An Update. Corrosion 1984;40:425–30.

[61] Kroenke WC, Economy G, Jacko RJ, Powell GJ, Hyatt BZ. Acclerated steam plus hydrogen tests for Alloy 600 wrought and welded specimens. Philadelphia, PA: 1995.

[62] Scott PM. An Overview of Internal Oxidation as a Possible Explanation of Intergranular Stress Corrosion Cracking of Alloy 600 in PWRs. 9th Int. Conf. Environ. Degrad. Mater. Nucl. Power Syst. — Water React., Newport Beach, CA: The Minerals, Metals and Materials Society.; 1999.

[63] Sedricks AJ, Schultz JW, Cordovi MA. Inconel Alloy 690 - A New Corrosion Resistant Material. Corros Eng 1979;28:82–95.

[64] Sarver JM, Crum JR, Mankins WL. Carbide Precipitation and the Effect of Thermal Treatments on the SCC Behavior of Inconel Alloy 690. 3rd Int. Conf. Environ. Degrad. Mater. Nucl. Power Syst. — Water React., Traverse City, MI: 1987, p. 581–6.

[65] Watanabe Y, Abe H, Daigo Y. Environmentally Assisted Cracking of Sensitized Stainless Steel in Supercritical Water : Effects of Physical Property of Water 2003:1–4.

[66] Olszta MJ, Schreiber DK, Toloczko MB, Bruemmer SM. Microstructure, Corrosion and Stress Corrosion Crack Initiation of Alloy 600 in PWR PRimary Water Environments (Technical Milestone Report: M3LW-13OR0403032). 2013.

[67] Was GS, Teysseyre S, Jiao Z. Corrosion of Austenitic Alloys in Supercritical Water. Corrosion 2006;62:989–1005.

[68] Alexandreanu B, Was GS. A priori determination of the sampling size for grain-boundary character distribution and grain-boundary degradation analysis. Philos Mag A 2001;81:1951–65.

[69] Lozano-Perez S. A guide on FIB preparation of samples containing stress corrosion crack tips for TEM and atom-probe analysis. Micron 2008;39:320–8.

[70] Attanasio SA, Morton DS. Measurement of the Nickel/Nickel Oxide Transition in Ni-Cr-Fe Alloys and Updated Data and Correlations to Quantify the Effect of Aqueous Hydrogen on Primary Water SCC. 11th Int. Conf. Environ. Degrad. Mater. Nucl. Power Syst. — Water React., 2003, p. 143–55.

[71] Lemmon EW, McLinden MO, Friend DG. NIST Standard Reference Database. In: Linstrom PJ, Mallard WG, editors. NIST Chem. Webb. 69th ed., Gaithersburg MD, 20899: National Institute of Standards and Technology; n.d.

[72] Bronson HL, Hewson EW, Wilson AJC. The Heat Capacity of Silver and Nickel Between 100 and 500C. Can J Res 1936;14A:194–9.

[73] Connelly DL, Loomis JS, Mapother DE. Specific Heat of Nickel near the Curie Temperature. Phys Rev B 1971;3:924–34.

[74] Keem JE, Honig JM. Selected Electrical and Thermal Properties of Undoped Nickel Oxide. Cent Inf Numer Data Anal Synth 1978;52.

[75] Marshall WL. Complete Equilibrium Constants, Electrolyte Equilibria, and Reaction Rates. J Phys Chem 1970;74:346–55.

[76] Ziemniak SE. Metal Oxide Solubility Behavior in High Temperature Aqueous Solutions. J Solution Chem 1992;21:745–60.

[77] Kofstad P. High Temperature Corrosion. vol. 39. London – New York: Elsevier Applied Science Publishers Ltd.; 1988.

[78] Machet A, Galtayries A, Marcus P, Combrade P, Jolivet P, Scott P. XPS study of oxides formed on nickel-base alloys in high-temperature and high-pressure water. Surf Interface Anal 2002;34:197–200.

[79] Zhong X, Han E-H, Wu X. Corrosion behavior of Alloy 690 in aerated supercritical water. Corros Sci 2013;66:369–79.

[80] El-Gomati M, Zaggout F, Jayacody H, Tear S, Wilson K. Why is it possible to detect doped regions of semiconductors in low voltage SEM: a review and update. Surf Interface Anal 2005;37:901–11.

[81] Olszta MJ, Schreiber DK, Thomas LE, Bruemmer SM. Penetrative Internal Oxidation from Alloy 690 Surfaces and Stress Corrosion Crack Walls during Exposure to PWR Primary Water. 15th Int. Conf. Environ. Degrad. Mater. Nucl. Power Syst. React., John Wiley & Sons, Inc.; 2012, p. 331–42.

[82] Fujii K, Miura T, Nishioka H, Fukuya K. Degradation of Grain Boundary Strength by Oxidation in Alloy 600. 15th Int. Conf. Environ. Degrad. Mater. Nucl. Power Syst. React., John Wiley & Sons, Inc.; 2012, p. 1447–58.

[83] Bruemmer S, Olszta MJ, Schreiber DK, Toloczko MB. SCC Initiation Measurements on Alloy 600 and 690 in PWR Primary Water. Alloy 690 PWSCC Collab. Meet., Tampa, FL: 2014.

[84] Boursier JM, Vaillant F, Saulay P, Brechet Y, Zacharie G. Effect of the Strain Rate on the Stress Corrosion Cracking in High Temperature Primary Water : Comparison between the Alloys 690 and 600. 11th Int. Conf. Environ. Degrad. Mater. Nucl. Power Syst. — Water React., Stevenson, Washington: 2003.

[85] Gulsoy G. MECHANISM OF INTERNAL OXIDATION OF ALLOY 617 IN CONTROLLED IMPURITY HELIUM ENVIRONMENTS AT HIGH TEMPERATURES. University of Michigan, 2014.

[86] Atkinson A, Taylor RI. The diffusion of 63Ni along grain boundaries in nickel oxide. Philos Mag A 1981;43:979.

[87] Smith AF, Gibbs GB. Volume and Grain-Boundary Diffusion in 20 Cr/25 Ni/Nb Stainless Steel. Met Sci 1969;3:93–4.

[88] Atkinson A, O'Dwyer ML, Taylor RI. 55Fe diffusion in magnetite crystals at 500° C and its relevance to oxidation of iron. J Mater Sci 1983;18:2371–9.

[89] Tang J, Myers M, Bosnick KA, Brus LE. Magnetite Fe3O4 Nanocrystals: Spectroscopic Observation of Aqueous Oxidation Kinetics†. J Phys Chem B 2003;107:7501–6.

[90] Kofstad P, Lillerud KP. Chromium transport through Cr2O3 scales I. On lattice diffusion of chromium. Oxid Met 1982;17:177–94.

[91] Chen T-F, Tiwari G, Iijima Y, Yamauchi K. Volume and Grain Boundary Diffusion of Chromium in Ni-Base Ni-Cr-Fe Alloys. Mater Trans 2003;44:40–6.

[92] HAGEL WC. Anion Diffusion in α-Cr2O3. J Am Ceram Soc 1965;48:70–5.

[93] Nam HO, Hwang IS, Lee KH, Kim JH. A first-principles study of the diffusion of atomic oxygen in nickel. Corros Sci 2013;75:248–55.

[94] Zholobov SP, Malex MD. Diffusion of Oxygen in a Metal in Electron Bombardment of the Surface. Sov Phys — Tech Phys 1971;16:488.